Viscoelastic Modeling of Microelectronic Packaging Polymers Including Moisture Effects

by

Nusrat Jahan Chhanda

A dissertation submitted to the Graduate Faculty of
Auburn University
in partial fulfillment of the
requirements for the Degree of
Doctor of Philosophy

Auburn, Alabama
May 10, 2015

Keywords: underfill, encapsulant, viscoelastic, material behavior, creep, constitutive models, moisture

Approved by

Jeffrey C. Suhling, Chair, Quina Distinguished Professor of Mechanical Engineering
Pradeep Lall, Thomas Walter Professor of Mechanical Engineering
Hareesh V. Tippur, McWane Professor of Mechanical Engineering
Edward Davis, Lecturer of Polymer and Fiber Engineering

Abstract

Reliable, consistent, and comprehensive material property data are needed for microelectronics encapsulants for the purpose of mechanical design, reliability assessment, and process optimization of electronic packages. Since the vast majority of contemporary underfills and other microelectronic packaging polymers used are epoxy based, they have the propensity to adsorb moisture, which can lead to undesirable changes in their mechanical and adhesion behaviors. In this study, the mechanical behavior of microelectronic packaging polymers including moisture effects has been evaluated experimentally and theoretically.

A novel specimen preparation procedure has been used to manufacture uniaxial tension test samples. The materials were dispensed and cured with production equipment using the same conditions as those used in actual flip chip assembly, and no release agent was required to extract the specimens from the mold. The fabricated uniaxial test specimens were then exposed in an adjustable thermal and humidity chamber to combined hygrothermal exposures for various durations. After moisture preconditioning, a microscale tension-torsion testing machine was used to evaluate the complete stress-strain behavior of the material at several temperatures. The viscoelastic mechanical response of the underfill encapsulant has also been characterized via creep testing for a large range of applied stress levels and temperatures before and after moisture exposure.

From the recorded results, it was found that the moisture exposures strongly affected the mechanical properties of the tested underfill and other polymers including the initial elastic modulus and ultimate tensile stress. With the obtained mechanical property data, a three-dimensional linear viscoelastic model based on Prony series response functions has been applied to fit the stress-strain and creep data, and excellent correlation had been obtained for samples with and without moisture exposure. The effects of moisture were built into the model using the observed changes in the glass transition temperature within the WLF Shift Function.

Moreover, the surface morphologies of the fractured polymer specimens have also been analyzed in some cases using optical microscopic view to understand the effect of moisture exposure. The viscoelastic model for underfill has also been implemented in finite element analysis. Quarter models of flip chip on laminate assembly have been developed. The first model was used to analyze the time dependent variations of the stresses in the underfill and silicon die obtained with the viscoelastic model which have then been compared to the time-independent results from the conventional elastic-plastic material model. The second model has been developed to study the effects of moisture exposure in underfill layer on the mechanical behavior of other components of the assembly.

Acknowledgments

It is indeed a great pleasure and proud privilege for the author to express her deepest sense of sincere thanks and gratitude to her supervisor, Dr. Jeffrey C. Suhling for his supervision and untiring support that were a constant source of inspiration throughout this research work. The author owes to him for his continuous guidance and valuable suggestions without which this study would be difficult. Sincere appreciation is sent to advisory committee members and university reader including Dr. Pradeep Lall, Dr. Hareesh V. Tippur, Dr. Edward Davis and Dr. Michael J. Bozack for their insightful instruction and discussion regarding this research. The author expresses her heartiest gratitude to Dr. Edward Davis for helping her with his laboratory equipments whenever necessary. Special thanks are also extended to all her co-workers and friends, Dr. Chang Lin, Dr. Zijie Cai, Dr. Mohammad Motalab, Dr. Jordan Roberts, Dr. Muhannad Mustafa, Safina Hussain, Munshi Basit, Kun-yen Wang, Md. Hasnine, Sudan Ahmed, Promod Chowdhury, Nianjun Fu, Chienchih Chen, Quang Nguyen, Mr. Michael Palmer and Mr. John Marcell for their help, encouragement and friendship.

The author also owe to her parents, Mrs. Niger Sultana and Mr. M. A. Mannan and her brothers, for their endless love and support to her life and study in the United States. Lastly, she would like to thank her husband Dr. Muhannad Mustafa, and daughter Ajrin J. Muhannad for their patience, continuous support and inspiration about the progress of this work.

Table of Contents

List of Tables

List of Figures

CHAPTER 1

INTRODUCTION

1.1 Microelectronic Packaging

Microelectronic packaging is a major discipline which refers to the interconnections that are established between various levels of electronic devices, components and systems to provide proper signal and power distribution, way of heat dissipation (cooling) and protection of components, devices or the system from the environment shown in Figure 1.1. The packaging process starts with a chip which has been diced from a wafer of silicon. The chip contains electronic devices (transistors, resistors etc.) that are interconnected to form integrated circuits in order to perform a desired electrical function. After testing, the chip is placed in a chip carrier and small wires or solder balls are used to electrically connect the chip to the carrier. The chip carrier is often referred to as the first level of packaging, while the electrical connections to the chip carrier are called the first level of interconnects. Then, several chip carriers are placed on a circuit board (PCB) or substrate (second level of packaging) and connected together with wiring traces (second level of interconnects). In the third level of packaging, edge connectors on the circuit boards are then inserted into contacts on a back panel of motherboard. Cables are used to connect the power supply to the back panel and which bring the input and output signals to and from the unit. Finally, the

entire array of circuit boards, back panels, power supplies and cables are housed in a cabinet (fourth level of packaging) shown in Figure 1.2.

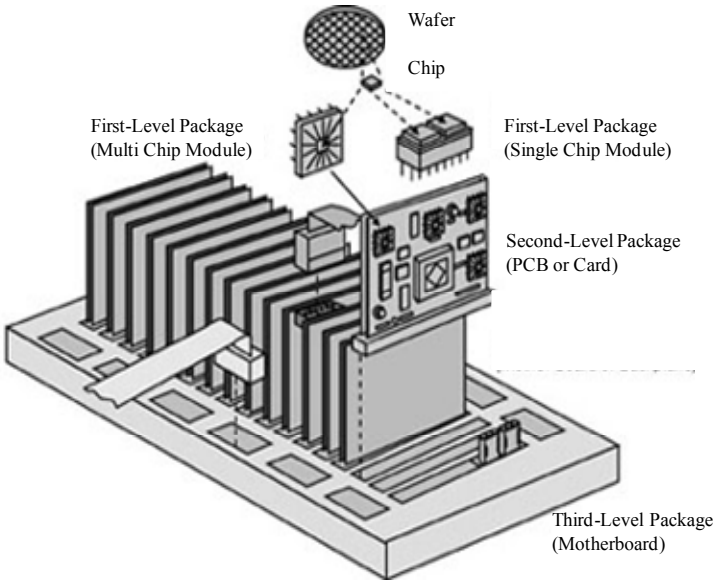

(http://www.ewh.ieee.org/soc/cpmt/press/graphics/Ch01_15.jpg)

Figure 1.1 Hierarchy of Microelectronic Packaging

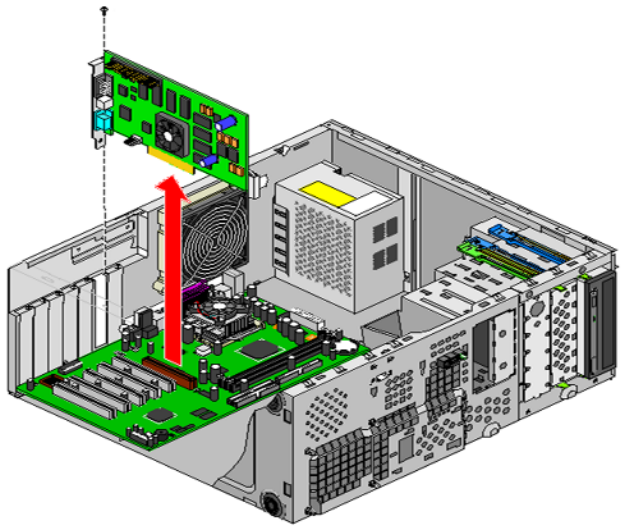

(http://techpubs.sgi.com/library/dynaweb_docs/hdwr/SGI_EndUser/books/230_UG/sgi_html/figures/2-27.rem.expansion.card.gif)

Figure 1.2 Different Levels of Microelectronic Packaging in a Casing

1.2 Polymers in Microelectronic Packaging

With long-term dimensional stability and long-term strength properties, polymer materials are widely used in microelectronic packaging. Some polymer materials are used in bulk form such as encapsulants (molding compounds), or as the matrix material in fiber-reinforced printed circuit boards (FR4 and BT). Encapsulation provides both the chemical and mechanical protection of the package to achieve a reasonable life expectancy of the device under different working environments. Other polymer materials are used as bonding agents such as die attachment adhesives, underfills, thermal interface materials, and structural/thermal adhesives. Polymers are also used in thin and thick films as isolation layers such as soldermasks on printed circuit boards or passivation layer at the wafer level. Figure 1.3 shows two different underfills (UF1 and UF2), thermal interface materials (TIM1 and TIM2) and adhesive are used in the flip chip ceramic ball grid array (FC-CBGA) packaging geometry.

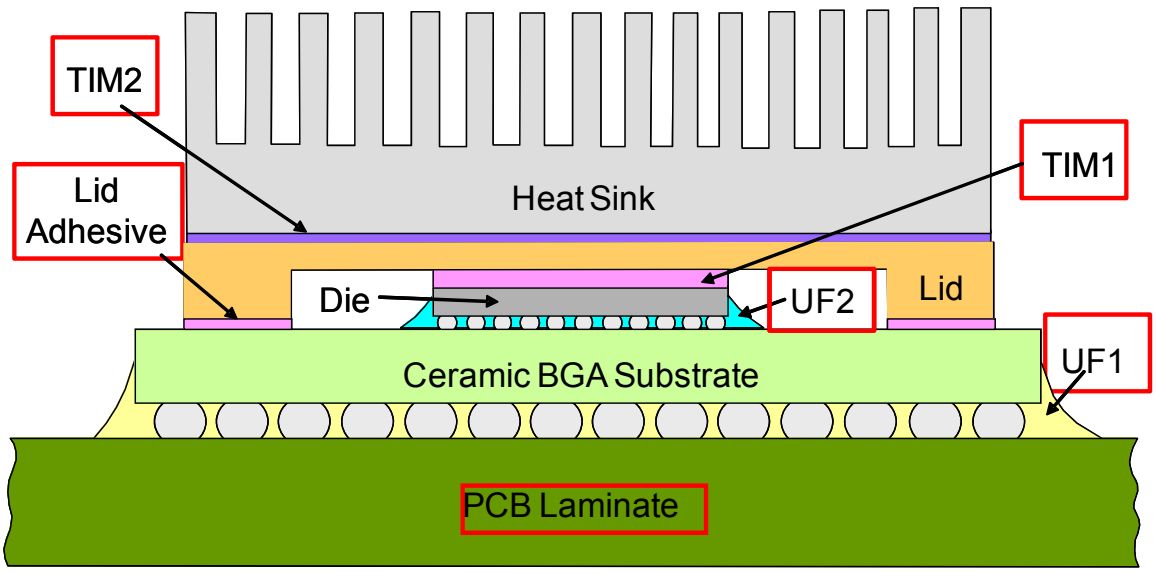

Figure 1.3 Flip Chip and BGA

1.2.1 Underfill (UF)

Underfill materials are critical for achieving reliability of several packaging architectures. These materials are added to provide a stronger mechanical connection and reduce the solder joint strains occurring with temperature changes due to the mismatches of coefficients of thermal expansion (CTE) of the various assembly materials. Since its origins at IBM in the 1970s, underfill technology has been part of the electronics manufacturing landscape [1]. There are three types of underfill systems currently in use: capillary underfills, fluxing (no-flow) underfills, and 4-corner or corner-dot underfill systems. While all have their advantages and limitations, capillary underfills are the most widely used of these materials.

Capillary underfills provide reliability enhancement by equally distributing stress across the chip's surface. In this process, the chip is attached to the substrate onto deposited solder paste attachment sites. When it is reflowed, a metallic interconnection is formed. Following this process, underfill material is applied using dispensing technologies to one or two of the edges of the CSP (Figure 1.4). Material flows underneath the package and gaps between the CSP and substrate are encapsulated.

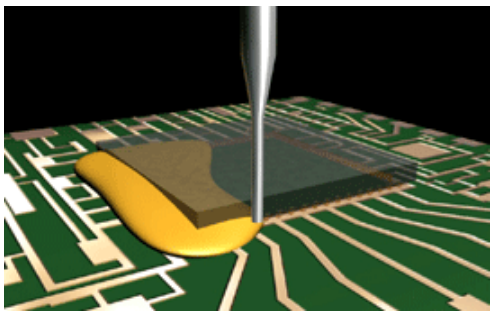

(http://www.namics.co.jp/e/product/img/chipcoat01_main.gif)

Figure 1.4 Capillary Underfill Applications

Despite of the advantages of capillary underfill, incorporating them into the manufacturing process requires dispensing equipment, floor space to house the equipment, and dedicated operator staff. Because of these investment requirements and the need for time-saving enhancements, fluxing (no-flow) underfill technology was introduced. The primary advantage of no-flow underfill technology over other underfill systems is process improvement, as opposed to significant material property enhancements. Moreover, no-flow underfills eliminate the need for a dedicated curing oven. By incorporating the fluxing function in the underfill, CSP attachment and material cure are combined into one step. During the assembly process, no-flow underfill is applied to the CSP attachment site before the component is placed. When the board goes through reflow, the underfill performs as the flux, allows the metallic interconnection to form, and completes cure in the reflow oven. So, underfilling can be achieved in the course of traditional assembly process steps (Figure 1.5).

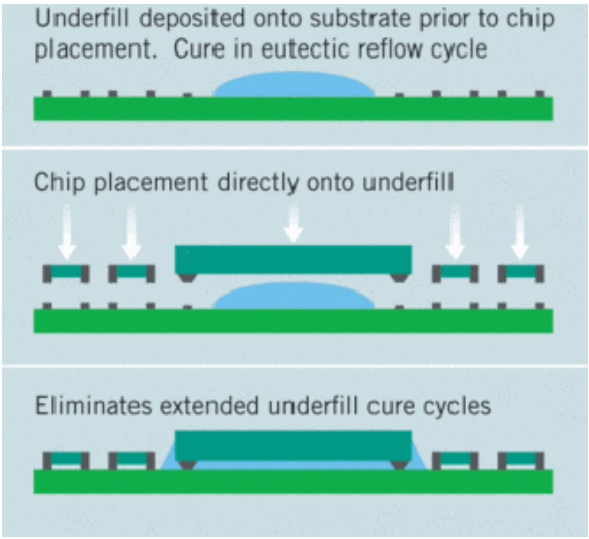

(http://www.ems007.com/articlefiles/61197-th_0805smtstepbystep03.gif)

Figure 1.5 Basic Process for No-Flow Underfill Materials

While no-flow underfills provide substantial cost and time savings from an equipment and personnel investment standpoint, there are some limitations. Unlike capillary underfills, no-flow materials are unfilled products by necessity. Filler materials in underfills can hinder contact between the solder balls and pads. By design, therefore, these systems are absent of particles to promote better solder joint formation during reflow. Without these particles, the coefficient of thermal expansion (CTE) is high, so thermal cycling performance is not as robust as that of capillary underfills. Also, being processed through traditional reflow can result in yield disadvantages if the process is not carefully controlled. Moisture trapped in the boards can escape during reflow, causing voids. However, new technology shows great promise for resolving these issues.

For applications such as CSPs with interposers, or corner arrays that are not as conducive to capillary flow or no-flow underfill systems, corner-dot underfill provides an alternative. This technology involves dispensing pre-applied underfill at the corners of the CSP pad site. Like no-flow underfills, corner-dot technology can be incorporated using existing assembly equipment resources and cured during normal solder reflow. Because these underfills are reworkable, manufacturers also can avoid scrapping an entire assembly if there is only one defective device.

1.2.2 Die Attach

Die attach adhesive (Figure 1.6) is an insulator that is dispensed in a pattern, and is used to bond the opposite side of the circuit on an IC chip, which has conductive bumps, to a mounting substrate. In the early 1980s, the uses of flexible die attach film and paste adhesives were introduced for larger die in microelectronic packaging.

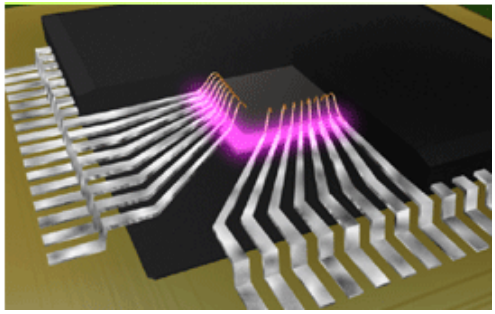

(http://www.namics.co.jp/e/product/img/chipcoat08_main.gif)

Figure 1.6 Die Attach Adhesive

1.2.3 Thermal Interface Material (TIM)

A material with high thermal conductivity that can conform to the imperfect mating surfaces is known as thermal interface material in microelectronic packaging. These materials are used to minimize the contact thermal resistance between the surfaces of the heat source (die) and the heat sink [2-3].

Thermal interface materials:

- Greases
- Phase change materials - A mixture of thermally conductive particles suspended in a base material like a fully refined paraffin, a polymer, a co-polymer, etc.
- Soft metal foils
- Elastomer paste
- Adhesives

Desired Properties of TIM:

- High thermal conductivity
- Easily deformed by small contact pressures
- Minimal thickness

- No leakage from the interface
- No deterioration over time
- Non-toxic
- Easy to apply/remove

1.2.4 Solder Mask

These are permanent solder resist (the green background surface that is seen on most circuit boards) is a very tough, durable epoxy or epoxy-acrylate coating (Figure 1.7).

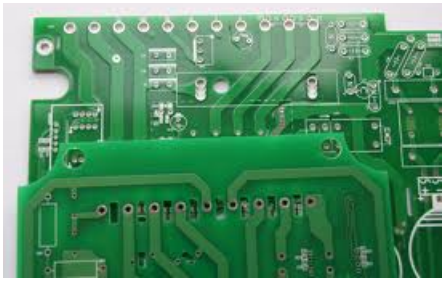

(http://www.chinapcbboard.com/photo/pl1572335-osp_double_sided_pcb_2_oz_copper_thickness_black_mat_green_solder_mask.jpg)

Figure 1.7 Solder Mask

Application

- Enable mass soldering techniques
- Prevent solder shorts under components
- Prevent corrosion to underlying circuitry
- Plating resist for surface finishes
- Prevent growth of metal whiskers
- Insulate substrate from debris and environment
- Assist with component placement

1.2.5 Passivation Layer

The processing of silicon wafers to produce integrated circuits involves a good deal of chemistry and physics. The finished wafer is covered with an insulating layer of glass and silicon nitride to protect it from contamination during assembly. This protective coating is called the passivation layer. Polymer Paasivation layer [4] can add a mechanical buffer to the front side of the wafer level chip scale package (WLCSP) and delivers improved reliability with conventional tools, short process times and lower costs.

1.2.6 Encasulants and Molding Compounds

Polymer encapsulants are materials that protect semiconductor devices and interconnects (e.g., wire bonding and solder bumps) from environmental factors such as moisture, corrosion-inducing contaminants, and ultraviolet radiation. Figure 1.8 shows typical designs of molding compounds used in microelectronic packaging.

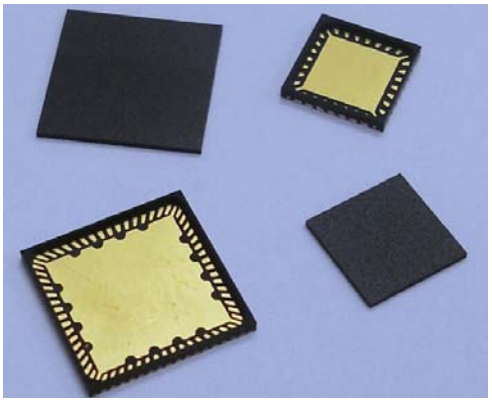

(http://icproto.com/typeroom/assets/uploads/images/OmPP_lids.jpg)

Figure 1.8 Molding Compounds

These polymers also protect the parts from mechanically induced damage such as bending, vibration, and material fatigue caused by thermal shock and temperature cycling during actual life applications.

1.2.7 Other Polymers

Polymers such as polycarbonates are capable of absorbing significant energy without cracking or breaking when they undergo large plastic deformations. Polycarbonate has a glass transition temperature of about 147 C (297 F), so it softens gradually above this point and flows above about 155 C (311 F). These types of polymers have found an extensive use in the field of microelectronic packaging for enclosures for cell phones and other products, as well as for the insulating housings used in connectors. Polycarbonate is mainly used for electronic applications that capitalize on its collective safety features. Being a good electrical insulator and having heat-resistant and flame-retardant properties, it is used in various products associated with electrical and telecommunications hardware. It can also serve as dielectric in high-stability capacitors. Moreover, Polycarbonates have been suggested as low cost temporary adhesives in wafer-wafer bonding [5].

1.3 Failure Mechanisms in Microelectronic Packaging Polymers

A reliable microelectronics package performs its electronic function properly throughout its expected lifetime in its normal ambient environment. Failure in microelectronics packaging mostly happens through polymer cracking, interface delamination and thermal fatigue, caused mainly by thermo-mechanical loadings [6]. As a result of device complexity and potentially harsh operating environments, the electrical and mechanical integrity of microelectronic packages becomes critical.

1.3.1 Moisture

Most polymeric materials, in spite of the diversities of the chemistry and compositions, are highly susceptible to the moisture adsorption. Using Dynamic Mechanical Analysis (DMA) testing, it is well known that hygrothermal exposures can lead to changes in the glass transition temperature and elastic modulus (storage modulus) of epoxy-based polymer encapsulants [7-8]. In addition, delamination and cracking in polymer encapsulants allows moisture to accumulate at the package interfaces, prompting additional failure modes and reducing reliability.

Historically, popcorn failures are well known moisture-induced failure modes in plastic packages subjected to humid environments. Such failures occur in four different stages (shown in Figure 1.9). In stage 1 (preconditioning), the package adsorbs moisture from the environment, which condenses in micropores in the polymeric package materials such as the PCB substrate, die-attachment adhesive, molding compound, as well as along the interfaces of these materials with other parts of the package such as the die, lead frame, etc. Preconditioning is a time-consuming process and usually takes a few days or even months in controlled or uncontrolled humid environments. In stage 2, the package is mounted on to the printed circuit board by soldering. During the reflow process, the entire package is exposed to temperatures as high as 250 C. As a result, the condensed moisture can vaporize under the sudden temperature rise associated with the soldering process. The vapor pressure and the reduction of the interface strength at high temperature due to the previous moisture intake will cause local interfacial delamination. In stage 3, the vapor pressure exerts compressive loading on the delaminated surfaces, eventually causing the package to bulge. In the final stage 4, a

package crack forms and propagates laterally outwards. When the crack reaches the package exterior, the high vapor pressure is suddenly released, producing an audible popping sound.

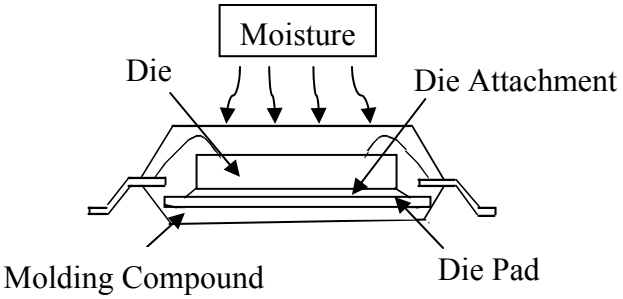

Stage 1: Package Absorbs Moisture

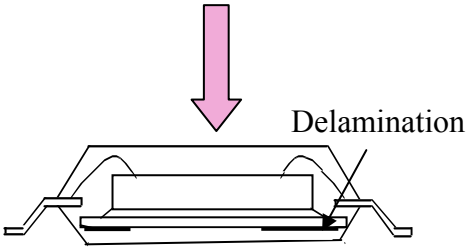

Stage 2: Interfacial Delamination

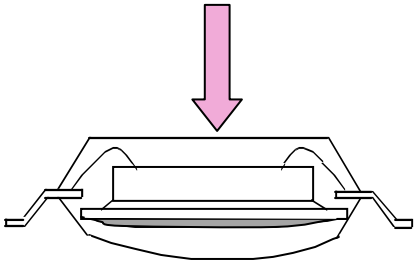

Stage 3: Package Bulging

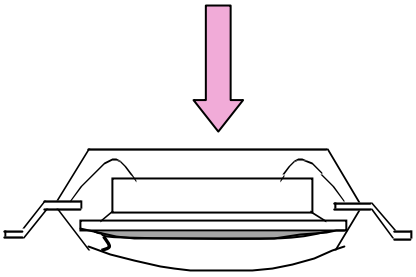

Stage 4: Package Cracking

Figure 1.9 Popcorn Failure Caused by Moisture

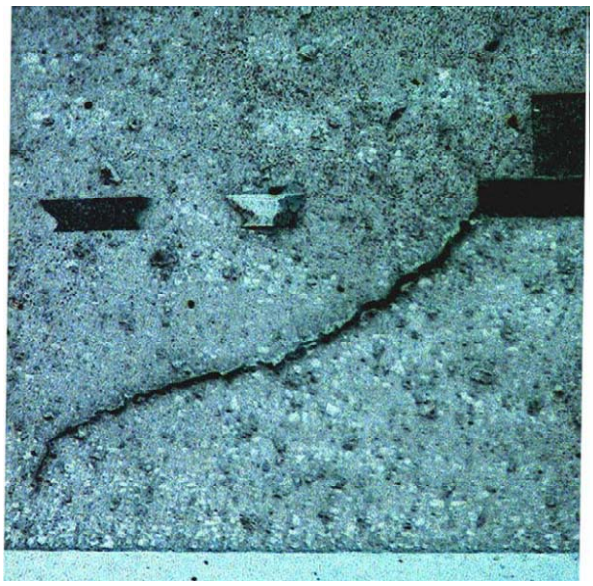

Figure 1.10 Popcorn Cracks [9]

Figure 1.10 depicts the response to the moisture adsorption which depends on the classification of the polymer present in the package assembly. Thermoplastic polymers, which are composed of long, flexible linear chains of smaller molecules, have a very porous structure, allowing the moisture to work its way in between the polymer chains. Such moisture penetration can separate the polymer chains enough to dissolve the polymer. Thermosetting polymers, which are composed of a rigid, three-dimensional cross-linked network between the polymer chains, are more resistant to moisture penetration and swell rather than dissolve in the presence of moisture. The amount of cross-linking between polymer chains affects the degree of swelling from moisture adsorption. Thermosetting polymers that are lightly cross-linked will swell more than those that are heavily cross-linked. Therefore, moisture uptake has an adverse effect on the polymer performance within the electronic package, resulting in either the polymer potentially dissolving or swelling.

1.3.2 Stress

Shrinkage of the polymer (as shown in Figure 1.11) [6] during cure as well as thermal expansion mismatches with the die, substrate, or lead frame creates mechanical stresses. The greatest source of stress at the die/substrate interface is the result of a thermal expansion mismatch between the components. When using underfill, delamination at the underfill/die or underfill/substrate interface often becomes the primary failure mode. Such delaminations occur when the interfacial stress between the underfill and silicon / substrate is higher than the interfacial adhesion strength of the underfill polymer. Figure 1.12 distinguishes a damaged part of Plastic Quad Flat Pack (QFP) due to delamination at the interface from a good part.

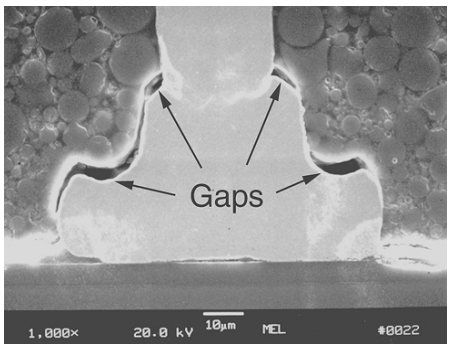

Figure 1.11 Molding Compound Shrinkage [9]

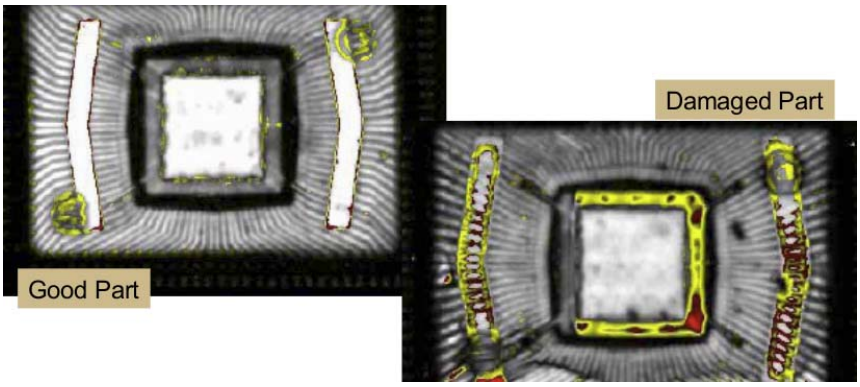

(http://aaq.auburn.edu/sites/default/files/images/counterfeitNewImages052.png)

Figure 1.12 Delamination at Die / Encapsulant Interface

Another detrimental consequences of stress developed in microelectronic packaging is cracking which may happen due to residual stresses from the production processes and initial strains due to the changing thermal and humidity conditions together with acting mechanical loading. Some examples of cracking in microelectronic packaging polymers are shown in Figure 1.13.

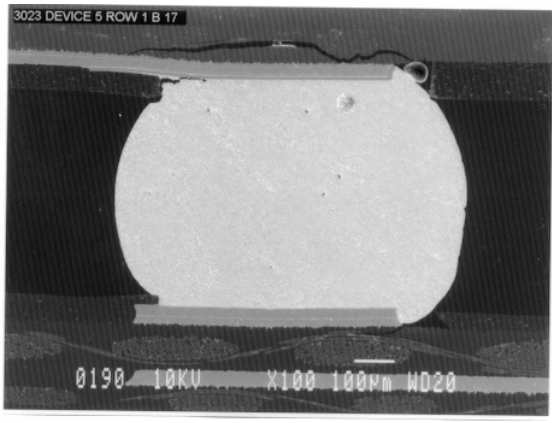

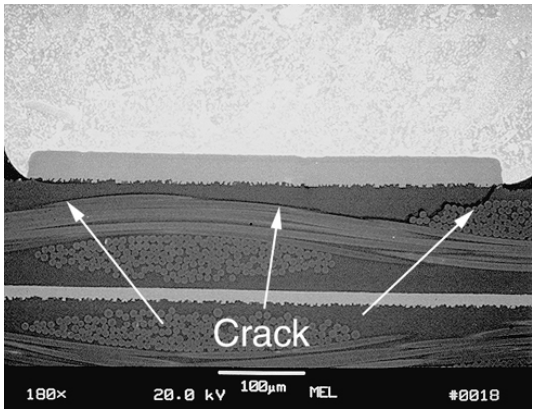

(a) Substrate Cracking [9]

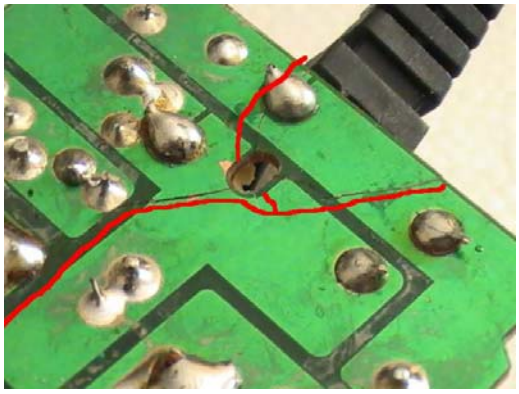

(http://i.imgur.com/c33yZ.jpg)

(b) Broken PCB

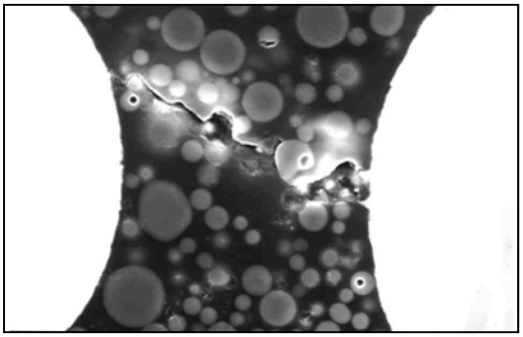

(c) Underfill Cracking

Figure 1.13 Cracking in Microelectronic Packaging Polymers

1.3.3 Corrosion

Corrosion refers to the degradation of the semiconductor metal traces on or within the die surface. This corrosion involves water and usually an ionic species that catalyzes the metal oxidation to a nonconductor. For epoxy molding compounds, the ionic species of greatest concern is the chloride ion [6]. Commercial polymer resins have tolerably low chloride levels, but other ions can come from the environment, typically from solder fluxes and other processing chemicals. These ions can quickly enter the package along any delamination pathway.

1.4 Mechanical Properties of Polymer Materials

Most polymers exhibit visco-elastic-plastic response. Viscoelasticity is a nonlinear material behavior having both an elastic (recoverable) part of the deformation as well as a viscous (non-recoverable) part. For this type of behavior the relationship between the stress and strain depends on time [10]. Viscoplasticity is characterized by the irreversible straining that occurs in a material over time. The deformation of materials is assumed to develop as a function of strain rate. In some applications, even a small viscoelastic response can be significant. Since polymers exhibit a complicated viscoelastic mechanical response that is highly sensitive to the temperature, isothermal aging, and thermal cycling effects, etc. so it is imperative to study the mechanical behavior of polymer materials to achieve reliability of microelectronic packaging. A viscoelastic material such as polymer has the following properties:

- Hysteresis: It is seen upon loading and unloading in the stress–strain curve
- Stress relaxation: step constant strain causes decreasing stress
- Creep: step constant stress causes increasing strain

1.4.1 Stress-Strain Behavior

The mechanical properties of polymers are most often obtained using a uniaxial tensile test at a constant strain rate. Tensile properties indicate how the material will react to forces being applied in tension. For perfectly elastic materials, extension and applied force are directly and simply proportional to each other. For extension, what is actually measured is the increase in length of the whole sample or a part of the sample. This difference is then expressed as a function of the starting length called the strain, ε.

$$\varepsilon = \frac{\Delta L}{L} = \frac{L_f - L_0}{L_0} \tag{1.1}$$

$L_{f\ is}$ the final (current) gage length and L_0 is the initial gage length. The force divided by the area across which the force is acting, is called the stress, σ.

$$\sigma = \frac{F}{A_0} \tag{1.2}$$

where F is the applied force, A_0 the original (unstressed) cross-sectional area. The stress and strain initially increase with a linear relationship. This is the linear-elastic portion of the curve where no plastic deformation has occurred. This means that when the stress is reduced, the material will return to its original shape. In this linear region, the material obeys the relationship defined by Hooke's Law where the ratio of stress to strain is a constant:

$$E = \frac{\sigma}{\varepsilon} \tag{1.3}$$

E is called the effective modulus, which is the slope of initial part of a stress-strain curve.

Unlike purely elastic materials, a viscoelastic material like polymer has an elastic component and a viscous component where the relationship between the stress and strain

depends on time. Purely elastic materials do not dissipate energy (heat) when a load is applied, then removed. However, a viscoelastic material loses energy when a load is applied, then removed. Hysteresis is observed in the stress–strain curve (shown in Figure 1.14), with the area of the loop being equal to the energy lost during the loading cycle. Since viscosity is the resistance to thermally activated plastic deformation, a viscous material will lose energy through a loading cycle.

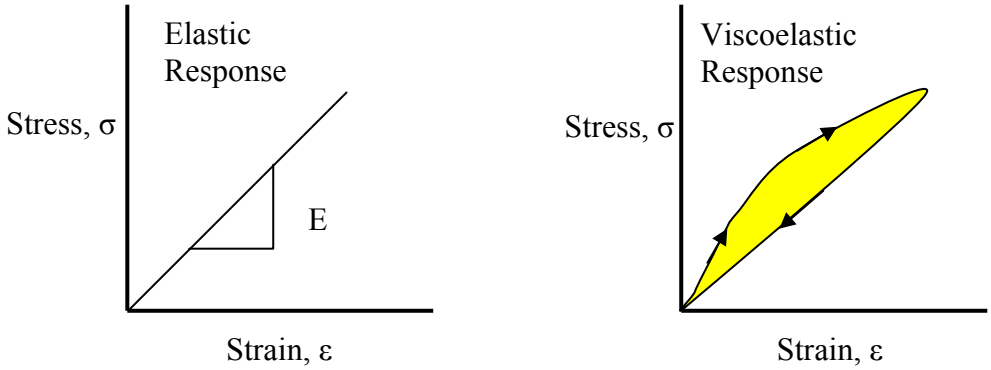

Figure 1.14 Elastic vs. Viscoelastic Response

A typical Stress-Strain curve for polymer is shown in Figure 1.15. The elastic modulus, E, is defined as the slope of the initial linear part of the stress-strain curve. The ultimate stress, σ_u is the maximum stress attained before failure and ε_f is the corresponding strain of ultimate stress.

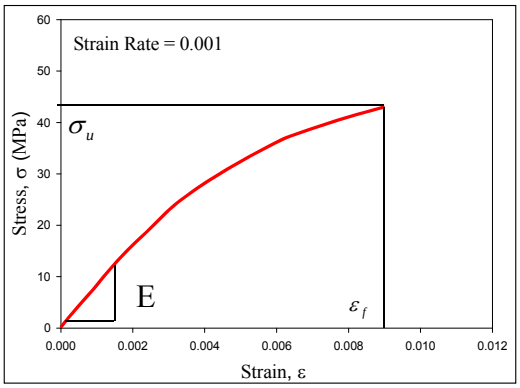

Figure 1.15 Typical Stress-Strain Response for Polymers

1.4.2 Glass Transition Temperature

The bonds of a polymer constantly break and reform due to thermal motion, and thereby viscoelastic properties change with increasing or decreasing temperature. In most cases, the creep modulus, defined as the ratio of applied stress to the time-dependent strain, decreases with increasing temperature. Moreover, it takes less work to stretch a viscoelastic material an equal distance at a higher temperature than it does at a lower temperature.

The glass transition temperature indicates the transition from the glassy (solid) state to the liquid or rubbery state. For polymers the glass transition temperature is not a single temperature but covers a range of about 20-50 C [11]. Figure 1.16 demonstrates three regions of viscoelastic behavior. The next region of visoelastic behavior is flow region: (rubbery flow and liquid flow) which is not shown in the figure.

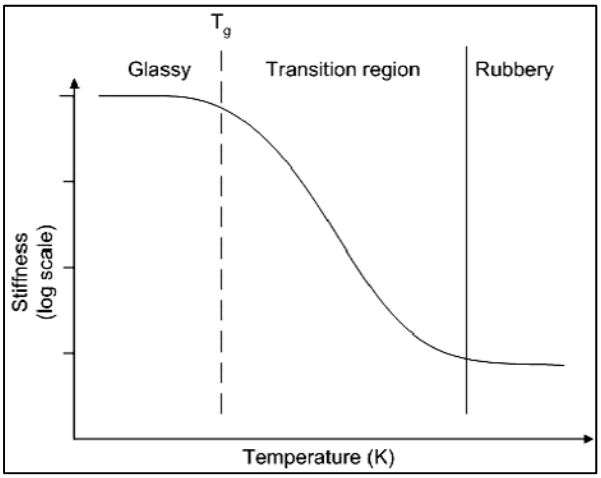

(http://www.tangram.co.uk/images/TI-Low%20Temperature1.jpg)

Figure 1.16 Modulus vs. Temperature Behavior

1.4.3 Stress Relaxation

One of the fundamental methods used to characterize the viscoelastic time-dependent behavior of a polymer is the relaxation test. In a relaxation test, a constant strain is applied quasi-statically to a uniaxial tensile sample at zero time. The sudden strain must not induce any dynamic or inertia effects.

In a relaxation test, it is also normal to assume that the material has no previous stress or strain history or if one did exist, the effect has been nullified in some way. If a polymer is loaded in the described manner, the stress needed to maintain the constant strain will decrease with time. The strain input and the stress output for typical polymer materials is shown in Figure 1.17.

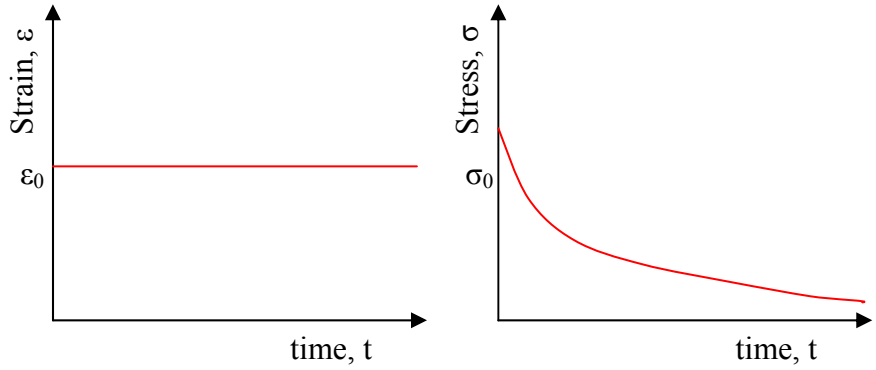

Figure 1.17 Relaxation Test: Strain input (left) and qualitative stress output (right)

Obviously, if the stress (σ) is a function of time and strain (ε_0) is constant, the modulus will also vary with time. The modulus so obtained is defined as the relaxation modulus of the polymer and is given by:

$$E(t) = \frac{\sigma(t)}{\varepsilon_0} = \text{RelaxationModulus} \tag{1.4}$$

1.4.4 Creep

In addition to the relaxation test, another fundamental characterization test for viscoelastic materials is the creep test in which a uniaxial tensile bar specimen is loaded with a constant stress at zero time as shown in Figure 1.18. Again, the load is applied quasi-statically or in such a manner as to avoid inertia effects and the material is assumed to have no prior history. In this case, the strain under the constant load increases with time and the test defines a new quantity called the creep compliance,

$$J(t)=\frac{\varepsilon(t)}{\sigma_0}=\text{Creep Compliance} \tag{1.5}$$

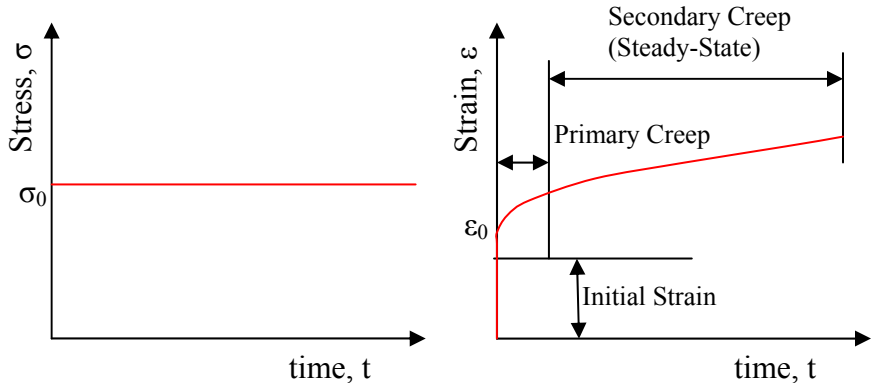

Figure 1.18 Creep Test: Stress input (left) and qualitative material strain response (right)

As indicated in Figure 1.18, the response begins with a quick transition to the initial "elastic" strain level, followed by two stages; namely, primary and secondary creep. In the primary stage, strain occurs at a relatively rapid rate after the instantaneous strain but then the rate gradually decreases until it becomes approximately constant during the secondary stage. This constant creep rate due to the dynamic balance of strain hardening is defined as the steady state creep rate. Unlike solder alloys, polymers do not

exhibit tertiary creep region. To determine the steady-state creep rate, the linear part of the curve is considered and the slope at the end is used.

1.5 Objectives of This Research

The motivation of this research is to systematically study viscoelastic modeling for microelectronic packaging polymers that can accurately represent mechanical behavior (both stress-strain and creep) before and after moisture absorption and to implement the observed response in finite element analysis (FEA). The following objectives will be achieved in this research:

1. To study the stress-strain (for different temperatures and different strain rates) and creep behavior (for different stress levels) of microelectronic packaging polymers;
2. To apply a 3D linear viscoelastic model based on Prony series response functions to predict stress-strain and creep behavior of microelectronic packaging polymers;
3. To develop analytical methods and finite element approaches to calculate the viscoelastic response using the Prony series model;
4. To explore the effects of moisture exposure on the mechanical behavior (glass-transition temperature and the total stress-strain response) of microelectronic packaging polymers;
5. To use the developed viscoelastic model in finite element analysis to predict the stress evolution in the silicon chip and underfill encapsulant in an underfilled flip chip assembly.

1.6 Organization of the Dissertation

This dissertation mainly focuses on understanding viscoelastic modeling of microelectronic packaging polymers including moisture effects and is presented in the following chapters:

Chapter 1: Introduction to microelectronic packaging polymers, failure mechanisms and mechanical properties of polymer materials in microelectronic packaging.

Chapter 2: Literature review on isothermal aging effects, mechanical properties, constitutive models and moisture effects on microelectronic packaging polymers.

Chapter 3: Description of experimental procedure, uniaxial tensile and creep tests and data processing.

Chapter 4: Description of experimental characterization of underfill encapsulants

Chapter 5: Study on constitutive modeling of microelectronic packaging polymers.

Chapter 6: Study on effects of moisture absorption on the mechanical behaviors of microelectronic packaging polymers.

Chapter 7: Implementation of the developed viscoelastic model in Finite Element Analysis (FEA).

Chapter 8: Summary and conclusions of the dissertation.

CHAPTER 2

LITERATURE REVIEW

2.1 Introduction

Polymers have been used as structural components of microelectronic packaging. So the packaging of microelectronic devices requires a number of unique properties from these materials. Electrical properties must be balanced with other performance requirements, such as environmental protection, the resistance to mechanical shock and the effects of temperature both above and below ambient conditions. Ease of application and good overall properties make polymers ideal candidates for microelectronic packaging. Such properties include excellent adhesion to many surfaces, superior thermal resistance, low dielectric constant, and ease of processing. The vast majority of contemporary polymers used are epoxy based and the adhesion and the mechanical properties of epoxies can be adapted to meet different requirements by using various additives. Moreover, these polymer materials exhibit time dependent mechanical response (viscoelasticity). This is potentially an important factor in the design of mechanical structures in which polymer is subjected to sustained loads. During the design process, finite element analysis (FEA) has been widely used to simulate the reliability of flip chip on laminate assemblies subjected to thermal cycling. Unfortunately, polymer mechanical property data are scarce on vendor datasheets, and

typically only the room temperature elastic modulus is available. To accurately model microelectronic packaging polymers, the time and temperature dependent mechanical properties of these materials must be investigated. The developed constitutive models can then be used for subsequent mechanics and reliability analyses performed using finite element analysis.

2.2 Effect of Fabrication on Material Properties

During experimental characterization, much of the challenge in obtaining a database of material properties for polymers results from the difficulty in preparing representative uniaxial test samples for mechanical testing. The material is cured rather evenly, with a cure profile dependent on the oven temperature profile and the thermal properties and configuration of the assembly materials. If large bulk strip samples of underfill (e.g. Feustal, et al., [12]) are prepared for material characterization using a molding procedure, it is likely that they will be subjected to nonuniform curing, and thus they will not illustrate the same mechanical response of actual flip chip underfill layers. If thin samples are manufactured, great care must be taken to achieve the correct cure profile, constant thickness, desired shape, etc. For any size specimen, a method must be developed to extract cured test samples from the mold that is utilized without inflicting damage or chemically changing the material. This can be challenging since underfills are by their nature also great adhesives.

Qian and coworkers [13] have made mechanical measurements on small underfill test samples. In their work, 0.5 mm (20 mil) thick samples were prepared in a metal mold exposed to the cure profile recommended by the underfill vendor. But the metal mold required use of a release agent, which chemically altered the surface of the underfill

samples. Their paper also focused on modeling mechanical properties of underfill (HYSOL FP4526) under glass transition region (110 C) as they claimed that the normal temperature of service conditions of packaging devices is usually lower than 100 C. In the work of Rao, et al. [14], small samples were cast in a dogbone shaped Teflon® mold. The samples in that study were also 0.5 mm thick. In addition, their work focused on use of a Dynamic Mechanical Analyzer (DMA) to characterize the stress-strain curves, and temperature dependent storage and loss moduli of the underfills.

A method for generating thin (0.1 mm thick) underfill test samples had been developed by Shi, et al. [15], and comprehensive mechanical testing was performed on a typical underfill material over a range of temperatures and strain rates. In that work, a complicated molding procedure was utilized to fabricate the specimens. The sample preparation procedure included steps to pour the underfill into the uncovered heated mold, and then place the steel cover onto the filled silicone rubber middle layer. Surplus underfill was pressed out through an exit trough, and the completed mold stack was placed in a box oven for curing. After molding, it was necessary to use fine sandpaper on the samples to remove undesired material and adjust the specimen dimensions. The completed samples had nominal dimensions of 20 x 3 x 0.1 mm. However, 10 mm of the length of the samples were buried in the specimen grips, leaving only a 10 x 3 x 0.1 mm sample of underfill being subjected to stress and strain. The length to width aspect ratio these samples was only 3.33, while at least 10-20 is typically desired to yield a reasonably pure uniaxial stress state in the specimen.

In the work of Islam and co-workers [16-18], an underfill mechanical test specimen preparation procedure had been developed that yielded 90 x 3 mm samples of

desired thickness (e.g. 0.075-0.125 mm). In the developed method, the test samples were dispensed between Teflon® coated plates and cured using production equipment and the same processing conditions as those used with actual flip chip assemblies. In addition, the active area of the extracted tensile samples (region between the specimen grips) was 60 x 3 mm, giving a highly desirable aspect ratio of 20. The specimens were dispensed using capillary flow (for which underfills were optimized). Using the developed samples, a microscale tension-torsion testing machine was used to evaluate the uniaxial tensile stress-strain behavior of underfill materials as a function of temperature and strain rate [17]. A three parameter hyperbolic tangent empirical model had been shown to provide accurate fits to the observed underfill nonlinear stress-strain behavior over a range of temperatures and strain rates. Kuo, et al. [19] had developed a similar method to fabricate freestanding thin sheets of underfill material by dispensing and curing between Teflon® coated sheets. They then cut samples with dimensions of 20 x 6 mm between the specimen grips (aspect ratio of 3.33), and performed investigations on the effects of temperature and strain rate on the tensile stress-strain behavior.

2.3 Characterization of Polymers

The mechanical properties of polymer materials are always the key concern of microelectronic packaging industry. Wun and Lau [20] illustrated the strong dependence of underfill material parameters on the cure schedule in their study. All the thermal and mechanical analysis reported in the analysis were performed using a Perkin-Elmer Series 7 TA System consisting of a DSC unit (Differential Scanning Calorimeter), a DMA/TMA unit (Dynamic Mechanical Analyzer / Temperature Mechanical Analyzer), and a TGA (Thermal Gravimetric Analyzer), and with all the standard softwares for kinetics and

viscoelasticity analysis. The study focused on the approach and data that were considered in selecting the appropriate underfill for flip chip application. Bimaterial strip bending experiment was employed successfully by Sham and Kim [21] to monitor the evolution of the residual stresses in underfrill resins for flip chip applications. Residual stresses were introduced in the plastic package when the polymer was cooled from the curing temperature to ambient, from which many reliability issues arose, including warpage of the package, premature interfacial failure, and degraded interconnections. A numerical analysis was developed to predict the residual stresses, which agreed well with the experimental measurements. Gilleo, et al. provided a status report on state-of-the-art underfill technologies in [22]. The authors discussed the necessity of using underfill, merits and demerits of different types of underfill and also the flip chip cost issues in the description..

The viscoplastic behavior of high density polyethylene, polypropylene, and polycarbonate under uniaxial tensile loading at constant strain rate and large strains were studied by [23]. Standard ASTM samples of the polymers cast by injection molding were tested at room temperature and constant crosshead speed. Speed maintained during the study was in the range of 5 to 300 mm/min. The authors found that yield strength increased with strain rate for the three polymers while the nominal strain for yielding was constant for polycarbonate, and decreased slightly for polypropylene and high density polyethylene. The large deformations that occur in polycarbonate take place after necking. This is opposite behavior to metals, which can sustain large deformations before necking and eventual failure. Mechanical behavior of such polymers was discussed by Boyce, et al. [24-25]. Temperature dependent behavior of polycarbonate

(tension, compression and shear) was illustrated in [26-27]. The yield behavior of polycarbonate in simple shear at constant shear strain rate is shown in Figure 2.1. Test temperature ranges from – 100 C to + 160 C (T_g = 140 C). The diagram shown in Figure 2.1 encompasses a wide range of interest, i.e. $T_{low} < T_g < T_{high}$, showing the change of behaviour from an elasto-plastic below T_g to a rubbery viscoelastic above T_g. In uniaxial modes of testing it is always observed that the yield strength is highest in compression, followed by tension, with the lowest value measured in shear as shown in Figure 2.2. This inequality, $\sigma_{yc} > \sigma_{yt} > \tau_{ysh}$, appears to be fundamental and ubiquitous for all amorphous polymers and any theory of yield strength must be consistent with this observation. Lobo and Croop [28] developed a consistent approach to obtaining clean, high quality tensile data on polymers at high strain rates. A variety of post-yield behaviours were also noted depending on polymer type and the presence of fillers in the study.

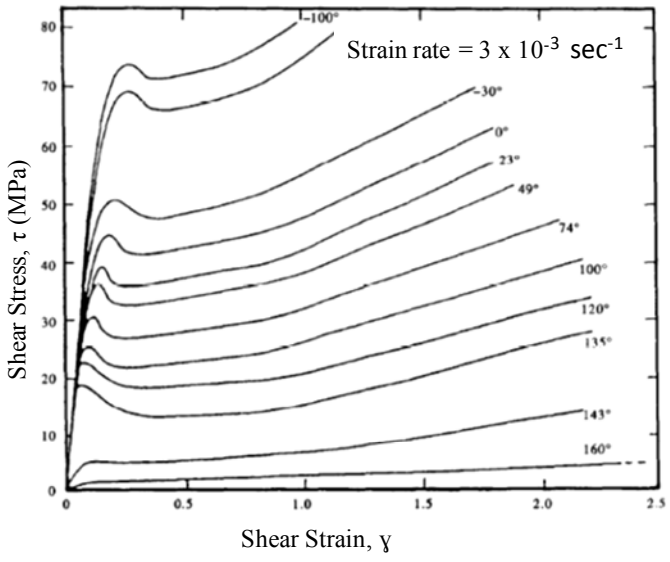

Figure 2.1 Temperature dependence of yield behavior of Polycarbonate in simple shear at constant shear strain rate [26, 27]

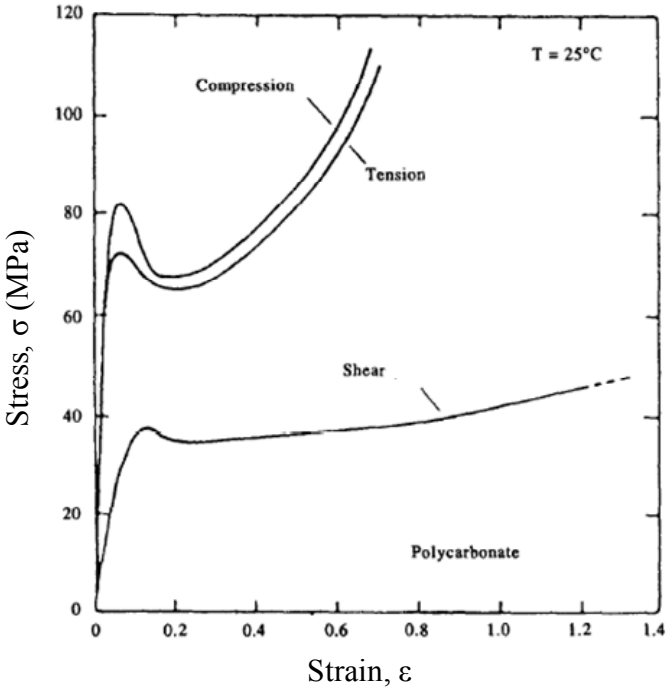

Figure 2.2 True-stress vs. true-strain behavior of polycarbonate (PC) under three modes of deformation: compression, tension and shear [26, 27]

Effects of the organoclay modifiers on the flammability, thermal and mechanical properties of the polycarbonate nanocomposites were studied by Feng, et al. [29]. This study employed limiting oxygen index, UL-94 burning test, thermo-gravimetric analysis, differential scanning calorimetry, tensile testing, and dynamic mechanical analysis. Their analysis demonstrated that a modifier bearing two long alkyl tails shows stronger affinity with the matrix than the one bearing a single tail. The feasibility of reprocessing had been investigated as a possible alternative of polycarbonate recycling by Pérez, et al. [30]. The effect on thermal and mechanical properties of polycarbonates after up to 10 reprocessing cycles and the effect of the combined reprocessing and accelerated weathering were analyzed in the study. Measurements collected after each molding cycle revealed a slight decrease of thermal properties. The same behavior was observed from

accelerated weathering tests. This study also illustrated that the modulus of elasticity or the tensile strength were not affected in the first seventh reprocessing cycles, whereas the impact strength decreased sharply. A similar study was conducted by Ronkay [31]. This research was aimed at analyzing the polycarbonate scrap arising during production and its possible secondary utilization. Changes in the mechanical properties were monitored by measuring the tensile and flexural impact properties. Test specimens were injection molded from various mixtures of the virgin pellets and reground material, using 10% steps. It was found that the tensile strength and the tensile elastic modulus did not change significantly, but that the elongation at break and the impact strength values decreased significantly. Based on these findings, the author concluded that the use of more than 20% reground recyclate results in significant deterioration of the mechanical properties (especially of the impact strength) of the material.

2.4 Moisture Effects on Material Properties

Since polymers are widely utilized in the microelectronic packaging industry, numerous studies have been carried out to characterize the effects of moisture on their behavior and reliability. For example, there have been several investigations on the effects of environmental exposures (isothermal aging with and without controlled humidity) on the behavior of molding compounds (encapsulants) and underfills. These studies have primarily focused on the evolution/degradation of interfacial failure properties with duration of exposure. For example, Lin, et al. [32] reported that adsorption of moisture in epoxy molding compounds can be problematic for plastic packaging manufacturers especially in areas where the weather is humid. They applied Differential Scanning Calorimetry (DSC), to characterize moisture uptake testing of

epoxy molding compounds. Ferguson and Qu [33] studied on the effect of moisture on the interfacial fracture toughness of two no-flow underfills. Bilayer underfill-soldermask/PCB specimens with prefabricated interface cracks were subjected to four-point bending testing to quantify the interfacial fracture toughness. Both fully dried and moisture preconditioned specimens were tested. It was found that moisture preconditioning strongly influenced the interfacial adhesion, decreasing the adhesion strength by approximately 50% for both underfill/solder mask interfaces after 725 hours of exposure at 85 C and 85% RH.

Fan, et al. [34] presented analytical solutions for void behavior at different stages, in bulk and at interface, based on the large deformation theory. Their results showed that the vapor pressure is not only responsible for the increasing of interfacial stresses, but also for the decreasing of interface strength. Moreover, the critical stress that resulted in unstable void growth and delamination at an interface was significantly reduced and comparable to the magnitude of vapor pressure. To investigate the mechanism for moisture induced failure in IC packages, a two-parameter delamination criterion was proposed by Fan and Lim [35] where the local void volume fraction was introduced. A rigid-plastic model was introduced to analyze the package bulging, and the limit pressure that leads the package to collapse was obtained. Kuo, et al. [19] have shown that there are dramatic reductions in the interfacial (adhesion) strength of the underfill/soldermask interface in lap shear specimens exposed to a combined humidity-temperature exposure (60 C and 95% RH for 168 hours). In addition, their data demonstrated a change in the constitutive behavior after thermal/humidity aging. In other studies of Ferguson and Qu [36-38], exposures to various combined humidity-temperature exposures (e.g. 85 C and

85% RH for 168 hours) were shown to have negligible long-term effects on the elastic modulus of the samples once the current conditions of the samples were all equilibrated by dry baking shown in Figure 2.3. However, the interfacial toughness was shown to drop with duration and severity of environmental exposure, including exposure to 85 C with no moisture (dry heat). Similar results were observed by Luo and Wong [39], who found the interfacial strength in special mechanical test specimens to degrade with duration of combine thermal/humidity aging at 85 C and 85% RH. They attributed this to build up of water at the interface. Finally, Zhang and co-workers [40] have measured crack opening displacements to characterize the changes occurring in the stress intensity factors at an interfacial crack along an underfill and silicon chip passivation interface as a function of both dry and moist aging at 85 C.

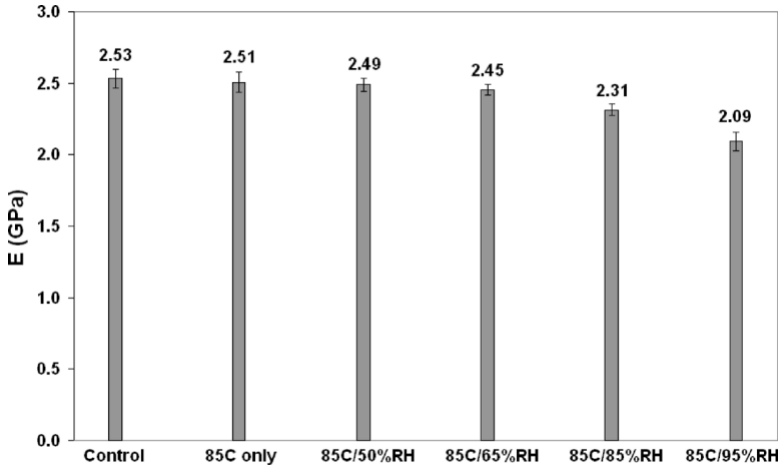

Figure 2.3 Elastic Modulus Variation of Underfill with Moisture Absorption [36-38]

DMA testing has been extensively utilized to characterize the effects of moisture adsorption on the glass transition temperature and elastic modulus vs. temperature response of polymers. Lu, et al. [41] demonstrated such changes for epoxy molding compounds used in microelectronic packaging. In addition, Park, et al. [42] had used DMA, DSC,

FTIR, shear strength, and tensile strength testing to study moisture effects on epoxy underfills. The modulus and strength behaviors were found to be strongly influenced by moisture adsorption. The adsorbed water acts as a plasticizer that reduces the modulus. However, there were also permanent chemical changes (hydrolysis) of the organic compounds that were not reversible. Their FTIR results showed that both the hydroxyl and carboxyl groups increased, and that the ester groups decreased with increased hygrothermal exposure (aging) in a high moisture (steam) environment. There have been relatively few studies on the effects of moisture on the total stress-strain response of microelectronic encapsulants and adhesives. Tian, et al. [43] have measured the effects of sample preconditioning (JEDEC MSL3) and cure profile on the stress-strain curves and mechanical properties of underfills, as well as the reliability of flip chip assemblies.

In the work of Lin, et al. [44-46], the enhancement of the mechanical properties of underfill with thermal aging has been reported. Both the effective elastic modulus (E, initial slope of the stress-strain curve) and ultimate tensile strength (UTS, highest stress before failure) increased monotonically with the amount of isothermal aging or aging temperature, regardless of whether the aging temperature is below, at, or above the T_g of the material. In general, the changes (increases) in E and UTS with aging were typically in the range of 10-40% of the non-aged values. Aging was also found to dramatically decrease (100X) the secondary creep rate of underfills subjected to up to 6 months of aging before testing. As expected, the largest changes were observed to occur with the higher aging temperatures (100, 125, and 150 C) near the T_g of the underfill material. At a given aging temperature, the properties were most affected in the temperature range 75-125 C. The evolutions of the material properties with time were found to be nonlinear

during the first 25-50 days of isothermal aging. After 50 days of aging, the changes become milder and progress in approximately a linear manner (steady state). Initial experimental measurements of material behavior changes occurring in polymer encapsulants exposed to a controlled temperature and humidity of 85 C and 85 % RH were presented by Chhanda, et al. [47]. The changes in mechanical behavior (e.g. stress-strain behavior) were recorded for the various durations of hygrothermal exposure. Reversibility tests were also conducted to evaluate whether the degradations in the mechanical properties were recoverable.

Problems associated with moisture in Polycarbonate during molding are described by Long and Sokol [48]. They found that molding with excess moisture content causes a chemical and physical degradation resulting in reduction in tensile impact strength, tensile elongation, ultimate tensile strength, proportional limit, and molecular weight. The authors used bolt holes in the tensile impact specimens to prevent slippage in the jaws. The samples were oven dried at 250 F for 23 hours prior to exposure of 49% RH at 75 F (23.8 C, room temperature). To detect the degradation, they used different techniques such as intrinsic viscosity, infrared spectrometry, and thermal methods of analysis. All tests were done at room temperature. The properties and structure of polycarbonate under hydrothermal aging were also investigated by Weibin, et al. [49]. Their results of mechanical testing indicated that there was an obvious reduction in elongation caused by the hygrothermal aging exposure. In addition, tensile testing, differential Scanning Calorimetry (DSC), Fourier Transform Infrared (FTIR) Spectroscopy, and Scanning Electron Microscopy (SEM) were employed in their analysis. The samples were exposed to 70 C and 80% RH

condition in a weathering durability tester for 26 days and tested at room temperature for different durations of moisture exposure.

2.5 Constitutive Modeling for Polymer Materials

Most of the investigations presented in the previous sections have concentrated on the effects of hygrothermal or isothermal aging on the mechanical properties of polymeric materials specially underfills and encapsulants used in microelectronic packaging. However, there has been little work on exploring constitutive models to depict the response of such materials under different loadings and thermal conditions [50-56]. According to the reported studies from1994 for the industry in Great Britain, the cost of destruction as a result of material plasticization was evaluated at a level of 300 million £ per year, from which 10% was attributed to destructions proceeding as a result of the creep process and stress-relaxation effects [57]. Majda and Skrodzewicz [58] performed experimental investigations of the creep behavior of epoxy adhesive- hardened samples. The examined adhesive was a nonlinear viscoelastic medium and did not obey the Boltzmann's superposition principle. The authors have considered several mathematical models which can ensure a proper description of the observed behavior of the material and the modified Burgers model had been finally developed for the studied adhesive. The creep deformations calculated for this model have demonstrated a very good consistency with the results of experimental investigations over the assumed range of stresses and the duration time of measurements. The thermo-mechanical behavior and constitutive modeling of HYSOL FP4526 underfill was reported by Qian, et al. [59]. The authors also confirmed that they did not observe any tertiary-stage creep until the rupture of a specimen. A micromechanics model based on the Mori–Tanaka method was

developed to estimate the elastic modulus of underfill materials by Qu and Wong [60]. An explicit expression of the underfill modulus was derived as a function of filler content and the properties of the matrix and the fillers. Predictions of the modulus from this theory were compared with experimentally measured values. Excellent agreement was observed. Wang, et al. [61] studied the rate-dependent strain-stress behavior of underfills based on two-phase composite assumption. The authors employed micromechanical method to predict the overall strain-stress behavior of underfills. However, they also agreed that the adopted method could not predict well the experimental data at elevated temperatures, especially temperatures near T_g.

A cure-dependent viscoelastic constitutive relation was applied to describe the curing process of epoxy underfill in Flip Chip on Board (FCOB) by Yang, et al. [62]. As known, polymer underfill is usually applied to improve the reliability of the package, by reducing the stresses of the solder bumps. Thus the fatigue life of solder joints of FCOB is strongly influenced by the mechanical properties of underfill polymers. In their analysis, the cure dependent constitutive relation and the corresponding parameters for underfill epoxy were incorporated in the finite element analysis code MARC. The solder bumps were modeled with temperature dependent visco-plastic properties. The curedependent viscoelastic model and a temperature dependent viscoelastic model were applied to describe the properties of the underfill resin during the curing process and subsequent thermal cycling, respectively. The fatigue life predictions were based on simulations with and without considering the curing process. The results showed that when the curing induced initial stress and strain fields were taken into account, the FEM fatigue life predictions matched better with the experimental results. Similar studies to

investigate curing process induced stresses were proposed originally by Kiasat, et al. [63, 64] for polyester resins. Then Ernst, et al. generalized the method in [65]. Further it was applied for describing cure dependent viscoelastic behavior of epoxy resin [66, 67] and was used to investigate the effect of curing process induced stresses on the die crack stress of a Flip Chip [68]. Thompson, et al. [69] built a finite element model of flip chip and applied viscoelastic model incorporated in ANSYS to depict the mechanical behavior of underfill polymers. Besides using conventional approach, the authors also attempted to utilize user-defined programmable function (UPF) of ANSYS to simulate polymer behavior during cure.

To examine the effects of moisture on the viscoelastic properties Ma, et al. [70] carried out several creep tests on moisture conditioned samples. The moisture contents were varied during the study. The authors have constructed master curves of creep compliance (shown in Figure 2.4(a)) for the dry samples and for the samples which were exposed to different amount of moisture content. They found that master curve shifted to the left with the increase of moisture content in the samples. As seen from Figure 2.4(b), the most left master curve was the one with the highest (1.4%) moisture content and the rightmost master curve was for the dried sample. The same authors have also studied the effect of filler contents on moisture exposure [71] and established the fact that the moisture content decreases with the increase of filler content as expected. Popelar and Liechti [72] conducted a series of experiments in order to evaluate and characterize the nonlinear behavior of epoxy. In their work, the Prony coefficients consisted of 12^{th} order expansionn for the shear modulus function, and a 9^{th} order expansion for the bulk modulus function. The developed linear viscoelastic model was then extended to account

for the nonlinear behavior of adhesive as illustrated in Figure 2.5. The proposed nonlinear model could capture nonlinear response in pure shear, and for shear with various amounts of superimposed tension or compression. Nitta, et al. [73] presented a method for the analysis of stress-strain curves for crystalline polymers such as polypropylene and polyethylene. A nonlinear Maxwell element consisting of a nonlinear spring and a linear dashpot with a tensile viscosity connected in series was the basis of their work. They reported that such a model made possible the evaluation of the plastic deformation fraction for crystalline polymers.

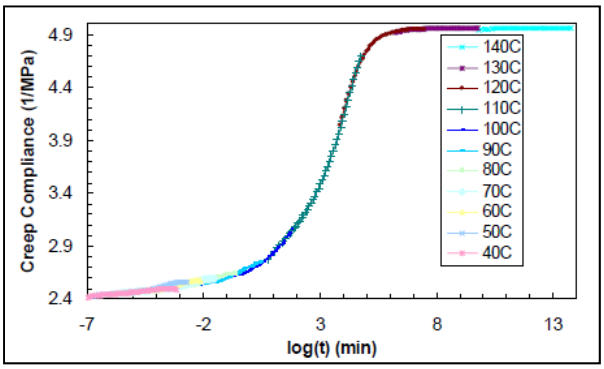

(a)

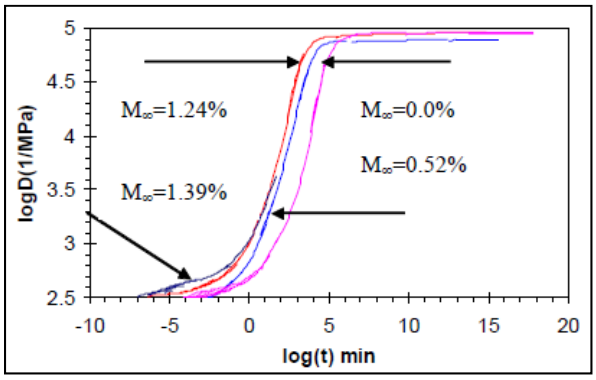

(b)

Figure 2.4 (a) Master Curve of Creep Compliance (b) Moisture Effects on Master Curves [70]

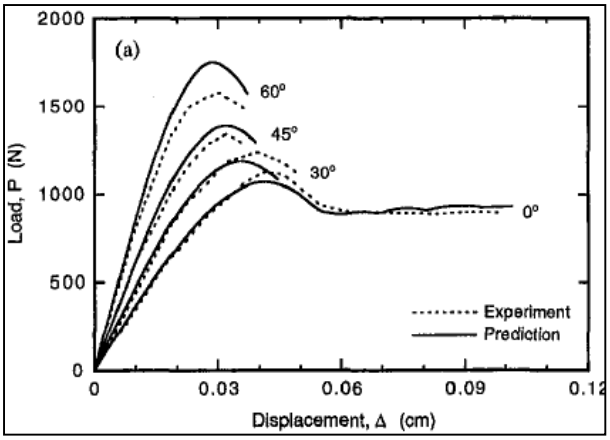

Figure 2.5 Viscoelastic Modeling Predictions for Adhesive [72]

The effects of underfill mechanical response on the thermomechanical behavior of flip chip packages were studied by Chen and coworkers [74]. Their investigation included thermal cycling of the package using both experimental testing and two-dimensional finite element simulations. They considered three different material models which were used to describe the mechanical response of the underfill. These included: (a) constant elastic model (elastic modulus and CTE are constant during thermal cycling with room temperature values); (b) elastic model with (temperature dependent elastic modulus and CTE; (c) viscoelastic model. Their results showed that the use of underfill encapsulant increased the thermal fatigue lifetime of solder joints tremendously, weakened the effects of stand-off height on the reliability, and changed the deformation mode of the package. The viscoelastic model they applied in their analysis was based on generalized Maxwell elements in an ANSYS finite element code. The master curve they generated was described as Prony series and the shift function had the form of Arrhenius relation. They found that using a constant elastic model for the underfill caused the thermal fatigue lifetime of solder joint to be overestimated. In addition, the viscoelastic model for underfill gave similar results to the temperature dependent elastic model.

Sham, et al. [75] also studied the reliability and mechanical performance of electronic packaging incorporating underfills using finite element analysis. They found that use of an elastic model for the underfill caused the thermal stress and the strain level in the solder joints to be underestimated significantly. In addition, the stress concentrations in the underfill fillet around the die corner were overestimated relative to the predictions of a viscoelastic model. Their results showed that it was essential to consider the viscoelastic nature of underfill for the failure of solder joints and lifetime of the package to be accurately predicted.

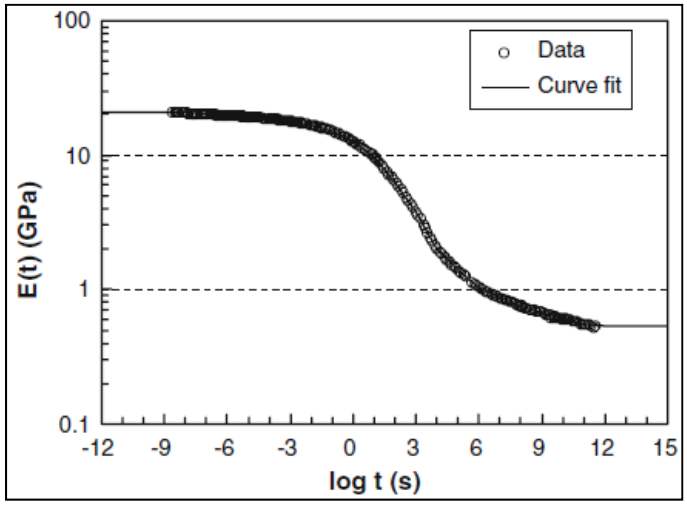

Figure 2.6 Master Curve Generated by Shifting the Relaxation Moduli [76]

Chae, et al. [76] performed stress relaxation experiments on a molding compound. A thermo-rheologically simple model was assumed to deduce the master curve of relaxation modulus (Figure 2.6) using the time–temperature equivalence assumption. A Prony series expansion (21st Order) was used to express the material's relaxation behavior. The Prony coefficients were determined for two reference temperatures. Two methods were utilized to carry out the curve fitting and to determine the Prony pairs and shift factors.

As discussed above, prior researches have demonstrated the effects of moisture exposures on the glass-transition temperature and elastic modulus and the importance of using viscoelastic models for underfill encapsulants and other polymers whereas there are few studies available on the viscoelastic modeling of a material that can accurately represent mechanical behavior (both stress-strain and creep) before and after moisture adsorption. In this work, the mechanical response of typical underfill encapsulant and other polymers such as adhesive and polycarbonate material have been characterized via rate dependent stress-strain testing over a wide temperature range, and via creep testing (for underfills) for a large range of applied stress levels and temperatures. The test specimens were dispensed and cured with production equipment using the same conditions as those used in actual flip chip assembly, and a microscale tension-torsion testing machine has been used to evaluate stress-strain and creep behavior of the materials as a function of temperature. To determine the effects of moisture, some test specimens were exposed to controlled temperature and humidity and tested at different temperatures. With the obtained mechanical property data of underfill, a linear viscoelastic model based on a Prony series expansion has been fit to the data (with and without moisture exposure), and optimum constitutive model coefficients for subsequent use in finite element simulations have been determined.

CHAPTER 3

SPECIMEN PREPARATION AND EXPERIMENTAL SET UP

3.1 Introduction

In this chapter, a unique preparation procedure of specimen is presented. This approach is able to fabricate micro-scale uniaxial specimens without further modification and machining. Four different types of microelectronic packaging polymers have been utilized during the study which were then subjected to mechanical testing i.e., tensile and creep test. The polymers include:

- Commercial BGA/CSP underfill manufactured by Zymet, Inc. (Zymet X6-82-5LV50), denoted as UF1 in this study
- Silica filled epoxy: Underfill (ME 525), denoted as UF2 in this study
- Polymer Encapsulant
- Polycarbonate

The preparation procedure of underfill is quite different from other polymers from the method point of view. However, for all polymer samples, the final dimension has been maintained as 80 x 3 mm. Uniaxial tensile and creep tests were then carried out by using a micro tension torsion testing system. Besides uniaxial testing, Differential Scanning Calorimetry (DSC) and Dynamic Mechanical Analyzer (DMA) have also been used to study glass transition region of polymers in some cases. To determine the effects of moisture, the specimens were exposed to controlled humidity. Programmable Tenney

BTRC and HOTPACK temperature/humidity chambers have been used for this purpose. An electronic scale has been used to monitor weight gain of specimen after moisture adsorption. Also, Normaski Optical Microscope (OM) was utilized to capture microscopic view of the failed surface of a polymer.

3.2 Specimen Preparation Procedure

3.2.1 Underfill

In this study, free standing underfill samples of UF1 and UF2 for mechanical testing were prepared using the procedure discussed in references [77-78]. A stacked assembly view of the "mold assembly" utilized in this investigation is pictured in Figure 3.1 (a), and Figure 3.1 (b) shows example uniaxial specimens after curing. The various parts of the assembly are clamped together by removable end clips (not shown). The middle layer consists of precision shims with a thickness (usually of 0.5 mm (20 mils) or 125 μm (5 mils)) defines the sample thickness. Usually the thickness is chosen depending on the typical thickness for BGA underfills in application. The molds are made from stainless steel and are coated with a thin Teflon® layer on all surfaces. The top portion of the mold assembly has been machined to contain 9 rectangular crossbars (80 x 3 mm) with a constant separation via the remaining steel material at the ends of the crossbars. The shims separating the two plates are only present under the front and rear "connecting regions" of the steel sheet, and not under the crossbars themselves. The mold assemblies were preheated to 112 C, and underfill encapsulant was dispensed along one side of each steel crossbar via a production line programmable dispense system (CAM/ALOT 3700 shown in Figure 3.2).

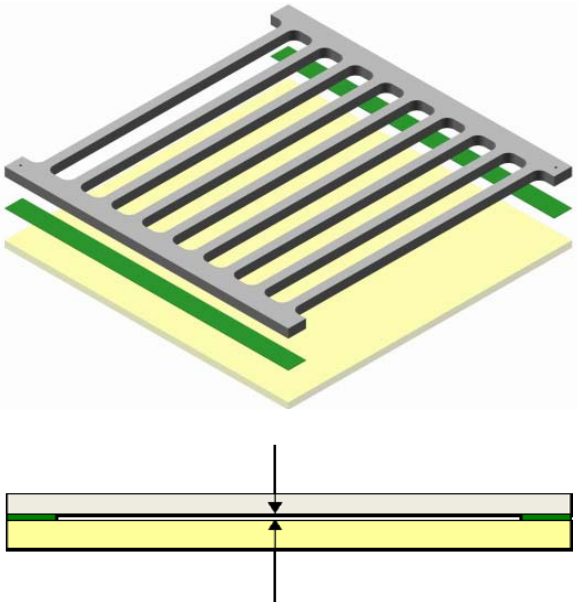

(a)

(b)

Figure 3.1 (a) Mold Assembly for Underfill (b) Underfill Test Specimens

Figure 3.2 Specimen Preparation Machine and Mold Assembly

Fuducial markings are included on the top of the steel sheet to aid in the programmability and repeatability of the dispense procedure. After dispense, the underfill encapsulant quickly ran under the gap under each crossbar via capillary flow. This procedure produced a set of constant thickness 80 x 3 mm rectangular underfill regions, which were sandwiched between the Teflon® coated top and bottom "mold plates". The uncured mold assemblies were then cured in a box oven (Figure 3.3) using the vendor recommended underfill cure profile. Due to the Teflon® coatings, the uniform thickness cured rectangular samples were easily separated from the mold. A razor blade and fine SiC paper were used to trim any unevenness from the ends of the samples. In the described method, the samples have a controllable constant thickness, and are easily removed from the mold assembly without the aid of chemical release agents. The lengths of the final trimmed samples (see Figure 3.1 (b)) were typically in the range of 70-90 mm, giving a specimen length to width aspect ratio of more than 20.

Figure 3.3 Box Oven for Curing

3.2.2 Polymer Encapsulant

A stacked assembly view of the specimen "mold assembly" utilized for polymer encapsulant is shown in Figure 3.4. The molds are made from stainless steel and are coated with a thin Teflon layer on all surfaces. The middle layer consists of precision shims with a thickness of 125 μm (5 mils). The shims separating the two plates were present under the front and rear "connecting regions" of the steel sheet.

The mold assemblies were first heated to 80 C for 10 minutes for dehydration of the Teflon layer. After this, a reasonable amount of polymer encapsulant was dispensed on the surface of an uncovered plate. Then, another plate was placed on top of it keeping a middle layer of specific thickness in between as shown in Figure 3.4. The various parts of the assembly were then clamped together by removable end clips (not shown in the figure). After clamping, the uncured mold assemblies were cured in a programmable thermal cycling chamber (Figure 3.5) using the vendor recommended cure profile. Thus this procedure produced a set of 0.125 mm constant thickness polymer regions, which were sandwiched between the Teflon coated top and bottom "mold plates".

The commercially available polymer encapsulant utilized in this work was epoxy-based with a glass transition region from 70 C to 90 C. The material was cured in 3 steps. In first step, the material was heated up from room temperature (25 C) to 85 C over 45 minutes. In second step, it was held at 85 C for 150 minutes. In the final step, it was ramped down from 85 C to 25 C over 45 minutes. The curing profile followed during the study is depicted in Figure 3.6. Thermocouples were used to measure the oven air temperature and actual temperature between molds.

Due to the Teflon coatings, the uniform thickness cured rectangular samples were easily separated from the mold. A precision saw (Figure 3.7) with diamond blade was used for cutting the samples to desired dimensions. In the described method, the samples have a controllable constant thickness, and are easily removed from the mold assembly without the aid of chemical release agents. The lengths of the final trimmed samples (see Figure 3.8) were typically in the range of 70-90 mm, while the widths were all 3 mm, giving a specimen length to width aspect ratio of more than 20. After having the desired dimension, the test specimens were ready for mechanical testing.

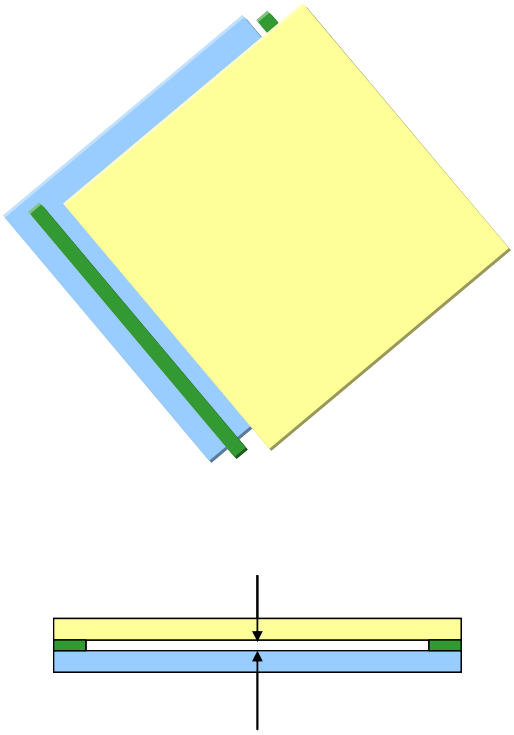

Figure 3.4 Mold Assembly for Polymer Encapsulant

Figure 3.5 Thermal Cycling Chamber

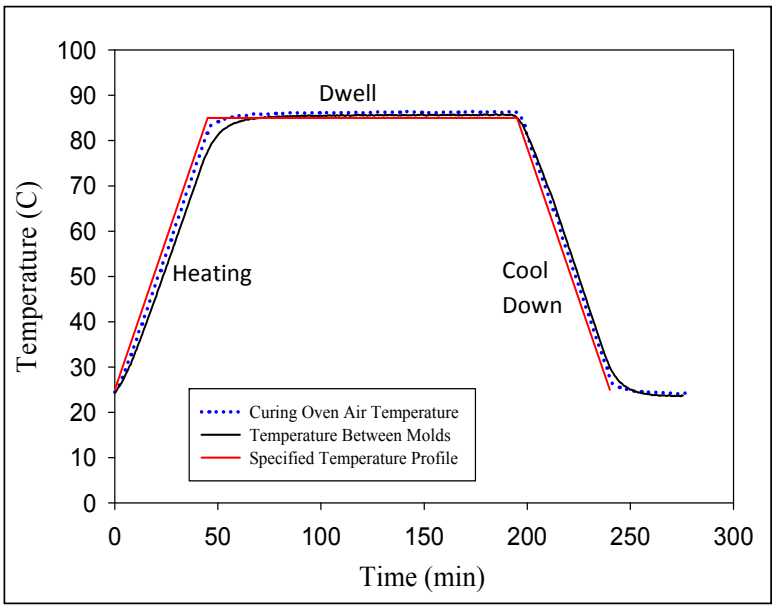

Figure 3.6 Curing Profile

Figure 3.7 Precision Saw

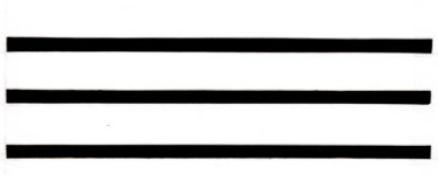

Figure 3.8 Test Specimens of Polymer Encapsulant

3.2.3 Polycarbonate

A limited number of dog-bone shaped polycarbonate specimens were provided by the material vendor. Each of these large specimens was then trimmed into several smaller uniaxial specimens with dimensions of 80 x 3 x 0.5 mm using a precision saw. The lengths of the final trimmed samples were typically in the range of 70-90 mm (shown in Figure 3.9), while the widths were all 3 mm, giving a specimen length to width aspect ratio of more than 20.

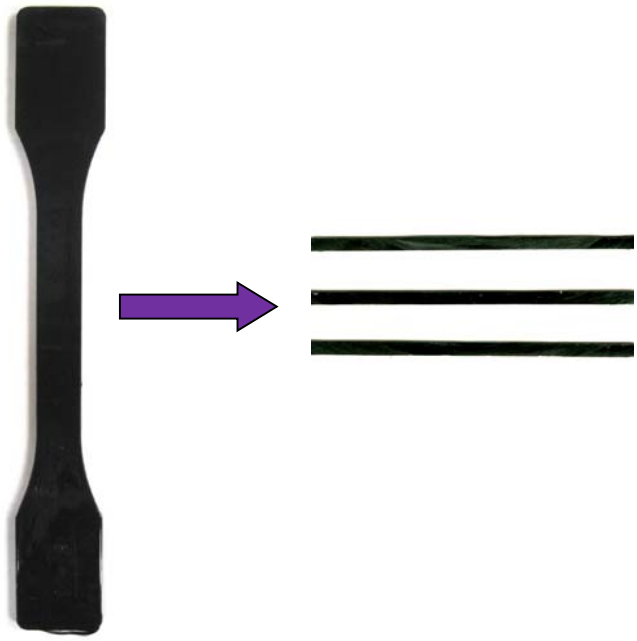

Figure 3.9 Final Test Specimens Cut from Dog-Bone Shaped Samples

3.3 Mechanical Testing System

In this study, a microscale tension/torsion thermo-mechanical test system from Wisdom Technology, Inc., as shown in Figure 3.10 has been utilized to load the samples. The associated environmental chambers are shown in Figure 3.11 and 3.12. The computer controlled actuators provide an axial displacement resolution of 0.1 micron and a rotation resolution of 0.001°. A universal 6-axis load cell was utilized to simultaneously monitor three forces and three moments/torques during sample mounting and testing. Testing can be performed in tension, shear, torsion, bending, and in combinations of these loadings, on small specimens such as thin films, solder joints, gold wire, fibers, etc. The hot and cold environmental chambers employ a resistance heater and liquid nitrogen diffuser to provide testing temperature ranges of +25 to +300 C and -185 to +25 C and, respectively.

During uniaxial testing, forces and displacements were measured. The axial stress and axial strain were calculated from the applied force and measured cross-head displacement using

$$\sigma = \frac{F}{A} \qquad \varepsilon = \frac{\Delta L}{L} = \frac{\delta}{L} \tag{3.1}$$

where σ is the uniaxial stress, ε is the uniaxial strain, F is the measured uniaxial force, A is the original cross-sectional area, δ is the measured cross-head displacement, and L is the specimen gage length (initial length between the grips). For the tests in this study, stroke (displacement) control was utilized.

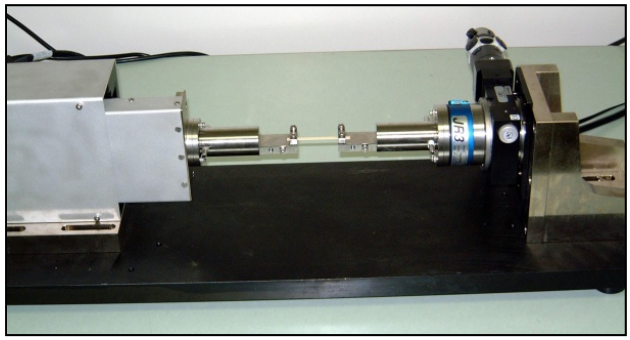

Figure 3.10 Testing System

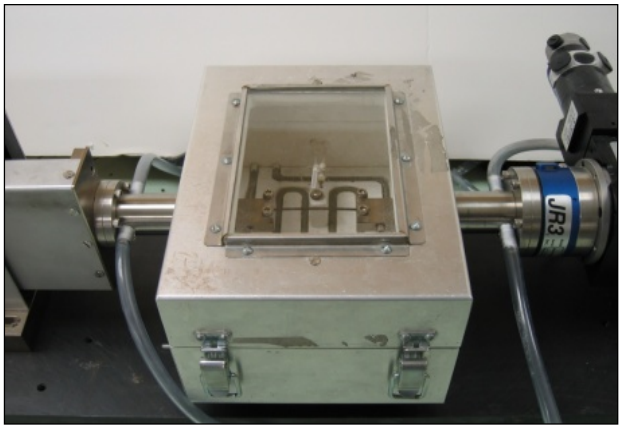

Figure 3.11 Chamber for Elevated Temperature Testing (+25 to +300 C)

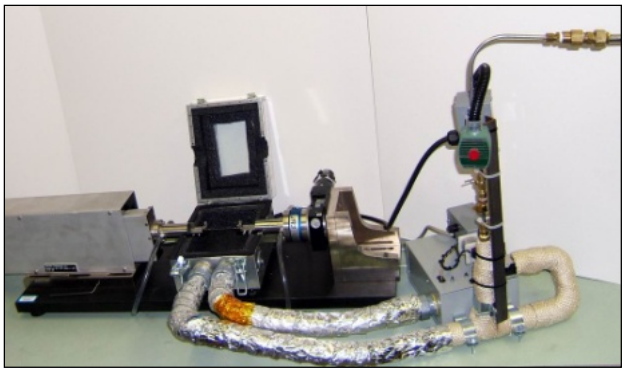

Figure 3.12 Chamber for Low Temperature Testing (-185 to +25 C)

3.4 Typical Testing Data and Data Processing

3.4.1 Stress-Strain Curve

A typical recorded tensile stress strain curve for polymer with labeled standard material properties is shown in Figure 3.13. The notation "E" is taken to be the effective modulus, which is the initial slope of the stress-strain curve. The ultimate stress, σ_u is the maximum stress attained before failure and ε_f is the corresponding strain of ultimate stress.

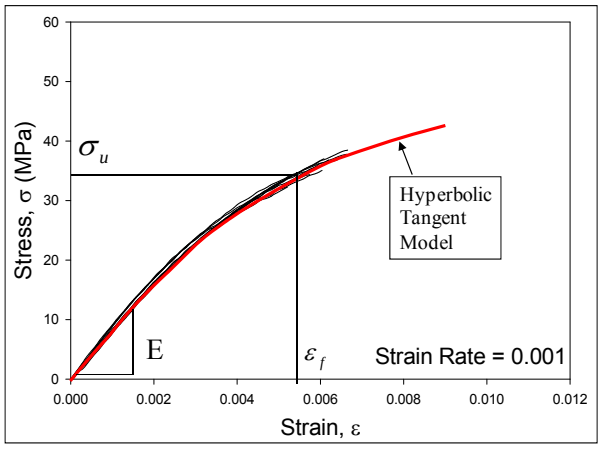

Figure 3.13 Typical Polymer Stress-Strain Curve and Material Properties

An empirical three-parameter hyperbolic tangent model has been used to accurately model the observed nonlinear stress-strain data at any temperature. The general representation of this relation is

$$\sigma(\varepsilon) = C_1 \tanh(C_2\varepsilon) + C_3\varepsilon \tag{3.2}$$

The unit of C_1 and C_3 are MPa whereas C_2 is unitless. C_1, C_2 and C_3 are material constants that can be determined by performing a nonlinear regression fit of eq. (3.2) to a given set of experimental data. For example, Figure 3.13 shows the associated hyperbolic tangent model fit to all of the raw stress-strain data at a temperature. The observed variation in the data between different tests at one condition is typical for cured polymeric materials. The hyperbolic tangent model fit (red curve) provides an excellent representation to the data that lies in the middle of all of the experimental curves. The accurate representation obtained using the hyperbolic tangent empirical model suggests that it provides a mathematical description of a suitable "average" stress-strain curve for a set of experimental curves measured under fixed test conditions. Thus, all data presented in this study have been processed in this manner. In each case, from 3-5 experimental stress-strain curves were initially measured, and then fit by an "average" stress-strain curve that mathematically represents the entire data set.

When the strain is very small ($\varepsilon \to 0$), the effective modulus (E) can be estimated from the relation as:

$$\begin{aligned}\lim_{\varepsilon\to 0}\frac{d\sigma(\varepsilon)}{d\varepsilon} &= \lim_{\varepsilon\to 0} C_1C_2\left\{\left(1-\tanh^2(C_2\varepsilon)\right)+C_3\right\}\\ &= C_1C_2 + C_3\end{aligned} \tag{3.3}$$

Thus the initial elastic modulus has been calculated from the three material constants which is shown as:

$$E = \sigma'(0) = C_1 C_2 + C_3 \tag{3.4}$$

3.4.2 Creep Curve

Figure 3.14 illustrates a typical polymer creep curve (strain vs. time response for a constant applied stress). The load input of a creep test has been calculated as:

$$F = \left(\sigma \times w \times t \times 10^3\right)/g \tag{3.5}$$

where F is the input holding force in gram, σ is the applied stress level for the creep test in MPa, w is the specimen width in mm, t is the specimen thickness in mm, and g is the acceleration of gravity (9.8 m/sec^2).

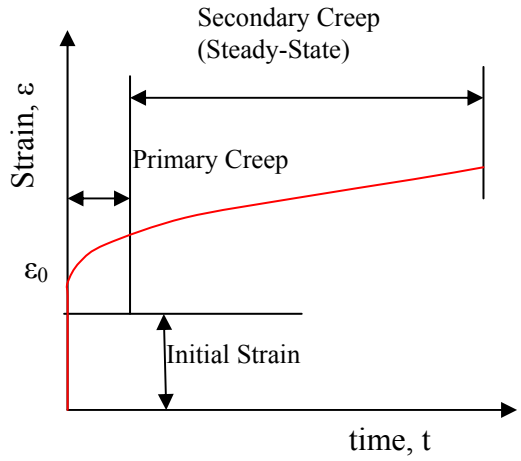

Figure 3.14 Typical Creep Curve and Material Properties

Creep response begins with a quick transition to the initial "elastic" strain level, followed by regions of primary and secondary creep. The secondary creep region is typically characterized by a very long duration of nearly constant slope. This slope is referred to as the "steady state" secondary creep rate, and it is often used by practicing engineers as one of the key material parameters in finite element simulations. In this

work, the measured creep rates were taken to be the slope values at the end of the linear portion in the observed secondary creep regions.

In the creep experiments, constant stress levels on the order of 25-75% of the observed UTS have been applied. Due to the long testing time involved, only 3 specimens have been tested for each set of condition. The curves in each set were fitted with an empirical strain-time model to generate an "average" representation of the creep response for those conditions. For the range of test conditions considered in this work, the raw strain versus time data in the primary and secondary creep regions were found to be well fitted by an empirical Log Hyperbolic Tangent model (see Figure 3.15):

$$\varepsilon_{cr} = C_1 t + C_2 \ln(1+t) + C_3 \tanh(C_4 t) \tag{3.6}$$

Constant C_1 is the long-term (steady state) creep rate in the secondary creep region. Constants C_2 and C_3 are parameters used to describe the nonlinear response in the primary creep region. From the recorded strain vs. time curves under constant stress, the "steady state" creep strain rates have been extracted. Variations of the secondary creep rates with temperature and stress levels have been determined and then Generalized Garofalo Model has been used to fit the data. The expression of Generalized Garofalo Mode [79] is as follows:

$$\dot{\varepsilon}_{cr} = C_1 [\sinh(C_2 \sigma)]^{C_3} e^{-C_4/T} \tag{3.7}$$

The unit of C_1, C_2 and C_4 are sec^{-1}, 1/MPa and Kelvin respectively. C_3 is unitless.

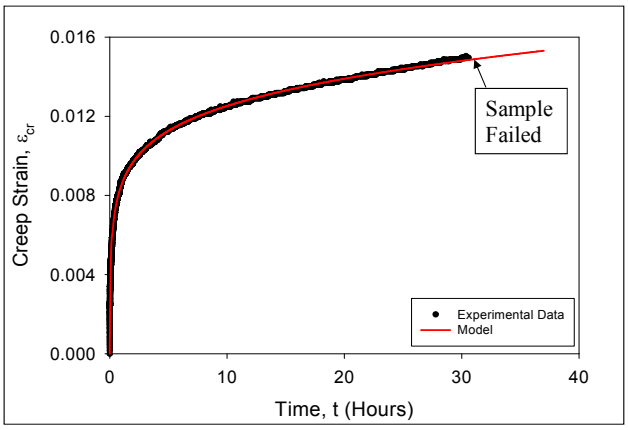

Figure 3.15 Polymer Creep Curve and Log Hyperbolic Tangent Model

3.5 Investigation of Glass Transition Region

The glass transition temperature, T_g is widely used in the electronic industry to depict indirectly the cure of epoxy coatings, underfill, encapsulants, adhesives and printed circuit boards. T_g can be measured by a variety of thermal analysis techniques such as Dynamic Mechanical Analysis (DMA), Differential Scanning Calorimetry (DSC), Thermomechanical Analysis (TMA) etc [80-88]. In this study, DSC and DMA were used for polymer encapsulant and underfill (UF2) respectively to determine the glass transition temperature.

3.5.1 Dynamic Mechanical Analysis (DMA)

Most of the microelectronic packaging polymer is viscoelastic. Purely elastic materials have stress and strain in phase, so that the response of one caused by the other is immediate. In purely viscous materials, strain lags stress by a 90 degree phase lag. Viscoelastic materials exhibit behavior somewhere in the middle of these two types of material, exhibiting some lag in strain. Viscoelasticity is studied using dynamic mechanical analysis. In this study, strain controlled dynamic mechanical analyzer has

been used where the probe has been displaced and the resulting oscillatory stress of the sample has been measured by implementing a force balance transducer. The set up employed during the study is shown in Figure 3.16. Three point bending test has been performed. The frequency of 1 Hz and temperature range of -25 C to +200 C have been maintained during the analysis. The typical dimension of the DMA specimen (shown in Figure 3.17) was 35 × 8 × 2.5 mm.

The DMA technique measures the stress-strain relationship for a viscoelastic material. A real and imaginary component of modulus can be obtained by resolving the stress-strain components:

$$E^* = E' + iE'' \tag{3.8}$$

Where E* is complex dynamic modulus, E' is storage modulus, E" is loss modulus and "i" is the imaginary unit which satisfies the equation $i^2 = -1$.

Storage modulus (E') refers to the energy stored elastically during deformation. It is related to elastic modulus of solids.

$$E' = \frac{\sigma_0}{\varepsilon_0}\cos\delta \tag{3.9}$$

Loss modulus (E") is the energy converted to heat during deformation.

$$E'' = \frac{\sigma_0}{\varepsilon_0}\sin\delta \tag{3.10}$$

Loss tangent (tanδ):

$$\tan\delta = \frac{E''}{E'} \tag{3.11}$$

σ_0 and ε_0 are the amplitudes of stress and strain and δ is phase lag between applied stress and measured strain.

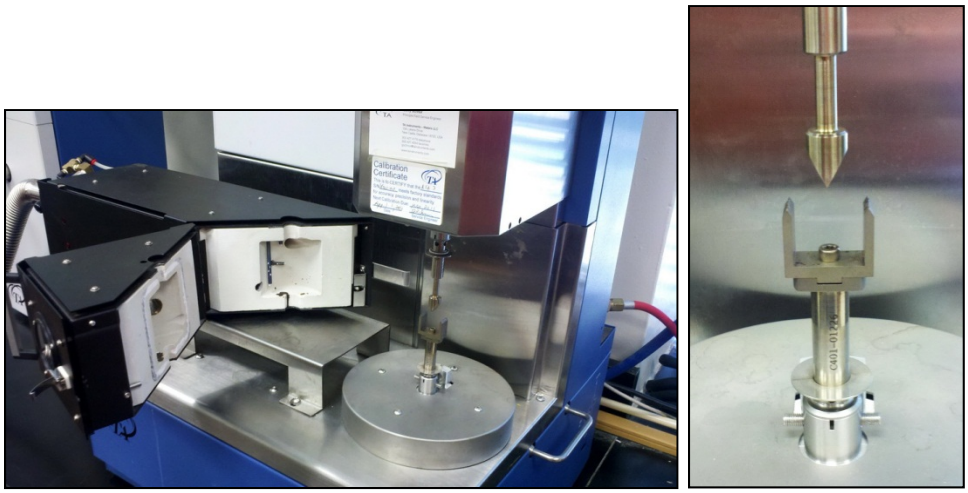

Figure 3.16 TA Instruments RSA3 DMA System

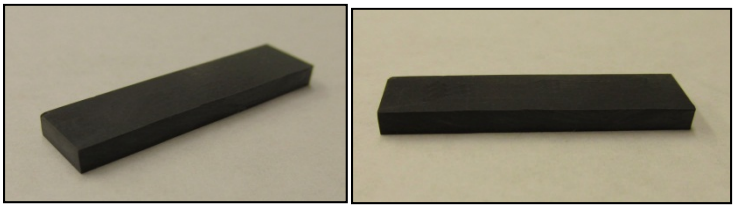

Figure 3.17 DMA Specimens

A typical dynamic mechanical analysis curve shows either E', E" or tanδ plotted as a function of time or temperature. In general, the most intense peak observed for either E" or tanδ in conjunction with a relatively pronounced drop in E' corresponds to the glass transition [82].

3.5.2 Differential Scanning Calorimetry (DSC)

DSC (Figure 3.18) analysis has also been applied to investigate the glass transition region of underfill and other polymers. The DSC instrument measures heat flow into or from a sample under heating, cooling or isothermal conditions [89]. The specimens were trimmed into small pieces (around 10 mg) and then a relative heat flow (aluminum served as a reference) vs. temperature curve has been recorded. In case of polymer, after the glass transition region, the curve shifts upward or downward suddenly depending upon the heat flow occurring into or from the sample. It happens because polymers have a higher heat capacity above the glass transition temperature than they do below it. Because of this change in heat capacity that occurs at the glass transition, DSC is used to measure polymer's glass transition temperature. Moreover, the change doesn't occur suddenly, it takes place over a temperature range. So the glass transition temperature is determined by taking the middle of the change in baseline (half-height method) [82].

Figure 3.19 shows that both DSC and DMA can be used to determine the glass transition temperature, T_g. According to DSC result, T_g is 115.17 C whereas DMA storage modulus, DMA loss modulus, and DMA tanδ shows the glass transition temperature as 126.47 C, 136.52 C, and 142.32 C respectively. The storage modulus

above T_g is related to the degree of cure (cross-link density) of the material: the higher the storage modulus above T_g, the higher the degree of cure.

Figure 3.18 DSC Device Setup

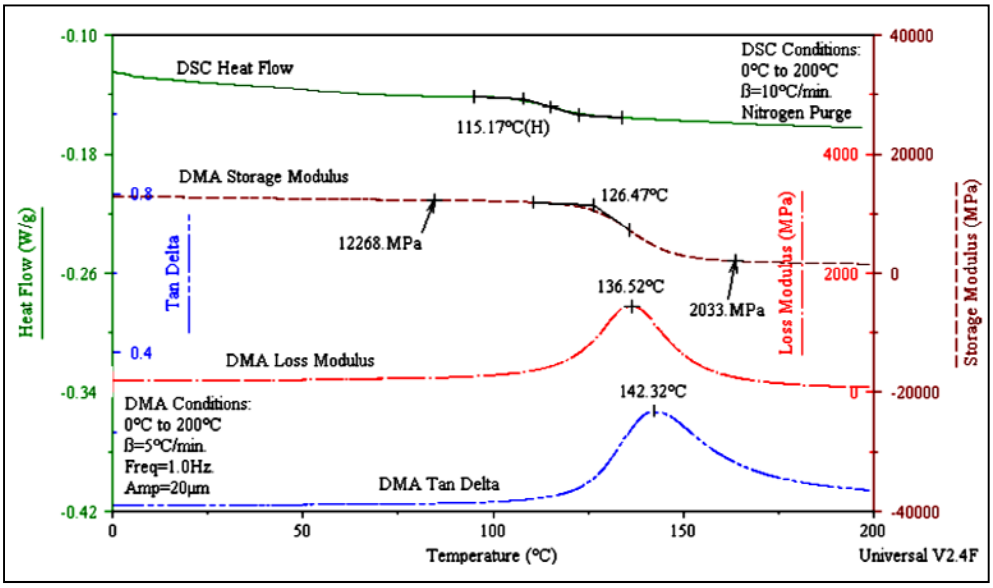

Figure 3.19 Determination of Glass Transition Temperature by DSC and DMA [81]

3.6 Study of Effect of Moisture on Mechanical Properties

3.6.1 Environmental Test Chamber

To study the effect of moisture uptake on the mechanical properties of microelectronic packaging polymers, the specimens have been exposed to controlled humidly. For this purpose, Programmable Tenney® and HOTPACK chambers (shown in Figure 3.20) were utilized. Besides having a wide range of controllable temperature, these chambers have humidification capabilities. The uniaxial test specimens and rectangular bar shaped DMA specimens have been exposed in these adjustable chambers to combined hygrothermal exposures for various durations and the effects of moisture adsorption on the stress-strain behavior and glass transition temperature of polymers were evaluated experimentally. The test conditions maintained during the study were 85 C and 85% RH, 60 C and 90% RH, 60 C and 50% RH and 40 C and 50% RH for different polymers.

Figure 3.20 Humidity Chambers Used for Moisture Exposure

3.6.2 FTIR Spectroscopy

Atoms vibrate with frequencies in the infrared range. In FTIR analysis a spectrum shows molecular vibrations in order to identify or characterize organic materials such as polymers and adhesives [90]. Infrared spectroscopy has also been used to monitor water uptake and diffusion coefficients have been determined using Fick's law [91]. In this study, a preliminary study using FTIR analysis demonstrating the effect of moisture on polymer samples has been conducted and absorption unit vs. wavenumber curve has been recorded. Figure 3.21 shows FTIR machine used during the study and an example of typical chemical bonds as FTIR is used to make quantitative measurements and analysis of chemical bonds in organic as well as inorganic compounds.

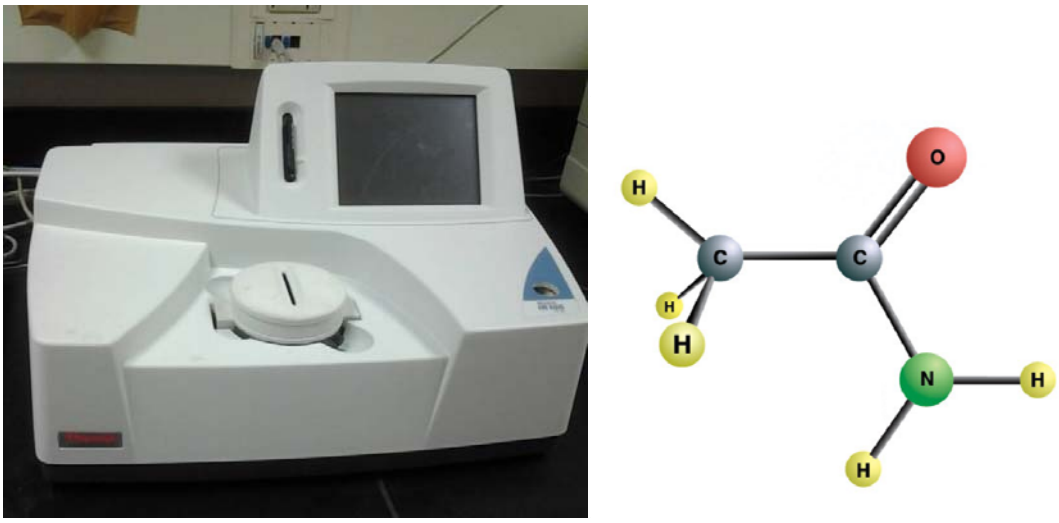

(a) (b)

Figure 3.21 (a) FTIR Equipment (b) Example of Typical Chemical Bonds

3.6.3 Electronic Balance

A Denver Instrument XS-210 (Figure 3.22) has been used to measure the weight of sample after moisture absorption. The balance is capable of measuring weight to the nearest 0.001g.

Figure 3.22 Electronic Balance

3.6.4 Optical Microscope

The uniaxial test specimens of Polycarbonate that were exposed to moisture adsorption and failed after uniaxial tesnsile testing were utilized then for study of microscopic view without involving any additional preparation procedure. An Olympus BX60 Optical Microscope (shown in Figure 3.23) has been utilized to analyze the surface morphologies of the fractured specimens. Typical optical microscopic views have been presented in the study to show the effect of moisture adsorption on the fracture behavior of the tested microtensile specimens.

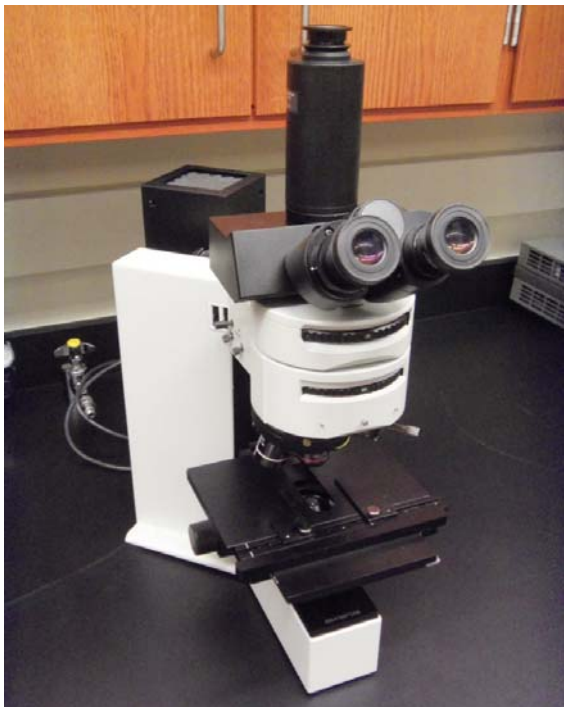

Figure 3.23 OLYMPUS BX60 Optical Microscope

3.7 Summary and Discussion

A unique specimen preparation procedure has been developed in this study to fabricate micro-scale uniaxial tensile specimens. A set of molds, made from stainless steel and coated with Teflon have been utilized to prepare the specimens. Typical uniaxial samples with nominal dimensions of 80 × 3 × 0.5 or 80 × 3 × 0.125 mm have been utilized. Uniaxial tensile and creep tests have been performed by using a multifunctional microtester. In this study, the experimental data have been modeled by empirical constitutive laws so that the corresponding mechanical properties of materials can be extracted. Moreover, DMA and DSC analysis have also been performed to study mechanical behavior of polymer materials. FTIR spectroscopy and microscopic views on fractured surfaces have also been examined to observe the effect of moisture on the mechanical properties of microelectronic packaging polymers.

CHAPTER 4

CHARACTERIZATION OF UNDERFILL ENCAPSULANTS

4.1 Introduction

The mechanical properties of polymer materials are always the key concern of microelectronic packaging industry. The theoretical analysis of stress, strain, ultimate stress and other mechanical properties induced by environmental conditions such as temperature, isothermal aging and thermal cycling require the characterization of mechanical properties for these materials. In this chapter, measurement results on the mechanical behavior of underfill materials are reported which have been investigated by uniaxial tensile and creep tests. Underfill materials have suitable mechanical strength and favorable viscous properties. Hence, they are widely used in flip chip packages to fill the gap between the chip and substrate around the solder interconnections for the purpose of reducing the thermal stresses imposed on the solder joints and further improving the long-term reliability of electronic devices [92].

In this study, two different types of underfill materials were studied: Commercial BGA/CSP underfill manufactured by Zymet, Inc. (Zymet X6-82-5LV50), denoted as UF1 and silica filled epoxy underfill (ME 525), denoted as UF2. The viscoelastic mechanical response of the tested underfills have been characterized via rate dependent stress-strain testing over a wide temperature range, and creep testing for a large range of applied stress levels and temperatures. A specimen preparation procedure has been

developed to manufacture 80 x 3 mm uniaxial tension test samples with a specified thickness. The test specimens are dispensed and cured with production equipment using the same conditions as those used in actual flip chip assembly, and no release agent is required to extract them from the mold. Using the manufactured test specimens, a microscale tension-torsion testing machine has been used to evaluate stress-strain and creep behavior of the underfill material as a function of temperature. The glass transition temperature (T_g), coefficient of thermal expansion (α) and curing conditions for the tested underfills are shown in Table 4.1.

Table 4.1 Thermo-mechanical Properties and Curing Conditions of UF1 and UF2

Underfill Material	T_g (C)	α (1/ °C)	Cure Conditions
UF1 (Zymet)	120	41×10^{-6}	150 C/ 15 min
UF2 (ME 525)	125	35×10^{-6}	150 C/ 30 min

4.2 Mechanical Characterization of Zymet X6-82-5LV50 (UF1)

The UF1 specimens were prepared with nominal dimensions of 80 × 3 × 0.5 mm. Stress-strain curves have been measured at 5 temperatures (25, 50, 75, 100 and 125 C), and strain rates spanning over 4 orders of magnitude. In addition, creep curves have been evaluated for the same 5 temperatures and several stress levels. For all tests, a 60 mm gage length was utilized between the specimen grips.

4.2.1 Stress-Strain Test Results of UF1

Figure 4.1 illustrates typical stress-strain curves for the UF1 (no moisture exposure) at temperatures from T = 0 C to T = +130 C, and a strain rate of $\dot{\varepsilon} = .001\ sec^{-1}$.

Plots of the initial effective elastic modulus E and ultimate tensile strength (UTS) vs. temperature extracted from these curves are shown in Figures 4.2 (each data point in these graphs represents the average of 3 to 5 tests). The glass transition region from +80 C to +100 C is clearly evident. The raw data for each temperature that were fit by an empirical model are shown in Figure 4.3.

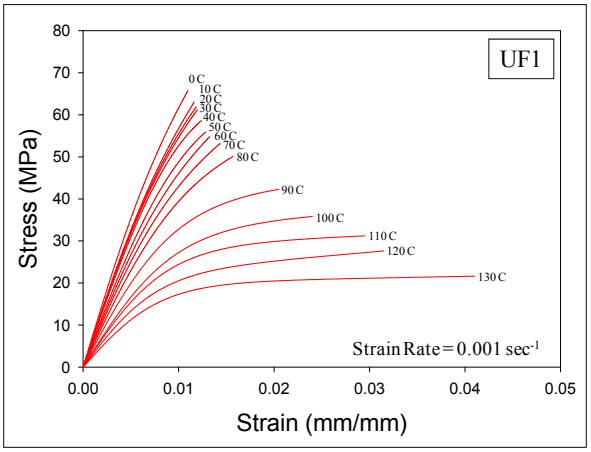

Figure 4.1 Temperature Dependent Underfill (UF1) Stress-Strain Curves ($\dot{\varepsilon}$ = .001 sec^{-1})

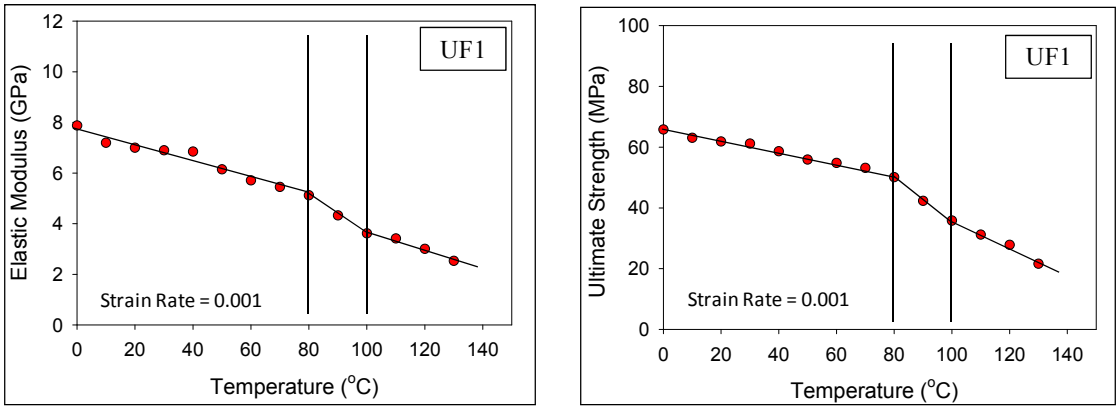

(a) (b)

Figure 4.2 (a) Effective Elastic Modulus and (b) Ultimate Strength vs. Temperature of underfill, UF1 ($\dot{\varepsilon}$ = .001 sec^{-1})

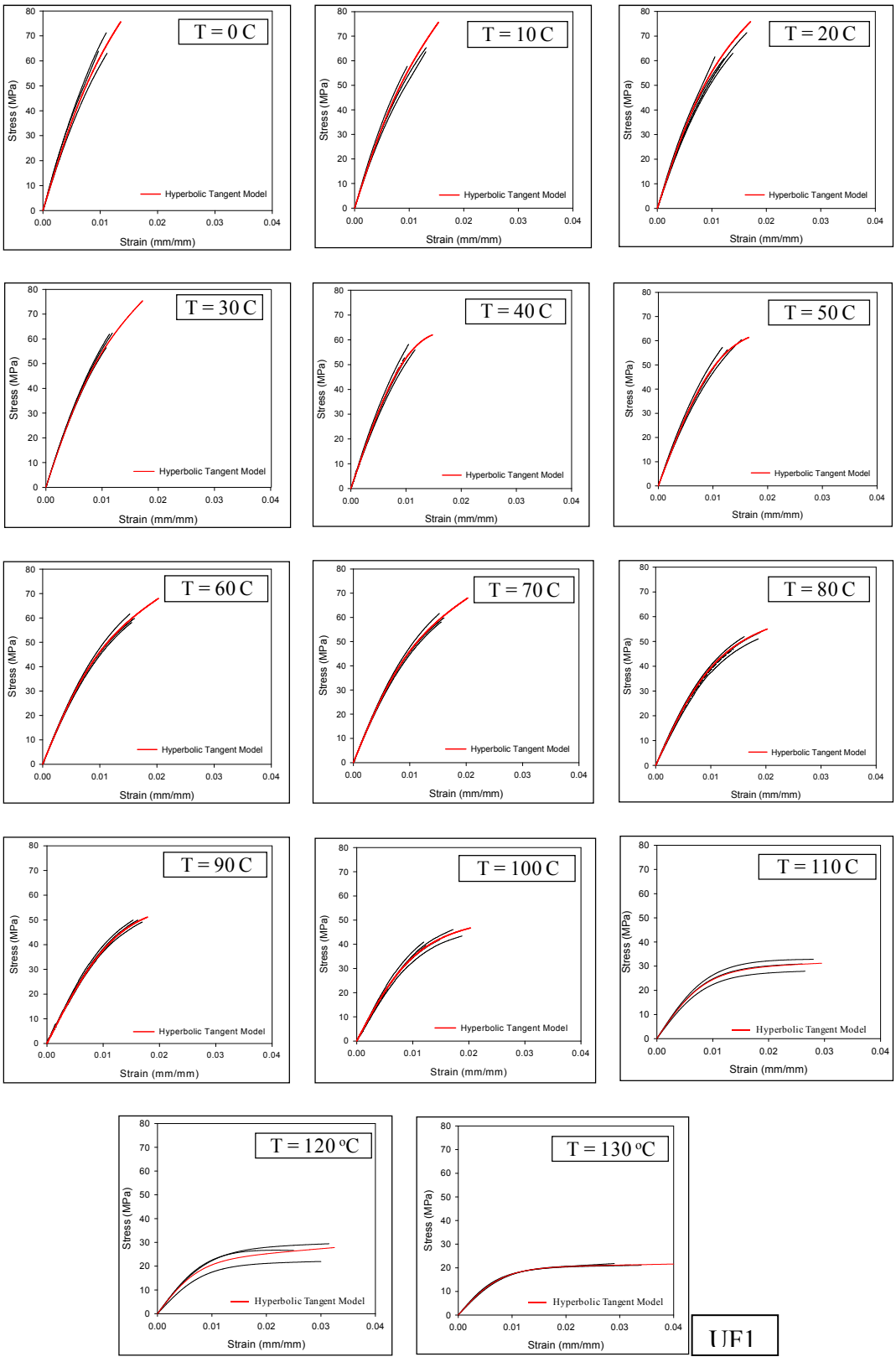

Figure 4.3 Raw data and Empirical Model of UF1 ($\dot{\varepsilon} = .001\ sec^{-1}$)

Analogous underfill stress-strain curves have been for a test matrix that included 5 temperatures (T = 25, 50, 75, 100 and 125 C) and 4 strain rates ($\dot{\varepsilon}$ = 0.01, 0.001, 0.0001, and 0.00001 sec^{-1}). For each combination of temperature and strain rate, 3-5 tensile stress-strain curves were measured and fit with the empirical hyperbolic tangent model as shown in Figure 4.4 through 4.8. The hyperbolic tangent model can be expressed as:

$$\sigma = C_1 \tanh(C_2\varepsilon) + C_3\varepsilon \tag{4.1}$$

where C_1, C_2, C_3 are material constants to be determined through regression fitting. The fits of eq. (4.1) to the various sets of 3 raw experimental curves at constant conditions were excellent in all cases. Thus, the empirical fit to a set of 3-5 experimental curves could be thought to be the "average" stress-strain curve for a particular set of conditions. As the hyperbolic tangent model was found to fit all of the stress-strain data extremely well, and it is used to represent the experimental results in future graphs.

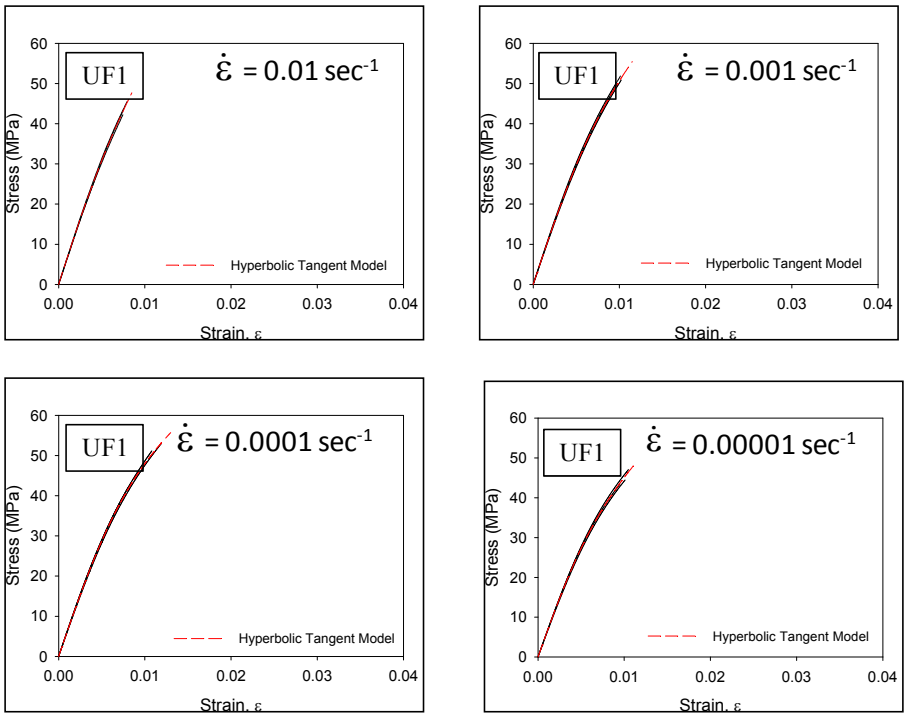

Figure 4.4 Raw data and Empirical Model of UF1 for Different Strain Rates (T = 25 C)

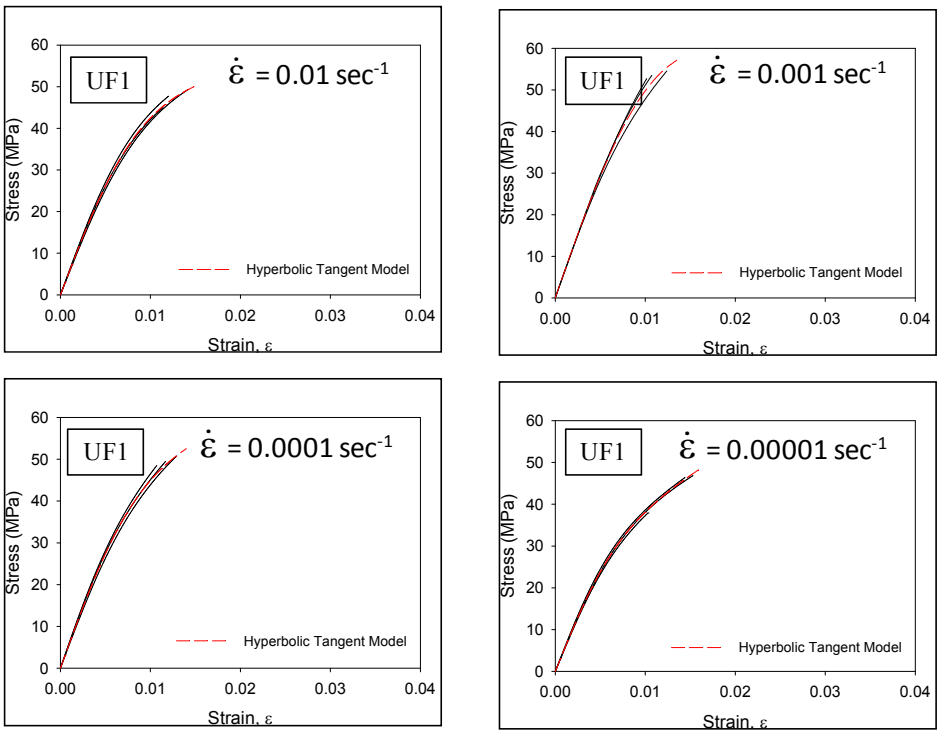

Figure 4.5 Raw data and Empirical Model of UF1 for Different Strain Rates (T = 50 C)

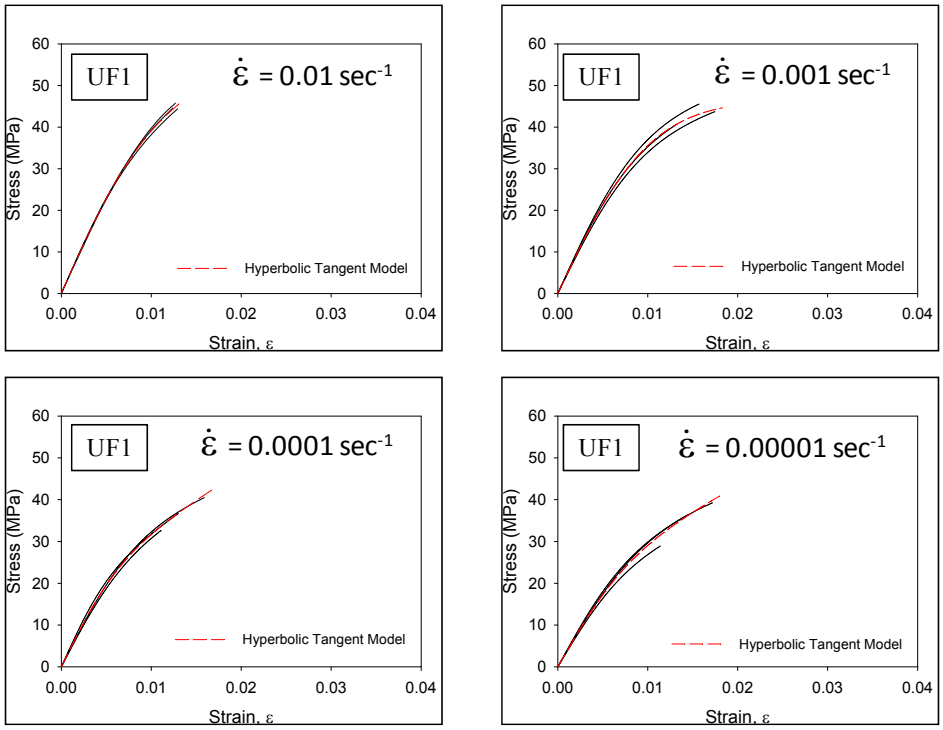

Figure 4.6 Raw data and Empirical Model of UF1 for Different Strain Rates (T = 75 C)

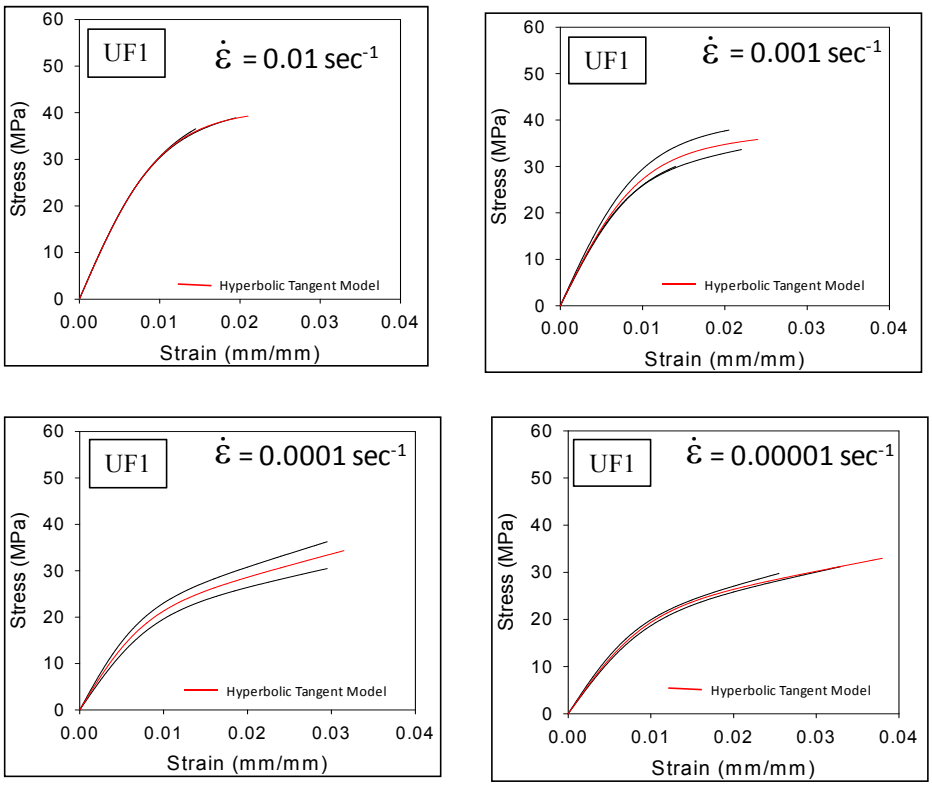

Figure 4.7 Raw data and Empirical Model of UF1 for Different Strain Rates (T = 100 C)

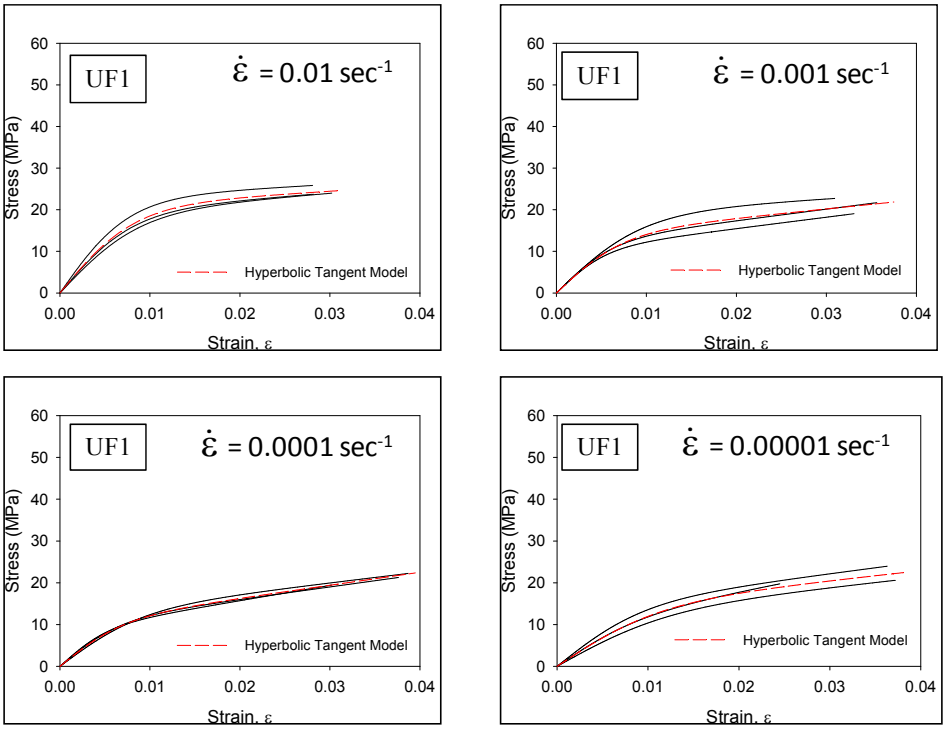

Figure 4.8 Raw data and Empirical Model of UF1 for Different Strain Rates (T = 125 C)

Figure 4.9 illustrates the average stress-strain curves extracted from the measured experimental curves for the tested underfill at the various strain rates and temperatures. The mechanical properties (effective initial elastic modulus and ultimate tensile strength) have been extracted from the average stress-strain curves shown in Figure 4.9. Figures 4.10 and 4.11 show how the mechanical properties vary with strain rate at the various temperatures. As expected, the modulus and strength decreases with increasing temperature and decreasing strain rate.

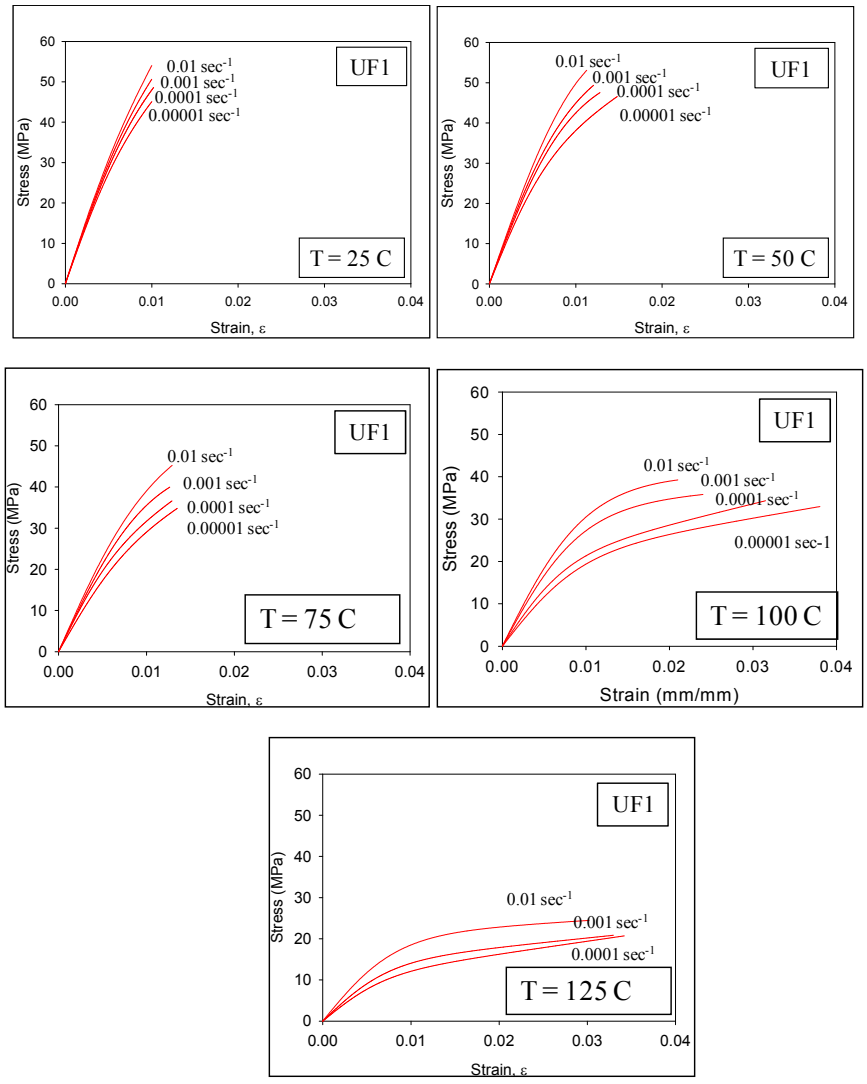

Figure 4.9 Average Experimental Stress-Strain Curves

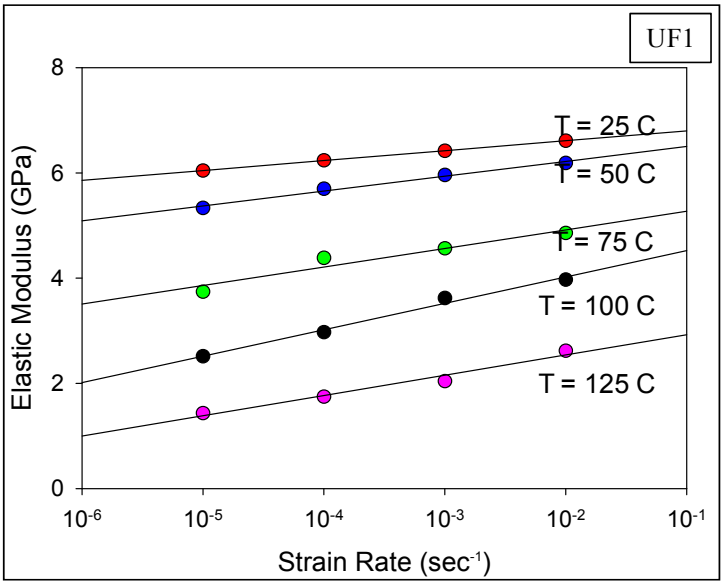

Figure 4.10 Effective Elastic Modulus vs. Strain Rate of underfill, UF1

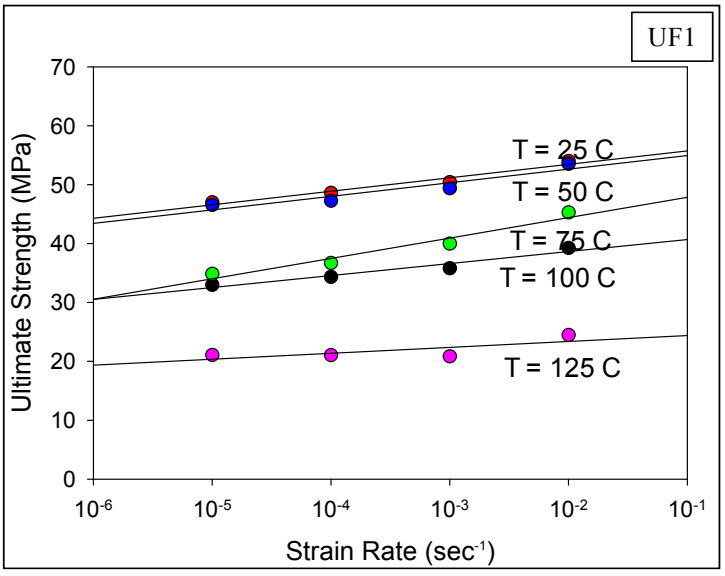

Figure 4.11 Ultimate Tensile Strength vs. Strain Rate of underfill, UF1

4.2.2 Creep Test Results of UF1

4.2.2.1 Long-Term Tests

Creep is rate dependent material nonlinearity in which the material continues to deform under a constant load. There are three stage of creep: primary, secondary and tertiary. Polymeric materials usually do not exhibit tertiary creep. The description of creep for polymers has been discussed in Chapter 1 and Chapter 3. Several different mathematical models are available to represent creep data [93]. Table 4.2 shows different models considered in this study to represent the observed creep (creep strain vs. time) data.

Table 4.2 Models Considered for Creep Analysis

No.	Models Considered	Mathematical Expressions
1	Log Hyperbolic Tangent Model	$\varepsilon_{cr} = C_1 t + C_2 \ln(1+t) + C_3 \tanh(C_4 t)$
2	Modified Power Law	$\varepsilon_{cr} = C_1 (t)^{C_2} (1 - \exp(-C_3 t))$
3	Generalized Garofalo (for Secondary Creep Rate)	$\dot{\varepsilon}_{cr} = C_1 [\sinh(C_2 \sigma)]^{C_3} e^{-C_4/T}$
4	Time Hardening Implicit Equation	$\varepsilon_{cr} = \frac{C_1 \sigma^{C_2} t^{(C_3+1)} e^{-\left[\frac{C_4}{T}\right]}}{C_3 + 1} + C_5 \sigma^{C_6} t\, e^{-\left[\frac{C_7}{T}\right]}$

Here, t is the time elapsed during the test and C_i's are constants to be determined by a regression analysis, ε_{cr} is strain, $\dot{\varepsilon}_{cr}$ is strain rate, σ is the applied stress level and T is temperature.

Figures 4.12, 4.13 and 4.14 show typical UF1 creep curve tested at 100 C for extremely long test duration (30 hours). Figure 4.12 is the creep data for stress level of 25 MPa and testing temperature of 100 C. Figure 4.13 and 4.14 are the same experimental creep data for stress level of 15 MPa but fitted with two empirical models: Log Hyperboilc Tangent Model and Modified Power Law respectively. The goodness of fit has been measured in terms of r^2 values for each curve.

When considering only creep strain, the Log Hyperbolic Tangent Model can be expressed as:

$$\varepsilon_{cr} = C_1 t + C_2 \ln(1+t) + C_3 \tanh(C_4 t) \tag{4.2}$$

For total strain, an additional coefficient (C_5) is added in the Eq. (4.2) to incorporate the elastic jump which is followed by creep strain during a creep test. Thus the expression for total strain becomes

$$\varepsilon_{total} = C_1 t + C_2 \ln(1+t) + C_3 \tanh(C_4 t) + C_5 \tag{4.3}$$

Taking the derivative on both sides of Eq. (4.2),

$$\frac{d\varepsilon_{cr}}{dt} = C_1 + C_2 \frac{1}{(1+t)} + C_3 C_4 \operatorname{sech}^2(C_4 t) \tag{4.4}$$

Strain rate is the rate of change in strain of a material with respect to time. Hence, the derivative of the eq. 4.2 with respect to time (t) has been determined to compare the calculated strain rate with measured strain rate from the slope of the linear part at the end of creep curve shown in Table 4.2. The comparison shown in Table 4.2 shows the strain rate values for the two methods. For long term the values tend to become very close. The strain rate values calculated from the derivative of the empirical model (Log Hyperbolic Tangent Model) have been plotted as a function of time in Figure 4.15.

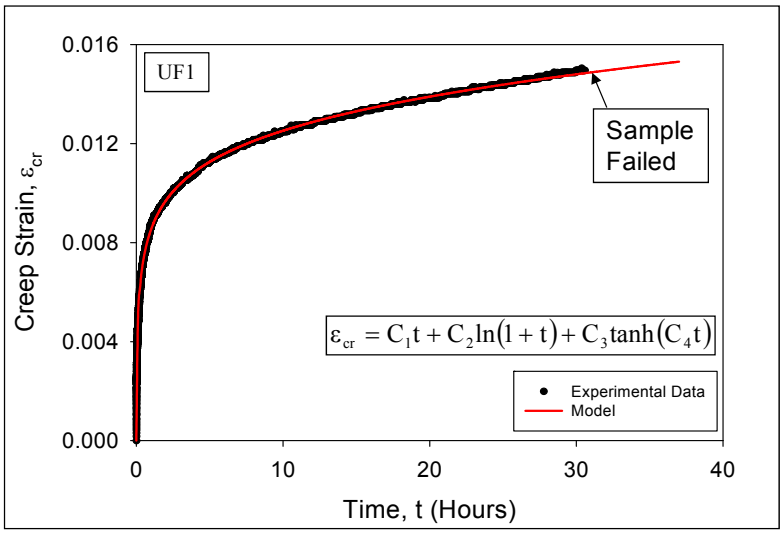

$r^2 = 0.9991$
Coefficient Data:
$c_1 = 0.0016$
$c_2 = -0.0049$
$c_3 = 0.0278$
$c_4 = 6.5970 \times 10^{-09}$

Figure 4.12 Log Hyperbolic Tangent Model Fit to Underfill (UF1) Creep Data (T = 100 C, σ = 25 MPa)

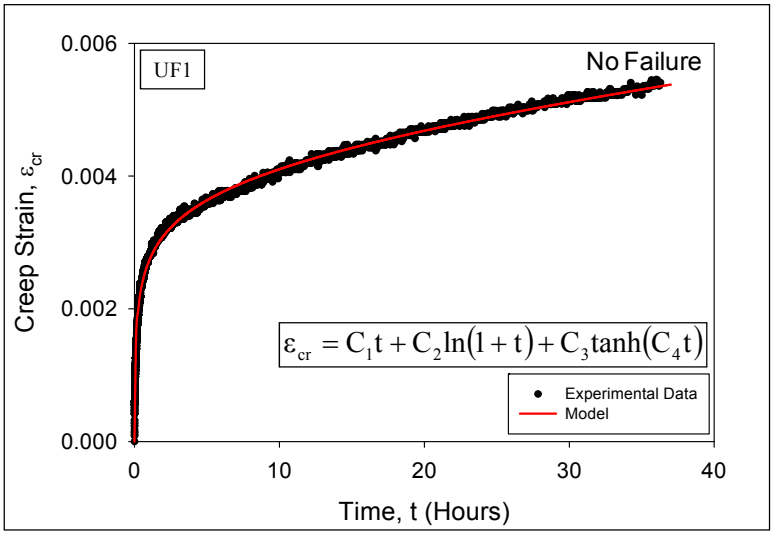

$r^2 = 0.9966$
Coefficient Data:
$c_1 = 0.0005$
$c_2 = 0.0015$
$c_3 = -2.2104$
$c_4 = 6.2042 \times 10^{-09}$

Figure 4.13 Log Hyperbolic Tangent Model Fit to Underfill (UF1) Creep Data (T = 100 C, σ = 15 MPa)

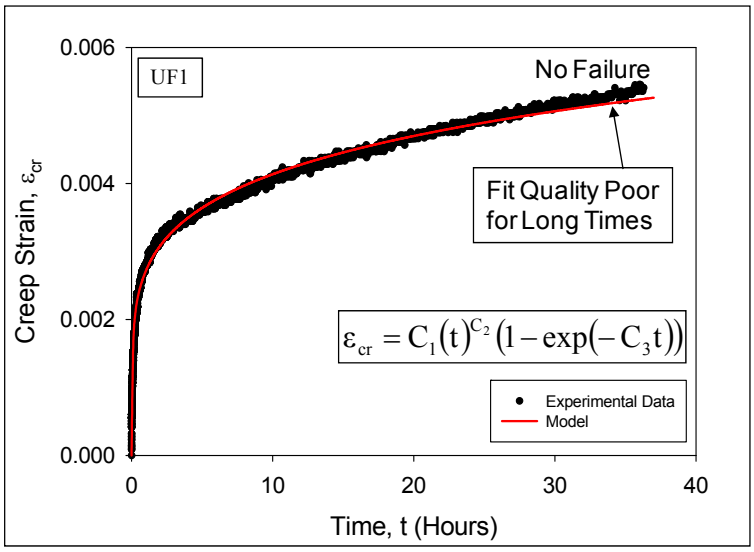

$r^2 = 0.9955$
Coefficient Data:
$c_1 = 0.0006$
$c_2 = 0.1839$
$c_3 = 0.0045$

Figure 4.14 Empirical Model (Modified Power Law) Fit to Underfill (UF1) Creep Data (T = 100 C, σ = 15 MPa)

Table 4.2 Comparison of Creep Strain Rate of underfill, UF1 for T = 100 C, σ = 15 MPa

Time (Hours)	Strain Rate (Experimental Data)
3	4.542×10^{-08}
6	2.558×10^{-08}
10	2.353×10^{-08}
14	1.652×10^{-08}
17	1.372×10^{-08}
21	1.318×10^{-08}
23	1.268×10^{-08}
27	1.288×10^{-08}
29	1.181×10^{-08}
33	1.007×10^{-08}
35	1.416×10^{-08}

Time (Hours)	Strain Rate (Model Fit to Data)
3	5.376×10^{-08}
6	2.998×10^{-08}
10	2.047×10^{-08}
14	1.639×10^{-08}
17	1.459×10^{-08}
21	1.299×10^{-08}
23	1.240×10^{-08}
27	1.148×10^{-08}
29	1.112×10^{-08}
33	1.052×10^{-08}
35	1.028×10^{-08}

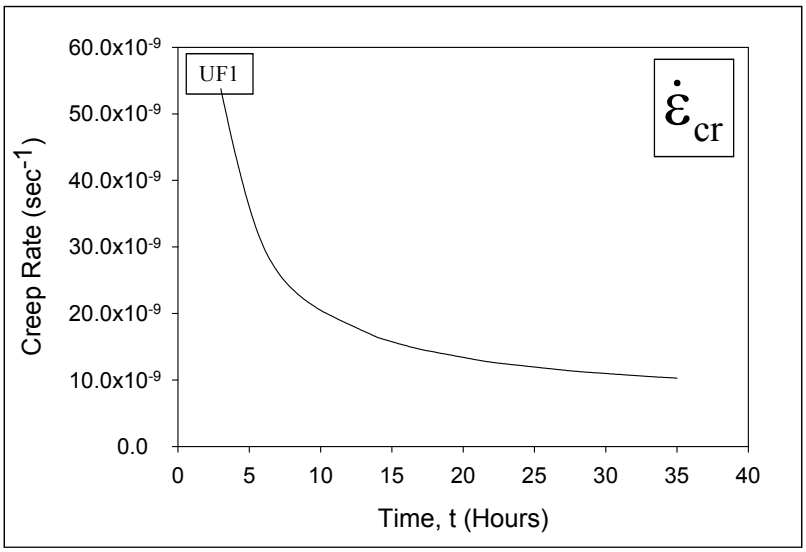

Figure 4.15 Creep Rate vs. Time for UF1 Creep Data (T = 100 C, σ = 15 MPa)

4.2.2.2 Short-Term Tests

Creep in polymers is much more prevalent near the glass transition region. Thus, the creep tests for UF1 were performed at five different testing temperatures (T = 25, 50, 75, 100 and 125 C). Specimens have been tested for up to 3 hours (10800 sec). The applied stress levels were in the range 5-25 MPa (25-90% of the UTS for the samples). Figure 4.16 shows the measured creep curves at the 5 testing temperatures and various stress levels. The Log Hyperbolic Tangent model was found to fit all of the test data extremely well, and it is used to represent the experimental results in future graphs. Thus, each experimental curve of Figure 4.16 is a fit of eq. (4.2) to the raw experimental data. All of the measured results showed primary and secondary creep regions, but no obvious tertiary creep region where failure will occur. Due to the long testing time involved, only 3 specimens were tested for each condition. The curves in each set were fitted with the same empirical Log Hyperbolic Tangent model to generate an "average" representation of the creep response for those conditions. For example, at 100 C, 5 stress

levels (5, 10, 15, 20 and 25 MPa) were considered and 3 tests were conducted for each stress level and were fitted with the empirical model (red curves in Figure 4.17) to generate a average curve.

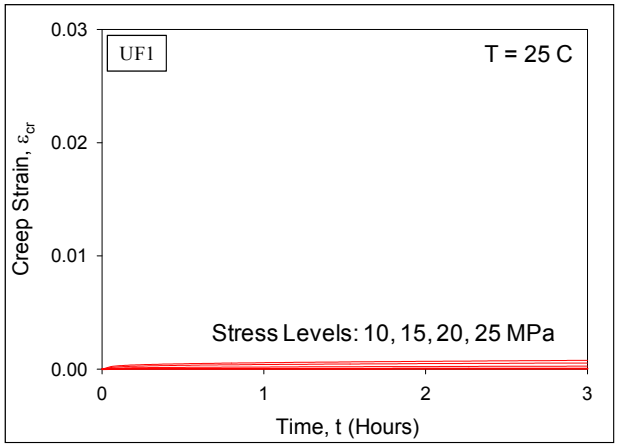

(a)

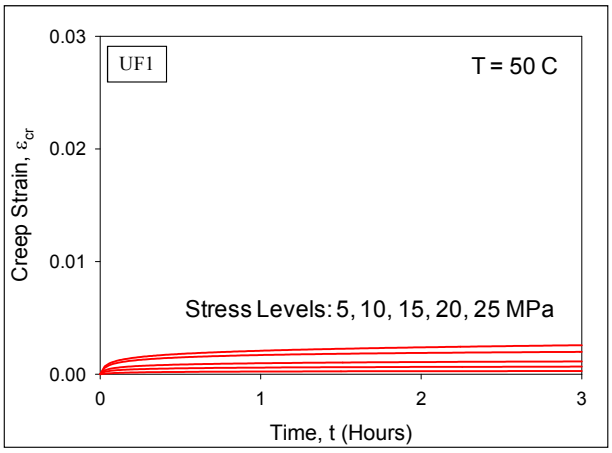

(b)

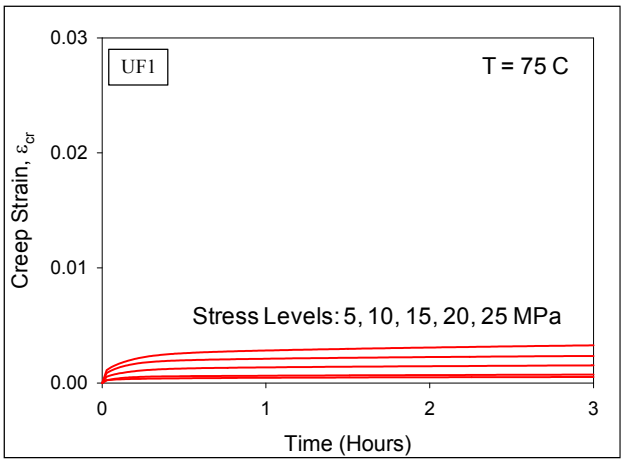

(c)

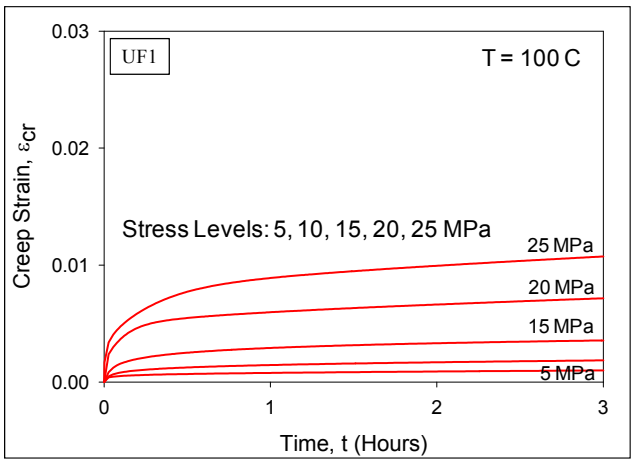

(d)

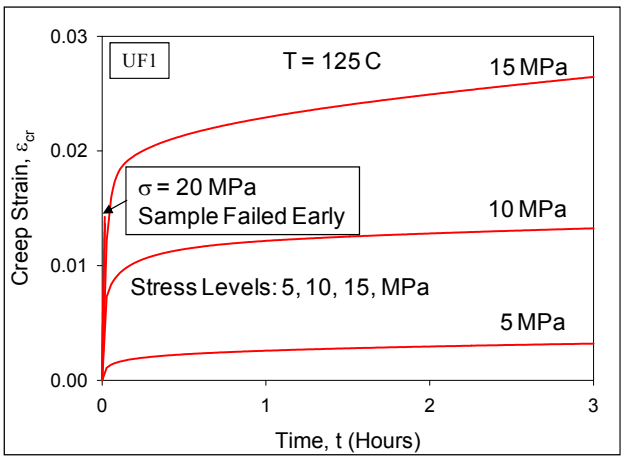

(e)

Figure 4.16 Experimental Creep Curves of UF1

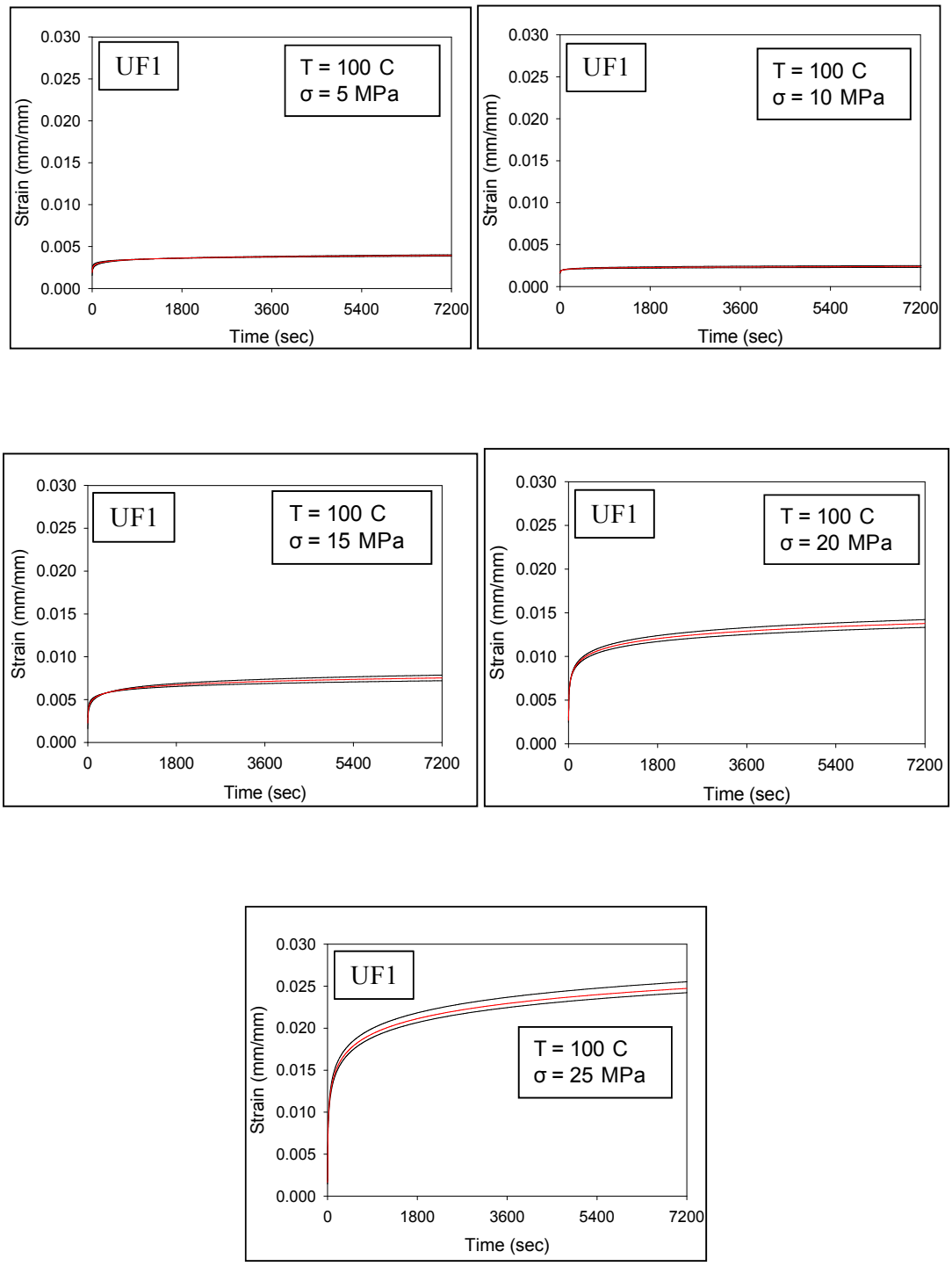

Figure 4.17 Raw Creep Data and Empirical Model of UF1 (T =100 C)

Besides other curve fitting tools, the ANSYS program has the capability of modeling first two stages (primary and secondary) of creep. It has thirteen creep models including Time Hardening Implicit Equation and Generalized Garofalo (for secondary creep rate), along with the tools to generate and fit derived coefficients to the experimental data. The Time Hardening Implicit Equation available in ANSYS was studied to fit the observed creep data as it has the capability to analyze the primary and secondary creep simultaneously. The goodness of curve fit has been measured by ANSYS curve fitting routine itself by calculating residual. The time hardening implicit equation consists of 7 constants and is expressed as:

$$\varepsilon_{cr} = \frac{C_1 \sigma^{C_2} t^{(C_3+1)} e^{-\left[\frac{C_4}{T}\right]}}{C_3 + 1} + C_5 \sigma^{C_6} t\, e^{-\left[\frac{C_7}{T}\right]} \qquad (4.5)$$

The constants C_1 to C_7 can be obtained from ANSYS creep curve fitting facilities, t is time, T is temperature, σ is the stress level and ε_{cr} is the creep strain. Figure 4.18 shows the correlation of Time Hardening Implicit Equation with the Experimental data which is fit of eq. (4.2). In this case, 5 different set of constants were obtained for 5 test temperatures which is listed in Table 4.3.

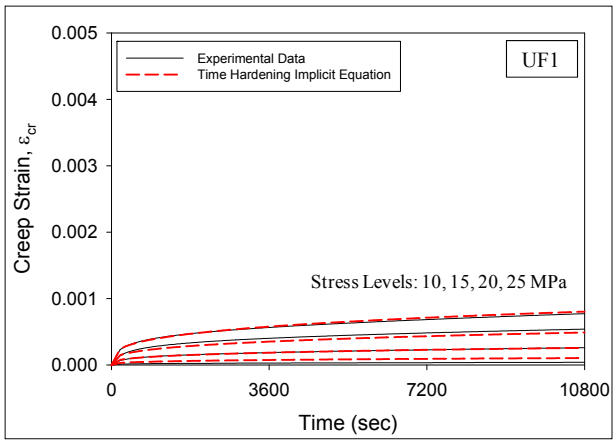

(a) T = 25 C

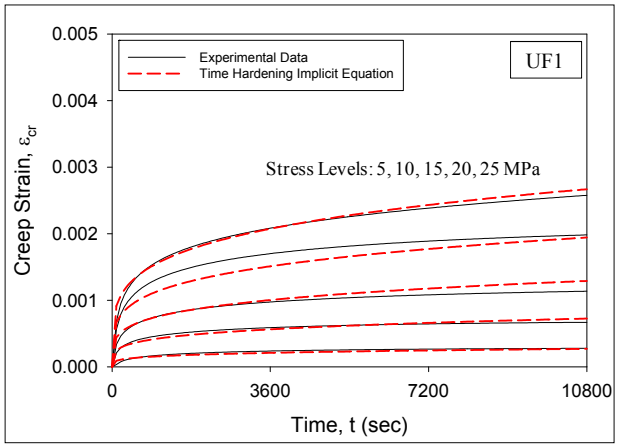

(b) T = 50 C

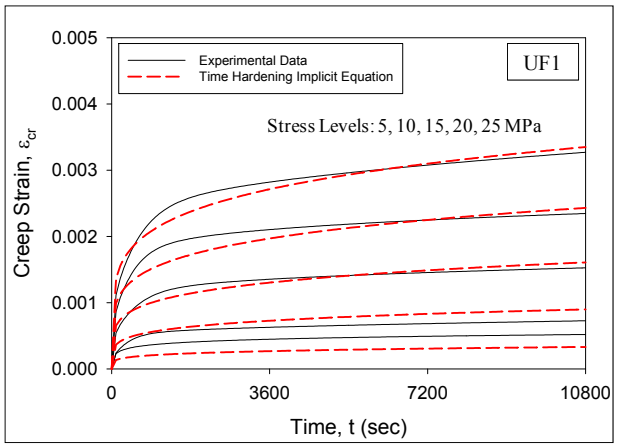

(c) T = 75 C

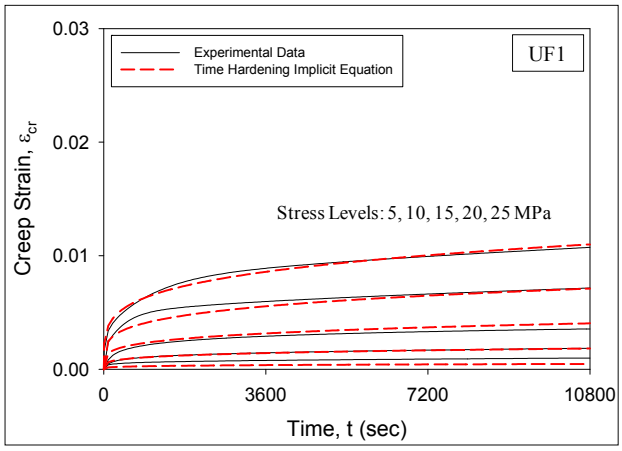

(d) T = 100 C

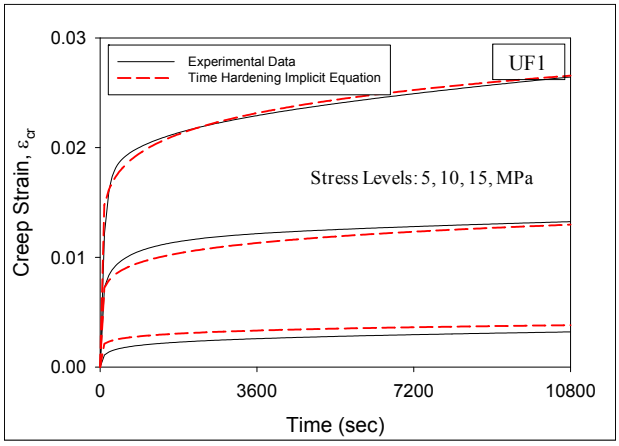

(e) T = 125 C

Figure 4.18 Comparison of Time Hardening Implicit Equation with UF1 Experimental Data

Table 4.3 Coefficients of Time Hardening Implicit Equation for UF1

Temperature	Coefficients	Calculated Residual
25 C	$C_1 = 1 \times 10^{-7}$ $C_2 = 2.224$ $C_3 = -0.699$ $C_4 = 9800$ $C_5 = 8 \times 10^{-10}$ $C_6 = -2.139$ $C_7 = 17.73 \times 10^{3}$	1.644×10^{-07}
50 C	$C_1 = 1.121 \times 10^{-7}$ $C_2 = 1.421$ $C_3 = -0.771$ $C_4 = 5729$ $C_5 = 8 \times 10^{-10}$ $C_6 = -2.139$ $C_7 = 17.732 \times 10^{3}$	1.139×10^{-6}
75 C	$C_1 = 1 \times 10^{-7}$ $C_2 = 1.435$ $C_3 = -0.808$ $C_4 = 6078$ $C_5 = 8 \times 10^{-10}$ $C_6 = -2.139$ $C_7 = 17.732 \times 10^{3}$	2.756×10^{-6}
100 C	$C_1 = 1.215 \times 10^{-10}$ $C_2 = 1.956$ $C_3 = -0.774$ $C_4 = 6937$ $C_5 = 8 \times 10^{-10}$ $C_6 = -2.319$ $C_7 = 17.732 \times 10^{3}$	1.859×10^{-5}
125 C	$C_1 = 8.033 \times 10^{-9}$ $C_2 = 1.767$ $C_3 = -0.874$ $C_4 = 6937$ $C_5 = 8 \times 10^{-10}$ $C_6 = -2.319$ $C_7 = 17.732 \times 10^{3}$	5.289×10^{-5}

The secondary (steady state) creep rates were extracted from the creep curves and plotted in Figure 4.19. The variations of the creep rate with testing temperature and stress level were then explored. The generalized Garofalo Model is given by

$$\dot{\varepsilon}_{cr} = c_1[\sinh(c_2\sigma)]^{c_3} e^{-c_4/T} \tag{4.6}$$

where T is the test temperature, σ is the stress level and C_i are constants to be determined by a regression analysis. The regression fit of eq. (4.6) to the experimental strain rate data is also shown in Figure 4.19. Good correlation of the model and experimental data is observed.

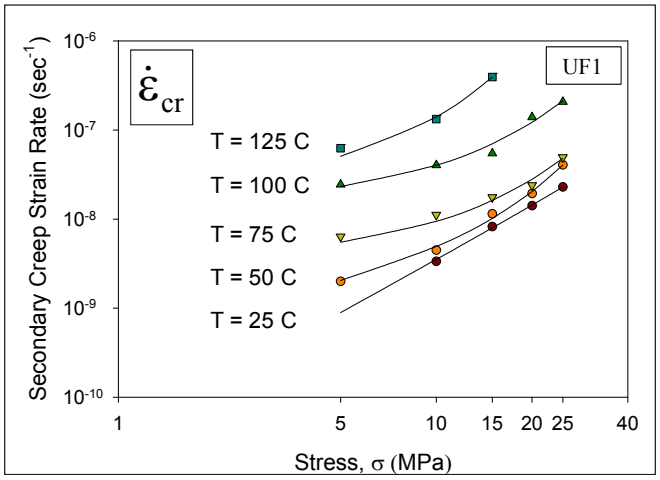

Figure 4.19 Variation of the Creep Strain Rate of UF1 with Stress and Temperature

4.3 Mechanical Characterization of ME525 (UF2)

4.3.1 Stress-Strain Test Results of UF2

Like the previous underfill, this one is also a silica filled epoxy with T_g = 125 C (TMA) and 145 C (DMA). Figure 4.20 illustrates typical stress-strain curves for the tested underfill (no aging) at temperatures from T = 25 C to T = +150 C, and a strain rate of $\dot{\varepsilon} = .001$ (1/sec). The plot of E vs. temperature (each data point represents the average of 3 to 5 tests) is shown in Figure 4.21. The glass transition region for temperature, T > + 100 C is clearly evident.

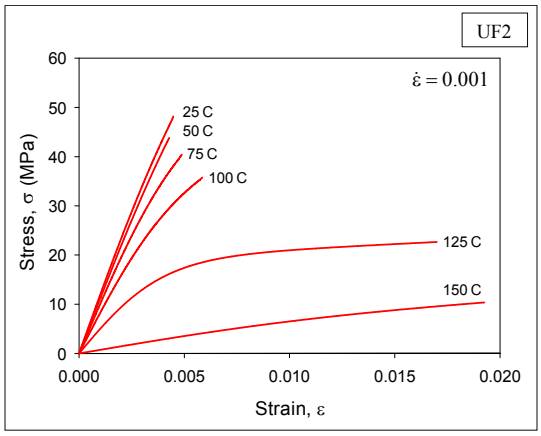

Figure 4.20 Temperature Dependent Underfill (UF2) Stress-Strain Curves ($\dot{\varepsilon}$ = .001 sec^{-1})

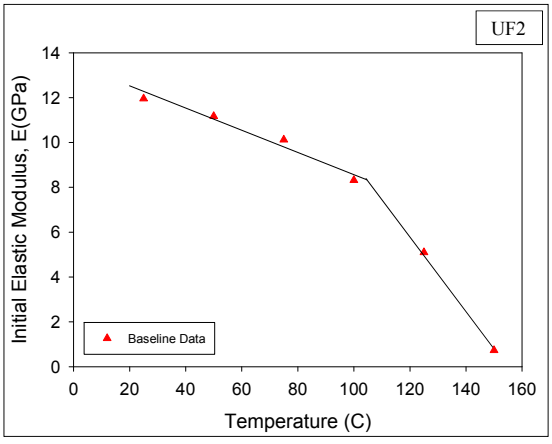

Figure 4.21 Effective Elastic Modulus vs. Temperature of UF2 ($\dot{\varepsilon}$ = .001 sec^{-1})

4.3.2 Creep Test Results of UF2

The creep tests for this underfill were performed at four different testing temperatures (T = 25, 80, 100 and 125 C). The applied stress levels were in the range 10-30 MPa (25-75% of the UTS for the samples). Figure 4.22 shows the measured creep curves at the 4 testing temperatures and various stress levels. Each experimental curve is a fit of eq. (4.3) to the raw experimental data. Specimens have been tested for up to 6000 seconds. All of the measured results showed primary and secondary creep regions, no tertiary creep regions were observed.

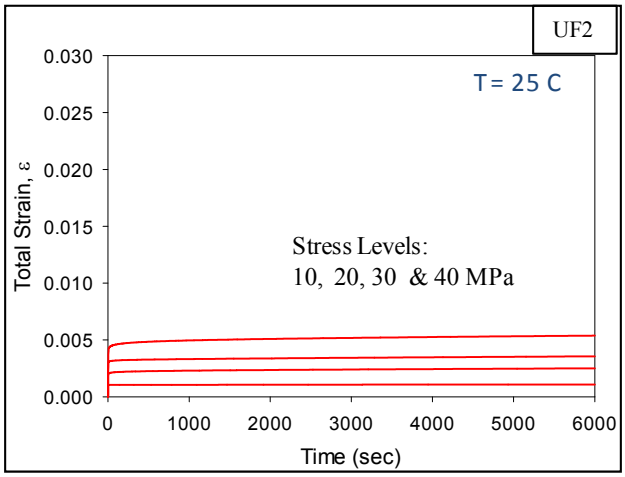

(a) T = 25 C

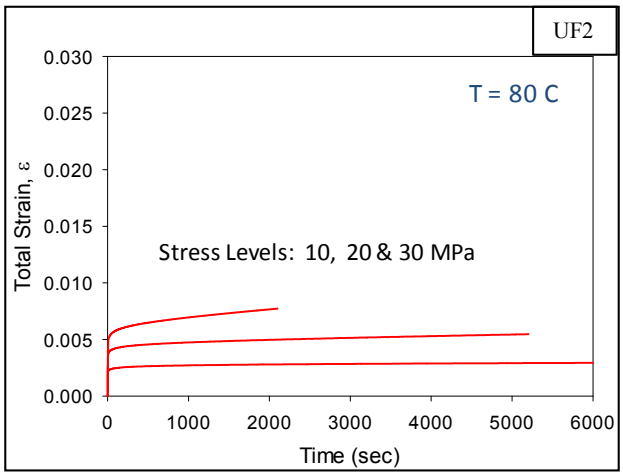

(b) T = 80 C

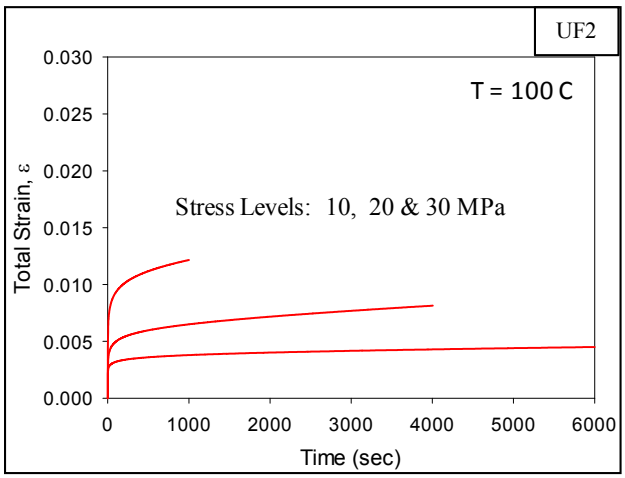

(c) T = 100 C

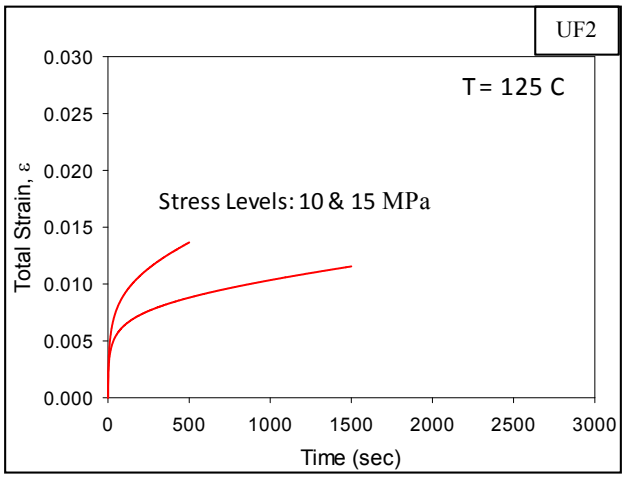

(d) T = 125 C

Figure 4.22 Experimental Creep Curves of UF2

4.4 Summary and Discussion

In this chapter, the effects of temperature and strain rate on mechanical behavior have been examined by performing stress-strain and creep tests on two underfill materials, indicated as UF1 and UF2. For both cases, a three parameter hyperbolic tangent empirical model has been used to fit the raw stress-strain data and the log hyperbolic tangent empirical model has been shown to accurately fit raw creep data (strain vs. time).

For UF1, stress-strain behavior curves have been evaluated for a temperature range of T = 0 C to T = 130 C for strain rate of .001 sec^{-1}. Tensile tests have also been performed at different strain rates at T = 25, 50, 75, 100 and 125 C. The glass transition region was observed between 80-100 C. Creep experiments have been performed at T = 25, 50, 75, 100, and 125 C with different stress levels at each temperature. The Generalized Garofalo model has been shown to accurately fit the secondary creep rate data as a function of temperature and stress.

For UF2, stress-strain behavior curves have been evaluated for T = 25, 50, 75, 100, 125 and 150 C for strain rate of .001 sec^{-1}. The glass transition region was observed above 100 C. Creep experiments have been performed at T = 25, 80, 100, and 125 C with different stress levels at each temperature.

The tensile results show that elastic modulus and ultimate strength have a linear dependence at different temperatures as well as at different strain rates. For creep, higher creep strains are attained with increasing stress level or increased test temperature as expected. As times passes, strain rate decreases gradually.

CHAPTER 5

CONSTITUTIVE MODELING FOR POLYMERS

5.1 Introduction

Reliable, consistent, and comprehensive material property data are needed for microelectronics packaging polymers for the purpose of mechanical design, reliability assessment, and process optimization of electronic packages. Additionally, it is widely acknowledged that polymer materials exhibit visco-elastic-plastic response when subject to deformation. As demonstrated in the previous chapter, dramatic changes occur in the tensile and creep behavior of polymer materials as the testing temperature or strain rate are varied. However, these effects have been largely observed when the temperature reaches the glass transition region. After the glass transition region, a hard or relatively brittle material starts to behave like a rubbery material. Constitutive models are needed to study and capture the rate-dependent stress–strain behavior of polymers below, at or above the glass transition temperature. In this study, viscoelastic and viscoplastic material models have been studied to represent the tensile and creep behavior of microelectronic packaging polymers. The models have been used to fit the experimental data, and optimum constitutive models for subsequent use in finite element simulations have been determined. At the end, the same model has been utilized to predict the material behavior (stress-strain and creep) before and after moisture adsorption. Besides demonstrating the theoretical background of the viscoelastic and viscoplastic models, the present chapter also includes the procedure of determining one set of coefficients for the corresponding

models. These coefficients along with material properties have then been used in ANSYS and MATLAB to predict the mechanical response of the material before hygothermal aging and to compare with the experimental data.

5.2 Viscoplastic Model (Anand Model)

The Anand model [94-95] is a popular viscoplastic constitutive model that is often applied to tin-based solders and other metals. In 1985, Dr. Lallit Anand proposed this simple set of constitutive equations for large isotropic viscoplastic deformations but small elastic deformations. This constitutive model has been embedded in commercial finite element simulation software such as ANSYS, and is now widely used in prediction of electronic packaging reliability. Although it is a well-known model for solder alloys, still it was attempted in this study to use it for illustrating the mechanical behavior of polymer like underfill of microelectronic packaging.

The Anand model unifies creep and rate independent plastic behavior of the materials by making use of a flow equation and an evolution equation. In the one-dimension (uniaxial) case, the constitutive equations include the stress equation:

$$\sigma = cs;\ c < 1$$
$$c = \frac{1}{\xi}\sinh^{-1}\left\{\left[\frac{\dot{\varepsilon}_p}{A}\exp\left(\frac{Q}{RT}\right)\right]^m\right\} \tag{5.1}$$

where c is a material parameter, A is the pre-exponential factor, Q is the activation energy, m is the strain rate sensitivity, ξ is the multiplier of stress, R is the ideal gas constant, and T is the absolute temperature, respectively. Material parameter c in eq. (5.1) is a constant for stress-strain tests run at a constant strain rate and fixed temperature. The other portions of the Anand model (1D) are the flow equation:

$$\dot{\varepsilon}_p = A \exp\left(-\frac{Q}{RT}\right)\left[\sinh\left(\xi\frac{\sigma}{s}\right)\right]^{\frac{1}{m}} \tag{5.2}$$

and the evolution equation:

$$\dot{s} = \left[h_0\left(1-\frac{s}{s^*}\right)^a \operatorname{sign}\left(1-\frac{s}{s^*}\right)\right]\dot{\varepsilon}_p; \quad a>1 \tag{5.3}$$

$$s^* = \hat{s}\left[\frac{\dot{\varepsilon}_p}{A}\exp\left(\frac{Q}{RT}\right)\right]^n \tag{5.4}$$

where h_0 is the hardening/softening constant, and a is the strain rate sensitivity of hardening/softening. The quantity s* represents a saturation value of parameter s associated with a set of given temperature and strain rate, $\hat{s}$ is a coefficient, and n is the strain rate sensitivity for the saturation value of deformation resistance. A detailed procedure for calculating the 9 constants in the Anand model from stress-strain tests performed at various strain rates and temperatures is described in references [96-99].

Figure 5.1 shows the procedure of determining parameters of Anand model. This approach has been used in this work for stress-strain data measured for underfill, UF1. The optimum values of the 9 coefficients in the Anand model has been calculated from the temperature and rate dependent underfill (UF1) stress-strain test data in Figure 4.9 of previous chapter. This approach yielded the coefficients which are tabulated in Table 5.1.

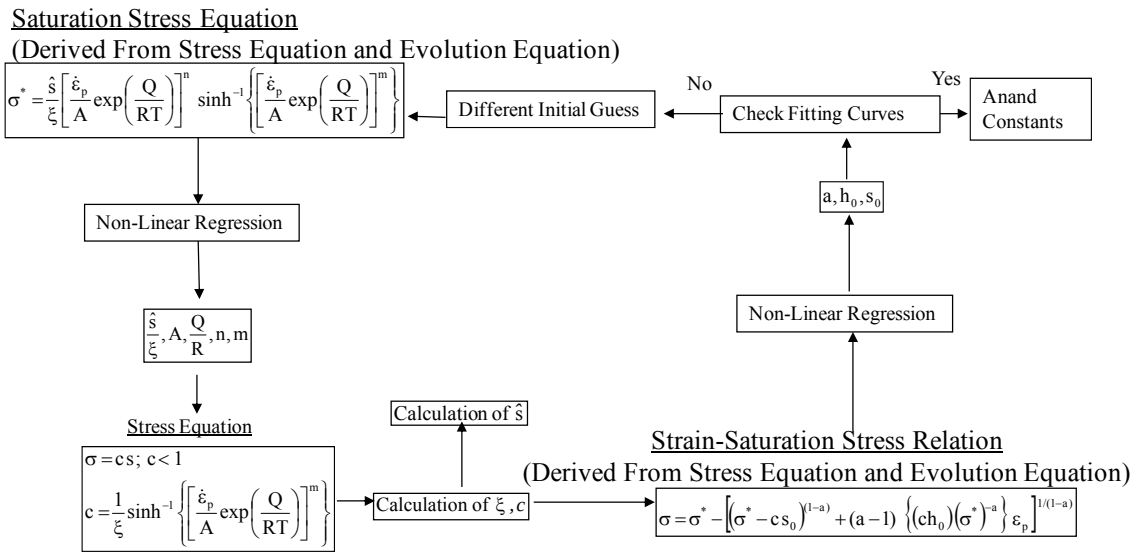

Figure 5.1 Determination of Anand Model Coefficients

Table 5.1 Anand Model Coefficients for UF1

Constant Number	Model Constant	Units	Value for Underfill
1	s_0	MPa	0.372
2	Q/R	K	441.4
3	A	sec^{-1}	1.43×10^{-3}
4	ξ	Dimensionless	2.5
5	m	Dimensionless	0.275
6	h_0	MPa	1.61×10^{4}
7	$\hat{s}$	MPa	9.0
8	n	Dimensionless	3.0
9	a	Dimensionless	1.24

5.2.1 FEA Model with Viscoplastic Properties

A 2D model of the full test specimen has been developed in ANSYS for finite element analysis using viscoplastic properties of Anand model as shown in Figure 5.2. Only stress-strain behavior of UF1 has been considered for the finite element analysis. The underfill specimen has been modeled with VISCO 106 element. The model geometry, applied boundary conditions and loadings are demonstrated in the Figure 5.2. All degree of freedom has been fixed at the left end and uniform temperature has been applied on the surface. As during the experiment, displacement control has been utilized, a prescribed displacement in y-direction has been applied at the right end of the model. The FEA model has been meshed with 11520 elements to ensure the solution is converged and also further increasing of elements does not have any effect on the results.

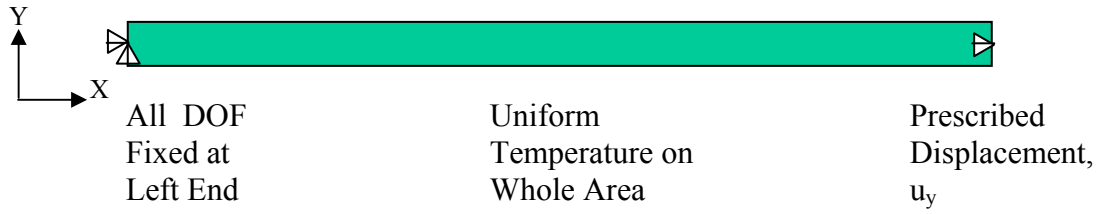

Figure 5.2 FEA Model with Viscoplastic Properties of the Tensile Specimen
Specimen Length, L = 60 mm, Width, W = 3 mm

5.2.2 FEA (Viscoplastic Model) Predictions for UF1

Figure 5.3 contains correlations of the Anand model predictions (using the coefficients in Table 5.1) with the underfill experimental stress-strain curves of UF1 from

Figure 4.9. It is obvious from the figure that while matching fairly well at low strain levels, the model and data deviate significantly at higher stress and strain levels.

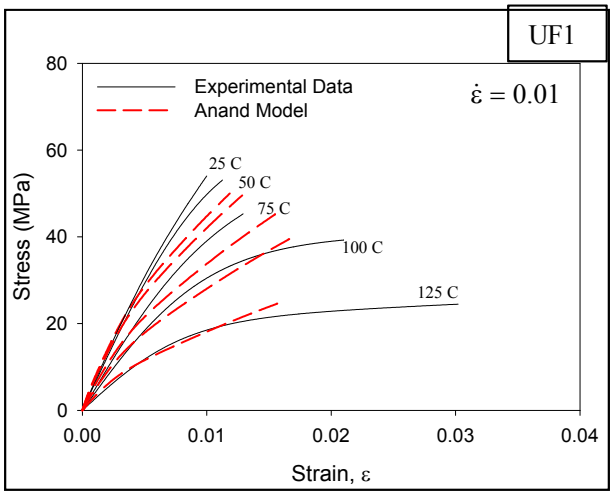

(a) $\dot{\varepsilon} = .01$ sec^{-1}

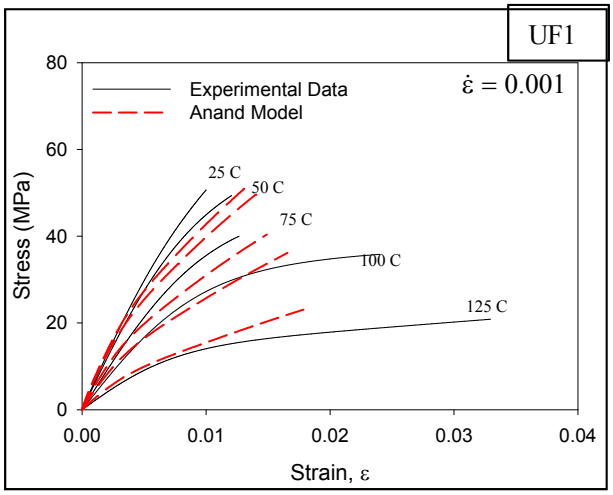

(b) $\dot{\varepsilon} = .001$ sec^{-1}

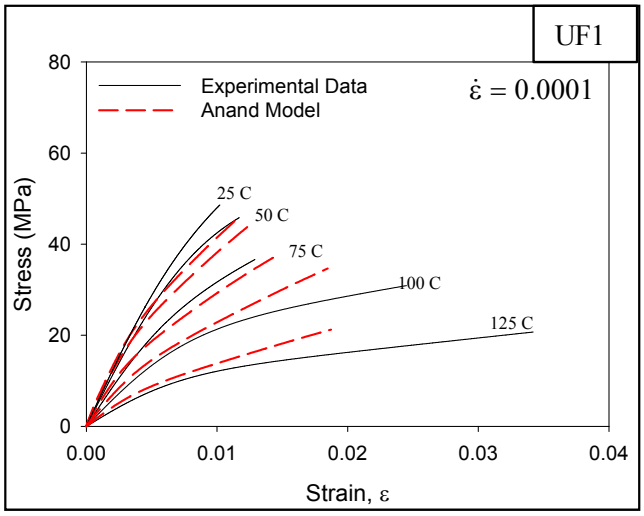

(c) $\dot{\varepsilon} = .0001$ sec^{-1}

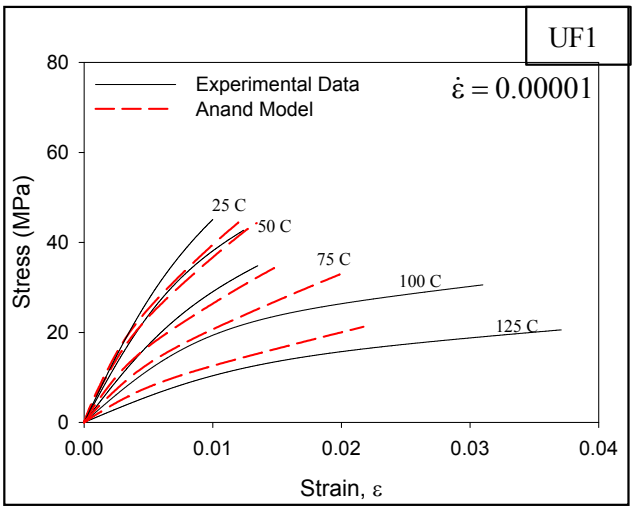

(d) $\dot{\varepsilon} = .00001$ sec^{-1}

Figure 5.3 Correlation of Anand Model Predictions with UF1 Stress-Strain Data

5.3 Viscoelastic Model (Generalized Maxwell Model)

The Maxwell Model is a simple mechanical analog that includes both elastic and viscous properties. It consists of a linear ideally elastic Hookean spring in series with a linear ideally viscous Newtonian damper as illustrated in Figure 5.4. The generalized Maxwell Model also known as the Maxwell–Wiechert model (after James Clerk Maxwell and E Wiechert) consists of several Maxwell elements connected in parallel [100-101]. It is often used in modeling of complicated linear viscoelastic materials. As shown in Figure 5.5, an extra spring is also added in parallel to represent the final (or equilibrium) modulus, E_∞.

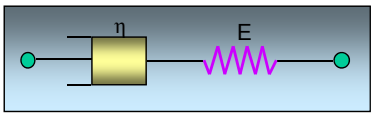

Figure 5.4 Maxwell Rheological Model

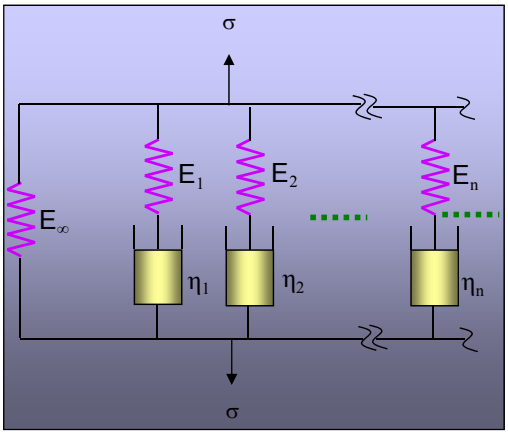

Figure 5.5 Generalized Maxwell Model

5.3.1 Constitutive Equations

The three-dimensional constitutive equation for an isotropic viscoelastic material is [100-101]:

$$\sigma_{ij} = \int_0^t 2G(t-\tau)\frac{de_{ij}}{d\tau}d\tau + \delta_{ij}\int_0^t K(t-\tau)\frac{d\Delta}{d\tau}d\tau \tag{5.5}$$

where σ_{ij} are the components of the Cauchy stress, e_{ij} are the Deviatoric strain components, Δ is the volumetric part of the strain, G(t) and K(t) are the shear and bulk modulus functions, t and τ are current and past time, and δ_{ij} are the components of the unit tensor (Kronecker delta).

$$\text{Stress, } \sigma_{ij} = \begin{bmatrix} \sigma_{11} & \sigma_{12} & \sigma_{13} \\ \sigma_{21} & \sigma_{22} & \sigma_{23} \\ \sigma_{31} & \sigma_{32} & \sigma_{33} \end{bmatrix} \tag{5.6}$$

Stress Component Equations:

$$\sigma_{11} = \int_0^t 2G(t-\tau)\frac{de_{11}}{d\tau}d\tau + \int_0^t K(t-\tau)\frac{d\Delta}{d\tau}d\tau$$

$$\sigma_{12} = \int_0^t 2G(t-\tau)\frac{de_{12}}{d\tau}d\tau$$

$$\sigma_{13} = \int_0^t 2G(t-\tau)\frac{de_{13}}{d\tau}d\tau$$

$$\sigma_{22} = \int_0^t 2G(t-\tau)\frac{de_{22}}{d\tau}d\tau + \int_0^t K(t-\tau)\frac{d\Delta}{d\tau}d\tau$$

$$\sigma_{23} = \int_0^t 2G(t-\tau)\frac{de_{23}}{d\tau}d\tau$$

$$\sigma_{33} = \int_0^t 2G(t-\tau)\frac{de_{33}}{d\tau}d\tau + \int_0^t K(t-\tau)\frac{d\Delta}{d\tau}d\tau \tag{5.7}$$

Deviatoric Part of Strain, $e_{ij} = \varepsilon_{ij} - \frac{\Delta}{3}\delta_{ij}$ (5.8)

Volumetric Part of Strain, $\Delta = \varepsilon_{11} + \varepsilon_{22} + \varepsilon_{33}$ (5.9)

$$e_{ij} = \begin{bmatrix} e_{11} & e_{12} & e_{13} \\ e_{21} & e_{22} & e_{23} \\ e_{31} & e_{32} & e_{33} \end{bmatrix} = \begin{bmatrix} \varepsilon_{11} - \frac{\Delta}{3} & \varepsilon_{12} & \varepsilon_{13} \\ \varepsilon_{21} & \varepsilon_{22} - \frac{\Delta}{3} & \varepsilon_{23} \\ \varepsilon_{31} & \varepsilon_{32} & \varepsilon_{33} - \frac{\Delta}{3} \end{bmatrix} \quad (5.10)$$

Kronecker delta, $\delta_{ij} = \begin{bmatrix} 1 & 0 & 0 \\ 0 & 1 & 0 \\ 0 & 0 & 1 \end{bmatrix}$ (5.11)

For the Generalized Maxwell Model, the shear and bulk modulus functions can be expressed in a Prony series format [102]:

$$G(t) = G_\infty + \sum_{i=1}^{n_G} G_i e^{\left(-t/\tau_i^G\right)} \quad (5.12)$$

$$K(t) = K_\infty + \sum_{i=1}^{n_K} K_i e^{\left(-t/\tau_i^K\right)} \quad (5.13)$$

Where G_∞ and G_i are the shear elastic moduli, K_∞ and K_i are the bulk elastic moduli and τ_i are the relaxation times for the various Prony series components.

Equations (5.12, 5.13) can be rewritten as:

$$G(t) = G_0\left[\alpha_\infty^G + \sum_{i=1}^{n_G} \alpha_i^G e^{\left(-t/\tau_i^G\right)}\right] \quad (5.14)$$

$$K(t) = K_0\left[\alpha_\infty^K + \sum_{i=1}^{n_K} \alpha_i^K e^{\left(-t/\tau_i^K\right)}\right] \quad (5.15)$$

Where $G_0 = G_\infty + \sum_{i=1}^{n_G} G_i$ (5.16)

$$K_0 = K_\infty + \sum_{i=1}^{n_K} K_i \tag{5.17}$$

are referred to as the instantaneous shear and bulk moduli, and

$$\alpha_i^G = G_i/G_0 \tag{5.18}$$

$$\alpha_i^K = K_i/K_0 \tag{5.19}$$

are referred to as the relative moduli.

Eq. (5.5) is the integral form of stress function of a viscoelastic material. The integral function can recover the elastic behavior at the limits of very slow and very fast load. Here, G_0 and K_0 are, respectively, the shear and bulk moduli at the fast load limit (i.e. the instantaneous moduli), and G_∞ and K_∞ are the moduli at the slow limit. The elasticity parameters input correspond to those of the fast load limit. Moreover by admitting Eq. (5.12) and (5.13), the deviatoric and volumetric parts of the stress are assumed to follow different relaxation behavior. The number of Prony terms for shear and for volumetric behavior need not be the same, nor do the relaxation times τ_i^G and τ_i^K [103].

5.3.2 Deviatoric and Dilatational Components of Stress and Strain

The Generalized Hooke's Law for a three dimensional state of stress and strain in a homogeneous and isotropic material can be written as

$$\varepsilon_{xx} = \frac{1}{E}\left[\sigma_{xx} - \nu\left(\sigma_{yy} + \sigma_{zz}\right)\right]$$

$$\varepsilon_{yy} = \frac{1}{E}\left[\sigma_{yy} - \nu\left(\sigma_{xx} + \sigma_{zz}\right)\right]$$

$$\varepsilon_{zz} = \frac{1}{E}\left[\sigma_{zz} - \nu\left(\sigma_{xx} + \sigma_{yy}\right)\right]$$

$$\gamma_{xy} = \frac{\tau_{xy}}{G}$$

$$\gamma_{yz} = \frac{\tau_{yz}}{G}$$

$$\gamma_{xz} = \frac{\tau_{xz}}{G} \tag{5.20}$$

The Generalized Hooke's Law from the above equation can be rewritten to relate tensorial stress and strain in index notation as follows

$$\varepsilon_{ij} = \frac{1+\nu}{E}\sigma_{ij} - \frac{\nu}{E}\sigma_{kk}\delta_{ij} \tag{5.21}$$

Again

$$G = \frac{E}{2(1+\nu)} \text{ and } K = \frac{E}{3(1-2\nu)}$$

$$\sigma_{kk} = \sigma_{xx} + \sigma_{yy} + \sigma_{zz} = 3\sigma_m$$

Equation (5.21) can also be expressed as

$$\frac{1+\nu}{E}\sigma_{ij} = \varepsilon_{ij} + \frac{\nu}{E}\sigma_{kk}\delta_{ij}$$

$$\sigma_{ij} = \frac{E}{1+\nu}\varepsilon_{ij} + \frac{\nu}{1+\nu}\sigma_{kk}\delta_{ij}$$

$$\Rightarrow \sigma_{ij} = 2G\varepsilon_{ij} + \frac{\nu}{1+\nu}\sigma_{kk}\delta_{ij}$$

$$\Rightarrow \sigma_{ij} = 2G\varepsilon_{ij} + \frac{\nu}{1+\nu}(3\sigma_m)\delta_{ij}$$

$$\Rightarrow \sigma_{ij} = 2G\varepsilon_{ij} + \frac{3\nu}{1+\nu}K\Delta\delta_{ij} \tag{5.22}$$

Bulk Modulus, K, is the ratio of the hydrostatic stress, σ_m to volumetric strain or unit change in volume, Δ

$$K = \frac{\sigma_m}{\Delta} \tag{5.23}$$

$$\Delta = \varepsilon_{xx} + \varepsilon_{yy} + \varepsilon_{zz} = \varepsilon_{kk}$$

$$\text{So } \sigma_{ij} = 2G\varepsilon_{ij} + \frac{3\nu E}{3(1+\nu)(1-2\nu)}\Delta\delta_{ij_{ij}}$$

$$\Rightarrow \sigma_{ij} = 2G\varepsilon_{ij} + \frac{\nu E}{(1+\nu)(1-2\nu)}\Delta\delta_{ij}$$

$$\Rightarrow \sigma_{ij} = 2G\varepsilon_{ij} + \lambda\Delta\delta_{ij} \tag{5.24}$$

$$\text{Lame's modulus, } \lambda = \frac{\nu E}{(1+\nu)(1-2\nu)} \tag{5.25}$$

Moreover, the general stress state can be separated into a volumetric component plus a shear component as shown,

$$\begin{bmatrix} \sigma_{11} & \sigma_{12} & \sigma_{13} \\ \sigma_{21} & \sigma_{22} & \sigma_{23} \\ \sigma_{31} & \sigma_{32} & \sigma_{33} \end{bmatrix} = \begin{bmatrix} s_{11} & s_{12} & s_{13} \\ s_{21} & s_{22} & s_{23} \\ s_{31} & s_{32} & s_{33} \end{bmatrix} + \begin{bmatrix} \sigma_m & 0 & 0 \\ 0 & \sigma_m & 0 \\ 0 & 0 & \sigma_m \end{bmatrix} \tag{5.26}$$

In indicial notation

$$\sigma_{ij} = \frac{1}{3}\sigma_{kk}\delta_{ij} + s_{ij} \tag{5.27}$$

Strains can also be separated into dilatational and deviatoric components and the equation for strain analogous to Eq. (5.27) is,

$$\begin{aligned} \varepsilon_{ij} &= \frac{1}{3}\varepsilon_{kk}\delta_{ij} + e_{ij} \\ \Rightarrow \varepsilon_{ij} &= \frac{1}{3}\Delta\delta_{ij} + e_{ij} \end{aligned} \tag{5.28}$$

From Eq. (5.24)

$$\sigma_{ij} = 2G\varepsilon_{ij} + \lambda\Delta\delta_{ij}$$

$$\Rightarrow \sigma_{ij} = 2G\left(\frac{1}{3}\Delta\delta_{ij} + e_{ij}\right) + \lambda\Delta\delta_{ij}$$

$$\Rightarrow \sigma_{ij} = 2Ge_{ij} + \frac{2}{3}G\Delta\delta_{ij} + \lambda\Delta\delta_{ij}$$

$$\Rightarrow \sigma_{ij} = 2Ge_{ij} + \Delta\delta_{ij}\left(\frac{2}{3}G + \lambda\right)$$

$$\Rightarrow \sigma_{ij} = 2Ge_{ij} + \Delta\delta_{ij}K \tag{5.29}$$

Comparing the equations (5.27) and (5.29)

Deviatoric stress, $s_{ij} = 2Ge_{ij}$

Volumetric stress, $\sigma_{kk} = 3K\Delta$ (5.30)

5.3.3 Derivation of Constitutive Equation (3D Viscoelastic Equation)

One dimensional Hooke's law: $\sigma = E\varepsilon$ (5.31)

σ is the normal stress

For shear stress, $\tau = G\gamma$ (5.32)

G is shear modulus, γ is tensorial strain

$\tau = 2G\varepsilon$ as $\gamma = 2\varepsilon$ (5.33)

The stress components in different directions can be expressed as,

$$\sigma_{11} = E\varepsilon_{11}$$

$$\sigma_{12} = 2G\varepsilon_{12} = \sigma_{21}$$

$$\sigma_{13} = 2G\varepsilon_{13} = \sigma_{31}$$

$$\sigma_{22} = E\varepsilon_{22}$$

$$\sigma_{23} = 2G\varepsilon_{23} = \sigma_{32}$$

$$\sigma_{33} = E\varepsilon_{33} \tag{5.34}$$

In Relaxation test shown in Figure 5.6

$$\sigma(t) = \Delta\varepsilon_0 R(t-\tau_0)H(t-\tau_0) + \Delta\varepsilon_1 R(t-\tau_1)H(t-\tau_1) + \Delta\varepsilon_2 R(t-\tau_2)H(t-\tau_2) + \\ \ldots\ldots\ldots + \Delta\varepsilon_n R(t-\tau_N)H(t-\tau_N)$$

$$\sigma(t) = \sum_{n=0}^{N} \Delta\varepsilon_n R(t-\tau_n)H(t-\tau_n) \tag{5.35}$$

Where R is Relaxation modulus and H is Heaviside step function.

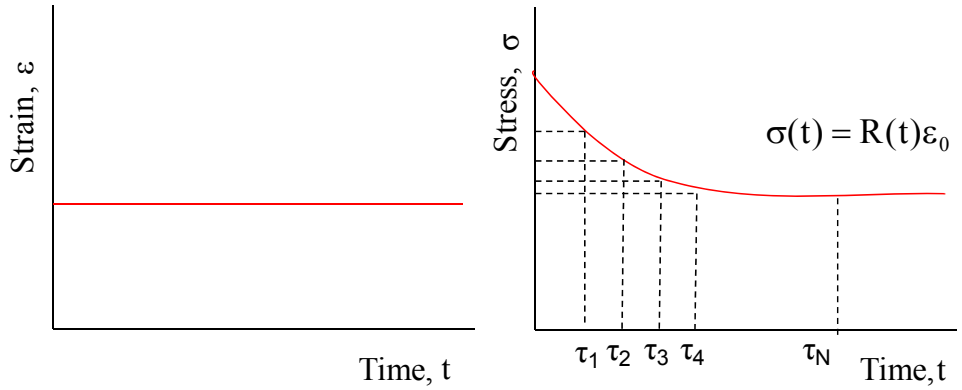

Figure 5.6 Relaxation Test: Strain input (left) and qualitative stress output (right)

$\tau_0 = 0$

$\Delta\varepsilon_0 = \varepsilon_0 = \varepsilon(0)$

$\Delta\tau = \tau_{n+1} - \tau_n$

Thus, $\sigma(t) = \sum_{n=0}^{N} \frac{\Delta\varepsilon_n}{\Delta\tau} R(t-\tau_n)H(t-\tau_n)\Delta\tau$

$\Delta\tau \longrightarrow 0, N \longrightarrow \infty$

Or, $\sigma(t) = \int_0^t \frac{d\varepsilon}{d\tau} R(t-\tau)H(t-\tau)d\tau$ (5.36)

$t - \tau > 0, H(t-\tau) = 1$

Therefore, $\sigma(t) = \int_0^t R(t-\tau)\frac{d\varepsilon}{d\tau}d\tau$ (5.37)

As the stress tensors can be separated into dilatational and deviatoric components

$$\sigma_{dev}(t) = s_{ij} = \int_0^t R_1(t-\tau)\frac{de_{ij}}{d\tau}d\tau \tag{5.38}$$

$$\sigma_{vol}(t) = \sigma_{kk} = \int_0^t R_2(t-\tau)\frac{d\Delta}{d\tau}d\tau \tag{5.39}$$

The elastic equations from Eq. (5.30)

$s_{ij} = 2Ge_{ij}$ and $\sigma_{kk} = 3K\Delta$

In integral form, these equations becomes

$$s_{ij} = 2\int_0^t G(t-\tau)\frac{de_{ij}}{d\tau}d\tau \tag{5.40}$$

$$\sigma_{kk} = 3\int_0^t K(t-\tau)\frac{d\Delta}{d\tau}d\tau \tag{5.41}$$

Recalling the general stress state,

$$\begin{bmatrix} \sigma_{11} & \sigma_{12} & \sigma_{13} \\ \sigma_{21} & \sigma_{22} & \sigma_{23} \\ \sigma_{31} & \sigma_{32} & \sigma_{33} \end{bmatrix} = \begin{bmatrix} s_{11} & s_{12} & s_{13} \\ s_{21} & s_{22} & s_{23} \\ s_{31} & s_{32} & s_{33} \end{bmatrix} + \begin{bmatrix} \sigma_m & 0 & 0 \\ 0 & \sigma_m & 0 \\ 0 & 0 & \sigma_m \end{bmatrix}$$

$\sigma_{11} = s_{11} + \sigma_m$

$$\Rightarrow \sigma_{11} = 2\int_0^t G(t-\tau)\frac{de_{11}}{d\tau}d\tau + \int_0^t K(t-\tau)\frac{d\Delta}{d\tau}d\tau \qquad \text{As, } \sigma_m = \frac{\sigma_{kk}}{3}$$

$$\sigma_{12} = 2\int_0^t G(t-\tau)\frac{de_{12}}{d\tau}d\tau$$

$$\sigma_{13} = 2\int_0^t G(t-\tau)\frac{de_{13}}{d\tau}d\tau$$

$$\sigma_{22} = 2\int_0^t G(t-\tau)\frac{de_{22}}{d\tau}d\tau + \int_0^t K(t-\tau)\frac{d\Delta}{d\tau}d\tau$$

In indicial notation, the above equations can be expressed as,

$$\sigma_{ij}(t) = 2\int_0^t G(t-\tau)\frac{de_{ij}}{d\tau}d\tau + \delta_{ij}\int_0^t K(t-\tau)\frac{d\Delta}{d\tau}d\tau \qquad \text{where, } e_{ij} = \varepsilon_{ij} - \frac{1}{3}\delta_{ij}\Delta$$

5.3.4 Time-Temperature Superposition and Shift Functions

Materials' viscous property depends strongly on temperature. For example, viscoelastic materials turn into viscous fluids at high temperatures while behave like solids at low temperatures. In reality, the temperature effects can be complicated. The so called time-temperature superposition is an assumption based on the observations for many viscoelastic materials, of which the relaxation curve at high temperature is identical to that at a low temperature if the time is properly scaled [104]. In essence, it stipulates that the relaxation times (of all Prony components) obey the scaling law. So according to the time-temperature superposition, the viscoelastic behavior at one temperature can be related to that at another temperature by a shift in the time scale. The change in the relaxation time of a Maxwell element due to a temperature change is resolved by the temperature shift factor, A(T).

$$A(T) = \frac{\tau(T)}{\tau_r} \tag{5.42}$$

where $\tau(T)$ is the relaxation time at temperature T, and τ_r is the relaxation time at the reference temperature T_r. The temperature dependency of the shift factor can be described by shift functions. Thus, the time dependent stress-strain relations in eq. (5.5) are typically extended to include temperature dependence by using the principle of time-temperature superposition and the empirical shift function [100]. Most widely used shift functions are:

- William-Landel-Ferry (WLF) equation
- Tool-Narayanaswamy (TN) equation (also known as Arrhenius equation)

The WLF equation is one of the most referenced equations ever in polymer literature and has the form:

$$\log_{10} A(T) = \log_{10}\left(\frac{t}{t_r}\right) = \frac{-C_1(T - T_r)}{C_2 + (T - T_r)} \tag{5.43}$$

Tool-Narayanaswamy (TN) equation (also known as Arrhenius equation):

$$\ln A(T) = -C_1\left(\frac{1}{T} - \frac{1}{T_r}\right) \quad \text{or} \quad \log_{10} A(T) = -\frac{C_1}{2.303}\left(\frac{1}{T} - \frac{1}{T_r}\right) \tag{5.44}$$

where a_T is the shift factor, C_1 and C_2 are material constants, T = T(t) is the temperature at time t, and T_r is the reference temperature at time t_r.

5.3.5 Determination of Prony Coefficients

In this study, the shear modulus G(t) was extracted from the measured instantaneous modulus E(t) (ratio of applied stress to strain) from the creep data as shown in Figure 5.7 using the eq. (5.47) , following the procedure as done by Mottahedi et al. [105].

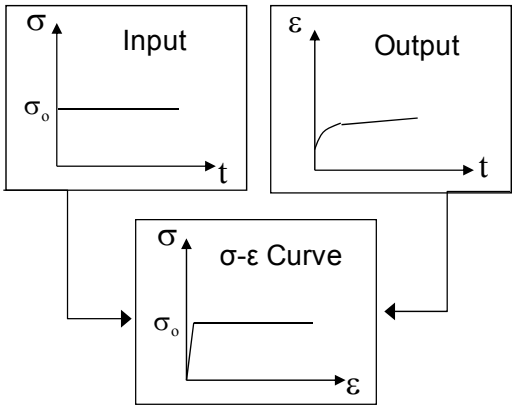

Figure 5.7 Stress-Strain Relations from Creep Data

For an applied stress level σ_o, the instantaneous modulus can determined as the ratio of stress to strain ε (t) at a certain time and the elastic compliance J is the inverse of the modulus E.

$$J = \frac{1}{E} \tag{5.45}$$

$$E(t) = \frac{\sigma_o}{\varepsilon(t)} \tag{5.46}$$

$$G(t) = \frac{E(t)}{2(1+\nu)} \tag{5.47}$$

$$K(t) = \frac{E(t)}{3(1-2\nu)} \tag{5.48}$$

Similarly, the bulk modulus K was extracted from test data using the incompressible approximation of eq. (5.48). After having shear modulus vs. time and bulk modulus vs. time data, the curve fitting to get the Prony coefficients can be done in two ways [76]. In the first method, the temperature dependent modulus data (shear and bulk) is loaded directly into the curve fitting routine of ANSYS to determine Prony pairs and shift function coefficients at the same time.

In alternative method, the temperature shift factor for each temperature can be determined one by one by constructing a master curve. A master curve can be constructed at an arbitrary temperature by shifting the shear moduli or bulk moduli at all other temperatures to the reference temperature. In a log-log of modulus vs. time, this is equivalent to a shift of the curves horizontally by a distance log $a_T(T)$. $a_T(T)$ is known as the shift factor. Then the Prony pairs can be determined for the reference temperature using MATLAB or other curve fitting routine. The temperature dependency of the shift factor can be expressed in terms of shift function coefficients.

5.3.6 Finite Element Solution

5.3.6.1 Determination of Prony Coefficients Using ANSYS

The viscoelastic model based on Prony series is readily available in the ANSYS program along with the tools to generate and fit derived coefficients to the experimental data. In this method, the experimentally characterized shear and bulk moduli as a function of time and temperature of UF1 and UF2 have been used as input data in the material property curve-fitting routines of ANSYS to determine Prony series and shift function coefficients simultaneously. The curve fitting tool determines the material coefficients by relating the experimental data to the Prony series expansion for both the shear and bulk modulus of the ANSYS hypoviscoelastic material option. Curve fitting can be performed either interactively or via batch commands. Once the experimental data has been input, the order of Prony series expansion is to be defined and then nonlinear regression is performed. After viewing the curve fitting results graphically and accepting the result, the fitted coefficients can be written to the database as ANSYS nonlinear data table commands for the subsequent finite elements analyses. The curve fitting tool of ANSYS is able to fit shear modulus and/or bulk modulus and/or shift functions, along with discrete temperature dependencies for multiple data sets.

The experimentally characterized creep curves of UF1 shown in Figure 4.16 of previous chapter at 5 different temperatures have been utilized with the curve-fitting routines within ANSYS to determine the optimal Prony series and shift function coefficients in eqs. (5.14-5.15, 5.43) simultaneously. After some trial and error optimization on the number of terms to truncate the Prony series, 4 terms in the shear response series in eq. (5.14) and 5 terms in the volumetric response series in eq. (5.15)

have been chosen. The coefficients calculated for UF1 using ANSYS are shown in Table 5.2. The α's and τ's of Eq. (5.14) and Eq. (5.15) are represented as a's and t's in Table 5.2.

Table 5.2 Prony Series Coefficients from ANSYS Curve Fitting Routine for UF1

Constants for Shear Response	Constants for Volumetric Response	Constants for Shift Function (Williams-Landel-Ferry (WLF) Equation)
a_1 = 0.1366 t_1 = 3556.6000 a_2 = 0.2300 t_2 = 30006.0000 a_3 = 0.3111 t_3 = 0.3009×10^6 a_4 = 0.0934 t_4 = 3.01×10^6	a_1 = 9.0746×10^{-10} t_1 = 86.8690 a_2 = 0.5313 t_2 = 0.8663 a_3 = 0.2403 t_3 = 94.8260 a_4 = 0.0845 t_4 = 999.9400 a_5 = 0.0726 t_5 = 10000.0000	T_{ref} = 88.9860 C_1 = -16.1830 C_2 = -469.2900

Where a is relative modulus, t is relative time, T_{ref} is reference temperature, C_1 and C_2 are WLF constants for UF1

5.3.6.2FEA Model with Prony Coefficients

A 2D model of the full test specimen has been developed in ANSYS for finite element analysis using viscoelastic (Prony series) properties as shown in Figure 5.8. An 8-node PLANE 183 element has been used during the analysis. The model geometry, applied boundary conditions and loadings for stress-strain and creep of underfill (UF1 and UF2) are demonstrated in Figure 5.8. For the FEA model of tensile specimen (upper model), a prescribed displacement in y-direction has been applied at the right end whereas the lower model which represents the creep model, has a constant, applied axial load and is free to stretch horizontally. In both cases, all degree of freedom has been fixed at the left end and uniform temperature has been applied on the surface. Like

previous, the FEA models have been meshed with 11520 elements to ensure the solution is converged and also further increasing of elements does not have any effect on the results. During the finite element analysis of creep, secant modulus has been used as the material property to capture the correct elastic jump of total strain whereas initial elastic modulus has been employed in case of finite element modeling of stress-strain.

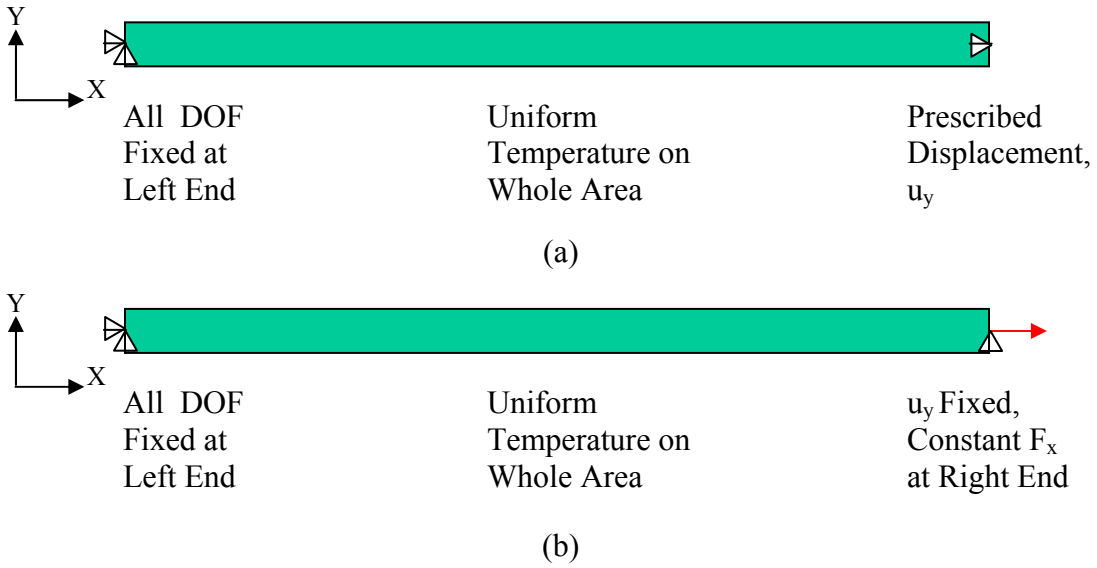

Figure 5.8 FEA Models with Viscoelastic Properties of the Full Specimen for (a) Tensile (b) Creep Test
Specimen Length, L = 60 mm, Width, W = 3 mm

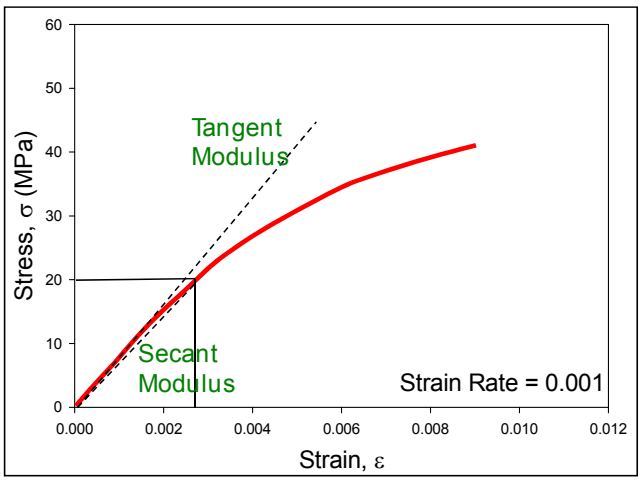

Figure 5.9 Determination of Secant Modulus

Table 5.3 Secant Modulus of UF1

Temperature (C)	Stress Level (MPa)	Secant Modulus (MPa)	Temperature (C)	Stress Level (MPa)	Secant Modulus (MPa)
25	10	6360.18	75	15	4406.84
	15	6297.50		20	4278.61
	20	6202.37		25	4200.00
	25	6084.31	100	5	3593.30
50	5	5941.30		10	3510.06
	10	5893.47		15	3381.44
	15	5817.13		20	3161.15
	20	5700.42		25	2913.11
	25	5556.52	125	5	1973.52
75	5	4547.78		10	1747.21
	10	4494.43		15	1286.13

Secant modulus of elasticity is the ratio of stress to strain at any point on curve in a stress-strain diagram. It is the slope of a line from the origin to any point on a stress-strain curve. Tangent modulus of elasticity is the slope of the stress-strain curve at any specified stress or strain. Below the proportional limit the tangent modulus is equivalent to Young's modulus (Figure 5.9). The values of secant modulus used in the finite element analysis of creep for UF1 are listed in Table 5.3.

5.3.6.3FEA (Viscoelastic Model) Predictions for UF1

Figure 5.10 contains correlations of the Prony Series viscoelastic model predictions (using the coefficients in Table 5.2). Unlike the Anand model predictions shown previously, the model correlates well with the experimental stress-strain data of UF1 at all strain levels, temperatures, and strain rates. Based on this success, we have also evaluated the ability of the Prony Series model to predict the UF1 creep data in

Figure 4.16. This correlation is shown in Figure 5.11, and it is seen that the agreement is excellent for all temperatures and stress levels.

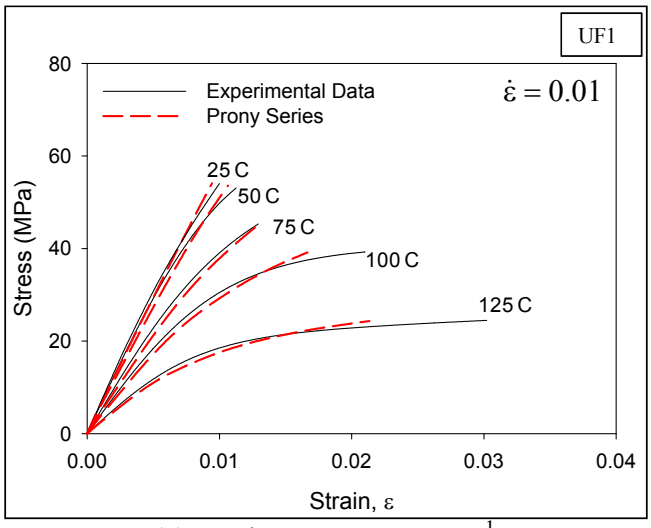

(a) Strain Rate = 0.01 sec^{-1}

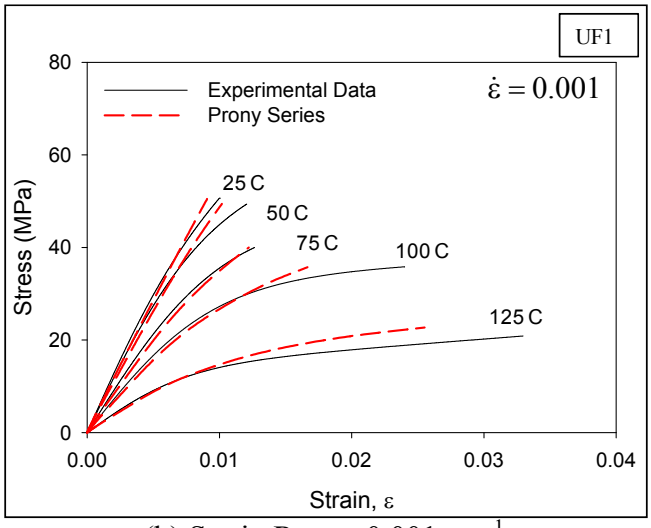

(b) Strain Rate = 0.001 sec^{-1}

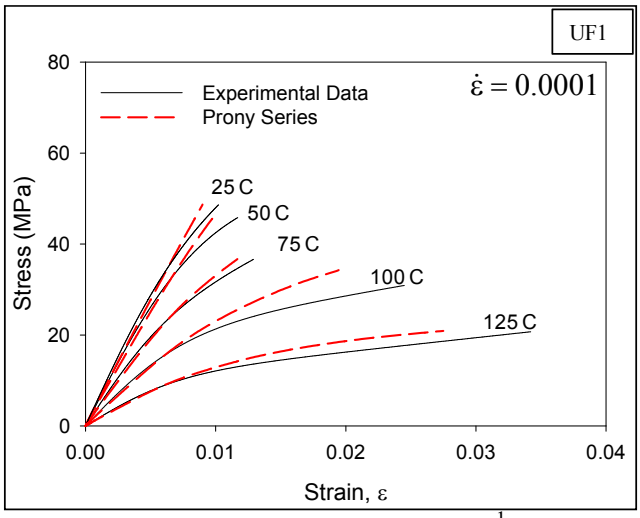

(c) Strain Rate = 0.0001 sec^{-1}

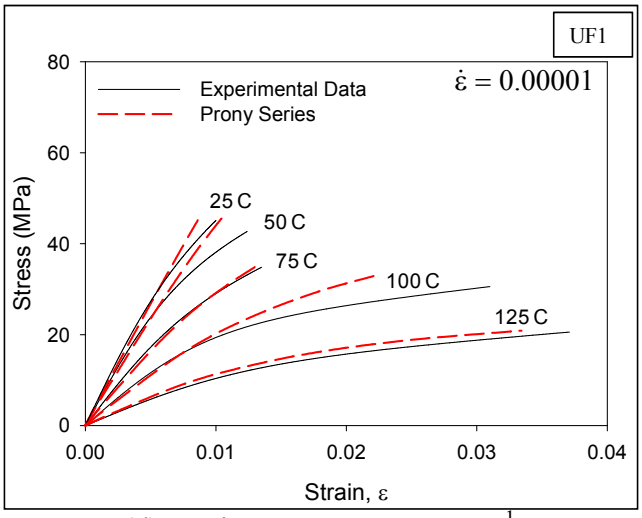

(d) Strain Rate = 0.00001 sec^{-1}

Figure 5.10 Correlation of Prony Series Viscoelastic Model Predictions with UF1 Stress-Stain Data

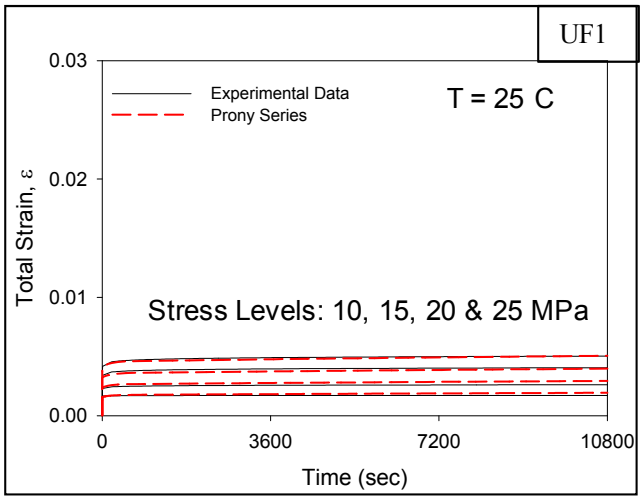

(a) T = 25 C

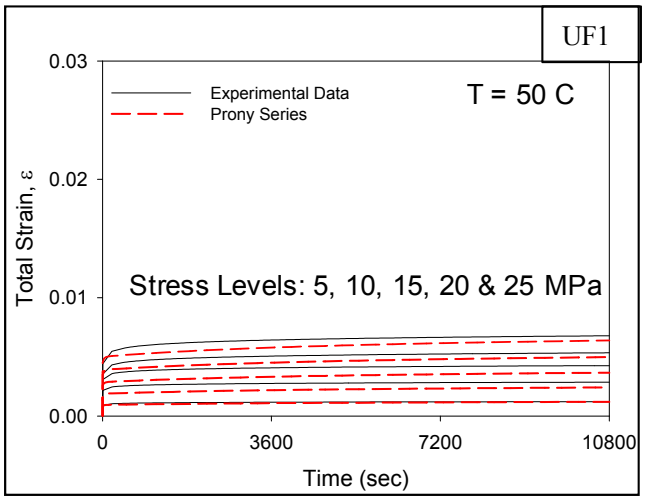

(b) T = 50 C

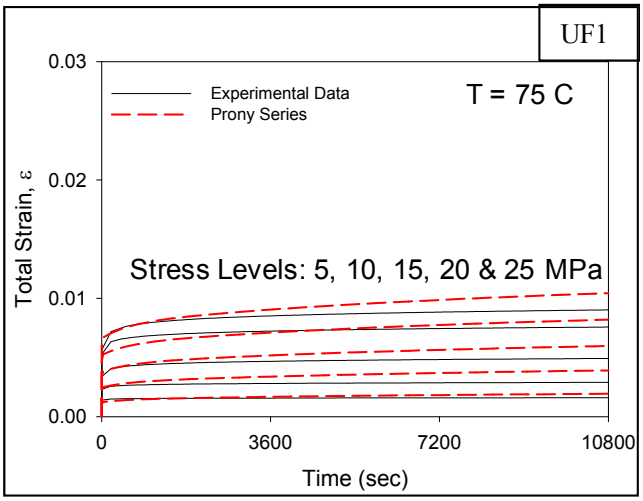

(c) T = 75 C

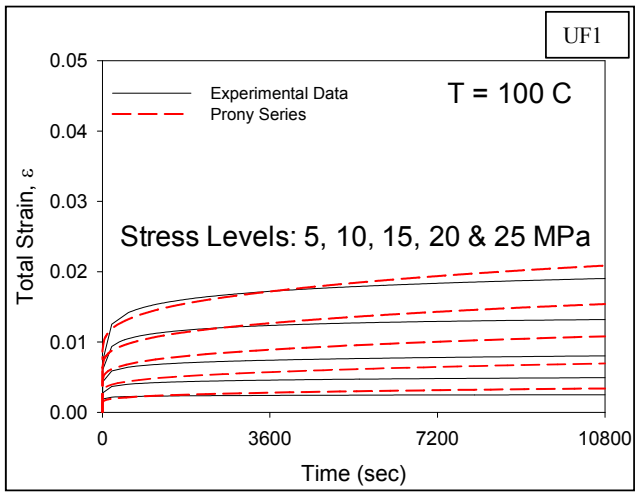

(d) T = 100 C

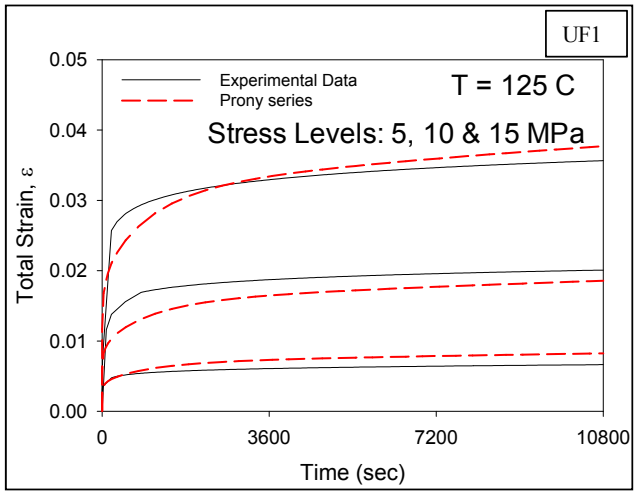

(e) T = 125 C

Figure 5.11 Correlation of Prony Series Viscoelastic Model Predictions with UF1 Creep Data

Table 5.4 lists the secondary creep strain rate values of UF1 derived from the experimental data and FEA predictions. In each case, the linear parts of the creep curves have been considered and slopes at the end have been recorded as strain rates. It is evident from the table that the strain rate values deviate from those obtained from experimental results. Especially for low stress levels, the difference is noticeable.

Table 5.4 Comparison of Strain rate obtained from Experimental Data and Prony Series Viscoelastic Model Predictions for UF1

Temperature	**Stress Level (MPa)**	**Strain Rate from Experimental Data**	**Strain Rate from FEA Prediction**
25 C	10	3.359×10^{-9}	1.439×10^{-8}
	15	8.233×10^{-9}	2.180×10^{-8}
	20	1.418×10^{-8}	2.949×10^{-8}
	25	2.292×10^{-8}	3.756×10^{-8}
50 C	5	1.999×10^{-9}	1.196×10^{-8}
	10	4.487×10^{-9}	2.409×10^{-8}
	15	1.147×10^{-8}	3.657×10^{-8}
	20	1.941×10^{-8}	4.972×10^{-8}
	25	4.058×10^{-8}	6.368×10^{-8}
75 C	5	6.376×10^{-9}	2.935×10^{-8}
	10	1.115×10^{-8}	5.932×10^{-8}
	15	1.758×10^{-8}	9.063×10^{-8}
	20	2.398×10^{-8}	1.243×10^{-7}
	25	4.947×10^{-8}	1.580×10^{-7}
100 C	5	2.435×10^{-8}	6.756×10^{-8}
	10	4.013×10^{-8}	1.379×10^{-7}
	15	5.457×10^{-8}	2.142×10^{-7}
	20	1.390×10^{-7}	3.044×10^{-7}
	25	2.071×10^{-7}	4.114×10^{-7}
125 C	5	6.237×10^{-8}	1.049×10^{-7}
	10	1.323×10^{-7}	2.381×10^{-7}
	15	3.930×10^{-7}	4.889×10^{-7}

5.3.6.4FEA (Viscoelastic Model) Predictions for UF2

The experimentally characterized creep curves shown in Figure 4.22 of previous chapter at 4 different temperatures have been utilized with the curve-fitting routines within ANSYS to determine the optimal Prony series and shift function coefficients in Eqs. (5.14-5.15, 5.43) simultaneously. After some trial and error optimization on the number of terms to truncate the Prony series, 4 terms in the shear response series in Eq. (5.14) and 5 terms in the volumetric response series in Eq. (5.15) have been chosen. The coefficients calculated for UF2 using ANSYS are shown in Table 5.5. The α's and τ's of Eq. (5.14) and Eq. (5.15) are represented as a's and t's in Table 5.5.

Table 5.5 Prony Series Coefficients from ANSYS Curve Fitting Routine for UF2

Constants for Shear Response	Constants for Volumetric Response	Constants for Shift Function (Williams-Landel-Ferry (WLF) Equation)
a_1 = 0.30055 t_1 = 44.1300 a_2 = 0.19892 t_2 = 1378.1000 a_3 = 0.32473 t_3 = 35530 a_4 = 0.16401 t_4 = 9.8788×10^5	a_1 = 0.90618 t_1 = 0.00195 a_2 = 0.00499 t_2 = 9.2235 a_3 = 0.01633 t_3 = 136.43 a_4 = 0.01703 t_4 = 10921 a_5 = 0.00732 t_5 = 3.1206×10^5	T_{ref} = 106.63 C_1 = -50.064 C_2 = -651.89

Where a is relative modulus, t is relative time, T_{ref} is reference temperature, C_1 and C_2 are WLF constants for UF2

Like previous, secant modulus has been used as the material property during the finite element analysis of creep in ANSYS. The values of secant modulus used in the finite element analysis of creep for UF2 are listed in Table 5.6.

Table 5.6 Secant Modulus of UF2

Temperature (C)	Stress Level (MPa)	Secant Modulus (MPa)	Temperature (C)	Stress Level (MPa)	Secant Modulus (MPa)
25	10	11909.9	80	30	9045.3
	20	11771.1	100	10	8100.3
	30	11544.9		20	7562.6
	40	11000.2		30	6402.4
80	10	9300.1	125	10	4677.4
	20	9278.2		15	4113.8

Figure 5.12 contains correlations of the Prony Series viscoelastic model predictions (using the coefficients in Table 5.5). Like UF1, the model correlates well with the experimental stress-strain data of UF2 at all strain levels, temperatures for strain rate of 0.001 sec^{-1} in Figure 4.20. Based on this success, we have also evaluated the ability of the Prony Series model to predict the UF2 creep data in Figure 4.22. This correlation is shown in Figure 5.13, and it is seen that the agreement is excellent for all temperatures and stress levels.

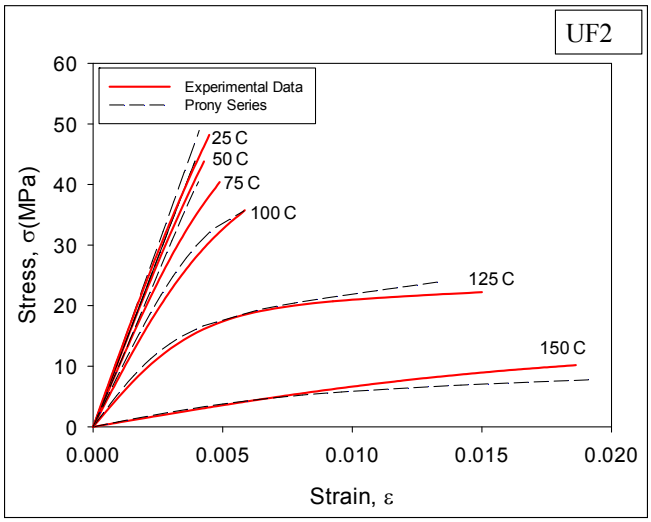

Figure 5.12 Correlation of Prony Series Viscoelastic Model Predictions with UF2 Stress-Stain Data

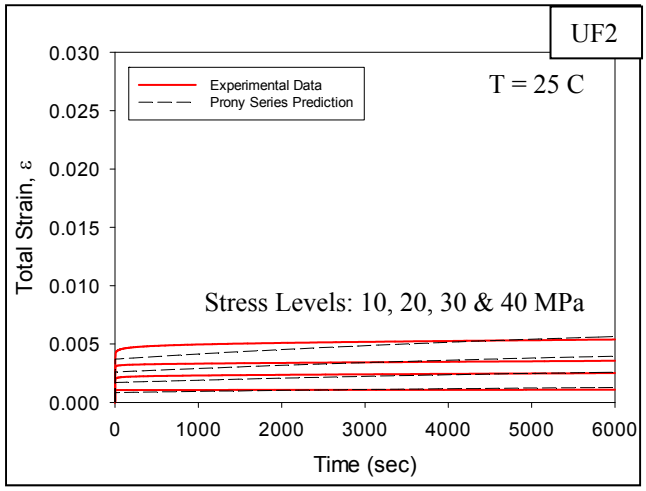
UF2
T = 25 C
Experimental Data
Prony Series Prediction
Stress Levels: 10, 20, 30 & 40 MPa
Total Strain, ε
Time (sec)
0.030
0.025
0.020
0.015
0.010
0.005
0.000
0
1000
2000
3000
4000
5000
6000

(a) T = 25 C

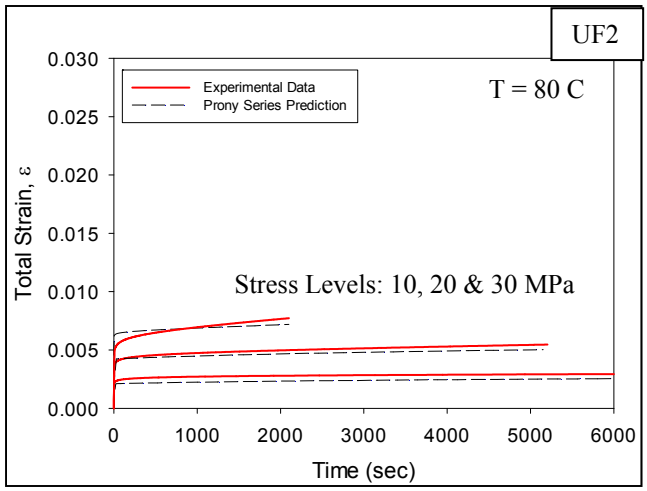
UF2
T = 80 C
Experimental Data
Prony Series Prediction
Stress Levels: 10, 20 & 30 MPa
Total Strain, ε
Time (sec)
0.030
0.025
0.020
0.015
0.010
0.005
0.000
0
1000
2000
3000
4000
5000
6000

(b) T = 80 C

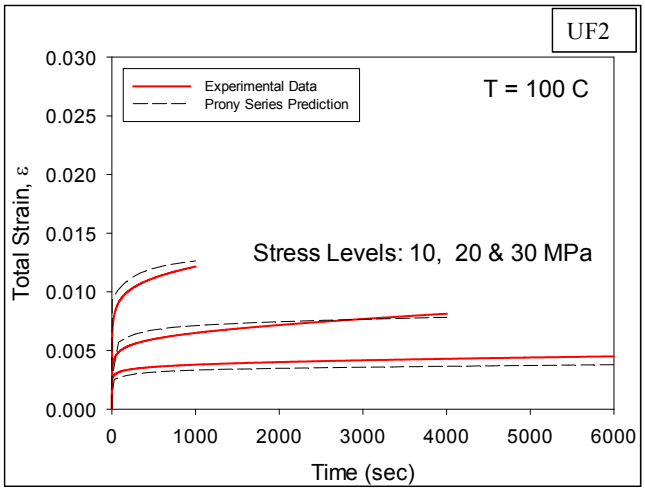

(c) T = 100 C

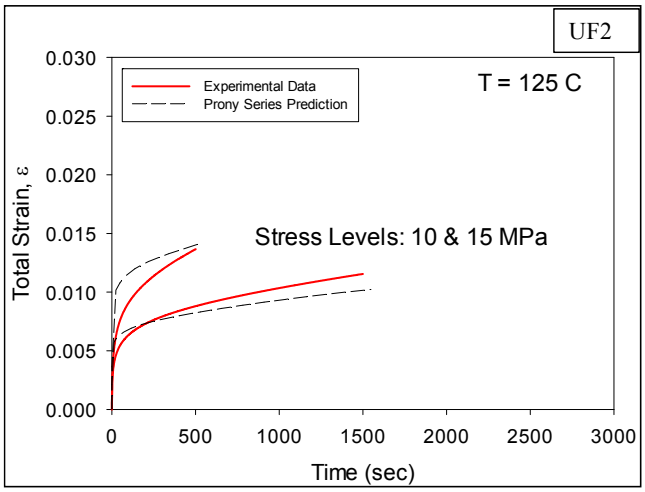

(d) T = 125 C

Figure 5.13 Correlation of Prony Series Viscoelastic Model Predictions with UF2 Creep Data

5.3.7 Analytical Solutions of Viscoelastic Model

In the preceding sections of this chapter, it was demonstrated that ANSYS curve fitting routine was used to determine the Prony coefficients and a FEA model with viscoelastic properties in ANSYS was developed to predict the stress-strain and creep behavior of underfill. In this section, an analytical procedure has been presented to do the same thing in MATLAB. The MATLAB uses shear and bulk modulus data that is calculated from the experimental creep curves. A non-linear regression routine has been used to extract the best fit of Prony series coefficients and analytical methods using MATLAB code has been developed to calculate the viscoelastic response using the Prony series model. At the end, the analytical methods and finite element approaches have been compared with the experimental results.

5.3.7.1Determination of Prony Coefficients Using MATLAB

The data can be fitted using the Fitting GUI from Curve Fitting Tool of MATLAB. The fitting process involves finding coefficients (parameters) for one or more models that fit to data. Parametric Curve Fitting Toolbox™ in MATLAB have different parametric library models like exponentials, Fourier series, Gaussian, polynomials, Power Series, Rationals, Sum of Sines and Weibull Distribution. Besides, these models the software also provides the option for using user-defined or custom models where a user can use his/her own model.

Custom equations have two options

1. Linear Equations
2. General Equations (for nonlinear terms)

The fitting method is automatically selected based on the library or custom models that have been used. For nonlinear models, the method is NonlinearLeastSquares where more options are available such as:

Robust — To specify whether to use the robust least-squares fitting method. The values are

- Off — For not using robust fitting (default).
- On — For fitting with default robust method (bisquare weights).
- LAR — For fitting by minimizing the least absolute residuals (LAR).
- Bisquare — For fitting by minimizing the summed square of the residuals, and down-weight outliers using bisquare weights. In most cases, this is the best choice for robust fitting.

Fitting Algorithms — The coefficients can be adjusted to determine whether the fit improves. The direction and magnitude of the adjustment depend on the fitting algorithm. The toolbox provides three algorithms:

- Trust-Region — This is the default algorithm and it can solve difficult nonlinear problems more efficiently than the other algorithms and it represents an improvement over the popular Levenberg-Marquardt algorithm.
- Levenberg-Marquardt — This algorithm has been used for many years and has proved to work most of the time for a wide range of nonlinear models and starting values. If the trust-region algorithm does not produce a reasonable fit, then this algorithm can be useful.

- Gauss-Newton —This algorithm is potentially faster than the other algorithms, but it assumes that the residuals are close to zero. It should be the last choice for most models and data sets.

Besides the above mentioned fitting methods and algorithms, other options are also provided in MATLAB to expedite the convergence of the solution.

Finite Differencing Parameters

- DiffMinChange — Minimum change in coefficients for finite difference Jacobians. The default value is 10^{-8}.
- DiffMaxChange — Maximum change in coefficients for finite difference Jacobians. The default value is 0.1.

Fit Convergence Criteria

- MaxFunEvals — Maximum number of function (model) evaluations allowed. The default value is 600.
- MaxIter — Maximum number of fit iterations allowed. The default value is 400.
- TolFun — Termination tolerance used on stopping conditions involving the function (model) value. The default value is 10^{-6}.
- TolX — Termination tolerance used on stopping conditions involving the coefficients. The default value is 10^{-6}.

To determine the Prony coefficients, the shear modulus and bulk modulus as function of time and temperature have been used as input parameters. The input data of shear moduli and bulk moduli for different temperatures are plotted against time in Figure 5.14 and 5.17 respectively. During the curve fitting, NonlinearLeastSquares

method has been applied where robust fitting has been kept off and Trust-Region has been used as fitting algorithms. The other fitting options have been set to their default values. After some trial and error optimization on the number of terms to truncate the Prony series, 4 terms in the shear response series and 5 terms in the volumetric response series have been chosen.

The experimentally characterized creep curves of UF2 shown in Figure 4.22 of previous chapter at 4 different temperatures have been utilized to extract the shear modulus and bulk modulus as function of time and temperature. At first, all the creep data which are a fit of eq. (4.3) are extended equally up to a limit of 10000 seconds. Specially, for 125 C where the specimen failed after 1500 seconds in real case has been extended. This was done to avoid complexity during finding coefficients which consists of Prony pairs (α, τ) of relative modulus and relative time. Then the shear modulus and bulk modulus have been calculated using Eq.s (5.47) and (5.48). To determine the Prony coefficients, a master curve has been constructed at 100 C by horizontally shifting the shear moduli or bulk moduli at all other temperatures (25 C, 80 C and 125 C) to the reference temperature (100 C) as shown in Figures 5.15, 5.16 and 5.18. Figure 5.16 and 5.18 show the fitting of master curve along with the goodness of fitting and calculated coefficients. Figures 5.15 and 5.16 demonstrate the procedure of constructing master curve of shear response and the curve is a fit of Eq. (5.12). Figure 5.18 shows master curve of bulk response is a fit of Eq. (5.13) and is constructed at 100 C. The coefficients of shear response and bulk response were then further used to determine Prony pairs at the reference temperature of 100 C. At the same time, the temperature shift factor for each temperature has been determined one by one while constructing a master curve.

Shift factors are tabulated in Table 5.7. The temperature dependency of the shift factor can be expressed in terms of WLF shift function coefficients and is shown in Figure 5.19. Table 5.8 shows the coefficients calculated using MATLAB for UF2.

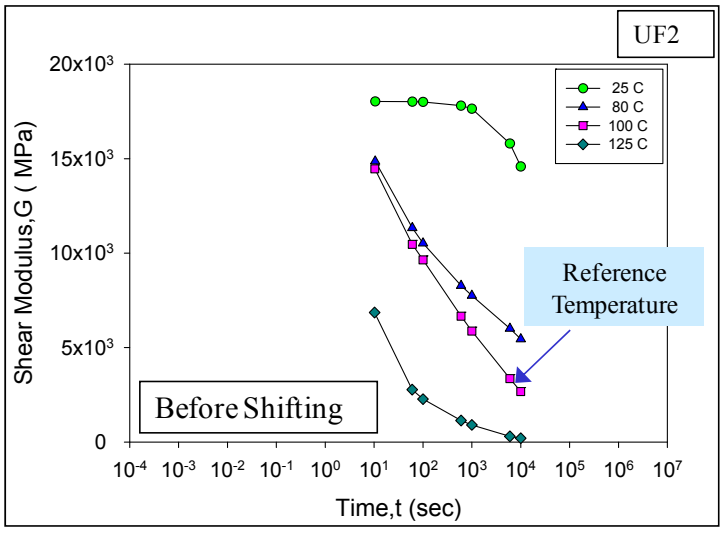

Figure 5.14 Shear Modulus vs. Time of UF2

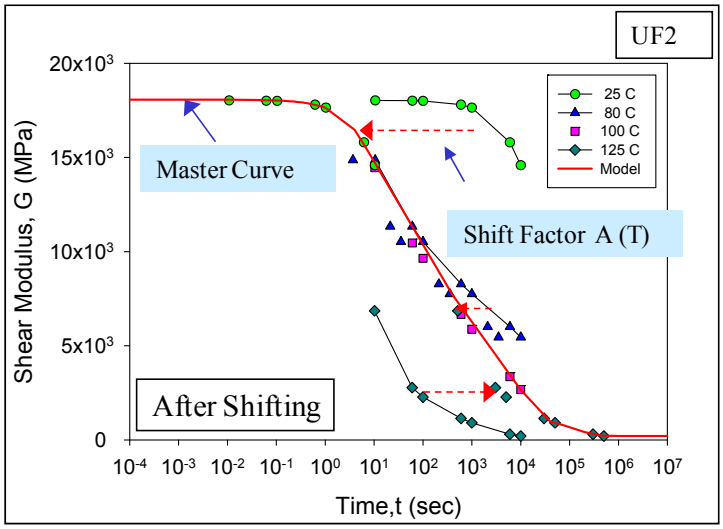

Figure 5.15 Construction of Master Curve of Shear Response With Respect to the Reference Temperature of 100 C for UF2

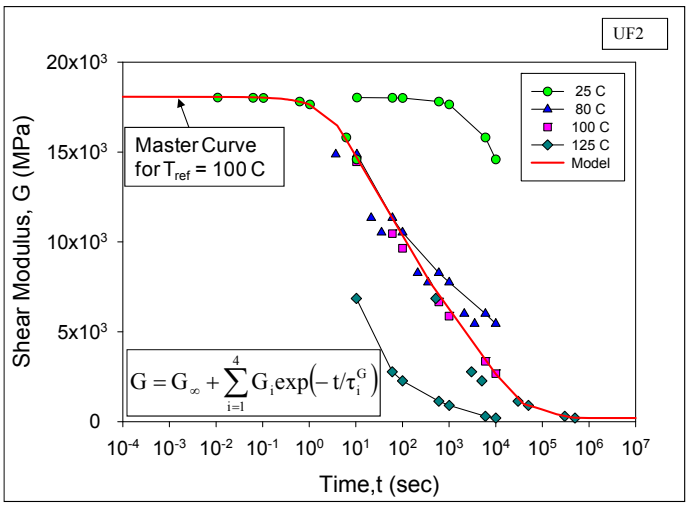

$r^2 = 0.9898$
Coefficient Data:
$G_\infty = 200.1$
$G_1 = 1286$
$\tau_1 = 285.6$
$G_2 = 9002$
$\tau_2 = 20.79$
$G_3 = 6546$
$\tau_3 = 6775$
$G_4 = 1035$
$\tau_4 = 1.286 \times 10^5$

Figure 5.16 Master Curve of Shear Response
at 100 C with Determined Coefficients of UF2

The Prony series approach assumes Eq. (5.12):

$$G = G_\infty + \sum_{i=1}^{n_G} G_i \exp\left(-t/\tau_i^G\right)$$

The instantaneous shear moduli (5.16):

$$G_0 = G_\infty + \sum_{i=1}^{n_G} G_i$$

$$G_0 = 18069.1$$

Relative moduli: $\alpha_i^G = G_i/G_0$

$$\alpha_1^G = 1286/18069.1 = 0.0712$$

Thus, $\alpha_2^G = 0.4982$, $\alpha_3^G = 0.3623$, $\alpha_4^G = 0.0573$

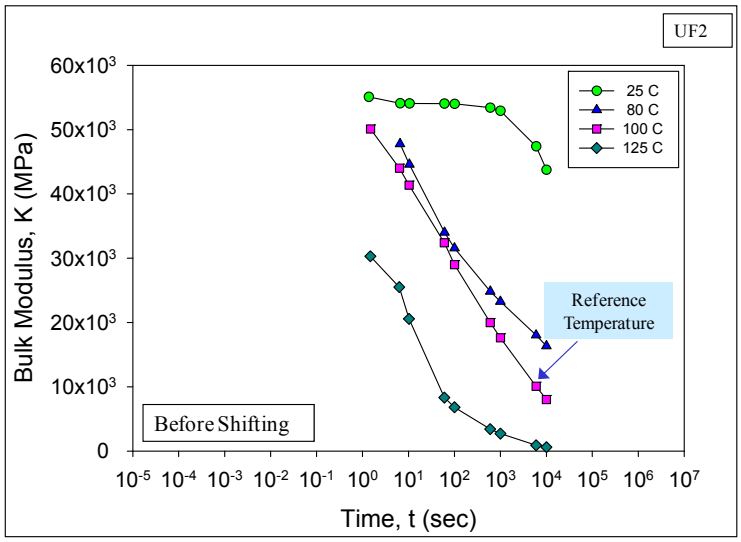

Figure 5.17 Bulk Modulus vs. Time of UF2

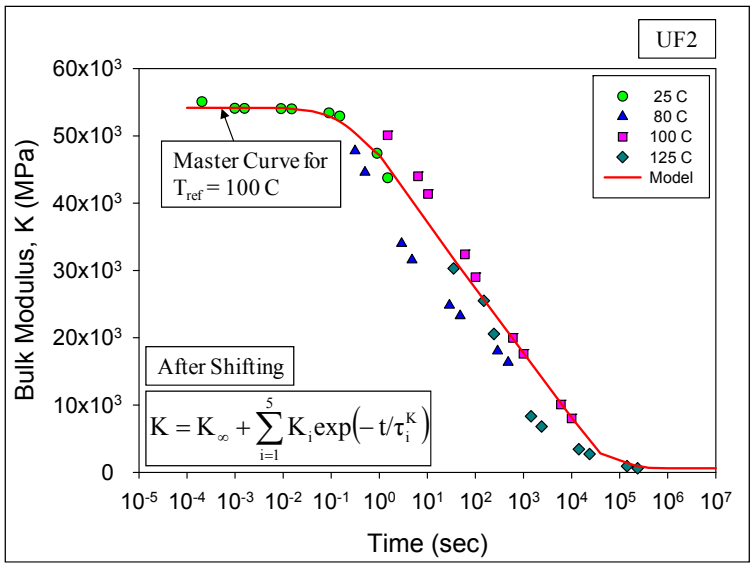

$r^2 = 0.9391$
Coefficient Data:
$K_\infty = 615$
$K_1 = 1.868 \times 10^5$
$\tau_1 = 7.822 \times 10^{-5}$
$K_2 = 7243$
$\tau_2 = 0.4401$
$K_3 = 2.318 \times 10^4$
$\tau_3 = 34.94$
$K_4 = 2.008 \times 10^4$
$\tau_4 = 6798$
$K_5 = 3199$
$\tau_5 = 1 \times 10^5$

Figure 5.18 Master Curve of Bulk Response
at 100 C with Determined Coefficients of UF2

For bulk response, the Prony series approach assumes (5.13):

The instantaneous shear moduli (5.17):

$$K_0 = K_\infty + \sum_{i=1}^{n_K} K_i$$

$$K_0 = 241117$$

Relative moduli: $\alpha_i^K = K_i / K_0$

$$\alpha_1^K = 1.868 \times 10^5 / 241117 = 0.7747$$

Thus, $\alpha_2^K = 0.0300$, $\alpha_3^K = 0.0961$, $\alpha_4^K = 0.0833$, $\alpha_5^K = 0.0133$

Table 5.7 Shift Factors at Different Temperatures for UF2

Shift Factors	
A(25)	5780.9
A(80)	39.81
A(100)	1
A(125)	0.0902

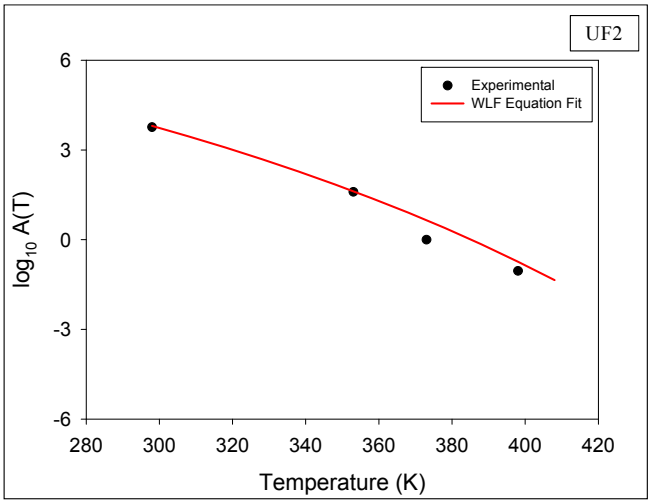

$r^2 = 0.9537$
Coefficient Data:
$C_1 = -18.22$
$C_2 = -330$
$T_r = 385.2$ K $= 112.2$ C

Figure 5.19 Determination of Shift Function Coefficients for UF2

Table 5.8 Prony Series Coefficients from MATLAB Curve Fitting Routine for UF2

Constants for Shear Response	Constants for Volumetric Response	Constants for Shift Function (Williams-Landel-Ferry (WLF) Equation)
a_1 = 0.0712 t_1 = 285.6 a_2 = 0.4982 t_2 = 20.79 a_3 = 0.3623 t_3 = 6775 a_4 = 0.0573 t_4 = 128600	a_1 = 0.7747 t_1 = 7.822×10^{-5} a_2 = 0.0300 t_2 =0.4401 a_3 = 0.0961 t_3 = 34.94 a_4 = 0.0833 t_4 = 6798 a_5 = 0.0133 t_5 = 1×10^5	T_{ref} = 112.2 C C_1 = -18.22 C_2 = -330

Where a is relative modulus, t is relative time, T_{ref} is reference temperature, C_1 and C_2 are WLF constants for UF2

5.3.7.2Analytical Procedure to Solve Creep with Viscoelastic Properties

The Prony series response functions for shear and bulk moduli can be expressed by eq. (5.14) and (5.15). In the equations, α_i and τ_i are Prony pairs, α_i's are relative moduli and τ_i are relative time for reference temperature (in this case 100 C), already determined from the curve fitting shown in Table 5.8.

$$\alpha_\infty = 1 - \sum_{i=1}^{n} \alpha_i \tag{5.49}$$

τ_i are determined from eq. (5.14)

$$\tau_i^{G,K} = A(T) \times \tau_r \tag{5.50}$$

Instantaneous shear and bulk moduli G_0 and K_0 are determined as:

$$G_0 = \frac{E}{2(1+\upsilon)} \tag{5.51}$$

$$K_0 = \frac{E}{3(1-2\upsilon)} \tag{5.52}$$

E is initial elastic modulus and ν is poisson's ratio.

The x-component of stress for an isotropic linear viscoelastic material is:

$$\sigma_{11} = \int_0^t 2G(t-\tau)\frac{de_{11}}{d\tau}d\tau + \int_0^t K(t-\tau)\frac{d\Delta}{d\tau}d\tau \tag{5.53}$$

The integral form of the two independent relaxation functions $R_1(t)$ and $R_2(t)$ are

Deviatoric part: $s_{11} = \int_0^t R_1(t-\tau)\frac{de_{11}}{d\tau}d\tau = \int_0^t 2G(t-\tau)\frac{de_{11}}{d\tau}d\tau$ (5.54)

Volumetric part: $\sigma_{kk} = \int_0^t R_2(t-\tau)\frac{d\Delta}{d\tau}d\tau = \int_0^t 3K(t-\tau)\frac{d\Delta}{d\tau}d\tau$ (5.55)

The relaxation functions $G(t-\tau)$ and $K(t-\tau)$ are determined from Eq.s (5.14) and (5.15).

The general stress state can be separated into a volumetric component plus a shear component:

$$\begin{bmatrix} \sigma_{11} & \sigma_{12} & \sigma_{13} \\ \sigma_{21} & \sigma_{22} & \sigma_{23} \\ \sigma_{31} & \sigma_{32} & \sigma_{33} \end{bmatrix} = \begin{bmatrix} s_{11} & s_{12} & s_{13} \\ s_{21} & s_{22} & s_{23} \\ s_{31} & s_{32} & s_{33} \end{bmatrix} + \begin{bmatrix} \sigma_m & 0 & 0 \\ 0 & \sigma_m & 0 \\ 0 & 0 & \sigma_m \end{bmatrix} \tag{5.56}$$

Where

$$\begin{aligned} &\sigma_{11} = s_{11} + \sigma_m \\ &\Rightarrow \sigma_{11} = s_{11} + \frac{1}{3}\sigma_{kk} \\ &\sigma_{kk} = \sigma_{11} + \sigma_{22} + \sigma_{33} \end{aligned} \tag{5.57}$$

The general strain state can also be separated into a volumetric component plus a shear component as shown:

$$\begin{bmatrix} \varepsilon_{11} & \varepsilon_{12} & \varepsilon_{13} \\ \varepsilon_{21} & \varepsilon_{22} & \varepsilon_{23} \\ \varepsilon_{31} & \varepsilon_{32} & \varepsilon_{33} \end{bmatrix} = \begin{bmatrix} e_{11} & e_{12} & e_{13} \\ e_{21} & e_{22} & e_{23} \\ e_{31} & e_{32} & e_{33} \end{bmatrix} + \begin{bmatrix} e_m & 0 & 0 \\ 0 & e_m & 0 \\ 0 & 0 & e_m \end{bmatrix} \quad \text{where} \quad e_{ii} = 0 \tag{5.58}$$

x-component of strain,

$$\varepsilon_{11} = e_{11} + e_m$$

$$\Rightarrow \varepsilon_{11} = e_{11} + \frac{1}{3}\Delta$$
$$\Delta = \varepsilon_{11} + \varepsilon_{22} + \varepsilon_{33} \tag{5.59}$$

The creep integral form of the deviatoric part of strain, $e_{ij} = \int_0^t J_1(t-\tau)\frac{ds_{ij}}{d\tau}d\tau$ (5.60)

and volumetric part of strain, $\Delta = \int_0^t J_2(t-\tau)\frac{d\sigma_{kk}}{d\tau}d\tau$ (5.61)

If $J_1(t)$ and $J_2(t)$ are the two independent creep functions, and $e_{ij} = \varepsilon_{ij} - \frac{1}{3}\delta_{ij}\Delta$ from eq. (5.58) then,

$$\varepsilon_{11} = \int_0^t J_1(t-\tau)\frac{ds_{11}}{d\tau}d\tau + \frac{1}{3}\int_0^t J_2(t-\tau)\frac{d\sigma_{kk}}{d\tau}d\tau$$
$$\text{where, } s_{11} = \sigma_{11} - \frac{\sigma_{11}+\sigma_{22}+\sigma_{33}}{3} = \frac{2}{3}\sigma_{11} \tag{5.62}$$
$$\text{and } \sigma_{kk} = \sigma_{11} + \sigma_{22} + \sigma_{33} = \sigma_{11}$$

(assumed as uniaxial problem)

It is seen that $R_1(t)$ and $J_1(t)$ are the relaxation and creep functions appropriate to states of shear, where $R_2(t)$ and $J_2(t)$ are defined relative to states of dilatation. Both the creep integral and relaxation integral characterize the linear viscoelastic behavior of one particular material. Hence these must exist a relation between the creep function J(t) and the relaxation function R(t). In order to find such a relation it is convenient to utilize the Laplace transfoms as,

$$\hat{s}_{ij}(s) = s\hat{R}_1(s)\hat{e}_{ij}(s)$$

$$\hat{\sigma}_{kk}(s) = s\hat{R}_2(s)\hat{\Delta}(s)$$

$$\hat{e}_{ij}(s) = s\hat{J}_1(s)\hat{s}_{ij}(s)$$

$$\hat{\Delta}(s) = s\hat{J}_2(s)\hat{\sigma}_{kk}(s) \tag{5.63}$$

It follows from the above expressions that

$$\begin{aligned} &\hat{J}_\alpha(s) = \left[s^2\hat{R}_\alpha(s)\right]^{-1} \quad \text{as, } \alpha = 1,2 \\ &\hat{J}(s)\hat{R}(s) = \frac{1}{s^2} \end{aligned} \tag{5.64}$$

Based upon Boltzmann's superposition principle, the creep response of linear viscoelastic materials can be described by the hereditary integral such as,

$$\varepsilon_{ij} = \int_{-\infty}^{t} J_1(t-\tau)\frac{d\sigma_{ij}(\theta)}{d\theta}d\theta + \delta_{ij}\int_{-\infty}^{t} J_2(t-\tau)\frac{d\sigma_{kk}(\theta)}{d\theta}d\theta \tag{5.65}$$

where, $\tau = t - \theta$

If is starts in the history at time $\theta = 0$, by the constitutive equation,

$$\varepsilon(t) = \int_0^t \frac{\partial\sigma(\theta)}{\partial\theta}A(t-\theta)d\theta \tag{5.66}$$

The integral can be interpreted as a convolution integral and can be solved by applying convolution theorem.

The convolution of two functions, say $f_1(t)$ and $f_2(t)$, is defined according to:

$$\varphi(t) := \int_0^t f_1(\theta)f_2(t-\theta)d\theta \equiv f_1 * f_2 \tag{5.67}$$

Introducing the substitution $\tau = t - \theta$, the definition can alternatively expressed in the form,

$$\varphi(t) := \int_0^t f_2(\tau)f_1(t-\tau)d\tau \equiv f_2 * f_1 \tag{5.68}$$

Comparing both forms, it can be seen that the convolution of two functions is commutative, i.e,

$$f_1 * f_2 = f_2 * f_1 \tag{5.69}$$

The convolution theorem is then arrived by applying the Laplace transform to the convolution integral φ(t),

$$\hat{\varphi}(s) = L\{f_1 * f_2\} = L\{f_1(t)\}L\{f_2(t)\} = \hat{f}_1(s)\hat{f}_2(s) \tag{5.70}$$

Considering deviatoric part,

$$e_{ij} = \int_0^t J_1(t-\tau)\frac{ds_{11}(\tau)}{d\tau}d\tau$$

Assuming,

$$f_1 = J_1(\theta)$$
$$f_2 = \frac{ds_{11}(t-\theta)}{d\tau}$$

Using relation between creep compliance and relaxation modulus,

$$L\{J_1(\theta)\} = \frac{1}{s^2 L\{G_1(\theta)\}} \tag{5.71}$$

And,

$$\begin{aligned} L\left\{\frac{ds_{11}(t-\theta)}{d\tau}\right\} &= \frac{2}{3}L\left\{\frac{d\sigma_{11}(t-\theta)}{d\tau}\right\} = \frac{2}{3}L\left\{\frac{d\sigma_0}{d\tau}H(t-\theta)\right\} \\ &= \frac{2}{3}\left[s\frac{\sigma_0}{s}e^{-\theta s} - 0\right] = \frac{2}{3}\sigma_0 e^{-\theta s} \end{aligned} \tag{5.72}$$

For creep, $\sigma_{11} = \sigma_0 H(t)$

From Laplace Transforms,

$$L\left\{\frac{df}{dt}\right\} = sF(s) - f(0)$$

$$L\{H(t-\tau)\} = \frac{1}{s}e^{-\tau s}$$

Assuming,

$$P = L\{J_1(\theta)\}L\left\{\frac{ds_{11}(t-\theta)}{d\tau}\right\} = L\{J_1\}\frac{2}{3}\sigma_0 e^{-\theta s} \tag{5.73}$$

Therefore, deviatoric part of total strain = $L^{-1}\{P\}$

Similarly assuming, $Q = L\{J_2\}\sigma_0 e^{-\theta s}$ (5.74)

And volumetric part of total strain = $L^{-1}\{Q\}$

Total strain,

$$\varepsilon_{11} = (\varepsilon_{11})_{dev.} + \frac{1}{3}(\varepsilon_{11})_{vol.} = L^{-1}\{P\} + \frac{1}{3}L^{-1}\{Q\} \tag{5.75}$$

5.3.7.3Analytical Procedure to Solve Stress-Strain with Viscoelastic Properties

In this case, eq.s (5.49) through (5.52) have been used again to determine α_∞, τ_i (for shear and bulk), G_0 and K_0 as were done during creep analysis. The relaxation functions $G(t-\tau)$ and $K(t-\tau)$ are then determined from Eq.s (5.14) and (5.15). The laplace transformed isotropic Young's modulus and the Poisson's ratio are defined by:

$$\hat{E}(s) = \frac{3\hat{R}_1(s)\hat{R}_2(s)}{\hat{R}_1(s) + 2\hat{R}_2(s)} = \frac{9\hat{G}(s)\hat{K}(s)}{\hat{G}(s) + 3\hat{K}(s)} \tag{5.76}$$

$$\hat{\upsilon}(s) = \frac{\hat{R}_2(s) - \hat{R}_1(s)}{s\left[\hat{R}_1(s) + 2\hat{R}_2(s)\right]} = \frac{3\hat{K}(s) - 2\hat{G}(s)}{2s\left[\hat{G}(s) + 3\hat{K}(s)\right]} \tag{5.77}$$

Where

$$R_1(t) = 2G(t) \tag{5.78}$$

$$R_2(t) = 3K(t) \tag{5.79}$$

Stress Calculation:

$$\Delta\sigma_i = E_t \Delta\varepsilon_i$$

$$\Delta\sigma_{i+1} = E_{t+\Delta t} \Delta\varepsilon_{i+1} \tag{5.80}$$

Again,

$$\sigma_{i+1} = \sigma_i + \Delta\sigma_i$$

$$\sigma_{i+2} = \sigma_{i+1} + \Delta\sigma_{i+1} \tag{5.81}$$

Simplifying for Uniaxial Stress-Strain Test at Constant Strain Rate

$$\varepsilon_{22} = \varepsilon_{33} = -\nu\varepsilon_{11} \tag{5.82}$$

$$e_{11} = \frac{2(1+\nu)}{3}\varepsilon_{11} \tag{5.83}$$

$$e_{22} = e_{33} = \frac{-(1+\nu)}{3}\varepsilon_{11} \tag{5.84}$$

$$\Delta = (1-2\nu)\varepsilon_{11} \tag{5.85}$$

If "L" be the length, "w" be the width and "th" be the thickness of the specimen then strain can be calculated as

$$\varepsilon_{11} = \sqrt{\left[1+\frac{\partial u_1}{\partial x_1}\right]^2 + \left[\frac{\partial u_2}{\partial x_1}\right]^2 + \left[\frac{\partial u_3}{\partial x_1}\right]^2} - 1 \tag{5.86}$$

$$\varepsilon_{11} = \sqrt{\left[1+\frac{\partial u_1}{\partial x_1}\right]^2 + \left[\frac{\partial x_2}{\partial x_1}\frac{\partial u_2}{\partial x_2}\right]^2 + \left[\frac{\partial x_3}{\partial x_1}\frac{\partial u_3}{\partial x_3}\right]^2} - 1 \tag{5.87}$$

$$\varepsilon_{11} = \sqrt{\left[1+\frac{\partial u_1}{\partial x_1}\right]^2 + \left[\frac{\partial x_2}{\partial x_1}\nu\frac{\partial u_1}{\partial x_1}\right]^2 + \left[\frac{\partial x_3}{\partial x_1}\nu\frac{\partial u_1}{\partial x_1}\right]^2} - 1 \tag{5.88}$$

Again,

$$\varepsilon_i = \sqrt{\left[1+\frac{u_i}{L}\right]^2 + \left[\frac{w}{L}\nu\frac{u_i}{L}\right]^2 + \left[\frac{th}{L}\nu\frac{u_i}{L}\right]^2} - 1 \tag{5.89}$$

$$u_{i+1} = u_i + \Delta u_i$$

$$\varepsilon_{i+1} = \sqrt{\left[1+\frac{u_{i+1}}{L}\right]^2 + \left[\frac{w}{L}\nu\frac{u_{i+1}}{L}\right]^2 + \left[\frac{th}{L}\nu\frac{u_{i+1}}{L}\right]^2} - 1 \tag{5.90}$$

$$u_{i+2} = u_{i+1} + \Delta u_{i+1}$$

$$\varepsilon_{i+2} = \sqrt{\left[1+\frac{u_{i+2}}{L}\right]^2 + \left[\frac{w}{L}\nu\frac{u_{i+2}}{L}\right]^2 + \left[\frac{th}{L}\nu\frac{u_{i+2}}{L}\right]^2} - 1 \tag{5.91}$$

5.3.8 Comparison of Finite Element and Analytical Approach

5.3.8.1 Method #1: Using One Set of Coefficients

In the first method, the set of Prony series coefficients determined using ANSYS curve fitting routine (shown in Table 5.5) has been used both in the FEA model of ANSYS and in MATLAB code to predict the material behavior. Then the results obtained from two approaches have been plotted together to have a better comparison of the two adopted approaches for the prediction of stress-strain and creep behavior of the viscoelastic material. Figures 5.20 and 5.21 show that analytical results and FEA predictions are in excellent agreement for creep curves as well as stress-strain curves.

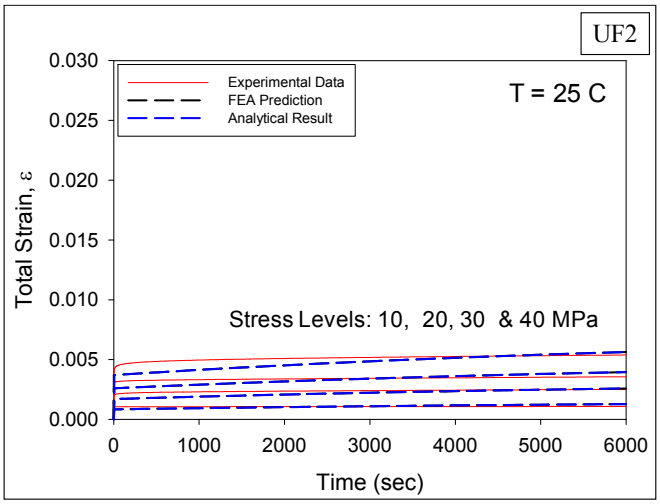

(a) Creep Curves at T = 25 C

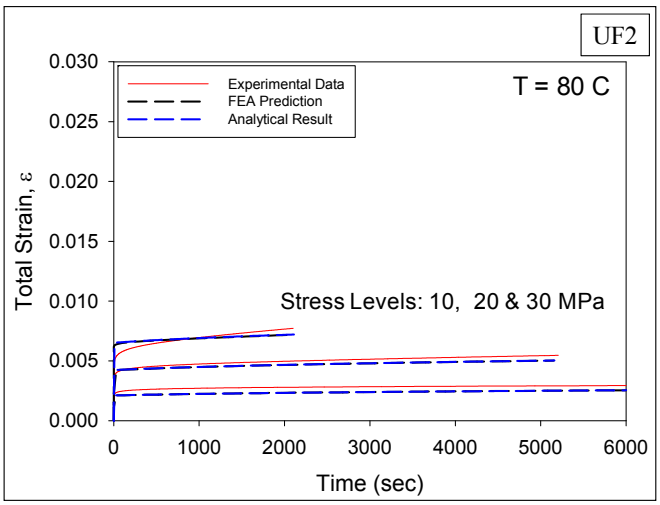

(b) Creep Curves at T = 80 C

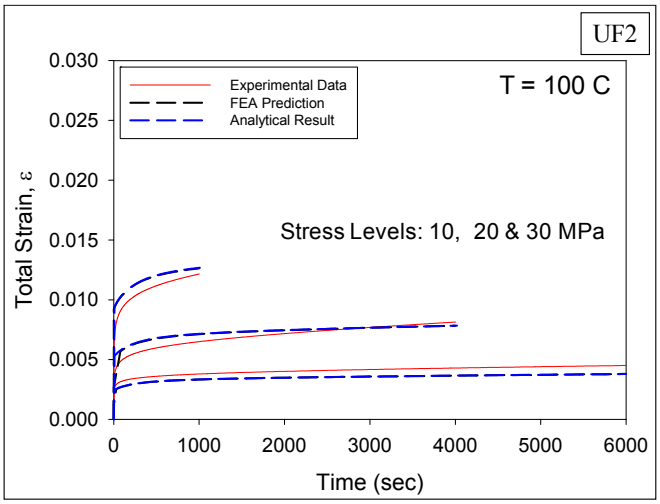

(c) Creep Curves at T = 100 C

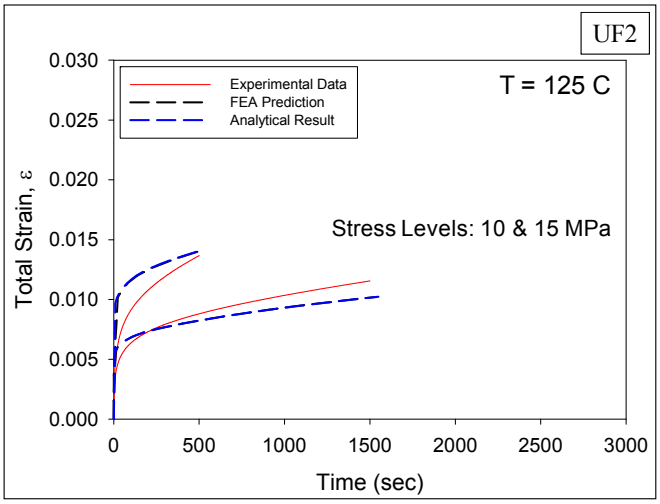

(d) Creep Curves at T = 125 C

Figure 5.20 Comparison of FEA Predictions and Analytical Results with UF2 Experimental Creep Data (Using One Set of Coefficients)

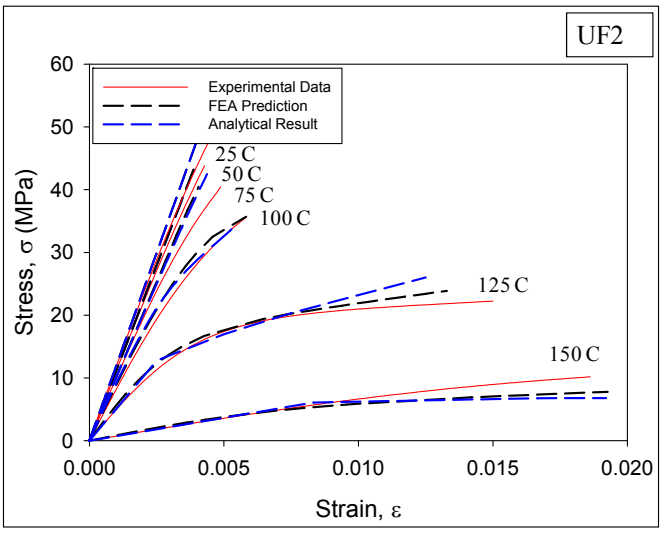

Figure 5.21Comparison of FEA Predictions and Analytical Results with UF2 Experimental Tensile Data (Using One Set of Coefficients)

5.3.8.2Method #2: Using Different Set of Coefficients

This method utilizes the Prony series coefficients determined using ANSYS as well as MATLAB. Both finite element approaches and analytical methods developed to calculate the viscoelastic response have been employed using the prony series model. The coefficients determined from the ANSYS curve fitting routine (listed in Table 5.5) has been further used in the FEA model with viscoelastic properties to predict the stress-strain and creep behavior of the material. Similarly, the Prony coefficients obtained from the curve fitting tool of MATLAB (as shown in Table 5.8) has been used in the MATLAB code following the analytical procedure stated in the sections of 5.3.7.2 and 5.3.7.3 to represent stress-strain and creep behavior of a viscoelastic polymer. The correlations of the Prony series viscoelastic model predictions using finite element and analytical approach (using the coefficients of Table 5.5 and 5.8) are shown in Figure 5.22 and 5.23. It is seen that there is a good agreement for all temperatures and stress levels of

creep curves. It is also evident from the figure that the results of two approaches are in fine agreement for stress-strain curves.

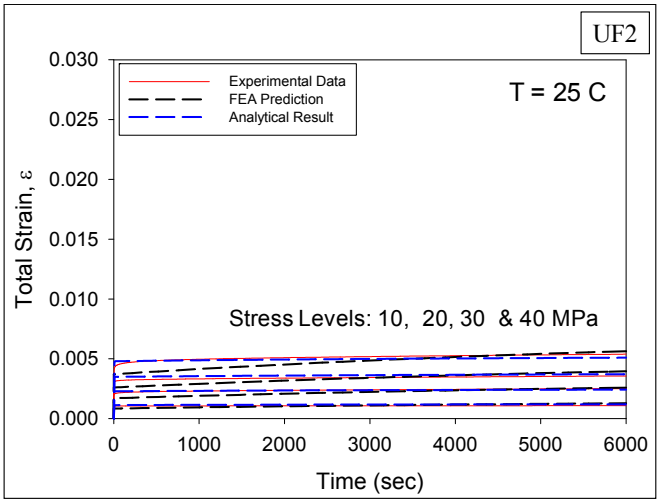

(a) Creep Curves at T = 25 C

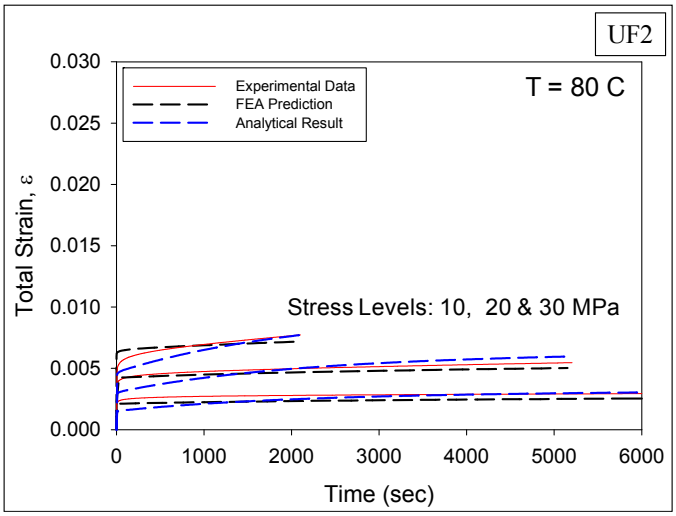

(b) Creep Curves at T = 80 C

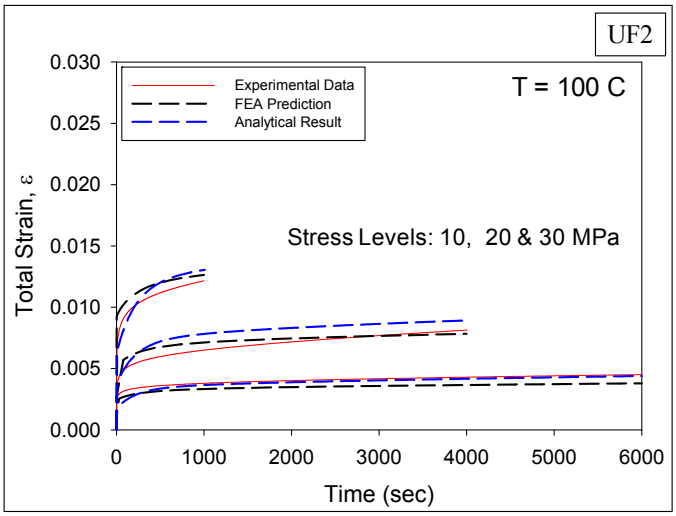

(c) Creep Curves at T = 100 C

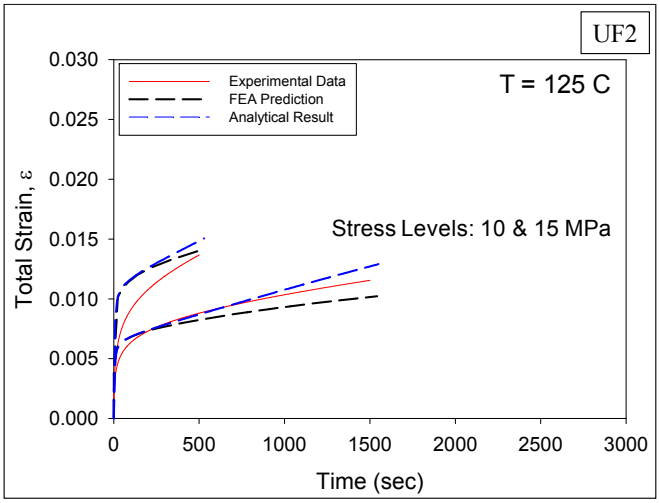

(d) Creep Curves at T = 125 C

Figure 5.22 Comparison of FEA Predictions and Analytical Results with UF2 Experimental Creep Data (Using Two Different Sets of Coefficients)

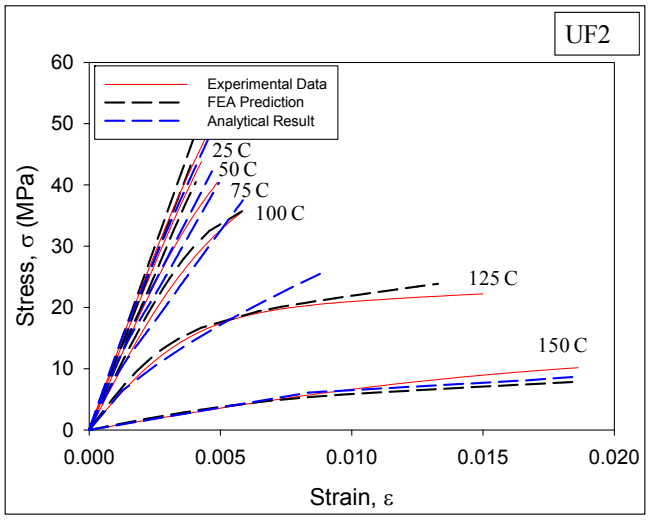

Figure 5.23 Comparison of FEA Predictions and Analytical Results with UF2 Experimental Tensile Data (Using Two Different Sets of Coefficients)

Table 5.9 Comparison of Strain rates obtained from Experimental Data and Prony Series Viscoelastic Model Predictions using ANSYS and MATLAB for UF2

Temperature	Stress Level (MPa)	Strain Rate from Experimental Data	Strain Rate from FEA Prediction	Strain Rate from Analytical Results
25 C	10	4.880×10^{-9}	5.058×10^{-8}	7.509×10^{-9}
	20	3.233×10^{-8}	1.022×10^{-7}	1.520×10^{-8}
	30	4.112×10^{-8}	1.562×10^{-7}	2.324×10^{-8}
	40	5.822×10^{-8}	2.222×10^{-7}	3.192×10^{-8}
80 C	10	2.511×10^{-8}	4.242×10^{-8}	7.437×10^{-8}
	20	1.406×10^{-7}	9.832×10^{-8}	2.024×10^{-7}
	30	7.039×10^{-7}	2.765×10^{-7}	1.094×10^{-6}
100 C	10	9.761×10^{-8}	6.674×10^{-8}	1.136×10^{-7}
	20	4.504×10^{-7}	1.773×10^{-7}	2.779×10^{-7}
	30	1.952×10^{-6}	1.210×10^{-6}	1.976×10^{-6}
125 C	10	2.410×10^{-6}	1.663×10^{-6}	3.894×10^{-6}
	15	8.498×10^{-6}	4.620×10^{-6}	7.299×10^{-6}

Table 5.9 shows the secondary creep strain rate values of UF2 derived from the experimental data and Prony series viscoelastic model predictions using finite element analysis (ANSYS) and analytical approach (MATLAB). In each case, the linear parts of the creep curves have been considered and slopes at the end have been recorded as strain rates. Like UF1, the strain rate values deviate from those obtained from experimental results and for low stress levels, the difference between experimental data and FEA prediction is noticeable.

5.4 Summary and Discussion

In this chapter, the Anand viscoplastic model and Prony Series viscoelastic model have been applied to fit the mechanical response data of underfill. Optimum model parameters have been calculated and the correlations of the models to the data have been evaluated. The Anand model predictions were found to match the UF1 experimental stress-strain curves fairly well at low strain levels. However, the model and data deviate significantly at higher stress and strain levels.

The three-dimensional linear viscoelastic model based on prony series response functions has been applied to fit the stress-strain and creep data of both UF1 and UF2. Optimum model coefficients have been calculated, the correlations of the models to the data have been evaluated and excellent correlation has been obtained. The Prony series viscoelastic model has been found to represent the rate dependent stress-strain data at all temperatures as well as the creep data at all temperatures and applied stress levels.

The correlations of the Prony Series viscoelastic model predictions using finite element and analytical approach with UF2 experimental data also exhibit good

agreement. The qualitative agreement of the results implies the validity of the analytical approach.

CHAPTER 6

EFFECT OF MOISTURE EXPOSURE ON MECHANICAL PROPERTIES OF MICROELECTRONIC PACKAGING POLYMERS

6.1 Introduction

The mechanical properties of polymer materials are always the key concern of microelectronic packaging industry. The theoretical analysis of stress, strain, and deformation induced in electronic assemblies by environmental exposures such as moisture adsorption, isothermal aging, and thermal cycling require the complete characterization of mechanical properties and constitutive behavior of the constituent materials. In this chapter, the effects of moisture adsorption on the mechanical behavior of microelectronic packaging polymers have been presented. Polymers subjected to controlled humidity during the study are as follows:

- Polymer Encapsulant
- Polycarbonate
- Silica filled epoxy: Underfill (ME 525), denoted as UF2 in this study

Uniaxial test specimens were exposed in a controlled temperature and humidity chamber to combined hygrothermal exposures at 60 C and 90% RH, 60 C and 50% RH, 40 C and 50% RH and 85 C and 85% RH for various durations. After moisture preconditioning, the mechanical behavior of the materials have been evaluated at several temperatures. In addition, experiments have been performed to characterize the increase in the moisture content of the polymers during hygrothermal exposure.

6.2 Effects of Moisture on Polymer Encapsulant

Polymer encapsulants are widely used in microelctronic packaging shown in Figure 6.1. These materials exhibit evolving properties that change significantly with environmental exposures such as moisture uptake, isothermal aging and thermal cycling. In this section, initial experimental measurements of material behavior changes occurring in polymer encapsulants have been presented which was exposed to a controlled temperature and humidity of 85 C / 85 % RH. The sample preparation procedure is discussed in Chapter 3. A microscale tension-torsion testing machine has been used to evaluate the uniaxial tensile stress-strain behaviors of the material at several temperatures. The changes in mechanical behavior were recorded for the various durations of hygrothermal exposure. Reversibility tests were also conducted to evaluate whether the degradations in the mechanical properties were recoverable.

6.2.1 Stress-Strain Data for Non-Aged Samples

Figure 6.2 illustrates typical average stress-strain curves for the tested encapsulant (no hygrothermal aging/preconditioning) at temperatures from T = 20 C to T = 70 C. In this work, the effective elastic modulus E is defined to be the slope of the initial linear portion of the stress-strain curves. The plot of E vs. temperature (each data point represents the average of 3 to 5 tests) is shown in Figure 6.3. The glass transition region for T > +50 C is clearly evident.

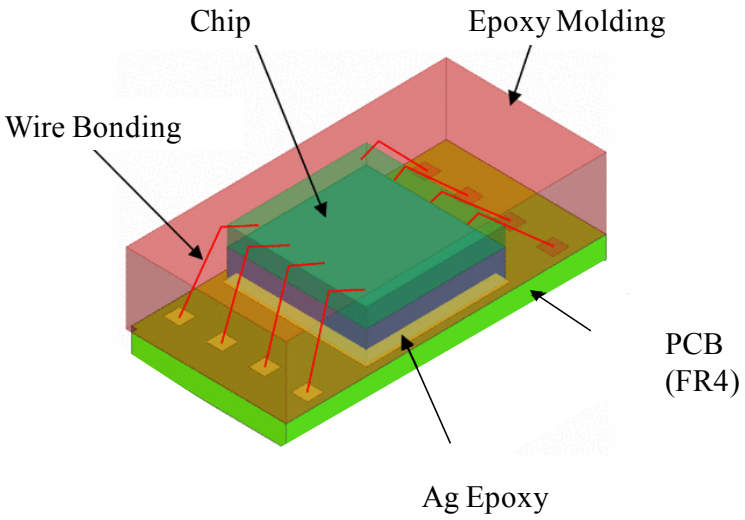

Figure 6.1 Polymer Encapsulant in Microelectronic Packaging

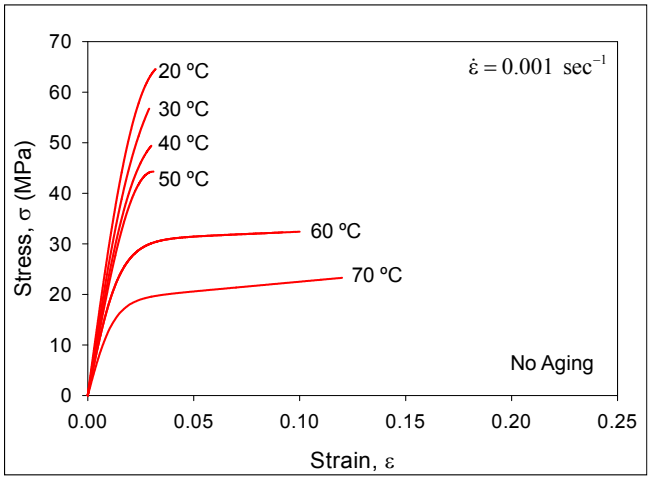

Figure 6.2 Temperature Dependent Stress-Strain Curves of Polymer Encapsulant (No Moisture Exposure)

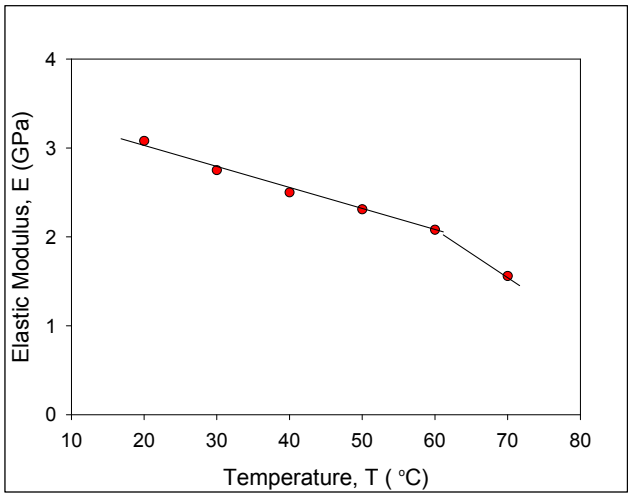

Figure 6.3 Effective Elastic Modulus vs. Temperature of Polymer Encapsulant (No Moisture Exposure)

For this material, the effects of moisture exposure on the stress strain curves from T = 20 C (room temperature) up to T = 70 C (the glass transition temperature of the material) have been explored. During the study, the range or maximum strain of the average curve for each temperature was found by averaging the failure strains from each of the 3-5 tests used in the regression fit for that temperature.

6.2.2 Stress-Strain Data after Moisture Adsorption and Comparisons

The effects of combined temperature/humidity exposures (85 C / 85% RH) on the polymer encapsulant stress-strain curves and mechanical properties have been explored. After hygrothermal aging/preconditioning, the samples were uniaxially tested with testing temperatures ranging from 20 C to 70 C. In addition to the group of non-aged samples described above, 3 other groups (A, B, C) of test specimens were prepared for moisture exposure. In each case the samples were baked in a box oven at 85 C for 24 hours prior to moisture preconditioning at 85 C / 85% RH conditions in a humidity chamber. Group A

had a moisture exposure for 3 days, and Group B had a moisture exposure or 10 days. Group C consisted of samples for reversibility testing. These specimens were first subjected to moisture exposure for 10 days. Then they were baked again for different durations of time (e.g. 0, 1, 3, 10 days) at 85 C to re-dry the sample to various degrees. With each amount of redrying, the stress-strain response and material properties were measured at room temperature, and compared to the original/baseline sample results.

For groups A and B, there were at least 30 samples. Before starting the tests, the samples were allowed to cool down to room temperature (T = 20 C) and 5 specimens were tested at each of 6 different temperatures (T = 20, 30, 40, 50, 60 and 70 C). The raw data from each set of conditions and testing temperature were then fit with the hyperbolic tangent empirical model to generate an average stress-strain curve representation for each set of data. For example, the average temperature dependent stress-strain curves at different testing temperatures after moisture adsorption for 3 and 10 days at 85 C / 85% RH conditions are shown in Figures 6.4 and 6.5, respectively.

The effects of moisture adsorption are not immediately obvious by casual comparison of the plots in Figure 6.2 with those in Figures 6.4 and 6.5. Direct comparisons of the curves at each temperature for moisture exposed and baseline samples are given in Figure 6.6. The decreases of the initial modulus (initial slope) and ultimate strength (failure stress) with humidity exposure are easily visualized in these plots. The modulus and strength values were extracted from stress-strain curves and plotted as a function of temperature as shown in Figures 6.7-6.8. Both properties are seen to decrease a large amount during the first 3 days of hygrothermal aging, and much smaller amounts during the next 7 days of moisture adsorption.

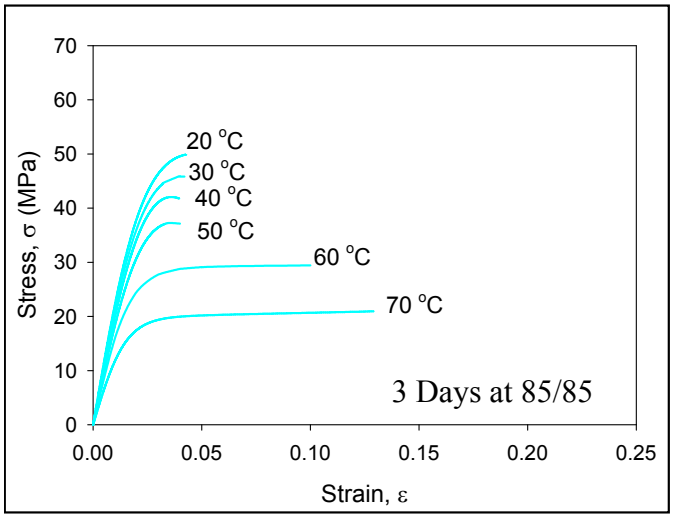

Figure 6.4 Temperature Dependent Stress-Strain Curves of Polymer Encapsulant (Moisture Exposure for 3 Days at 85 C/85 % RH)

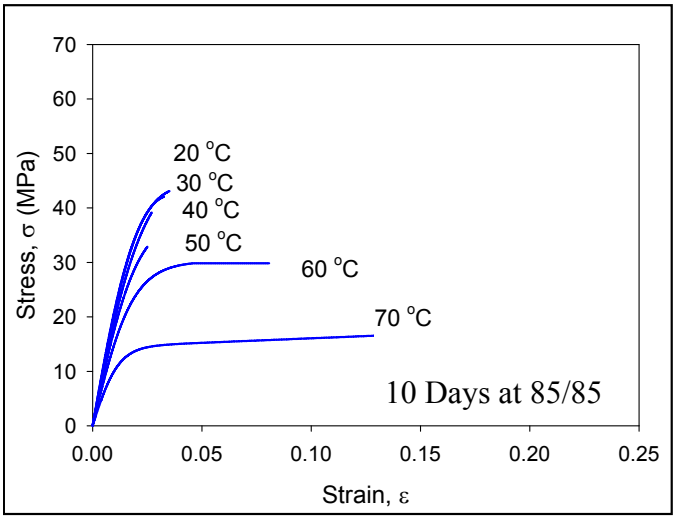

Figure 6.5 Temperature Dependent Stress-Strain Curves of Polymer Encapsulant (Moisture Exposure for 10 Days at 85 C/85 % RH)

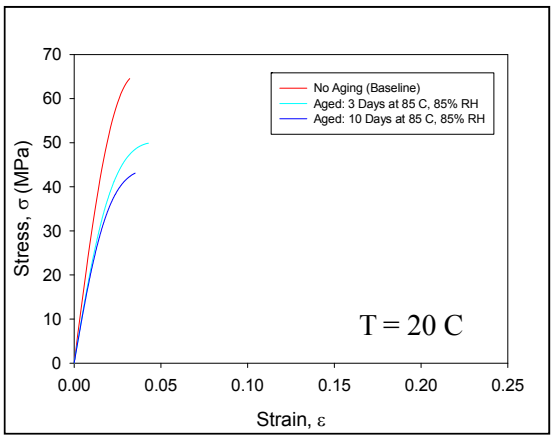

(a) T = 20 C

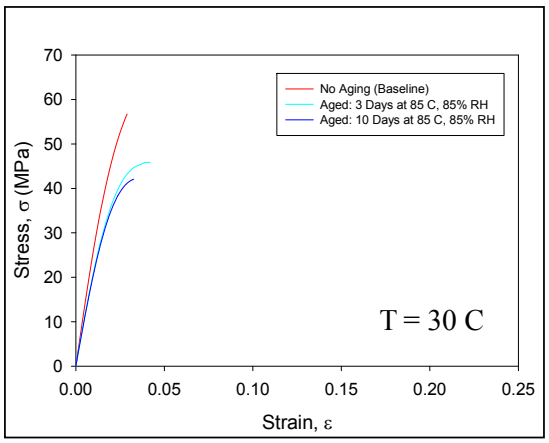

(b) T = 30 C

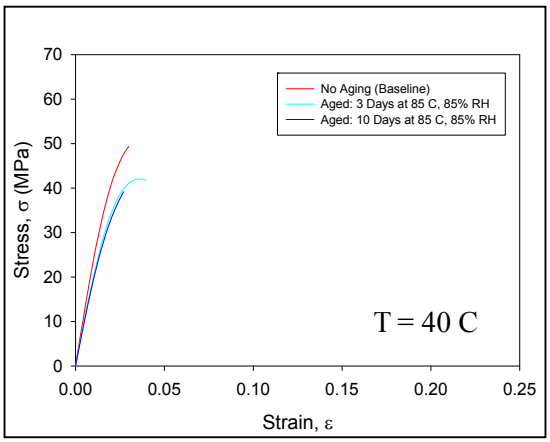

(c) T = 40 C

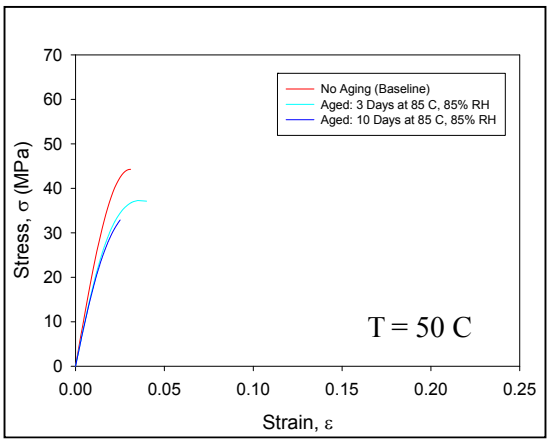

(d) T =50 C

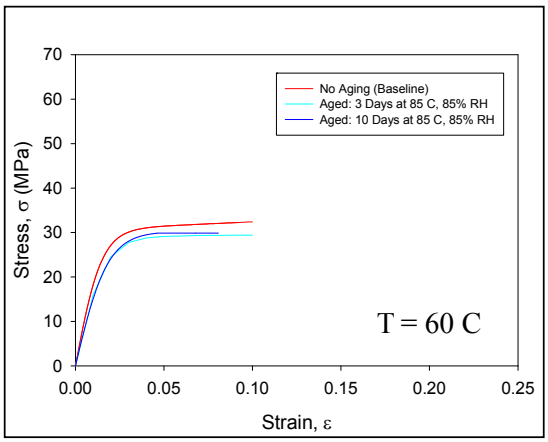

(e) T =60 C

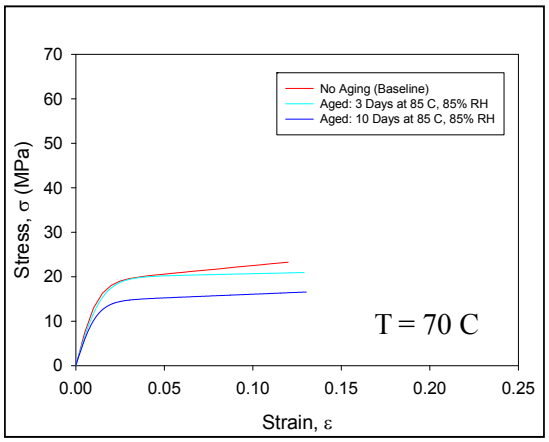

(f) T =70 C

Figure 6.6 Comparison of Stress-Strain Curves of Polymer Encapsulant for Moisture Exposed and Baseline Samples

Each plot in Figures 6.7-6.8 illustrates the glass transition behavior of the material as well as the degradation of the response with moisture adsorption (hygrothermal aging). In general, the changes (decreases) in E and UTS with aging were typically in the range of 10-40% of the baseline values, so that the moisture adsorption causes plasticization of the polymer. The larger changes were observed to occur with the samples which were tested at lower temperatures.

It was also seen that elastic modulus dropped rapidly at test temperatures above 50 C as the glass transition temperature was approached. Differential Scanning Calorimetry (DSC) was used to establish that T_g = 70.5 C for the baseline samples (see Figure 6.9).

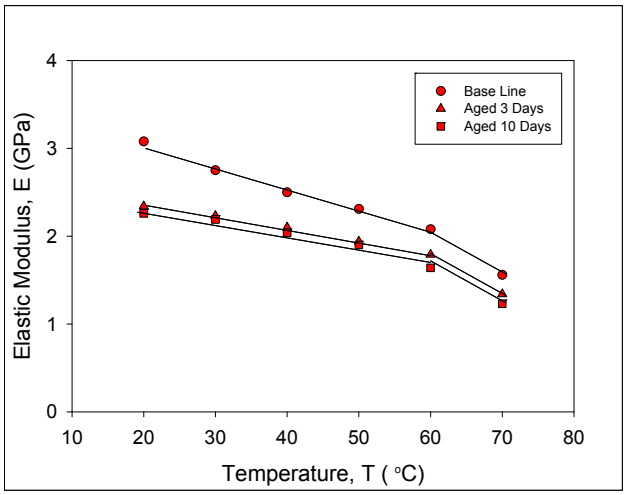

Figure 6.7 Effective Elastic Modulus vs. Temperature of Polymer Encapsulant for Different Hygrothermal Aging Conditions

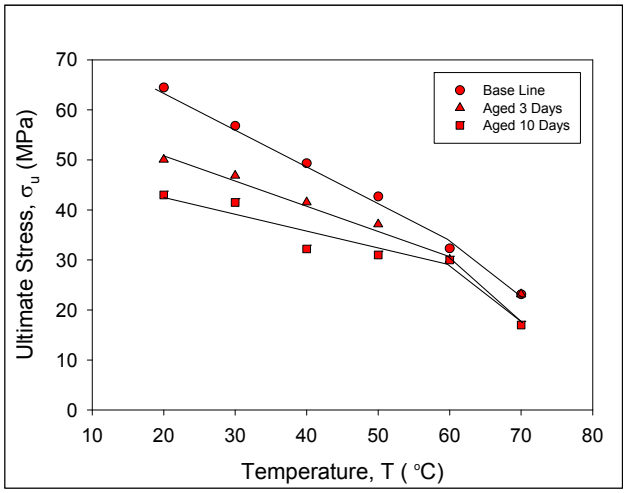

Figure 6.8 Ultimate Stress vs. Temperature of Polymer Encapsulant for Different Hygrothermal Aging Conditions

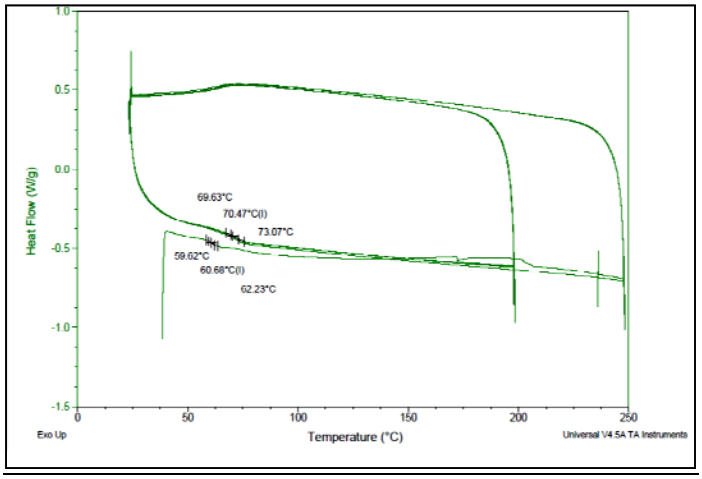

Figure 6.9 DSC result of Polymer Encapsulant, T_g = 70.5 C

6.2.3 Reversibility Testing

To characterize the stability of the mechanical properties after moisture adsorption, reversibility tests were conducted to examine whether the effects of moisture uptake are reversible/irreversible. The test specimens in this group were first dried by baking at 85 C for 24 hours. They were then subjected to moisture adsorption (hygrothermal aging) for 10 days at 85 C and 85% RH, which represents the same conditions and duration used previously to evaluate the effects of moisture on the elastic modulus and UTS of the encapsulant. After moisture preconditioning, specimens were placed in a box oven and baked/dried at 85 C for different time durations. Once dried, tensile tests were performed at room temperature. As shown in Figure 6.10 much of the observed loss in the elastic modulus from moisture uptake was recovered upon subsequent drying. This means that the majority of the loss in modulus resulted from plasticization of the material from moisture adsorption, which is regarded as a reversible process.

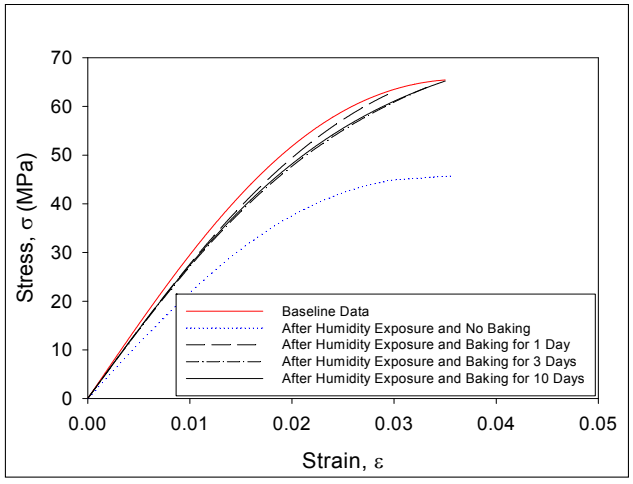

Figure 6.10 Typical Room Temperature Stress-Strain Curves of Polymer Encapsulant after Drying

The variations of elastic modulus and ultimate stress after reversibility tests are tabulated in Table 6.1. To evaluate the change in elastic modulus from moisture adsorption, the recoverability R of the elastic modulus is defined as follows [37]:

$$R(\%) = \frac{E_r - E_\infty}{E_{dry} - E_\infty} \times 100 \tag{6.1}$$

where E_r is recovered elastic modulus, E_∞ is the saturated elastic modulus, and E_{dry} is the initial elastic modulus for totally dry conditions. As discussed below, it was found that the samples were nearly saturated after 10 days of moisture exposure. Therefore, E_∞ in eq. (6.1) was determined from the average elastic modulus of samples after 10 days of hygrothermal aging. Table 6.2 shows the recoverability of hygrothermally aged samples after different baking time periods. It appears that about 25% of the initial elastic modulus was permanently lost due to hydrolysis, where water molecules have chemically modified the organic structure of the material. This has been verified by observations of the permanent changes in the FTIR spectra resulting in samples subjected to moisture adsorption and subsequent drying.

Table 6.1 Elastic Modulus and Ultimate Stress of Polymer Encapsulant after Drying

Test Condition	Elastic Modulus (GPa)	Ultimate Stress (MPa)
Baseline	3.08	64.48
After Humidity Exposure and No Baking	2.29	43.09
After Humidity Exposure and Baking for 1 Day	2.85	63.59
After Humidity Exposure and Baking for 3 Days	2.85	64.16
After Humidity Exposure and Baking for 10 Days	2.87	64.70

Table 6.2 Recoverability of Hygrothermally Aged Samples of Polymer Encapsulant

Test Condition	Recoverability (%)
After Humidity Exposure and Baking for 1 Day	71.95
After Humidity Exposure and Baking for 3 Days	71.95
After Humidity Exposure and Baking for 10 Days	74.39

6.2.4 Moisture Adsorption Measurements

To analyze the increase in moisture content, the test specimens were placed into a humidity chamber at 85 C / 85% RH, and then removed from the chamber after various durations of exposure and weighed on an electronic balance to the nearest 0.1 mg. The percentage weight gain was characterized for various durations of exposure up to 10 days to monitor the level of moisture adsorption with respect to time.

Figure 6.11 shows the variations of the sample weight for various durations of humidity exposure. The curve in this graph represents the prediction of Fick's Law [106], and fits the experimental data well. The moisture adsorption appeared to stabilize at 1.63% after 10 days of exposure, suggesting that saturation had occurred.

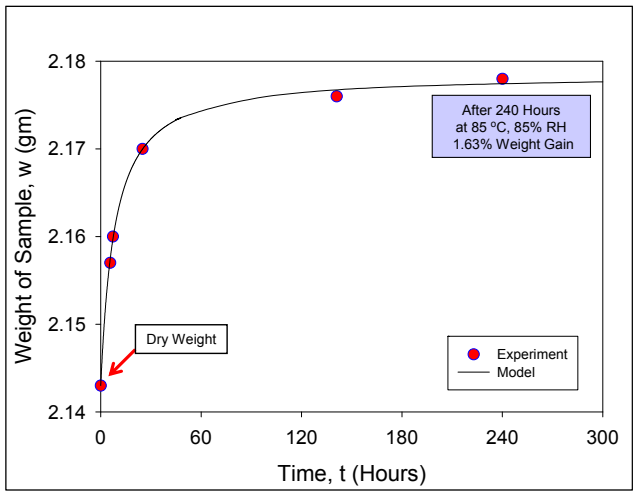

Figure 6.11 Weight Gain of Polymer Encapsulant due to Moisture Adsorption with Time

6.2.5 Fourier Transform Infrared (FTIR) Spectroscopy

Fourier Transform Infrared (FTIR) Spectroscopy is a measurement technique that records infrared spectra. The signal directly recorded, called an "interferogram", represents light output as a function of mirror position. The data-processing technique (Fourier Transform) turns this raw data into a spectrum (light output as a function of infrared wavelength or equivalently, wavenumber) shown in Figure 6.12.

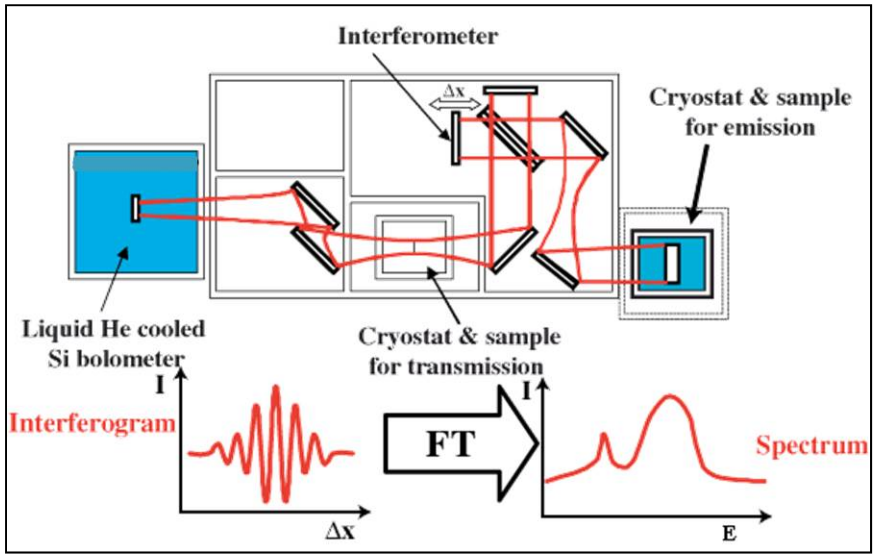

Figure 6.12 Schematic Diagram of FTIR Spectroscopy

IR absorption information is generally presented in the form of a spectrum with wavelength or wavenumber as the x-axis and absorption intensity or percent transmittance as the y-axis [83]. Transmittance, T_λ, is the ratio of radiant power transmitted by the sample (I) to the radiant power incident on the sample (I_0). Absorbance (A_λ) is the logarithm to the base 10 of the reciprocal of the transmittance (T_λ).

$$A_\lambda = \log_{10}\left(\frac{1}{T_\lambda}\right) = -\log_{10} T_\lambda = -\log_{10}\frac{I}{I_0} \tag{6.2}$$

Although absorbance is properly unitless, it is often reported in "Absorbance Units" or a.u. Transmittance ranges from 0 to 100% whereas absorbance ranges from infinity to zero [83]. Table 6.3 shows the values of absorbance for the range of 0 to 3 and the corresponding values in transmittance.

Table 6.3 Conversion from Absorbance to Transmittance

Absorbance	Transmittance
0	1
0.1	0.79
0.25	0.56
0.5	0.32
0.75	0.18
0.9	0.13
1	0.1
2	0.01
3	0.001

For FTIR analysis, specimens were trimmed into small pieces (around 10 mg) and then mortar and pestle was used to grind the small pieces. After grinding, 2-5 mg of powdered specimen is mixed with 90 mg of potassium bromide (KBr) powder. KBr served as a reference or background material.

In order to get meaningful information out of IR spectrum, a homogeneous mixture of KBr/sample has been prepared. Pellets have been formed with the KBr/sample-mixture using a die kit. The pellets were clear and much thicker than a liquid film.

For producing quality pellets, a simple pellet die kit was utilized where the press body was a stainless steel nut and the anvils were stainless steel bolts with optically polished ends shown in Figure 6.13. The pellet was formed by threading one anvil about half way into the body and then placing the KBr/sample matrix into the threaded hole in

the body so that it covered the face of the anvil. Then the body was mounted in a vice while the other threaded anvil was turned against the stationary anvil on which the sample had been placed. To perform the measurement, the bolts were removed and the body was placed in the holder of the IR machine. FTIR machine filtered the spectrum of the sample from that of the background material (KBr). Figure 6.14 shows the resultant spectrum of the polymer encapsulant sample after FTIR analysis.

Figure 6.13 Pellet Die Kit

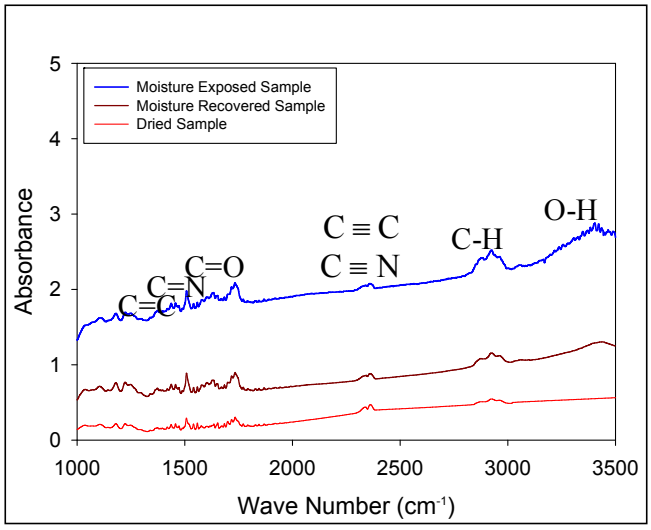

Figure 6.14 FTIR Analysis of Polymer Encapsulant

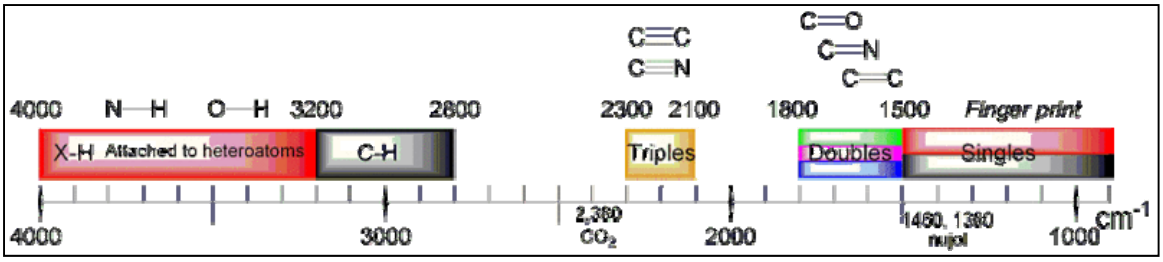

Figure 6.15 Infrared Spectroscopy Correlation Table

Water uptake can be easily quantified using FTIR analysis. Detailed analysis of OH bands allows extracting information about intermolecular interactions within the components of the resin. Water has three active vibration modes in infrared corresponding to the stretching of O-H bond (≈ 3800-3600 cm^{-1} in liquid state) and bending (≈ 1650-1590 cm^{-1} in liquid state) [84]. From Figure 6.14, it is seen that functional groups give rise to characteristic bands both in terms of intensity and position (frequency). Three distinct bands at fixed frequencies but with different intensities are seen in the spectrum depending on moisture contents. The O-H stretching band at 3418 cm^{-1} is more pronounced for the specimen exposed to controlled humidity than that for the recovered sample. In Figure 6.15, the O-H bond can also be observed in the range of 3200-3500 cm^{-1}.

6.3 Effects of Moisture on Polycarbonate

Polymers such as polycarbonates exhibit viscoplastic response. In this study, an experimental investigation has been performed on the effects of moisture adsorption on the stress-strain behavior of polycarbonate materials used in electronic packaging. After manufacture, the specimens (as discussed in Chapter 3) were been exposed to controlled hygrothermal exposures using a Tenney BTRC temperature/humidity chamber to combined hygrothermal exposures at 60 C and 90% RH, 60 C and 50% RH, and 40 C and 50% RH for various durations. After moisture preconditioning, microscale tension-torsion testing machine was used to measure the complete stress-strain curve of the sample to failure at several temperatures (T = 20 C, 40 C, and 60 C). Reversibility tests were also conducted to evaluate whether the degradations in the mechanical properties were recoverable. Finally, optical microscopy was utilized to examine the fracture surfaces of the failed specimens, and observe the influence of moisture exposure.

6.3.1 Typical Stress-Strain Curve of Polycarbonate

Using the prepared samples, the uniaxial stress-strain response for the polycarbonate have been measured at several test temperatures (T = 20, 40, 60 C). All test specimens were dry baked at 65 C for 24 hours prior to subsequent moisture preconditioning and mechanical testing. Samples without moisture preconditioning have been characterized, as well as samples with various hygrothermal exposures for different durations. For all tests, a 60 mm gage length was utilized between the specimen grips along with a strain rate of $\dot{\varepsilon} = .01\ sec^{-1}$. The stress-strain curves of polymers such as polycarbonate exhibits extensive regions of post-yield strain (draw), and are capable of absorbing significant energy in this phase of their deformation. A typical stress-strain

curve of polycarbonate material used in this study (without prior hygrothermal aging) is shown in Figure 6.16.

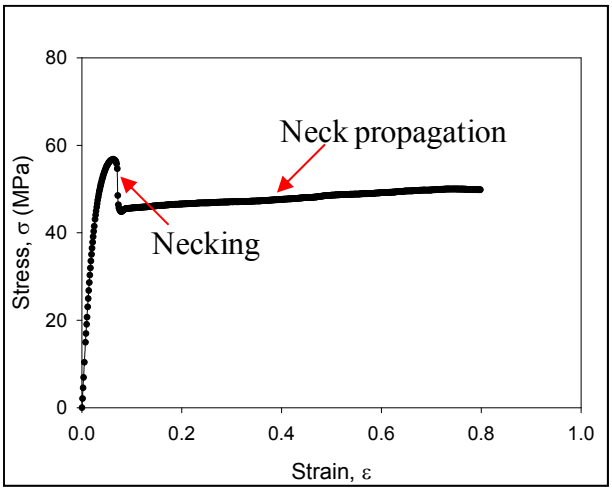

Figure 6.16 Typical Stress-Strain Curve of Polycarbonate (No Moisture Exposure)

The post yield draw behavior is accompanied by extensive necking and localized non uniform deformation, which leads to a condition where the cross-sectional area of the deformation zone is unknown [28]. To accurately represent the raw data with a mathematical model, the raw data are truncated up to the ultimate tensile strength (UTS, the maximum stress attained before entering the draw region), and then fit by an empirical model as illustrated in Figure 6.17. The three-parameter hyperbolic tangent model that has been used to accurately model the observed nonlinear stress-strain data of the material is described in Chapter 3. Figure 6.18 shows the associated hyperbolic tangent model fit to all of the raw stress-strain data for polycarbonate specimens with no moisture exposure that were tested at T = 40 C. The hyperbolic tangent model fit (red

curve) provides an excellent representation to the data that lies in the middle of all of the experimental curves.

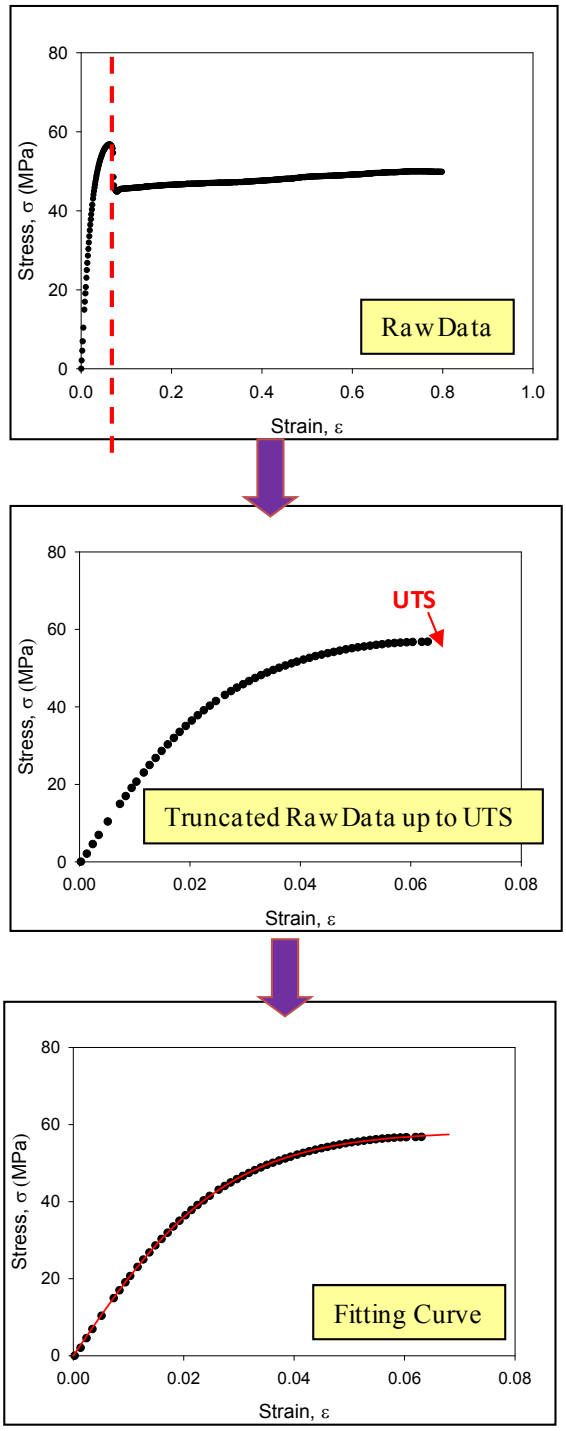

Figure 6.17 Truncation of Raw Data of Polycarbonate up to UTS

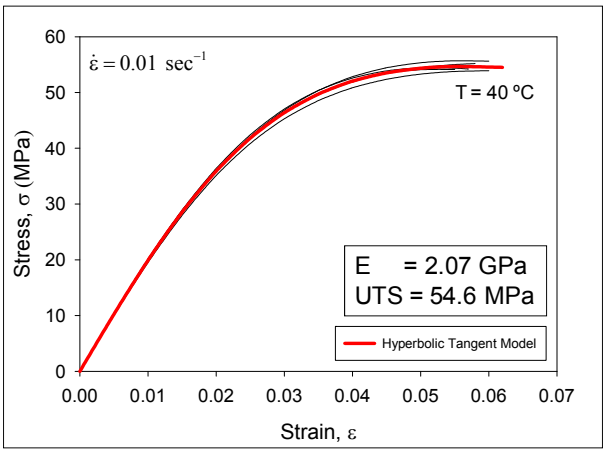

Figure 6.18 Experimental Stress-Strain Curves (Truncated) of Polycarbonate and Hyperbolic Tangent Model Regression Fit (No Moisture Exposure, T = 40 C)

Similar results were found for all of the other temperatures and hygrothermal exposure conditions considered in this work. For each set of testing conditions, from 3-5 experimental stress-strain curves were initially measured, and then fit by the hyperbolic tangent model to obtain an "average" stress-strain curve that mathematically represents the entire data set.

6.3.2 Stress-Strain Data for Initial Samples

Figure 6.19 illustrates typical raw stress-strain data for the tested polycarbonate with no hygrothermal preconditioning (no moisture exposure). Example curves are presented at the three testing temperatures (T = 20, 40, 60 C). It is seen that the polycarbonate material exhibited a large strain to failure at all temperatures before it was exposed to any moisture preconditioning. The largest strain attained was 1.15 (115%), which is the maximum strain possible in the testing system before it reached its cross-head displacement limit. Thus, failure did not occur in these tests, and it can only be said that the ultimate strain to failure was greater than 115% $(\varepsilon_f > 1.15)$.

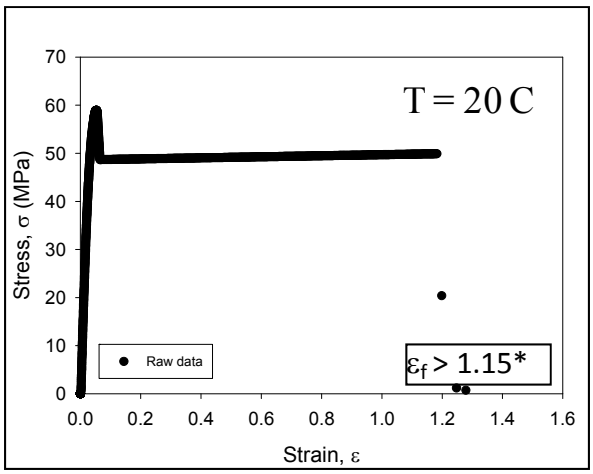

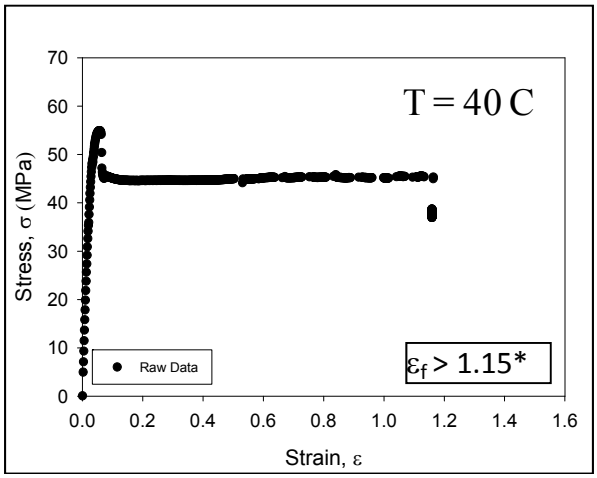

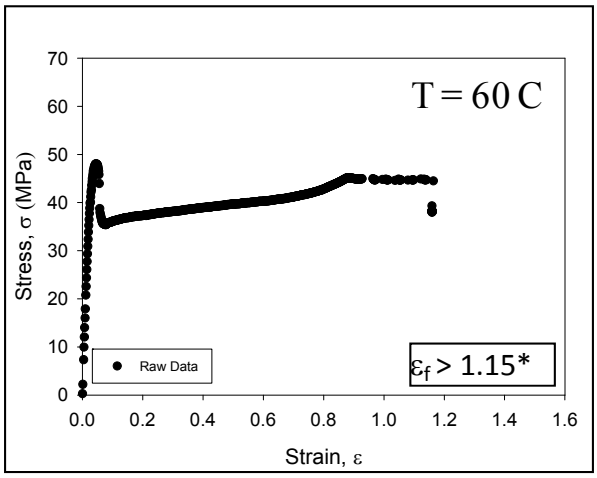

Figure 6.19 Raw Polycarbonate Stress-Strain Data (No Moisture Exposure)

The average initial (truncated) stress-strain curves for these samples at temperatures of T = 20, 40, and 60 C are shown in Figure 6.20. It can be seen from these plots that the initial effective elastic modulus and ultimate tensile strength decrease with temperature. The corresponding mechanical property values found from the average curves are tabulated in Table 6.4.

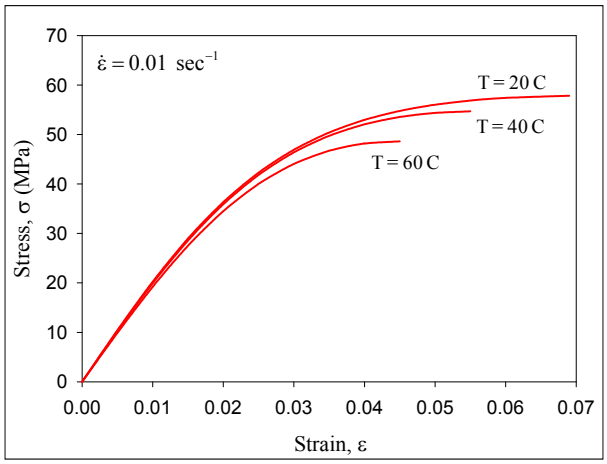

Figure 6.20 Temperature Dependent Stress-Strain Curves (Truncated) of Polycarbonate for No Moisture Exposure

Table 6.4 Material Properties of Polycarbonate for Different Temperatures
(No Moisture Exposure)
[Average Values and Standard Deviations]

Temperature T (°C)	Initial Elastic Modulus E (GPa)	Ultimate Stress (MPa)	Ultimate Strain ε_f
20	2.10 (0.01)	58.5 (1.17)	> 1.15*
40	2.07 (0.02)	54.6 (0.78)	> 1.15*
60	1.99 (0.03)	48.8 (0.87)	> 1.15*

*The Testing System was Limited to a Maximum Strain of 1.15

6.3.3 Stress-Strain Data after Moisture Adsorption and Comparisons

The effects of moisture preconditioning on the mechanical behavior of the tested polycarbonate material were evaluated for three different combined temperature/humidity exposure conditions: (1) 60 C and 90% RH, (2) 60 C and 50% RH, and (3) 40 C and 50% RH. For each of these sets of moisture conditions, samples were exposed for both 72 hours (3 days) and 240 hours (10 days) prior to mechanical testing. After hygrothermal aging/preconditioning, the samples were uniaxially tested with testing temperatures at 20 C, 40 C and 60 C. From 3-5 tests were performed for each unique set of moisture conditions, exposure time, and testing temperature. Testing was performed immediately after the exposure, with no significant delays that would allow for the moisture levels in the samples to change.

6.3.3.1 Condition #1: 60 C and 90% RH

Stress-strain curves for preconditioning at 60 C and 90% RH for 72 hours exposure are shown in Figures 6.21, 6.22 and 6.23 for testing temperatures of T = 20, 40, and 60 C respectively. Corresponding curves for the same hygrothermal conditions and 240 hours of exposure are shown in Figure 6.24 and 6.25 for testing temperatures of T = 20 and 60 C respectively.

By comparing the curves in Figures 6.21-6.25 with those in Figure 6.19 (no moisture preconditioning), it is clear that there were large decreases in the ultimate strain during the first 3 days of moisture adsorption, with additional but smaller decreases during the next 7 days of moisture adsorption. Direct comparisons of the quantitative material property results at each temperature for exposed and non-exposed samples are given in Table 6.5.

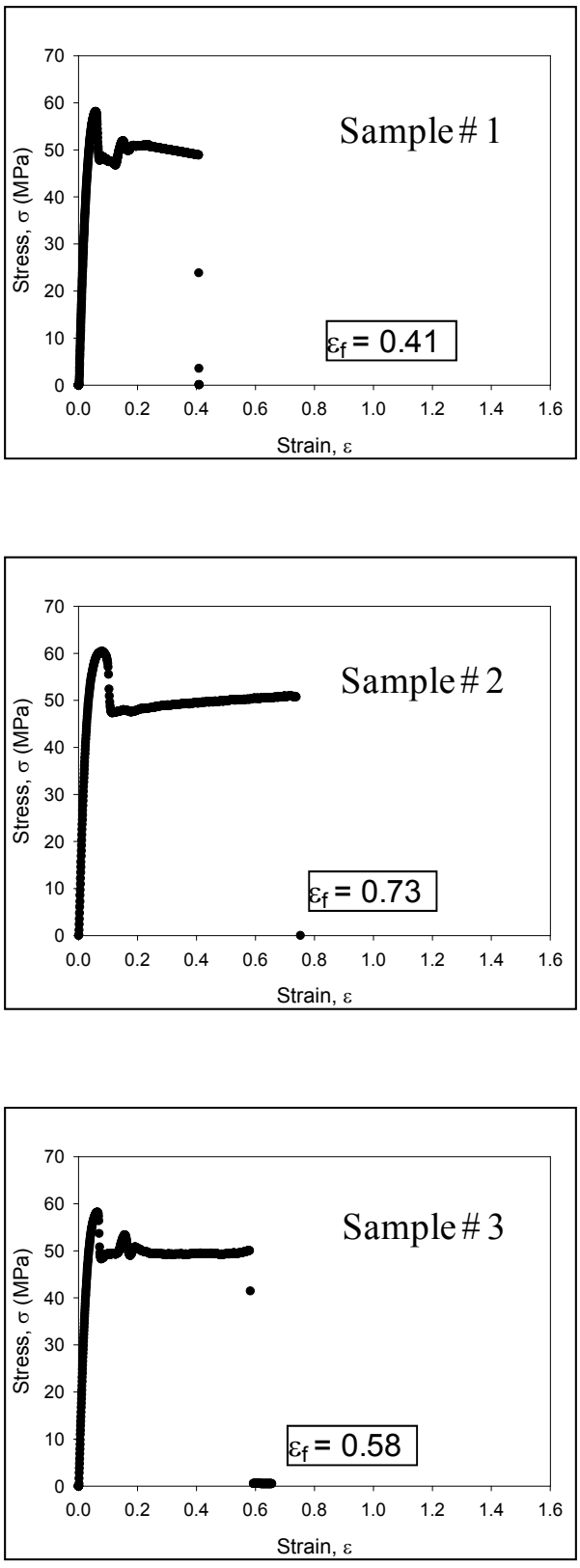

Figure 6.21 Polycarbonate Stress-Strain Curves at T = 20 C
Moisture Exposure at 60 C, 90% RH (72 Hours)

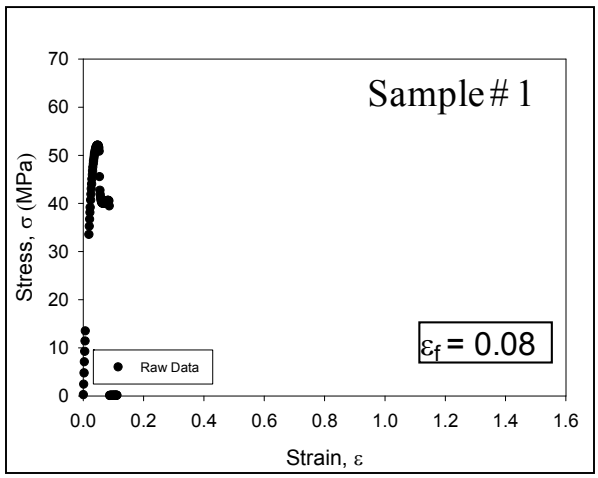

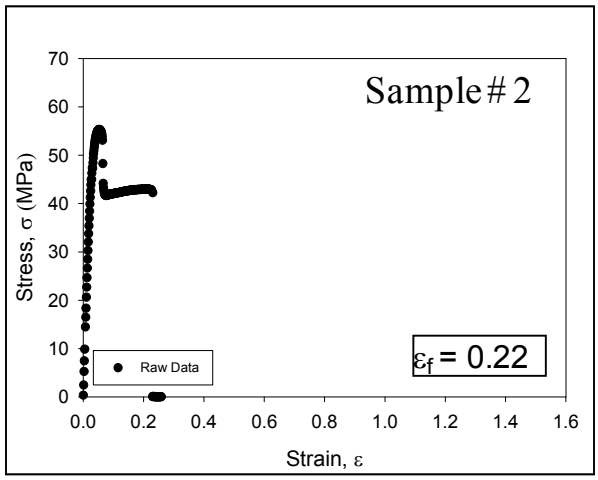

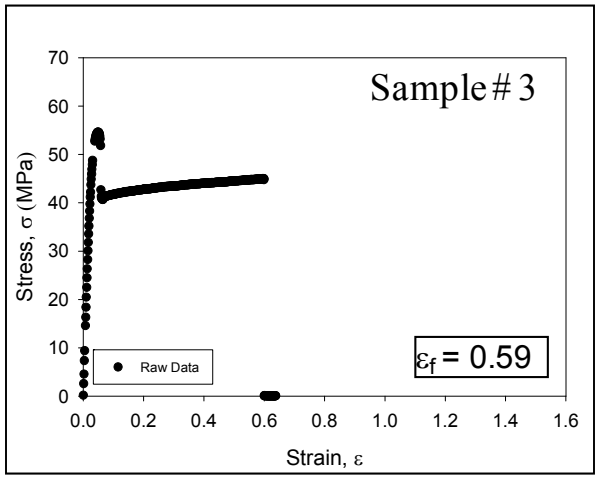

Figure 6.22 Polycarbonate Stress-Strain Curves at T = 40 C
Moisture Exposure at 60 C, 90% RH (72 Hours)

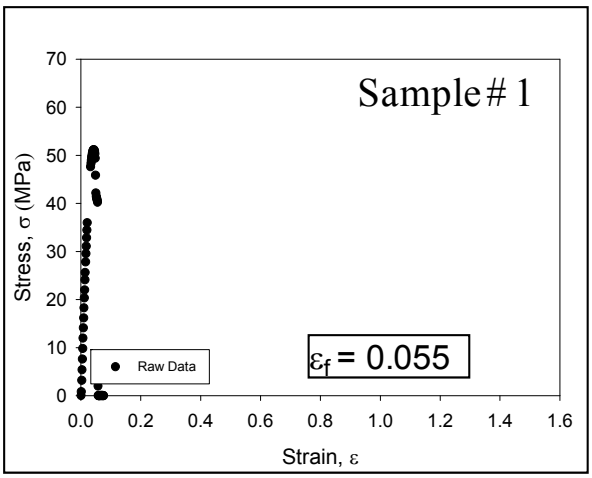

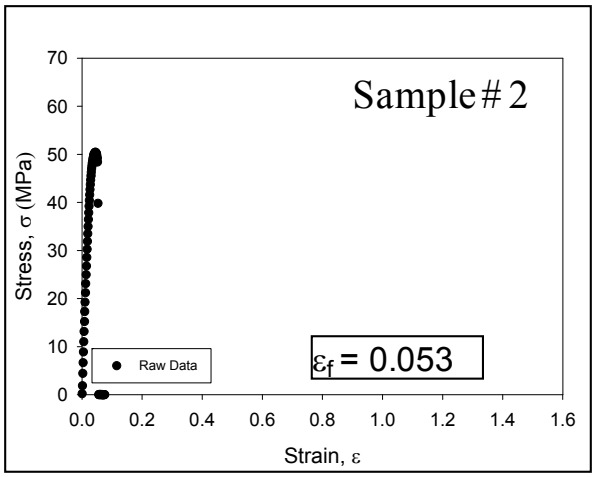

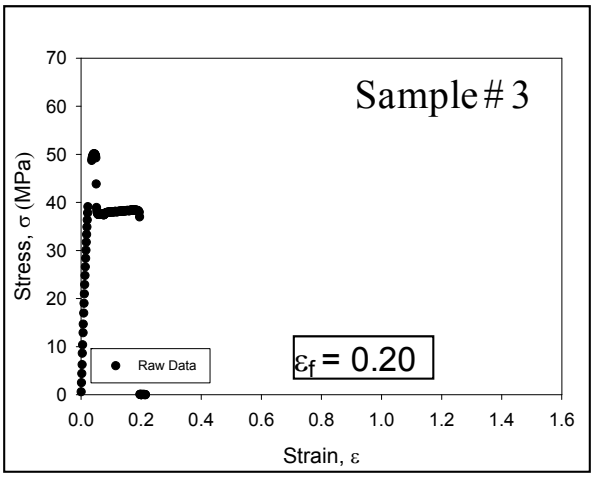

Figure 6.23 Polycarbonate Stress-Strain Curves at T = 60 C
Moisture Exposure at 60 C, 90% RH (72 Hours)

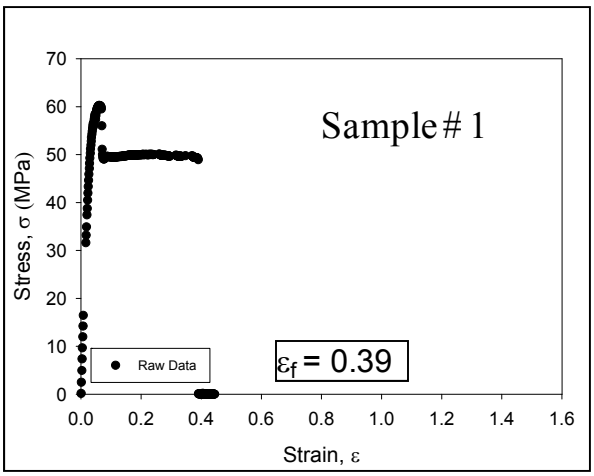

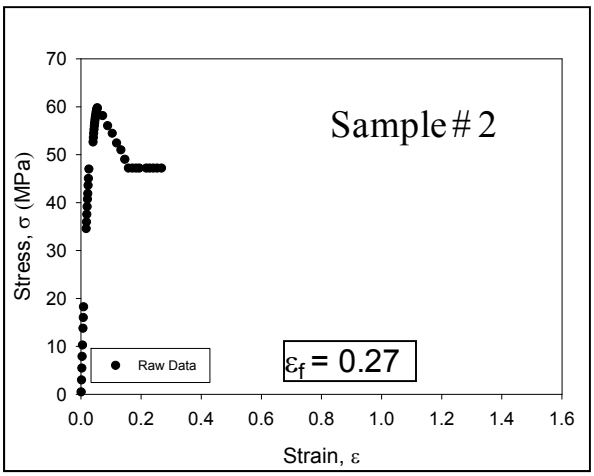

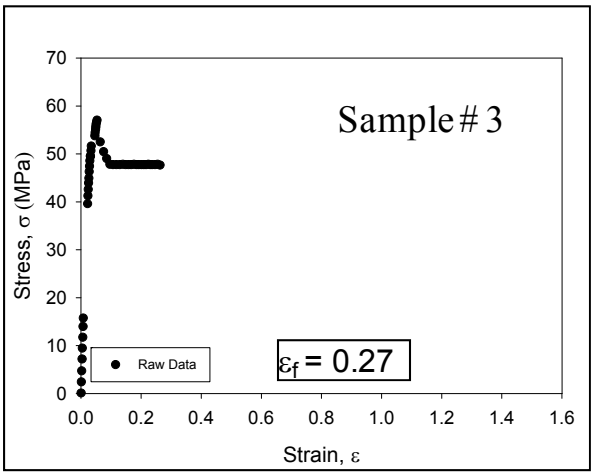

Figure 6.24 Polycarbonate Stress-Strain Curves at T = 20 C
Moisture Exposure at 60 C, 90% RH (240 Hours)

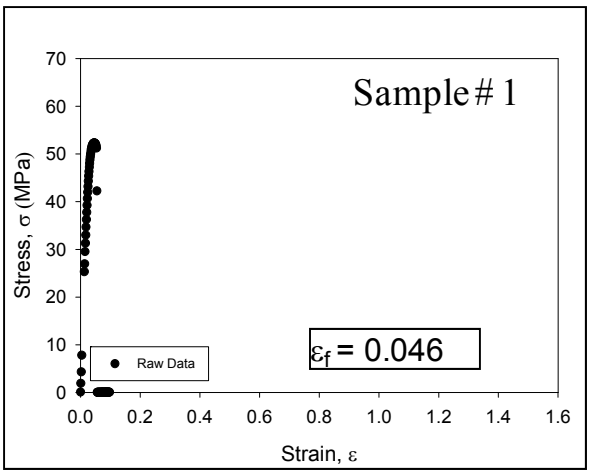

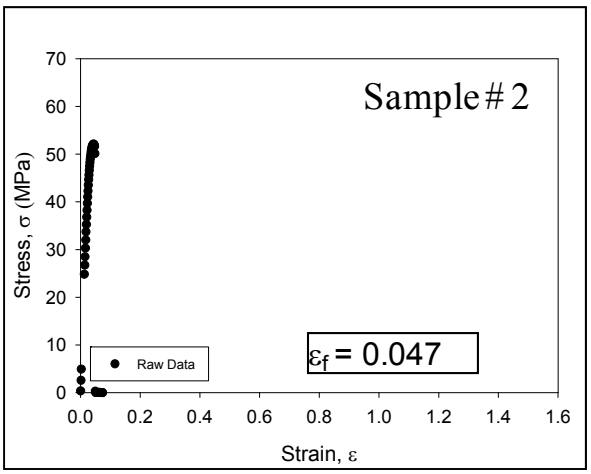

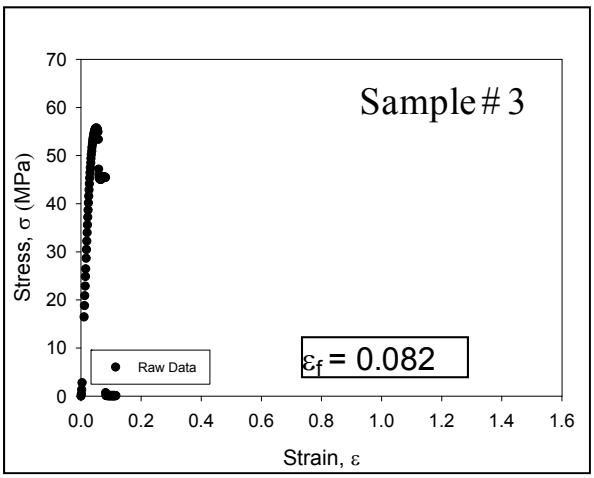

Figure 6.25 Polycarbonate Stress-Strain Curves at T = 60 C
Moisture Exposure at 60 C, 90% RH (240 Hours)

The initial modulus (initial slope) and ultimate strength (failure stress) were not affected by the humidity exposures. After moisture absorption, the samples failed with much reduced elongation before breaking. Moreover, the failures at lower strain levels become more dominant as the testing temperature is increased from 20 C to 60 C.

Table 6.5 Material Properties of Polycarbonate after Hygrothermal Exposure [Condition #1: 60 C, 90% RH] and Comparison to Baseline Data (No Moisture Exposure)

	Temperature T (^oC)	Initial Elastic Modulus E (GPa)	Ultimate Stress σ_u(MPa)	Ultimate Strain ε_f
Baseline	20	2.10 (0.01)	58.5 (1.17)	> 1.15*
Exposed (72 Hours)	20	2.18 (0.02)	58.6 (1.70)	0.57 (0.17)
Exposed (240 Hours)	20	2.21 (0.12)	58.8 (1.56)	0.31 (0.07)
Baseline	40	2.07 (0.02)	54.6 (0.78)	> 1.15*
Exposed (72 Hours)	40	2.14 (0.07)	54.0 (1.69)	0.30 (0.26)
Baseline	60	1.99 (0.03)	48.8 (0.87)	> 1.15*
Exposed (72 Hours)	60	2.02 (0.02)	50.5 (0.57)	0.10 (0.07)
Exposed (240 Hours)	60	2.06 (0.04)	52.3 (0.55)	0.06 (0.02)

*The Testing System was Limited to a Maximum Strain of 1.15

6.3.3.2Condition #2: 60 C and 50% RH

Stress-strain curves for preconditioning at 60 C and 50% RH for 72 hours exposure are shown in Figures 6.26, 6.27 and 6.28 for testing temperatures of T = 20, 40, and 60 C respectively. Analogous to the results in the previous section, large decreases in the ultimate strains occurred during the first 3 days of moisture adsorption. The quantitative material property results at each temperature for exposed and non-exposed samples are given in Table 6.6.

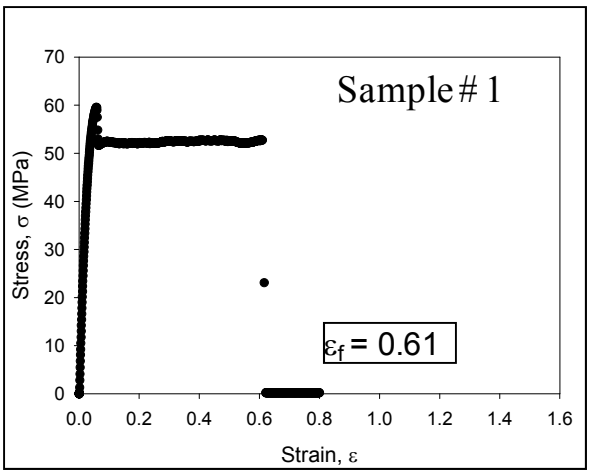

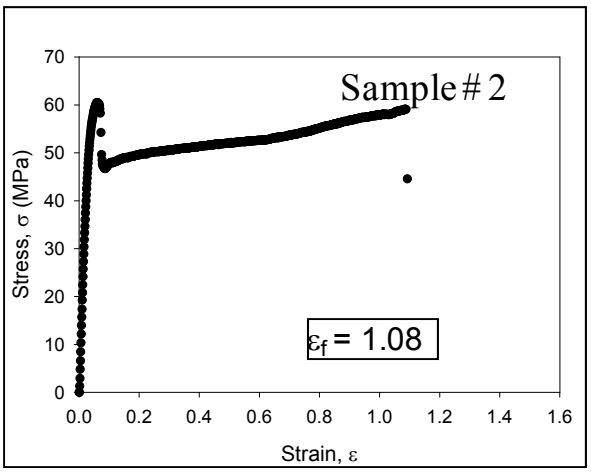

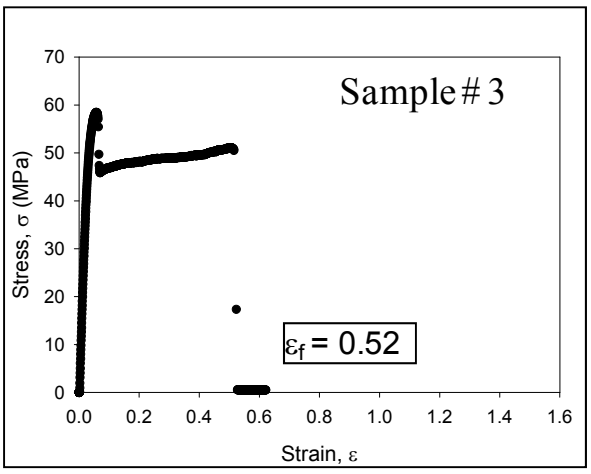

Figure 6.26 Polycarbonate Stress-Strain Curves at T = 20 C
Moisture Exposure at 60 C, 50% RH (72 Hours)

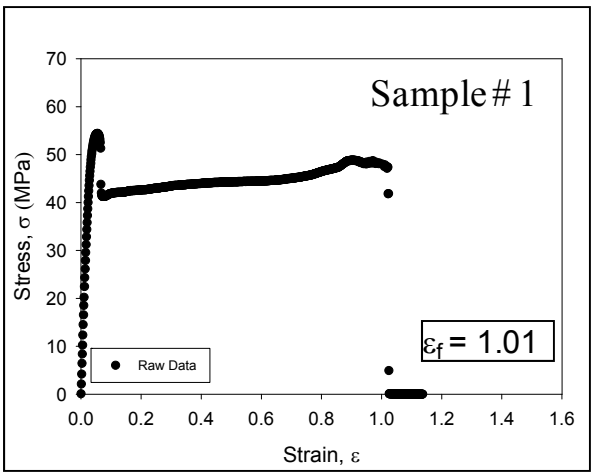

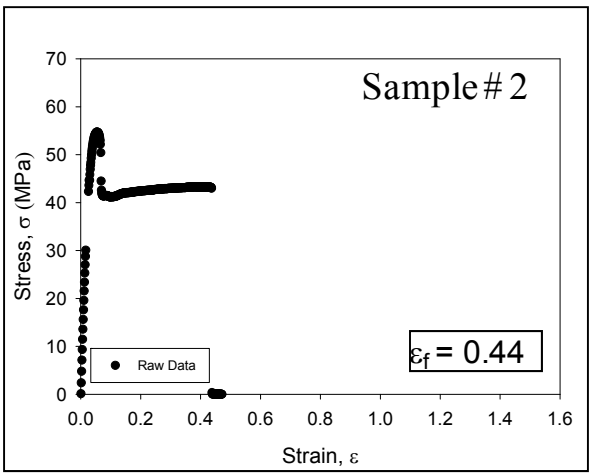

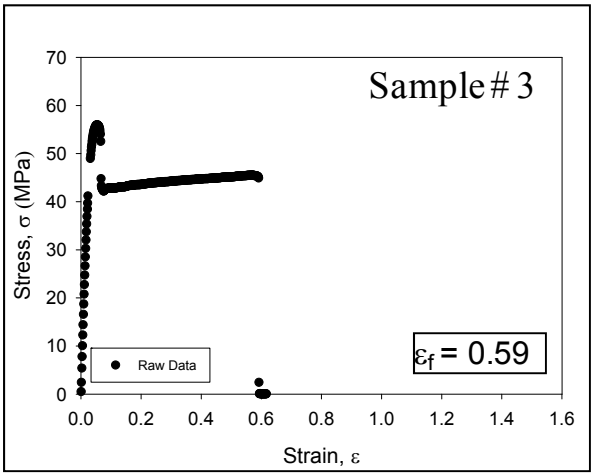

Figure 6.27 Polycarbonate Stress-Strain Curves at T = 40 C
Moisture Exposure at 60 C, 50% RH (72 Hours)

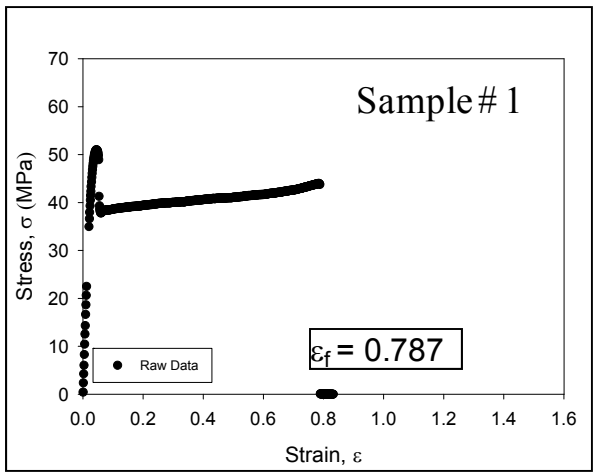

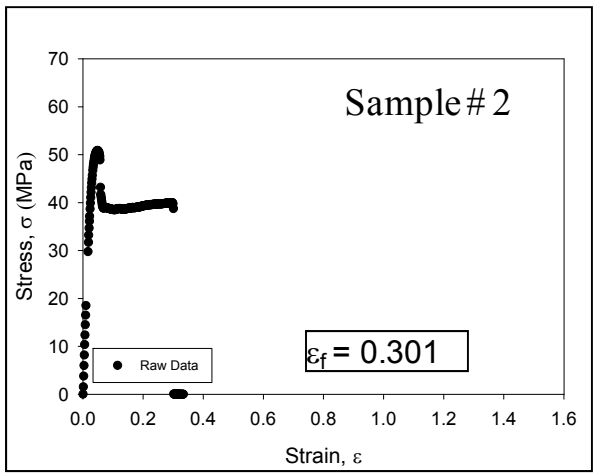

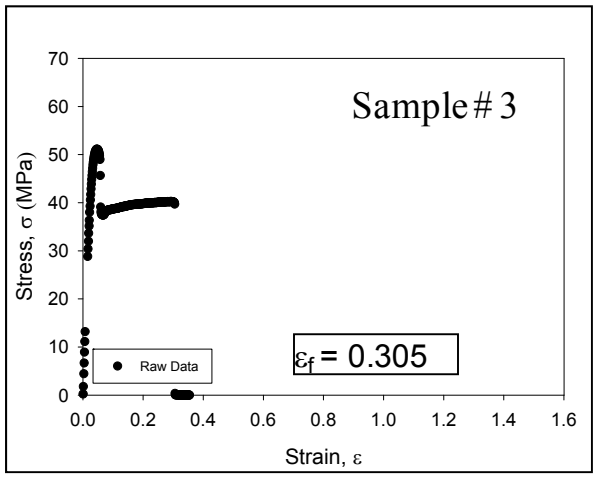

Figure 6.28 Polycarbonate Stress-Strain Curves at T = 60 C
Moisture Exposure at 60 C, 50% RH (72 Hours)

Again, the initial modulus (initial slope) and ultimate strength (failure stress) were not affected by the humidity exposure. The reductions in ultimate strain were smaller relative to those found in Table 6.5 for the more severe hygrothermal exposure of 60 C and 90% RH.

Table 6.6 Material Properties of Polycarbonate after Hygrothermal Exposure [Condition #2, 60 C, 50% RH] and Comparison to Baseline Data (No Moisture Exposure)

	Temperature T (°C)	Initial Elastic Modulus E (GPa)	Ultimate Stress σ_u(MPa)	Ultimate Strain ε_f
Baseline	20	2.10 (0.01)	58.5 (1.17)	> 1.15*
Exposed (72 Hours)	20	2.16 (0.01)	59.5 (1.02)	0.74 (0.30)
Baseline	40	2.07 (0.02)	54.6 (0.78)	> 1.15*
Exposed (72 Hours)	40	2.09 (0.04)	55.0 (0.81)	0.68 (0.29)
Baseline	60	1.99 (0.03)	48.8 (0.87)	> 1.15*
Exposed (72 Hours)	60	2.01 (0.04)	50.8 (0.17)	0.47 (0.27)

*The Testing System was Limited to a Maximum Strain of 1.15

6.3.3.3Condition #3: 40 C and 50% RH

Stress-strain curves for preconditioning at 40 C and 50% RH for 72 hours exposure are shown in Figures 6.29, 6.30 and 6.31 for testing temperatures of T = 20, 40, and 60 C. Analogous to the results in the previous two sections, large decreases in the ultimate strains occurred during the first 3 days of moisture adsorption. The quantitative material property results at each temperature for exposed and non-exposed samples are given in Table 6.7. Again, the initial modulus (initial slope) and ultimate strength (failure stress) were not affected by the humidity exposure. The reductions in the ultimate strains were smaller

relative to those found in Table 6.5 and 6.6 for the more severe hygrothermal exposures of 60 C and 90%, and 60 C and 50% RH, respectively.

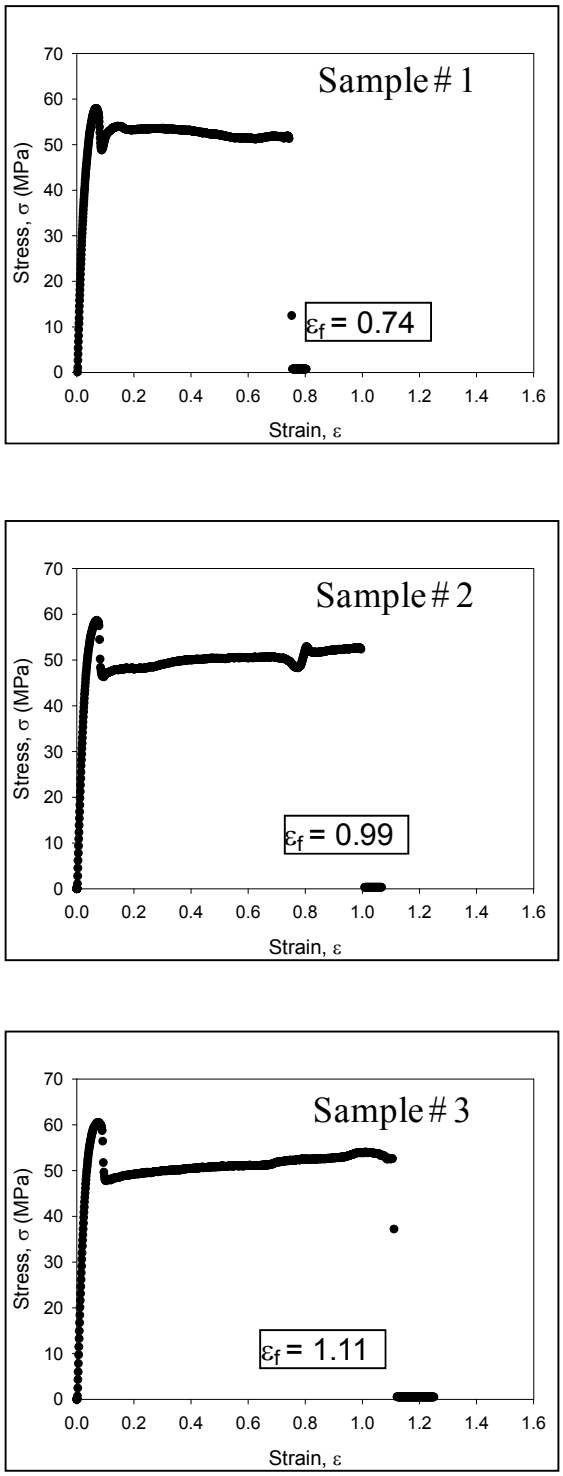

Figure 6.29 Polycarbonate Stress-Strain Curves at T = 20 C
Moisture Exposure at 40 C, 50% RH (72 Hours)

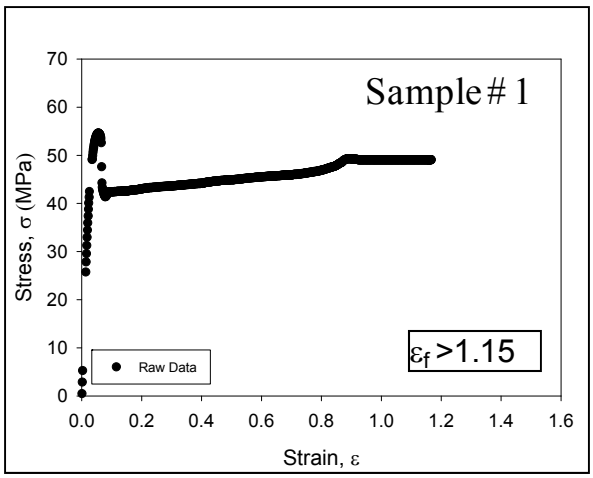

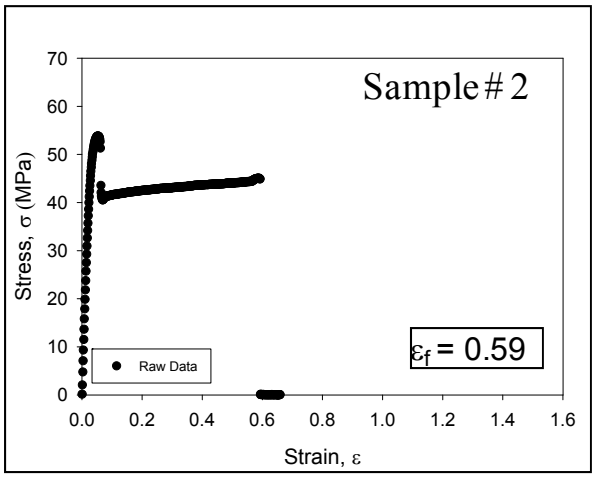

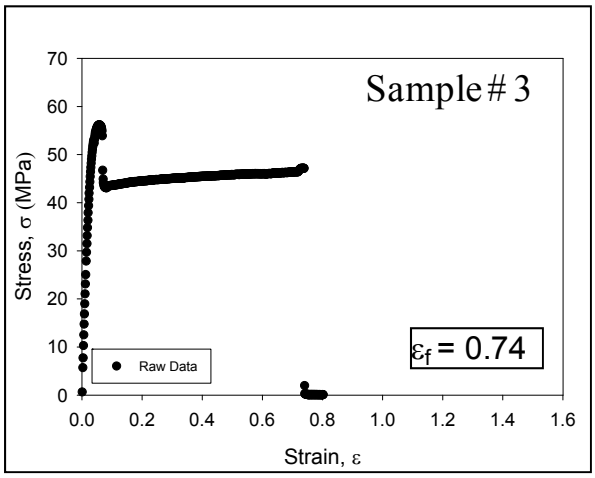

Figure 6.30 Polycarbonate Stress-Strain Curves at T = 40 C
Moisture Exposure at 40 C, 50% RH (72 Hours)

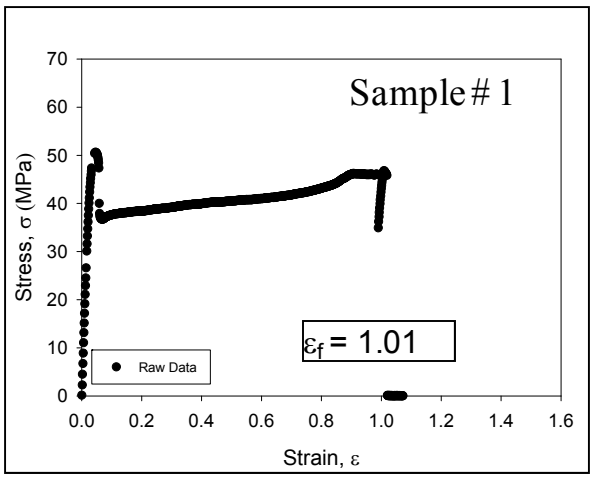

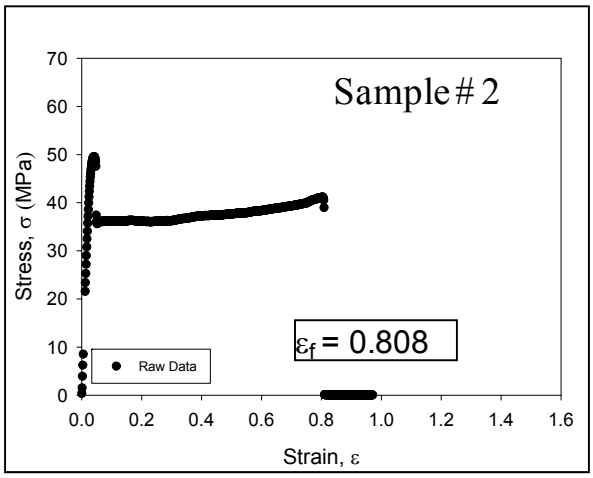

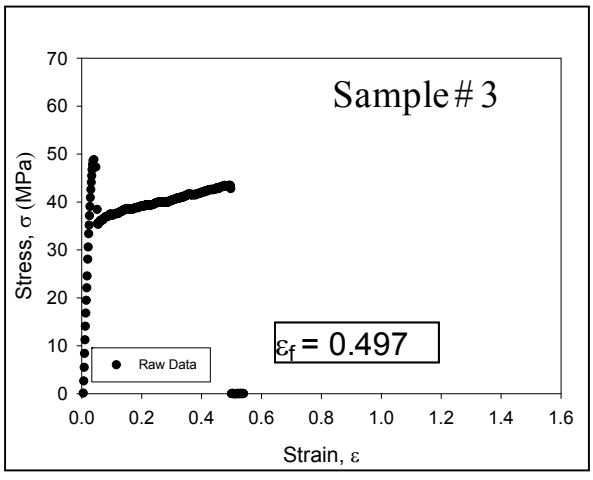

Figure 6.31 Polycarbonate Stress-Strain Curves at T = 60 C
Moisture Exposure at 40 C, 50% RH (72 Hours)

Table 6.7 Material Properties of Polycarbonate after Hygrothermal Exposure [Condition #3, 40 C, 50% RH] and Comparison to Baseline Data (No Moisture Exposure)

	Temperature T (^oC)	Initial Elastic Modulus E (GPa)	Ultimate Stress σ_u (MPa)	Ultimate Strain ε_f
Baseline	20	2.10 (0.01)	58.5 (1.17)	> 1.15*
Exposed (72 Hours)	20	2.14 (0.03)	59.04 (1.34)	0.95 (0.19)
Baseline	40	2.07 (0.02)	54.6 (0.78)	> 1.15*
Exposed (72 Hours)	40	2.08 (0.03)	54.8 (1.27)	0.83 (0.29)
Baseline	60	1.99 (0.03)	48.8 (0.87)	> 1.15*
Exposed (72 Hours)	60	2.00 (0.03)	49.6 (0.89)	0.77 (0.25)

*The Testing System was Limited to a Maximum Strain of 1.15

6.3.4 Reversibility Testing

To characterize the stability of the mechanical properties after moisture adsorption, reversibility tests were conducted to examine whether the detrimental effects of moisture uptake on the ultimate tensile strains were recoverable. The test specimens in this group were first subjected to moisture adsorption (hygrothermal aging) for 72 hours at 60 C and 90% RH (condition #1). After this moisture preconditioning, the specimens were placed in a box oven and baked/re-dried at 65 C for 24 hours. Once re-dried, tensile tests were performed at 60 C, which is the temperature that the largest degradations in ultimate strain were previously seen to occur (see Figure 6.23 and Table 6.5). Figure 6.32 shows typical raw stress-data for polycarbonate after the moisture exposure and subsequent redrying. These results illustrate very similar behavior with a large elongation as was seen for the baseline data (no moisture exposure) in Figure 6.19. Figure 6.33 shows a direct comparison of example truncated stress-strain curves for polycarbonate in the baseline case (no moisture exposure), and for the case of moisture exposure and subsequent redrying. It is apparent that much of the observed loss in the

elastic modulus from moisture uptake was recovered upon subsequent drying. This means that the majority of the modulus loss resulted from plasticization of the material during moisture adsorption, which is regarded as a nearly reversible process. The values of material properties after reversibility testing are listed in Table 6.8.

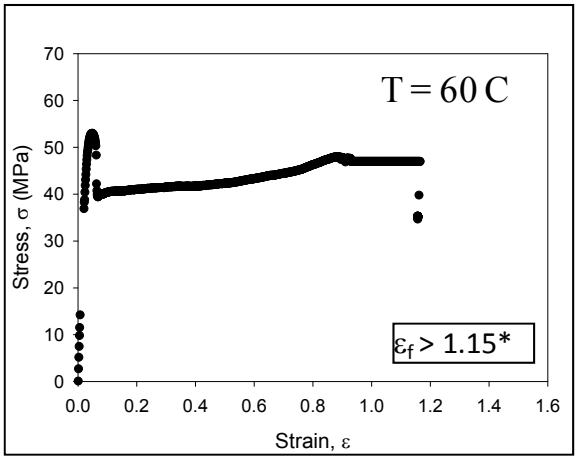

Figure 6.32 Example Raw Stress-Strain Data for Polycarbonate Subjected to Moisture Exposure at 60 C, 90% RH (72 Hours), Followed by Subsequent Baking

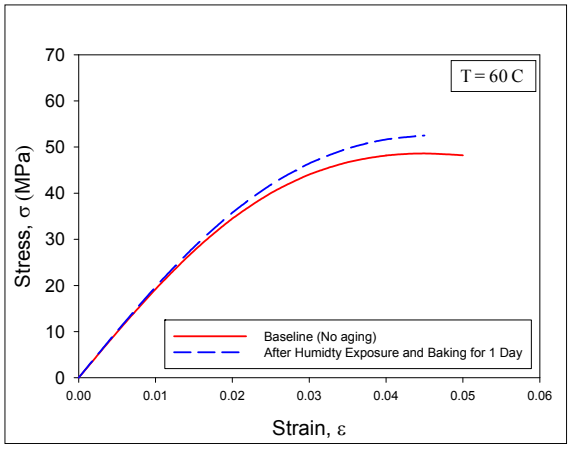

Figure 6.33 Typical Temperature Dependent Stress-Strain Curves of Polycarbonate (Baseline and after Redrying)

Table 6.8 Material Properties of Polycarbonate after Reversibility Testing [Exposure to 60 C, 90% RH and Baking] and Comparison to Baseline Data (No Moisture Exposure)

	Temperature T (°C)	Initial Elastic Modulus E (GPa)	Ultimate Stress σ_u(MPa)	Ultimate Strain ε_f
Baseline	60	1.99 (0.03)	48.8 (0.87)	> 1.15*
Exposed (72 Hours) & Baked (24 Hours)	60	2.03 (0.02)	52.0 (0.55)	> 1.15*

*The Testing System was Limited to a Maximum Strain of 1.15

6.3.5 Moisture Adsorption Measurements

Experiments were performed to characterize the increase in the moisture content (weight) of the polycarbonate material during hygrothermal exposure. Test specimens were placed into the humidity chamber at each of the 3 exposure conditions (60 C and 90% RH, 60 C and 50% RH, and 40 C and 50% RH), and the weight of the samples were measured as a function of exposure time. The specimens were removed briefly from the chamber after various durations of moisture exposure to perform the weight measurements using a high precision electronic scale that reads to the nearest 0.1 mg. The percentage weight gain was measured for the various durations of exposure to monitor the level of moisture adsorption with respect to time.

Figure 6.34 shows the variations of the sample weight for various durations of humidity exposure and the three different sets of hygrothermal conditions. In each case, the moisture adsorption appeared to nearly stabilize after about 72 hours, suggesting that saturation had approximately occurred. As expected, the maximum gain in weight was observed for the sample which was exposed to the most severe of the conditions (60 C and 90% RH).

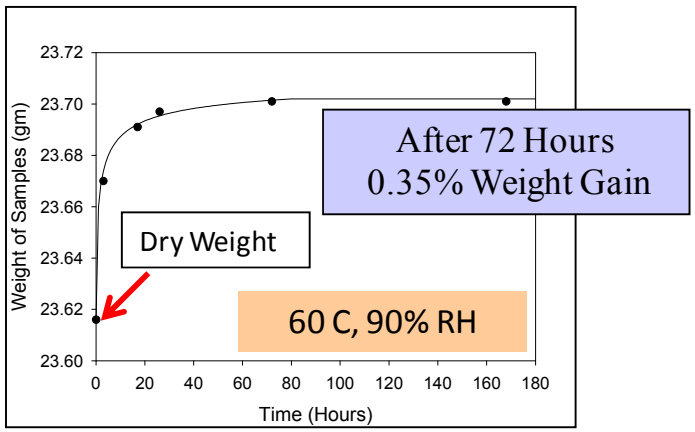

(a) 60 C and 90% RH

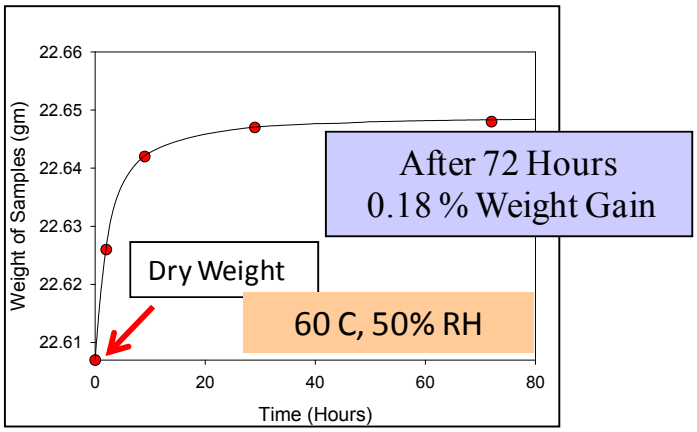

(b) 60 C and 50% RH

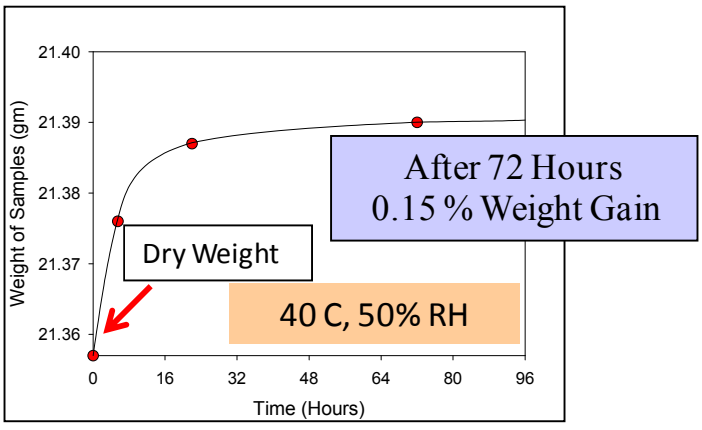

(c) 40 C and 50% RH

Figure 6.34 Weight Gain Variation of Polycarbonate with Time During Moisture Adsorption

6.3.6 Fracture Surface Analysis

After uniaxial testing, the fracture surfaces of the specimens were studied using optical microscopy. In Figure 6.35, it is observed that there are remarkable differences between the fracture surfaces of polycarbonate samples subjected to moisture absorption relative to those with no moisture exposure. As seen in Figure 6.36, cavities appeared on the fracture surfaces of the samples which were exposed to moisture. However, the exact mechanisms responsible for moisture induced reductions in the failure strains are still not understood.

It seems that when the sample failed after moisture exposure, the fragments debonded from the surface and cavities were formed by the fracture. In other words, due to the combined action of temperature and moisture, water molecules have chemically modified the organic structure of the material by breaking inter-chain bonds and then reacting with functional groups of polycarbonate [49]. On the contrary, the failure surfaces of the non-exposed specimens with longer strain to failure appeared to be quite smooth.

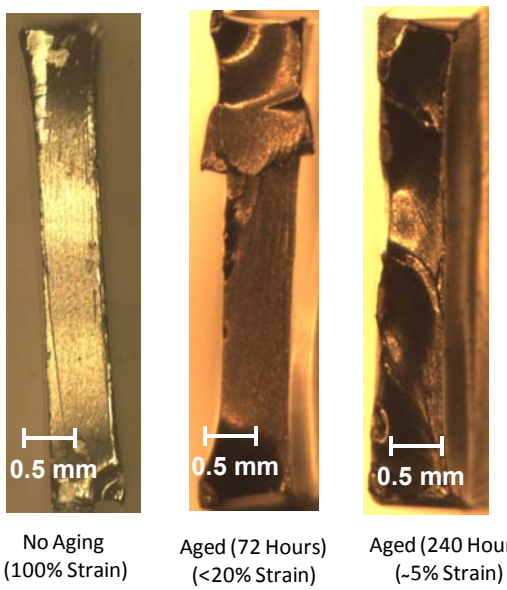

Figure 6.35 Fracture Surfaces of Polycarbonate - Non-Exposed (Baseline) Sample, and Samples Exposed to 60 C and 90% RH

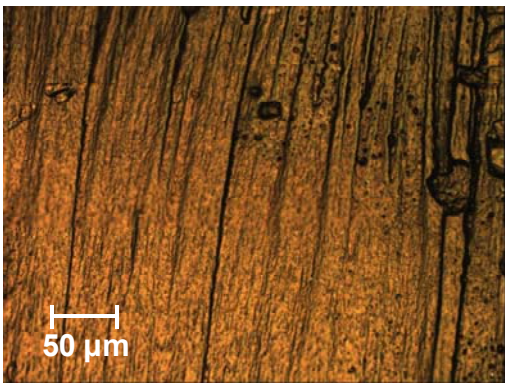

(a) Non-Exposed (Baseline) Sample

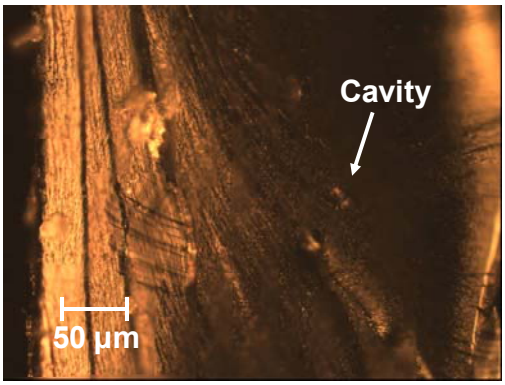

(b) Sample Exposed to 60 C and 90% RH

Figure 6.36 Microscopic View (200X) of Fracture Surfaces of Polycarbonate

6.4 Effects of Moisture on Flip Chip Underfill (UF2)

Reliable, consistent, and comprehensive material property data are needed for microelectronics encapsulants for the purpose of mechanical design, reliability assessment, and process optimization of electronic packages. Since the vast majority of contemporary underfills used are epoxy based, they have the propensity to absorb moisture, which can lead to undesirable changes in their mechanical and adhesion behaviors. In this section, the effects of moisture adsorption on the stress-strain behavior of an underfill encapsulant were evaluated experimentally and theoretically.

6.4.1 Stress-Strain and Creep Data for Initial Samples (No Moisture Exposure)

The underfill specimens have been prepared following the procedure as discussed in section 3.2.1 of Chapter 3. The stress-strain curves for the tested underfill (no moisture exposure) at temperatures from T = 25 C to T = +150 C, and a strain rate of $\dot{\varepsilon} = .001$ (1/sec) have been shown in Figure 4.20 of Chapter 4. During the study, the range or maximum stress of the average curve for each temperature was found by averaging the failure stresses from each of the 3-5 tests used in the regression fit for that temperature. The creep curves without moisture exposure are shown in Figure 4.22 at 4 testing temperatures and various stress levels. In each case, the tests have been conducted up to 6000 seconds.

6.4.2 Stress-Strain Data after Moisture Adsorption and Comparisons

For this material, the effects of moisture exposure on the stress strain curves have been explored from T = 25 C (room temperature) up to T = 150 C (above the glass transition temperature of the material). The specimens have been exposed to combined temperature/humidity exposures (85 C and 85% RH). After hygrothermal

aging/preconditioning, the samples were uniaxially tested. In addition to the group of baseline samples, 4 other groups (A, B, C, D) of test specimens were prepared for moisture exposure. In each case the samples were baked in a box oven at 85 C for 24 hours prior to moisture preconditioning at 85 C and 85% RH conditions in a humidity chamber. Group A had a moisture exposure for 1 day, whereas Group B, C and D had a moisture exposure for 3 days, 30 days and 60 days respectively. The average temperature dependent stress-strain curves at different testing temperatures after moisture adsorption for different durations at 85 C and 85% RH conditions are shown in Figure 6.37.

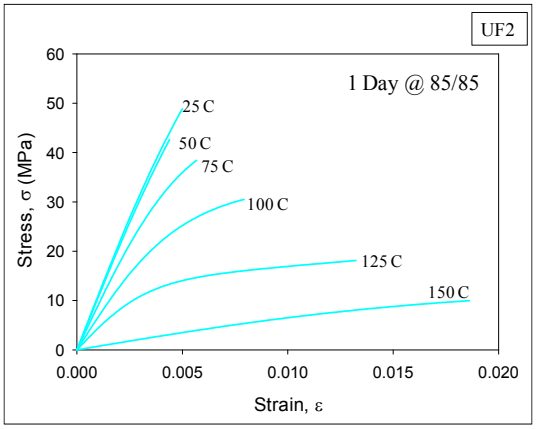

(a) Moisture Exposure for 1 Day at 85 C, 85 % RH (Group A Samples)

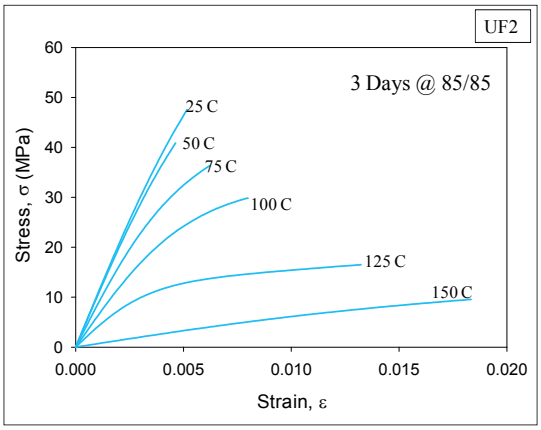

(b) Moisture Exposure for 3 Days at 85 C, 85 % RH (Group B Samples)

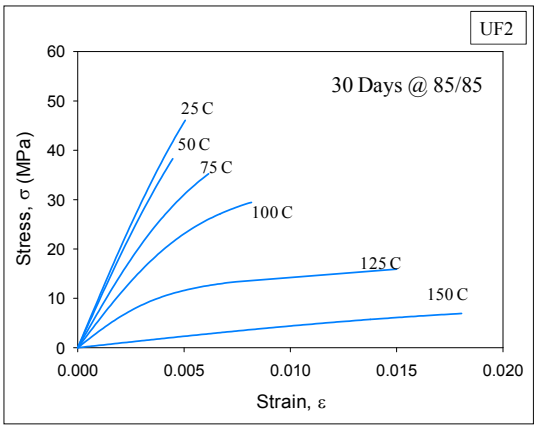

(c) Moisture Exposure for 30 Days at 85 C, 85 % RH (Group C Samples)

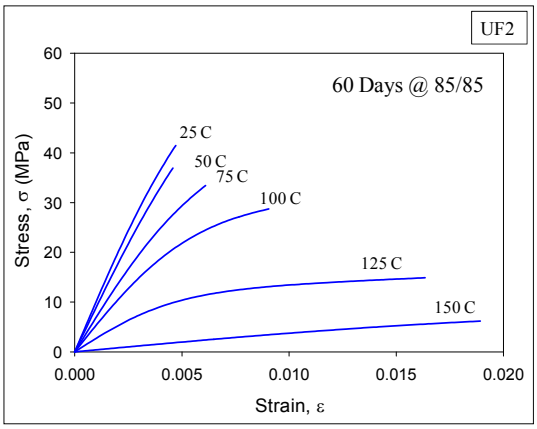

(d) Moisture Exposure for 60 Days at 85 C, 85 % RH (Group D Samples)

Figure 6.37 Typical Temperature Dependent Stress-Strain Curves of Underfill (UF2) After Moisture Absorption

For all groups, there were at least 120 samples. Before starting the tests, the samples were allowed to cool down to room temperature (T = 25 C) and 5 specimens were tested at each of 6 different temperatures (T = 25, 50, 75, 100, 125 and 150 C). The raw data from each set of conditions and testing temperature were then fit with the hyperbolic tangent empirical model to generate an average stress-strain curve representation for each set of data.

The effects of moisture adsorption are not immediately obvious by casual comparison of the plots in Figure 4.20 with those in Figures 6.37. Direct comparisons of the curves at each temperature for baseline and moisture espossed samples are given in Figure 6.38. The decreases of the initial modulus (initial slope) and ultimate strength (failure stress) with humidity exposure are easily visualized in these plots. The modulus values were extracted from stress-strain curves and plotted as a function of moisture exposure time and temperature as shown in Figure 6.39 and 6.40 respectively. It is evident from the Figure 6.40 that glass transition temperature (T_g) decreases with moisture exposure time.

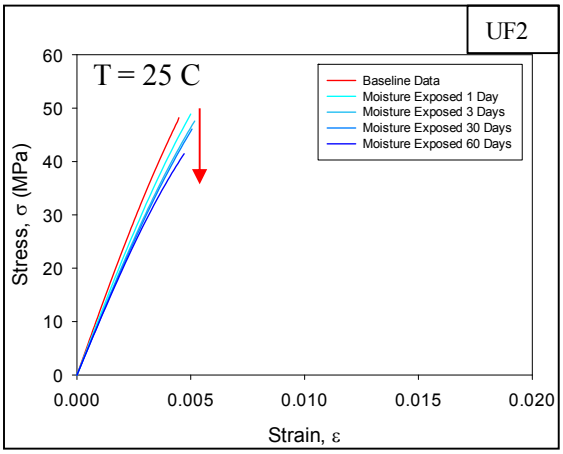

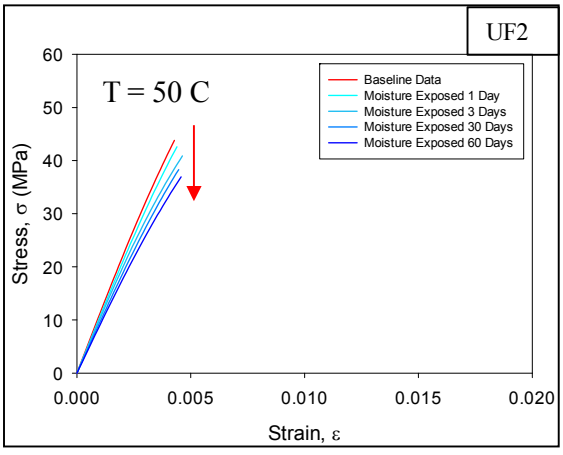

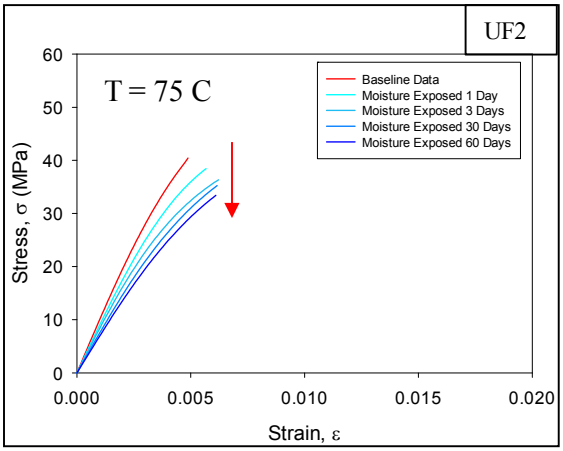
UF2
T = 75 C
Baseline Data
Moisture Exposed 1 Day
Moisture Exposed 3 Days
Moisture Exposed 30 Days
Moisture Exposed 60 Days
Stress, σ (MPa)
Strain, ε
0
10
20
30
40
50
60
0.000
0.005
0.010
0.015
0.020

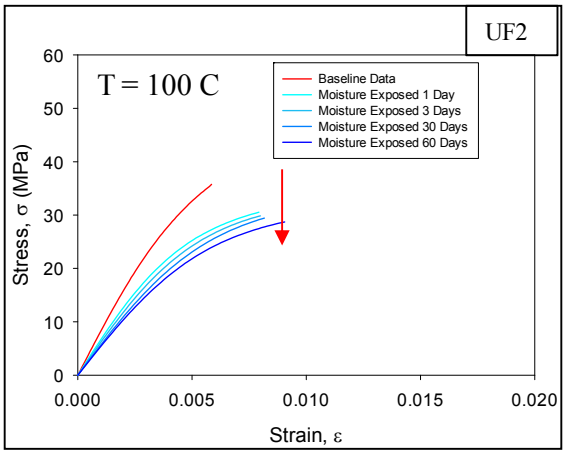
UF2
T = 100 C
Baseline Data
Moisture Exposed 1 Day
Moisture Exposed 3 Days
Moisture Exposed 30 Days
Moisture Exposed 60 Days
Stress, σ (MPa)
Strain, ε
0
10
20
30
40
50
60
0.000
0.005
0.010
0.015
0.020

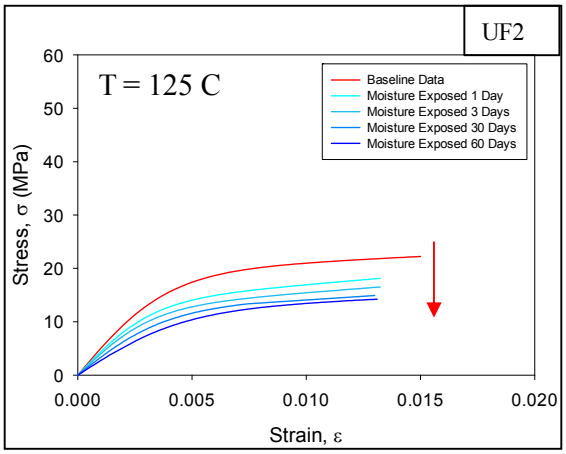
UF2
T = 125 C
Baseline Data
Moisture Exposed 1 Day
Moisture Exposed 3 Days
Moisture Exposed 30 Days
Moisture Exposed 60 Days
Stress, σ (MPa)
Strain, ε
0
10
20
30
40
50
60
0.000
0.005
0.010
0.015
0.020

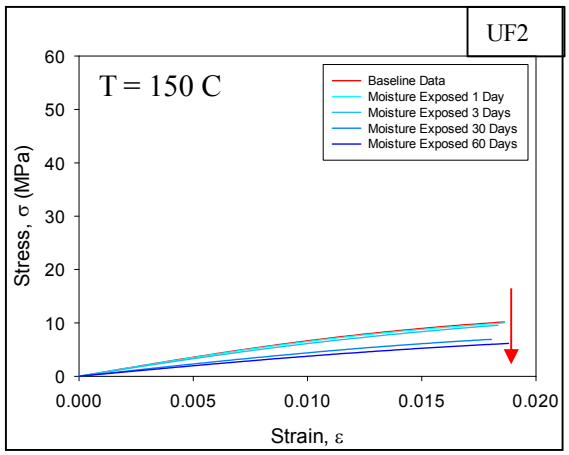

Figure 6.38 Comparison of Experimental Stress-Strain Curves of Underfill (UF2) for Moisture Exposed and Dry Samples

It is also observed that the elastic modulus has a linear dependence at different temperatures. For each condition, two different slopes were also visible indicating the effect of glass transition temperature of the material. For dry or baseline samples the weak glass transition was above 100 C. After this region, the underfill exhibits softening behavior. However, for the samples which were exposed to moisture, the initiation of glass transition region were not at the same temperature as was seen for dry samples.

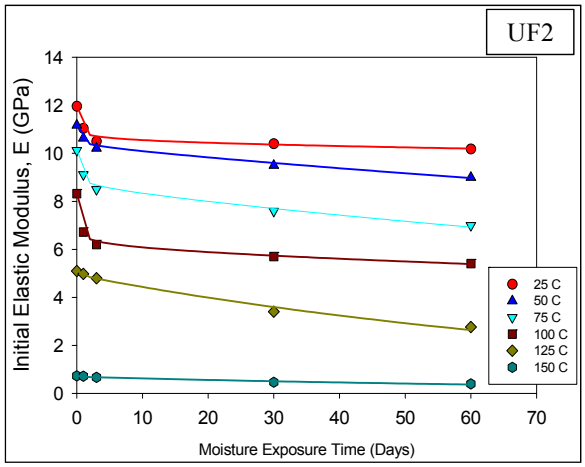

Figure 6.39 Effective Elastic Modulus vs. Moisture Exposure Time of Underfill (UF2) for Different Testing Temperature

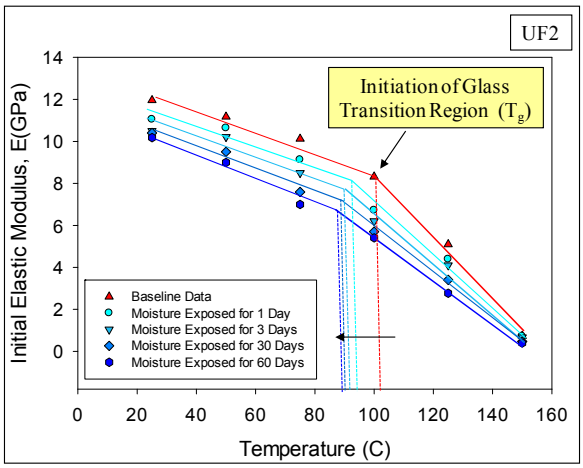

Figure 6.40 Effective Elastic Modulus vs. Temperature of Underfill (UF2) for Different Hygrothermal Aging Conditions

Figure 6.40 is an approximation to show how the glass transition region shifted with moisture exposure. Based on this figure, 106 C can be regarded as the starting of glass transition region for dry samples and for the samples those were exposed to controlled humidity for 1 day, 3 days, 30 days and 60 days, the glass transition temperature can be approximated as 95 C, 92 C, 90 C and 88 C respectively. The values have been tabulated in Table 6.9.

Table 6.9 Effect of Moisture Exposure on Glass Transition Temperature (Using Tensile Test Results)

Moisture Exposure Time (Days)	Glass Transition Temperatutre, T_g (C)
0	106.63
1	95
3	92
30	90
60	88

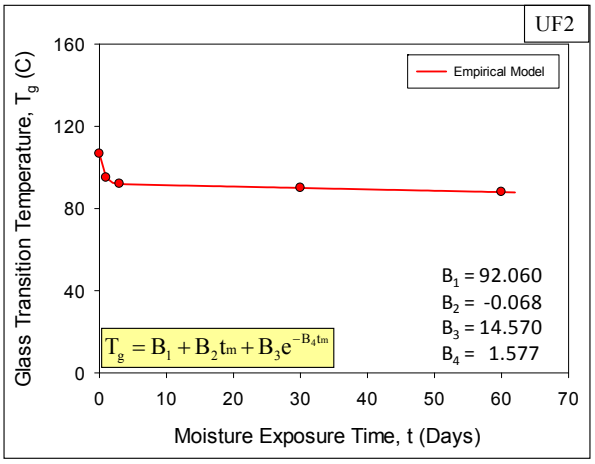

Figure 6.41 Shifting of Glass Transition Region Due to Moisture Absorption from Stress-Strain Curves

The observed changes in the glass transition temperature with moisture absorption are plotted in Figure 6.41 and a four parameter exponential model was used to predict the change of glass transition temperature (T_g) with moisture exposure time, t_m where B's are material constants.

6.4.3 Dynamic Mechanical Analysis (DMA) before and after Moisture Adsorption and Comparisons

So far, the initiations of glass transition region have been approximated using tensile test results. In this section, the results of Dynamic Mechanical Analysis (DMA) have been presented for no moisture exposure and also for moisture exposure for different durations of time such as 1 day, 3 days, 30 days and 60 days at 85 C and 85% RH. Most of the analyses have been conducted from -25 C to 200 C (shown in Figure 6.42 through 6.46). The DMA curves show storage modulus (E'), loss modulus (E'') and loss tangent (tanδ) plotted as a function of temperature.

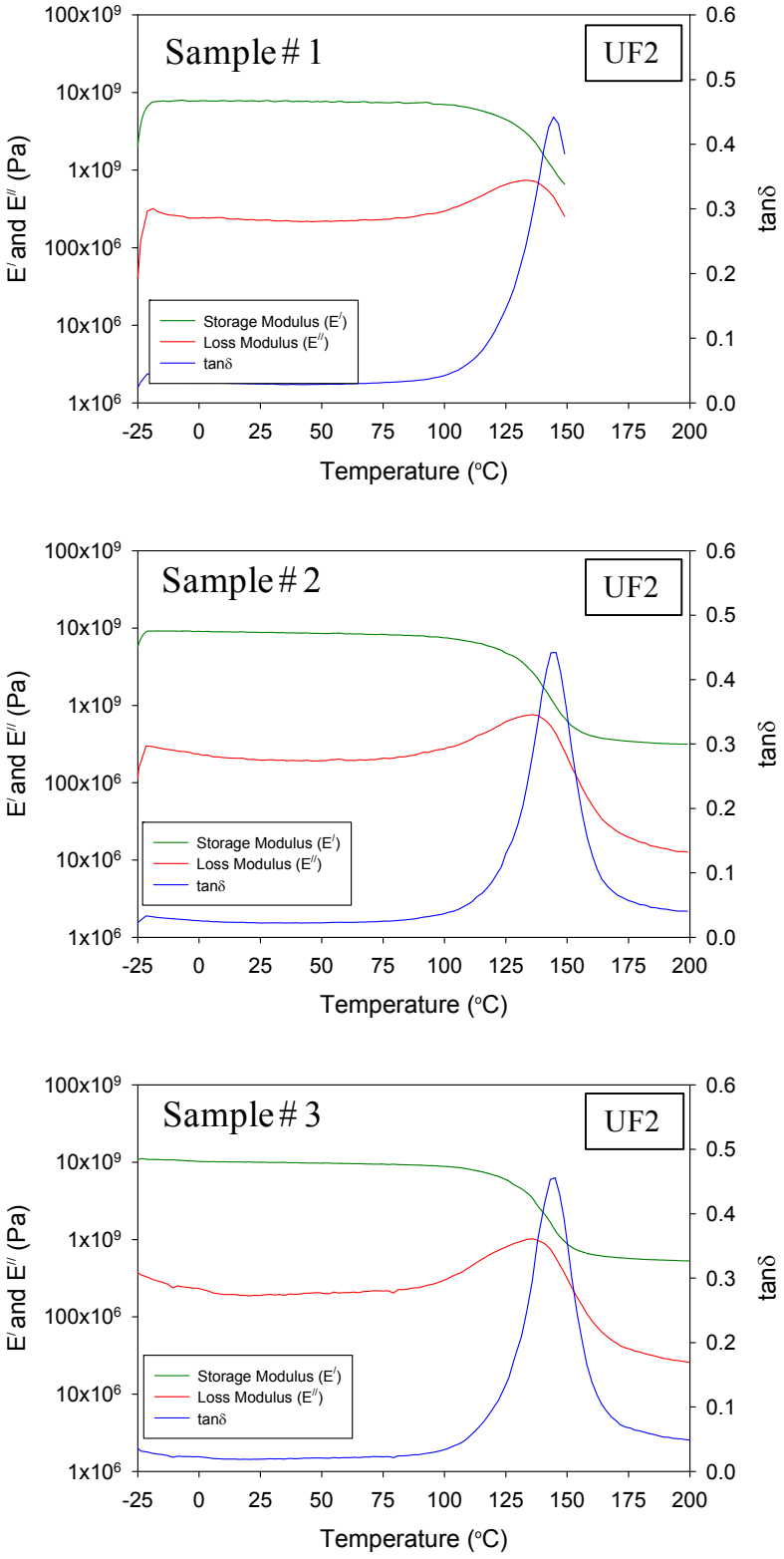

Figure 6.42 DMA Test Results of Underfill (UF2) before Moisture Adsorption

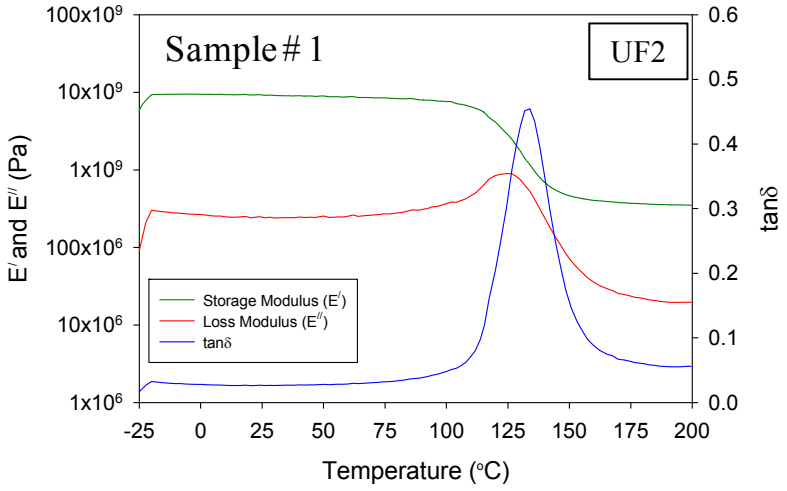

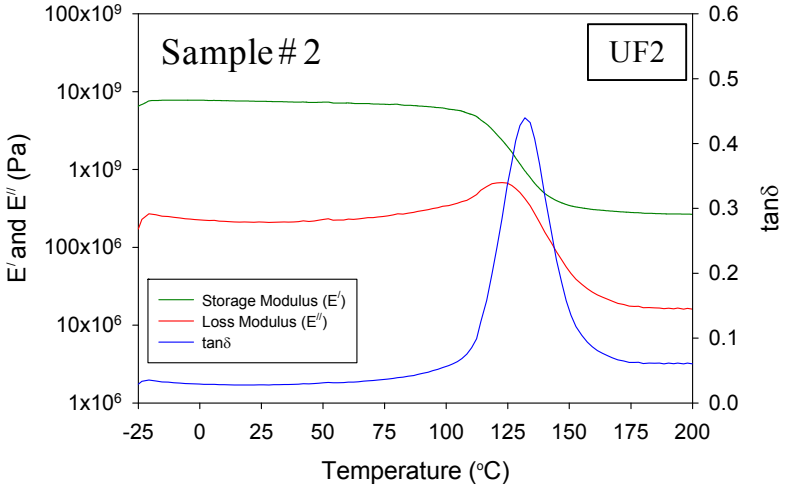

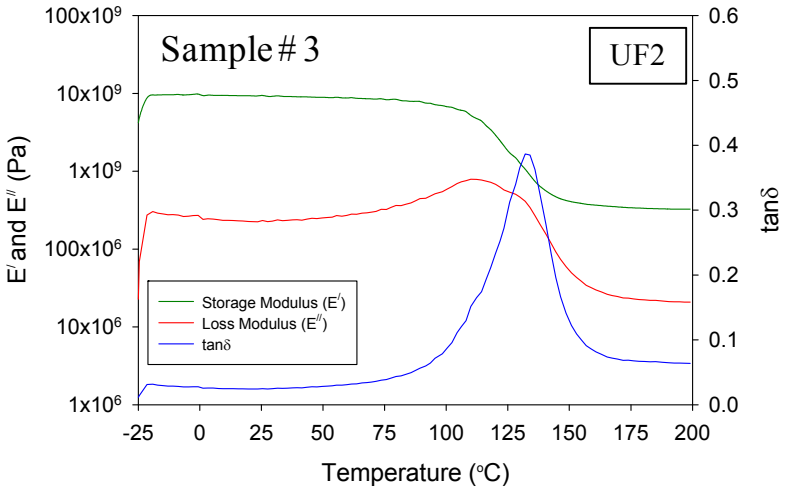

Figure 6.43 DMA Test Results of Underfill (UF2) after Moisture Adsorption (1 Day @ 85/85)

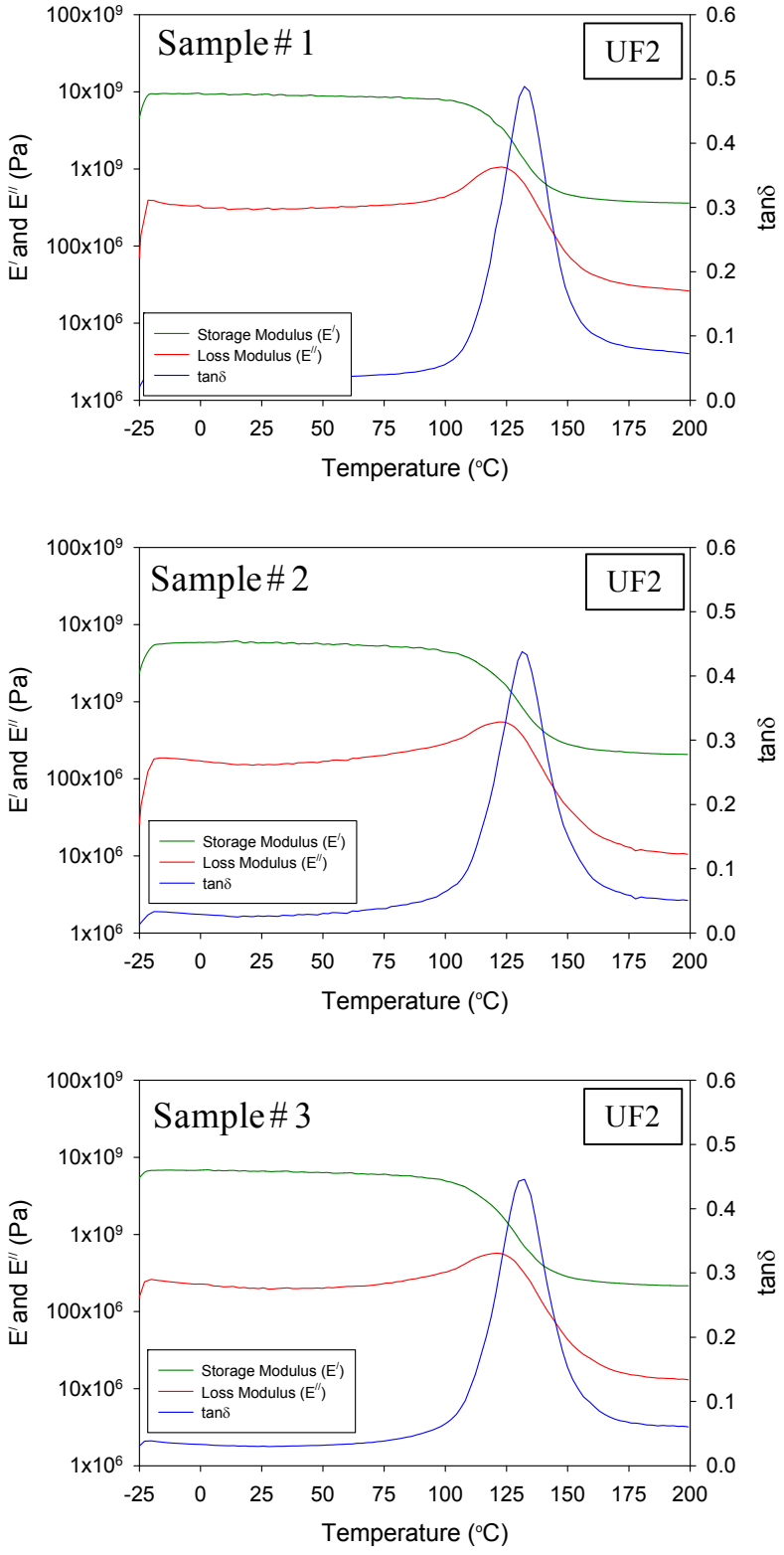

Figure 6.44 DMA Test Results of Underfill (UF2) after Moisture Adsorption (3 Days @ 85/85)

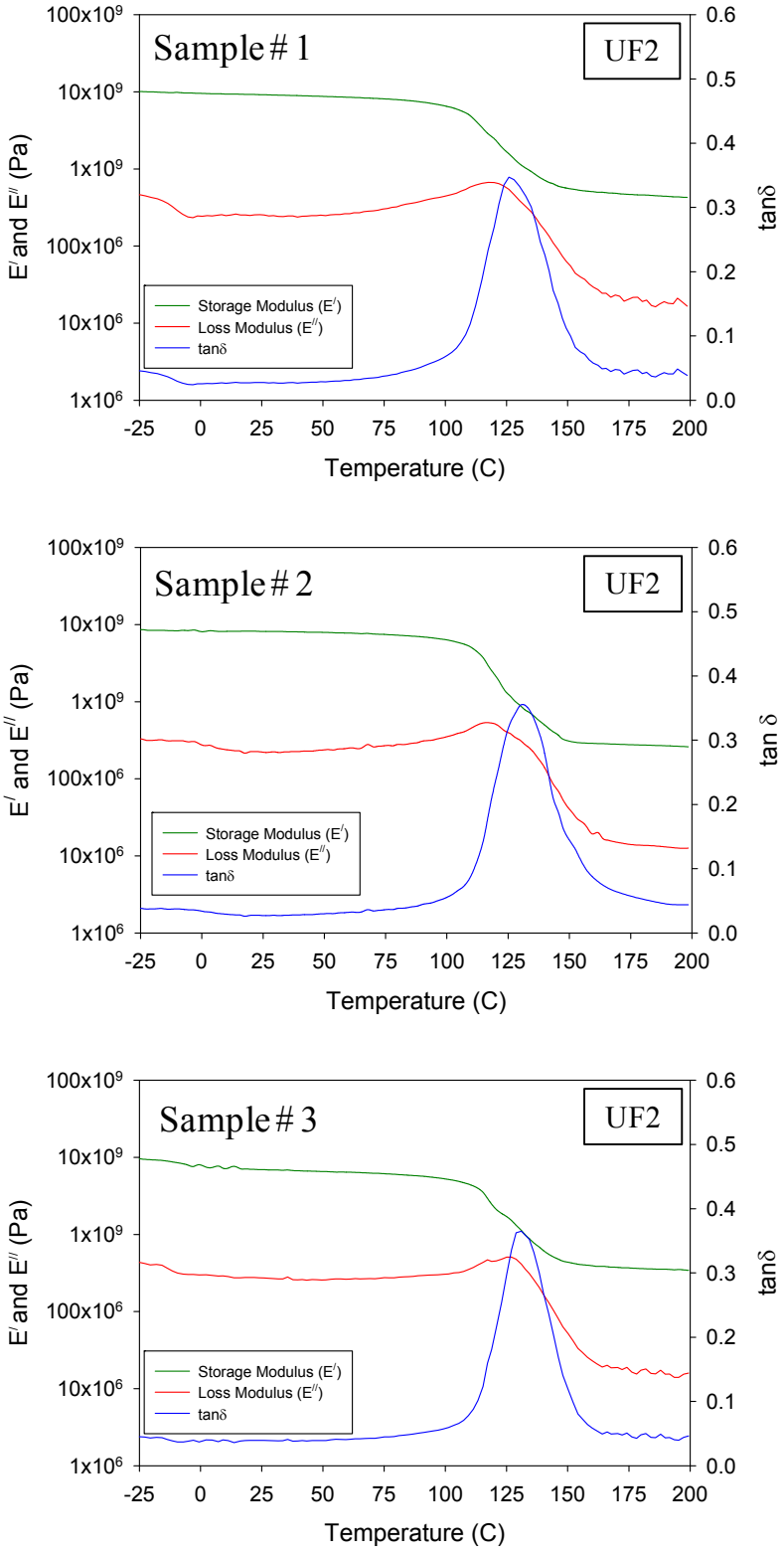

Figure 6.45 DMA Test Results of Underfill (UF2) after Moisture Adsorption (30 Days @ 85/85)

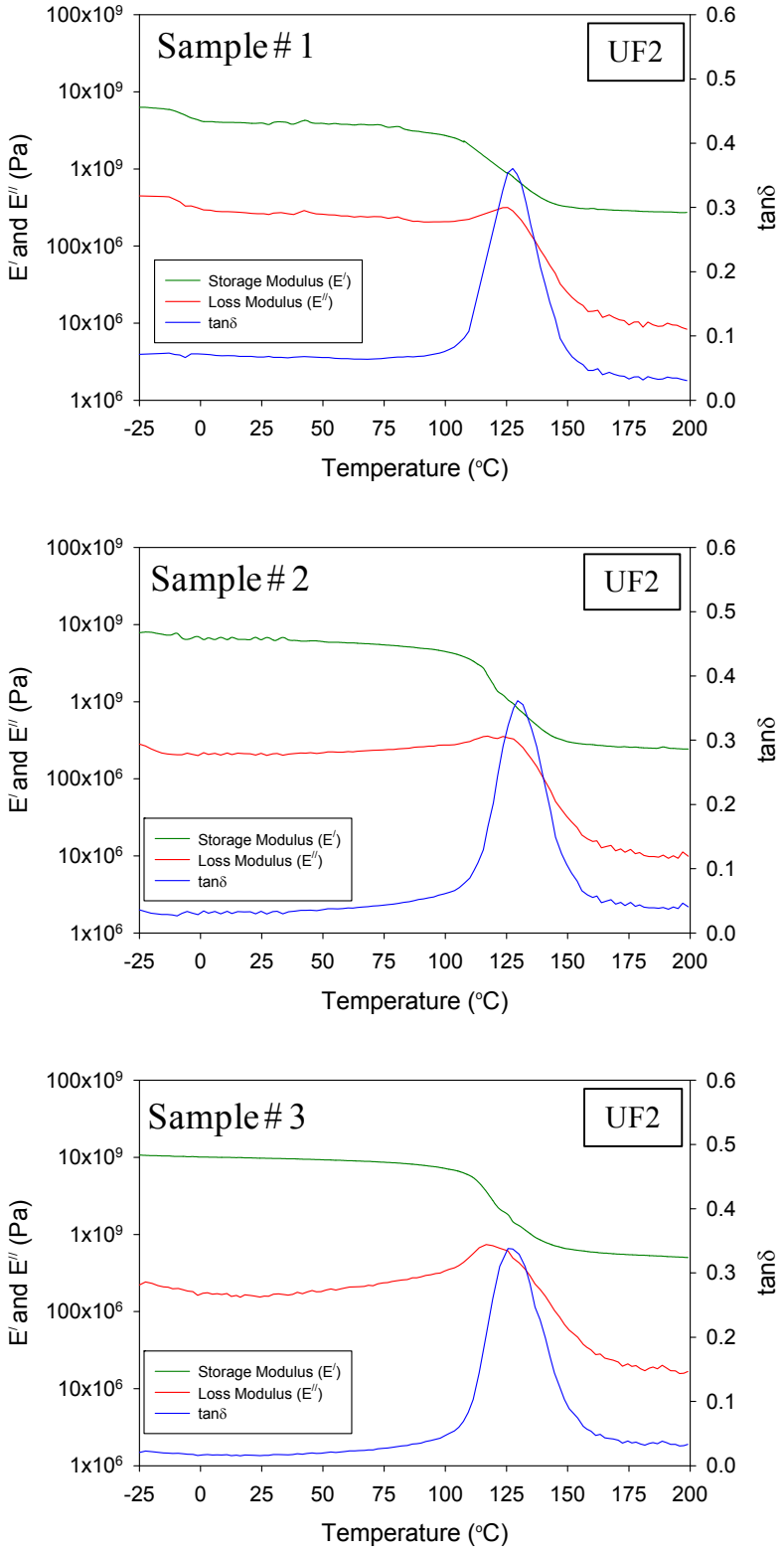

Figure 6.46 DMA Test Results of Underfill (UF2) after Moisture Adsorption (60 Days @ 85/85)

From DMA curves, the onset decrease in storage modulus, accompanied by a peak in loss modulus and tan delta are observed. The onset can be taken as the T_g [107]. In Figures 6.42 through 6.46, the glass transition (T_g) is seen as a large drop in storage modulus when viewed on a log scale against a linear temperature scale. The average curves of storage modulus for no moisture and with moisture exposure have been presented in Figures 6.47 through 6.51. Figure 6.52 shows the comparison of the average storage modulus data before and after moisture absorption and the shifting of glass transition temperature after moisture absorption are clearly visualized from the plots.

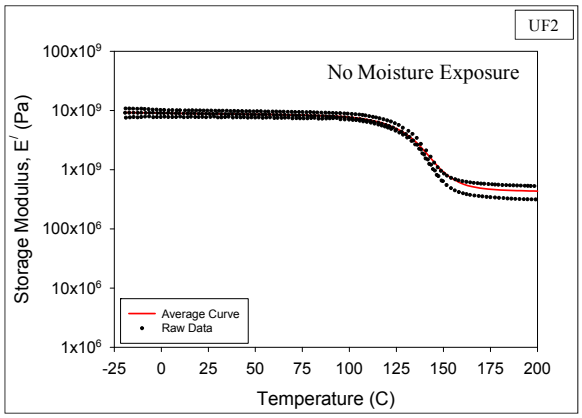

Figure 6.47 Average Storage Modulus Data of Underfill (UF2) before Moisture Adsorption

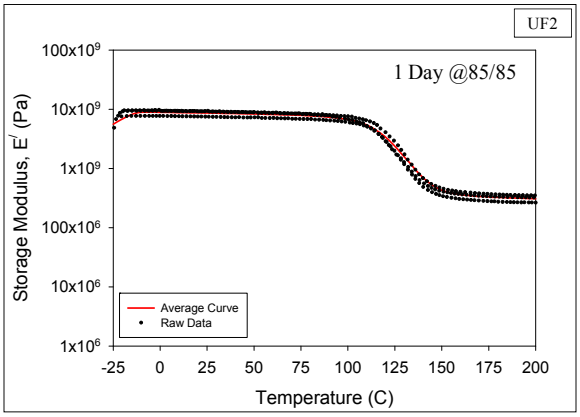

Figure 6.48 Average Storage Modulus Data of Underfill (UF2) after Moisture Adsorption (1 Day @ 85/85)

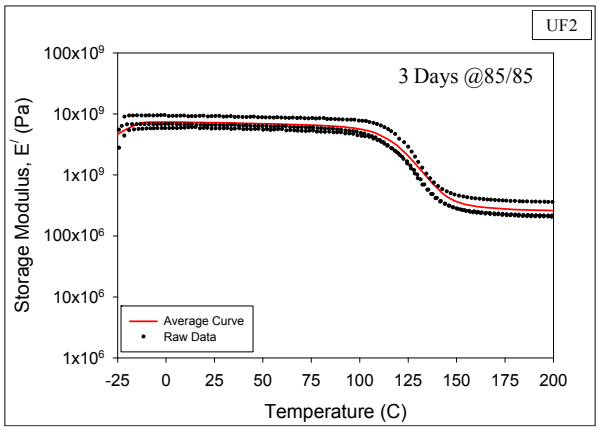

Figure 6.49 Average Storage Modulus Data of Underfill (UF2) after Moisture Adsorption (3 Days @ 85/85)

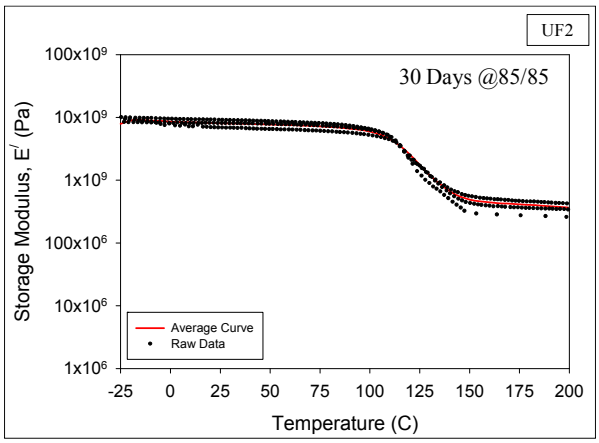

Figure 6.50 Average Storage Modulus Data of Underfill (UF2) after Moisture Adsorption (30 Days @ 85/85)

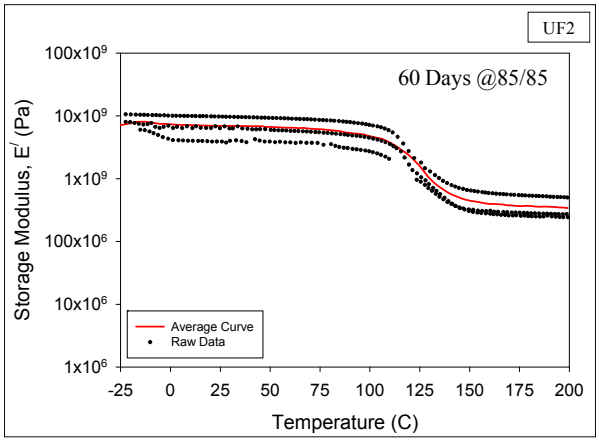

Figure 6.51 Average Storage Modulus Data of Underfill (UF2) after Moisture Adsorption (60 Days @ 85/85)

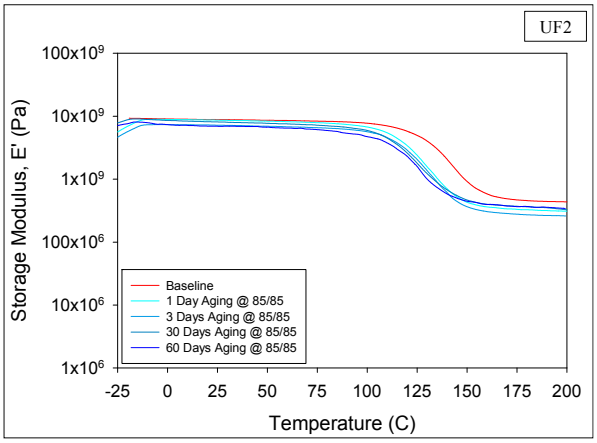

Figure 6.52 Effect of Moisture Exposure on Glass Transition Temperature of Underfill (UF2)

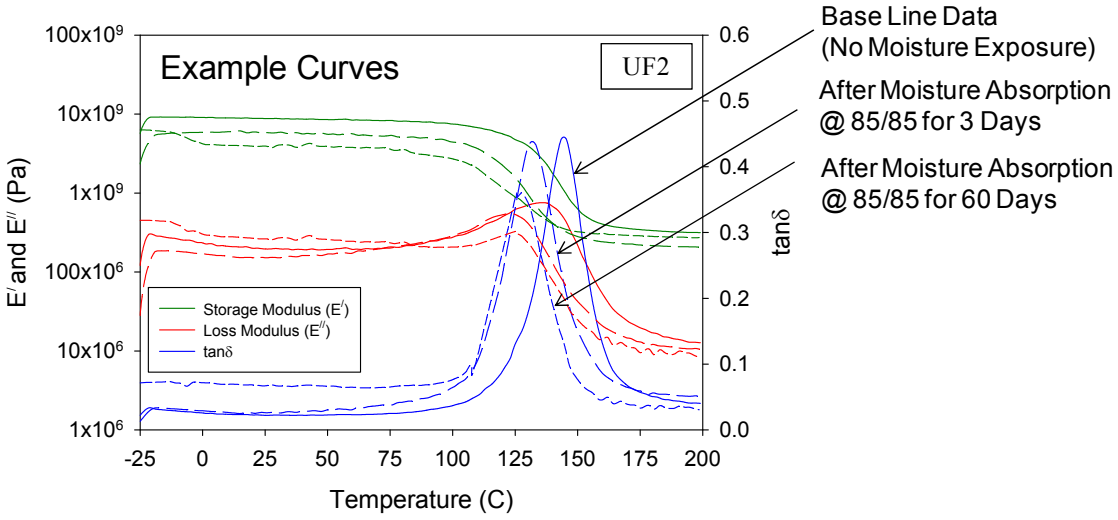

Figure 6.53 Effect of Moisture Exposure on DMA Test Results of Underfill (UF2)

Figure 6.53 illustrates the effect of moisture exposure on T_g. It is evident from the figure that DMA curves (storage modulus, loss modulus and tanδ) shifted to the left after moisture absorption indicating reduction in glass transition temperature. Solid line represents baseline data or no moisture exposure. Long dashed line and short dashed line represent data for 3 days and 10 days of moisture exposure respectively at 85 C and 85% RH.

An idealized DMA curve has a linear section before the transition (glassy region below the temperature of T_g) and a stepwise drop through the glass transition region. These linear sections are used in calculating T_g by onset of the modulus drop [108]. To do this, a tangent line has been constructed to the curve below the transition temperature in the modulus curve. Then another tangent has been drawn to the storage modulus curve at or near the inflection point approximately midway through the step change in the transition. The temperature where these tangents intersect is the reported T_g for the material. Figures 6.54 to 6.58 are the examples of this tangent intersection method. The determined glass transition temperatures are listed in Table 6.9. While comparing the values shown in Table 6.10 with the approximated values of T_g from Table 6.9, it is seen that the values are very close, thus validating the estimated values of T_g obtained from the tensile results and therefore the approximated values of T_g can be incorporated in the shift function of the viscoelastic model.

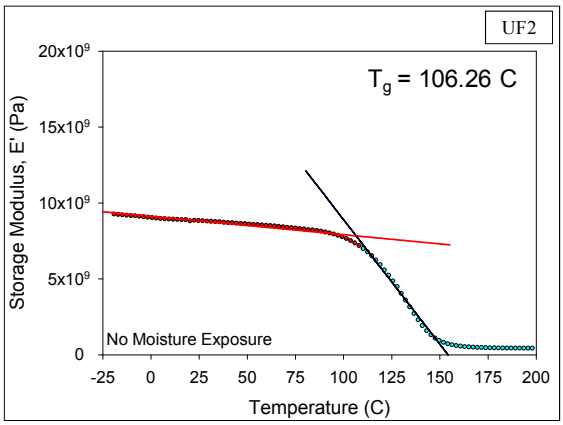

Figure 6.54 Determination of Glass Transition Temperature of Underfill (UF2) for Baseline Data

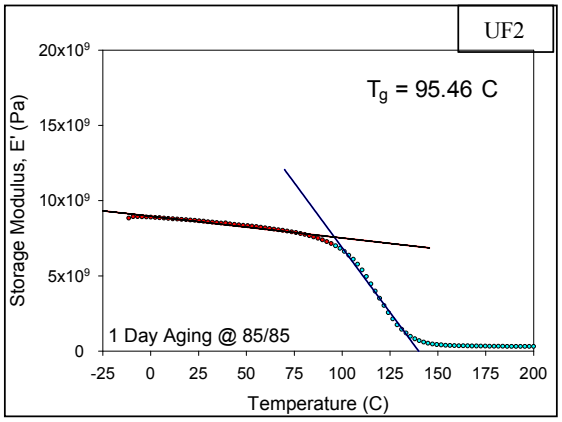

Figure 6.55 Determination of Glass Transition Temperature of Underfill (UF2) for 1 Day Moisture Exposure @ 85 C, 85%RH

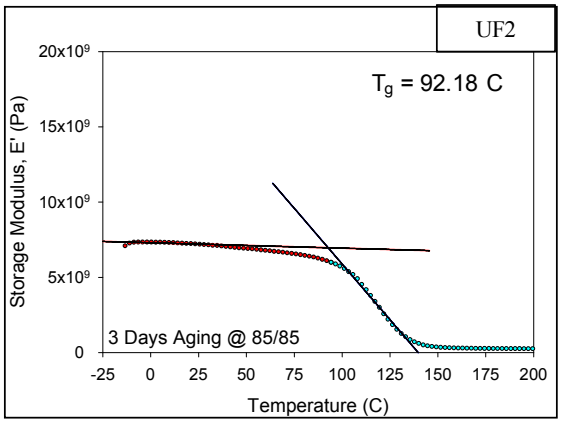

Figure 6.56 Determination of Glass Transition Temperature of Underfill (UF2) for 3 Days Moisture Exposure @ 85 C, 85%RH

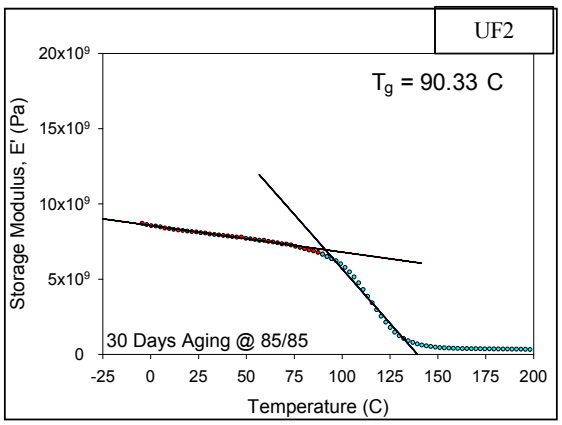

Figure 6.57 Determination of Glass Transition Temperature of Underfill (UF2) for 30 Days Moisture Exposure @ 85 C, 85%RH

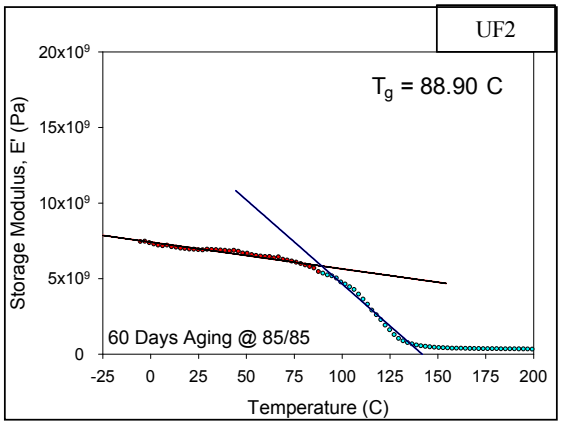

Figure 6.58 Determination of Glass Transition Temperature of Underfill (UF2) for 60 Days Moisture Exposure @ 85 C, 85%RH

Table 6.10 Effect of Moisture Exposure on the Glass Transition Temperature of Underfill (UF2) (Using Storage Modulus Data of DMA Results)

Moisture Exposure Time (Days) @ 85/85	Glass Transition Temperature, T_g (C)
0	106.26
1	95.46
3	92.18
30	90.33
60	88.90

6.4.4 Creep Data after Moisture Adsorption and Comparisons

The effects of moisture exposure on the creep curves of UF2 have been explored at room temperature (T = 25 C) and four stress levels. The specimens have been exposed to combined temperature/humidity exposures (85 C and 85% RH). After hygrothermal aging/preconditioning, the samples were uniaxially tested. Like tensile testing, 4 groups (A, B, C, D) of test specimens were prepared for moisture exposure. In each case the samples were baked in a box oven at 85 C for 24 hours prior to moisture preconditioning at 85 C and 85% RH conditions in a humidity chamber. Group A had a moisture exposure for 1 day, whereas Group B, C and D had a moisture exposure for 3 days, 30 days and 60 days respectively. The average creep curves at room temperature after moisture adsorption for different durations at 85 C and 85% RH conditions are shown in Figure 6.59. Table 6.11 shows the comparison of strain rates before and after moisture absorption. In each case, the linear parts of the creep curves have been considered and slopes at the end have been recorded as strain rates. It is evident from the table that the strain rate increases slightly with moisture adsorption.

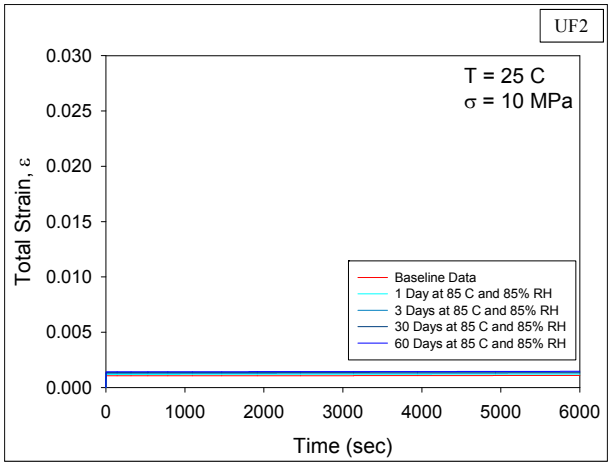

(a) T = 25 C, σ = 10 MPa

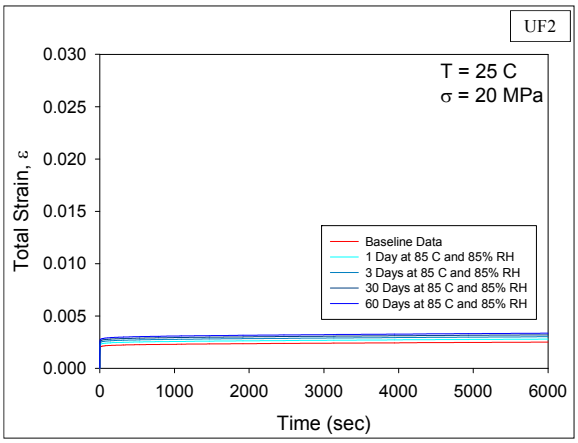

(b) T = 25 C, σ = 20 MPa

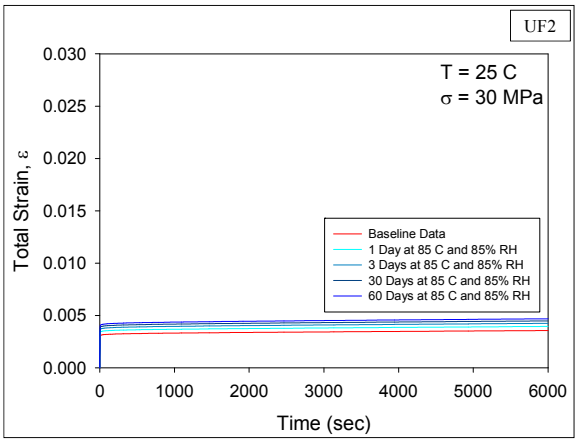

(c) T = 25 C, σ = 30 MPa

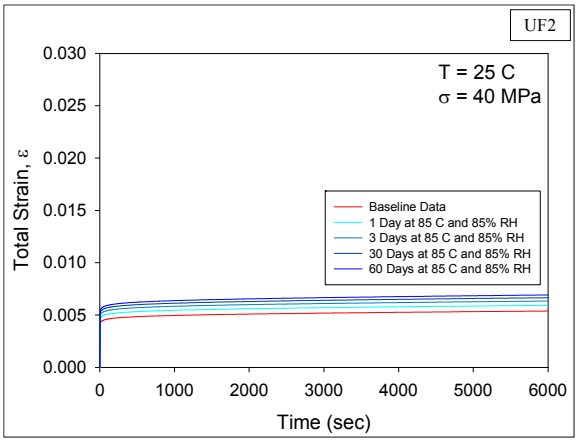

(d) T = 25 C, σ = 40 MPa

Figure 6.59 Comparison of Creep Curves of Underfill (UF2) for Moisture Exposed and Dry Samples

Table 6.11 Comparison of Strain Rates obtained from Experimental Data for UF2

Condition	Stress Levels			
	10 MPa	**20 MPa**	**30 MPa**	**40 MPa**
Baseline	4.880×10^{-9}	3.233×10^{-8}	4.112×10^{-8}	5.822×10^{-8}
1 Day at 85/85	5.441×10^{-9}	3.605×10^{-8}	4.564×10^{-8}	6.404×10^{-8}
3 Days at 85/85	5.882×10^{-9}	3.893×10^{-8}	4.907×10^{-8}	6.852×10^{-8}
30 Days at 85/85	6.241×10^{-9}	4.127×10^{-8}	5.177×10^{-8}	7.195×10^{-8}
60 Days at 85/85	6.559×10^{-9}	4.333×10^{-8}	5.409×10^{-8}	7.482×10^{-8}

6.4.5 Constitutive Model Applications

6.4.5.1Prony Series Viscoelastic Model for Baseline Data of UF2

The experimentally characterized creep curves in Figure 4.22 of Chapter 4 have been utilized with the curve-fitting routines of ANSYS to determine the optimal Prony series and shift function coefficients using eqs. (5.14-5.15, 5.43) simultaneously. The coefficients calculated using ANSYS have been shown in Table 5.5. The correlations of the Prony Series viscoelastic model predictions for dry samples (using the coefficients in Table 5.5) with the stress-strain and creep data from Figure 4.20 and 4.22 are shown in the previous Chapter 5 in Figures 5.12 and 5.13. It has been found that the model correlates well with the experimental data at all temperatures for dry samples. Based on this success, the ability of the Prony Series model has also been evaluated to predict the rate dependent stress-strain data at different temperatures and creep data at room temperature of UF2 after moisture adsorption in Figure 6.60 and 6.61 respectively.

6.4.5.2Prony Series Viscoelastic Model including Moisture Exposure for UF2

In viscoelastic model, the shift function is used to specify the change of mechanical behavior with temperature with respect to a base or reference temperature. From eq. (5.42) the shift factor is defined as the ratio of the relaxation time at one

temperature to that at a reference temperature. As the glass transition temperature is used as the reference temperature in the WLF shift function, the effect of moisture uptake can be included in the viscoelastic model.

Table 6.12 Prony Series and WLF Shift Function Coefficients for UF2 after Incorporating Moisture Effect

Constants for Shear Response	Constants for Volumetric Response	Constants for Shift Function (WLF Equation)
$a_1 = 0.30055$ $t_1 = 44.1300$ $a_2 = 0.19892$ $t_2 = 1378.1000$ $a_3 = 0.32473$ $t_3 = 35530$ $a_4 = 0.16401$ $t_4 = 9.8788 \times 10^5$	$a_1 = 0.90618$ $t_1 = 0.00195$ $a_2 = 0.00499$ $t_2 = 9.2235$ $a_3 = 0.01633$ $t_3 = 136.43$ $a_4 = 0.01703$ $t_4 = 10921$ $a_5 = 0.00732$ $t_5 = 3.1206 \times 10^5$	$T_{ref} = T_g$ $C_1 = -50.064$ $C_2 = -651.89$ Where: $T_g = B_1 + B_2 t_m + B_3 e^{-B_4 t_m}$ $B_1 = 92.060$ $B_2 = -0.068$ $B_3 = 14.570$ $B_4 = 1.577$

Moisture is known to plasticize epoxies, a phenomenon that translates to a reduction in the glass transition temperature (T_g) and softening [63], so to incorporate the change of reference temperature (T_{ref}) in the WLF equation with moisture diffusion in underfill while other coefficients of shear response and bulk response remaining the same, may represent the phenomenon of changing material behavior with moisture adsorption. Table 6.12 shows the same set of coefficients used for dry samples now with a small change in the reference temperature and has been proposed to be applicable not only for dry samples but also for moisture exposed samples. Figure 6.60 and 6.61 are attempts to show how the set of coefficients based on Prony Series can predict the stress-strain and creep behavior of the tested underfill UF2 after moisture adsorption. Again, a good agreement was found between the experimental results and Prony series prediction.

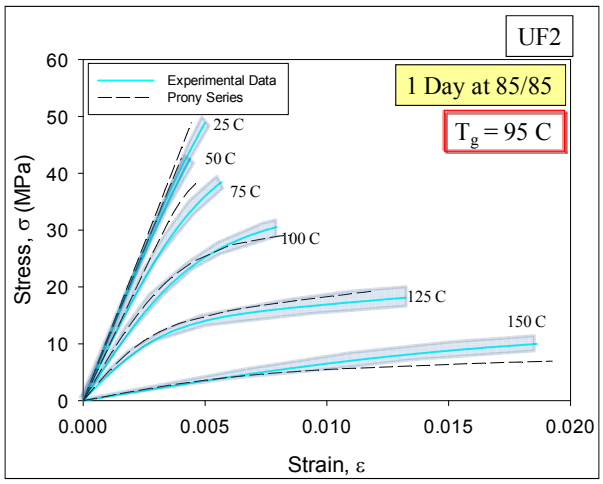

(a) Stress-Stain Data of Underfill (UF2) after 1 Day of Moisture Adsorption (Shaded Region Shows the Spread of the Curve)

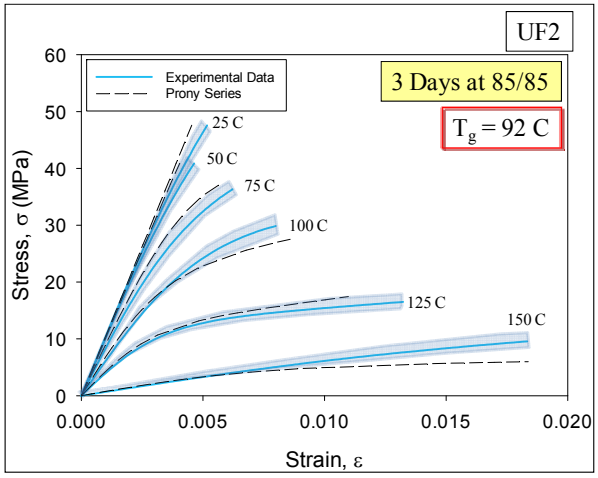

(b) Stress-Stain Data of Underfill (UF2) after 3 Days of Moisture Adsorption (Shaded Region Shows the Spread of the Curve)

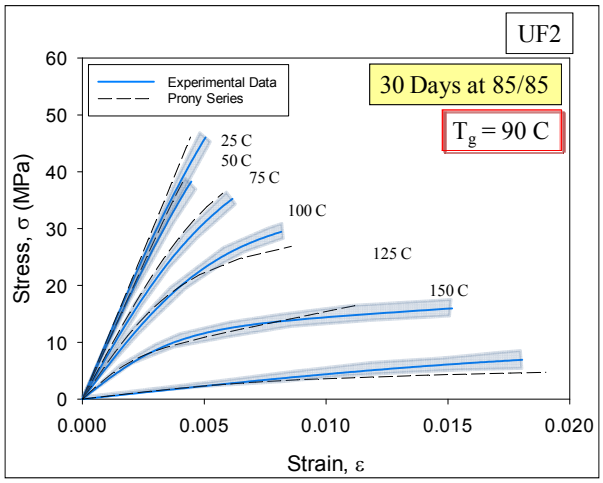

(c) Stress-Stain Data of Underfill (UF2) after 30 Days of Moisture Adsorption (Shaded Region Shows the Spread of the Curve)

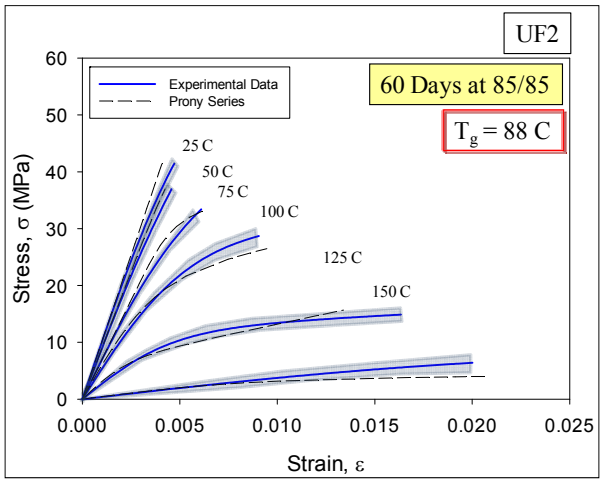

(d) Stress-Stain Data of Underfill (UF2) after 60 Days of Moisture Adsorption (Shaded Region Shows the Spread of the Curve)

Figure 6.60 Correlation of Prony Series Viscoelastic Model Predictions with UF2 Stress-Stain Data after Moisture Adsorption

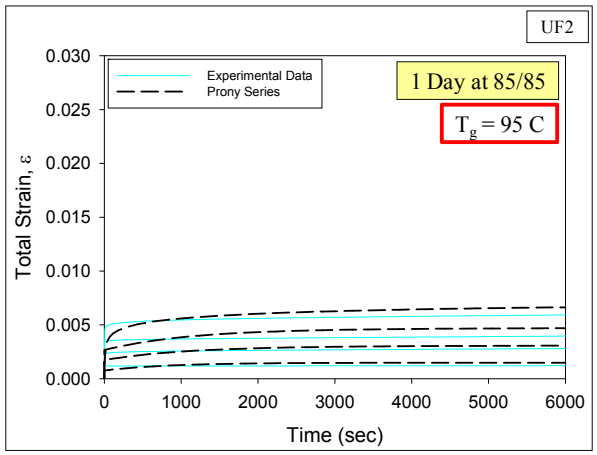

(a) Creep Data of Underfill (UF2) after 1 Day of Moisture Adsorption

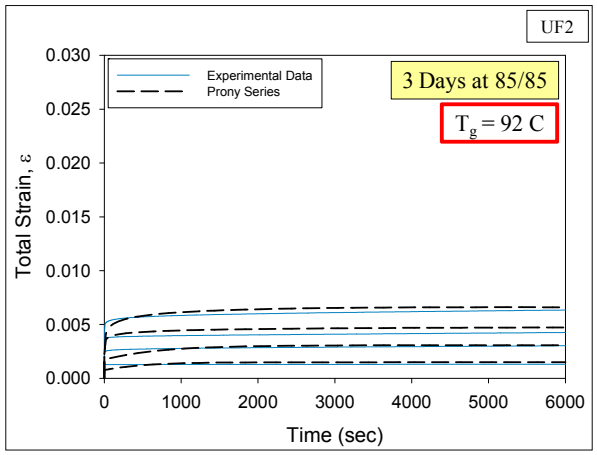

(b) Creep Data of Underfill (UF2) after 3 Days of Moisture Adsorption

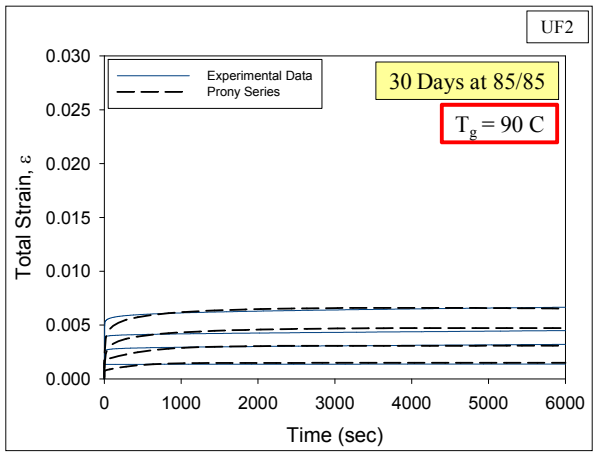

(c) Creep Data of Underfill (UF2) after 30 Days of Moisture Adsorption

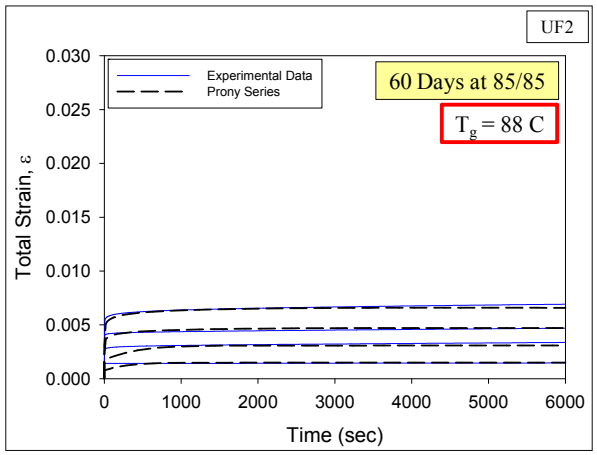

(d) Creep Data of Underfill (UF2) after 60 Days of Moisture Absorption

Figure 6.61 Correlation of Prony Series Viscoelastic Model
Predictions with UF2 Creep Data at T = 25 C after Moisture Adsorption

6.4.6 Moisture Adsorption Measurements

To analyze the increase in moisture content, the test specimens were placed into a humidity chamber at 85 C and 85% RH, and then removed from the chamber after various durations of exposure and weighed on an electronic balance to the nearest 0.1 mg. The percentage weight gain was characterized for various durations of exposure up to 60 days to monitor the level of moisture adsorption with respect to time.

Figure 6.62 shows the variations of the sample weight for various durations of humidity exposure and recovery. The moisture adsorption appeared to stabilize at 10 days of moisture exposure and the weight gain was 0.79% after 60 days of exposure. After redrying, the sample weight again reached approximately the same value of dry weight which also indicates the process as almost reversible.

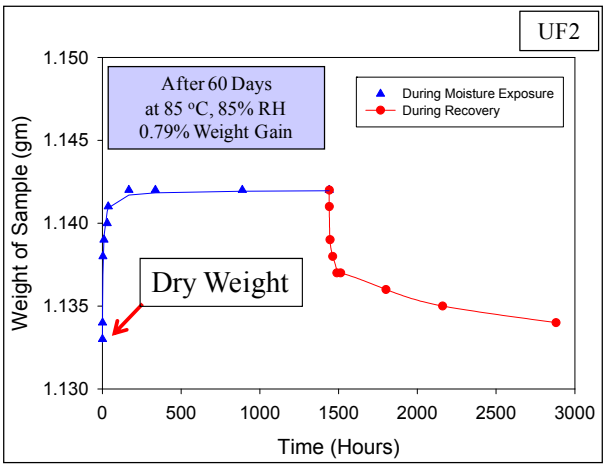

Figure 6.62 Weight Gain and Recovery of Underfill (UF2) with Time

6.5 Summary and Discussion

In this chapter, the effects of moisture exposure on the mechanical behavior of microelectronic packaging polymers have been discussed. In each case, the uniaxial test specimens were exposed in an adjustable thermal and humidity chamber to combined hygrothermal exposures for various durations. After moisture preconditioning, a microscale tension-torsion testing machine was used to evaluate the complete stress-strain behavior of the materials at several temperatures. It was found that moisture exposure caused plasticization and strongly reduced the mechanical properties of the materials. Reversibility tests were also conducted to evaluate whether the degradations in the mechanical properties were recoverable.

The uniaxial test specimens of polymer encapsulant were exposed at 85 C and 85% RH for various durations up to 10 days. It was found that moisture exposure reduced the mechanical properties of the encapsulant including the initial elastic modulus and ultimate tensile stress. Reversibility tests were also conducted where it was seen that upon fully redrying, the polymer was found to recover most but not all of its original

mechanical properties. A 25% permanent reduction in the elastic modulus was observed due to hydrolysis, where water molecules had chemically modified the organic structure of the material. This was verified by observations of permanent changes in the FTIR spectra of the material.

The polycarbonate uniaxial test specimens were exposed to combined hygrothermal exposures of 60 C and 90% RH, 60 C and 50% RH, and 40 C and 50% RH for various durations (0, 3, and 10 days). Then complete stress-strain behavior of the material was evaluated at several temperatures (T = 20, 40, 60 C). It was found that moisture exposure strongly reduced the strain to failure of the polycarbonate, with larger reductions occurring with the more severe moisture exposures. However, no changes occurred in the initial elastic modulus and ultimate stress due to moisture exposure. Reversibility tests were also conducted to evaluate whether the degradations in the mechanical properties were recoverable upon re-baking. Upon redrying, the polymer was found to recover most of its original mechanical properties. Moreover, the polycarbonate sample fracture surfaces were observed by optical microscopy. The microscopic features of the moisture exposed samples contained fragments and cavities, whereas no fragments were observed on the surface of the non-exposed samples.

In case of underfill, the viscoplastic mechanical response of underfill encapsulant (UF2) has been characterized via temperature dependent stress-strain testing over a wide temperature range, and creep testing for a large range of applied stress levels and temperatures. Stress-strain curves have been measured at 6 temperatures (25, 50, 75, 100, 125 and 150 C). In addition, creep curves have been evaluated for 4 different temperatures and several stress levels for dry samples. The viscoelastic model based on

Prony series has been applied to fit the mechanical response data. The model was found to represent both the stress-strain data and creep data pretty well at all temperatures and applied stress levels for dry samples. However, it was evident that moisture exposure caused plasticization and strongly reduced the mechanical properties of the underfill including the initial elastic modulus and ultimate tensile stress. The Prony series viscoelastic model was then utilized to predict the stress-strain and creep behavior of the moisture exposed samples of the tested underfill and again excellent correlation was achieved in case of moisture exposed samples. A set of constants has been found for the tested underfill that can be used to accurately represent mechanical behavior of the material before and after moisture absorption by including the effects of moisture exposure on the glass-transition temperature in the WLF equation. Since underfills are epoxy based, the modified model for including the moisture effect has the potential to be applied for modeling moisture absorption behavior of other microelectronic packaging polymers such as molding compounds and adhesives.

CHAPTER 7

FINITE ELEMENT MODELING

7.1 Introduction

Polymeric materials, including underfills, exhibit complicated vicoelastic response. In this chapter, the viscoelastic properties for underfill (UF1 and UF2) have been implemented in finite element analysis. For both cases, the thermomechanical behavior of a flip chip on laminate assembly has been simulated using three-dimensional FEA.

The first model was developed using UF1 (Zymet) properties for underfill. The loading condition consisted of a uniform cooling from 130 to 20 C. Due to symmetry, a one-quarter model was developed, and the mesh and applied boundary conditions are shown in Figure 7.1 (u_x and u_y denote the displacements in x and y directions, respectively). Two different material models have been used for the underfill, UF1: (a) Temperature Dependent Elastic-Plastic (material properties from Figure 4.1), (b) Temperature Dependent Linear Viscoelastic based on Prony Series (coefficients shown in Table 5.2) to compare the time dependent variations of the stresses in the underfill and silicon die obtained with the viscoelastic model to the time-independent results from the conventional elastic-plastic material model. In both cases elastic properties have been used for silicon die and ceramic substrate. The model has been meshed with 20 node SOLID 95 and SOLID 186 elements for the elastic-plastic and viscoelastic models, respectively. Over 27,000 elements were utilized.

The second model of flip chip on laminate assembly was used to explore the effects of moisture exposure on the plastic work per unit volume in C4 joints and also stress developed in underfill and die. In this case, UF2 (ME525) properties from Table 5.5 were utilized. The three dimensional finite element modeling of the underfilled flip chip assembly was done to simulate the uniform cooling of the components from 125 to 25 C. The simplified quarter model of the assembly with four C4 joints has been illustrated in Figure 7.6. The 9 Anand parameters for SAC305 were used to represent the mechanical behavior of C4 joints. Like before, the model was meshed with 20 node SOLID 186 elements and over 30,000 elements were utilized.

7.2 Simulation Results of UF1

The observed time dependent variations of stress with time during cooling of the assembly are shown in Figures 7.2 through 7.5 for the silicon die and underfill. Figure 7.2 and 7.3 shows that the results for the stress in the silicon die are nearly independent of time for the viscoelastic analysis, and both material models for the underfill yield almost identical magnitudes for the stress distributions. From Figure 7.4 and 7.5, it is observed that the stresses in the underfill are time dependent (~25% change) with the viscoelastic material model, and the magnitudes of the stresses are significantly different for the two material models.

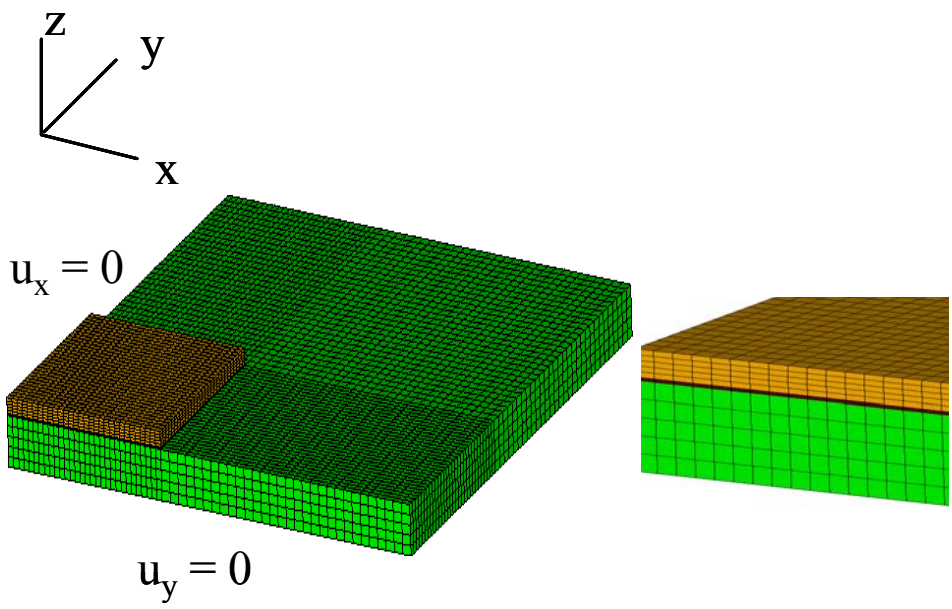

Figure 7.1 Finite Element Mesh for the Quarter Model of
Flip Chip on Laminate Assembly with UF1 Properties

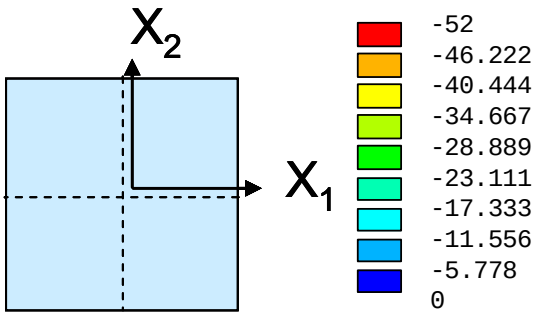

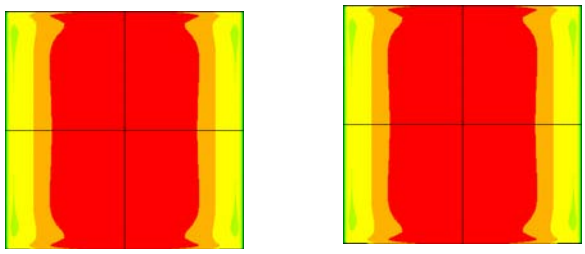

5 mins
Max σ_{11} = -50.459 MPa

10 mins
Max σ_{11} = -50.459 MPa

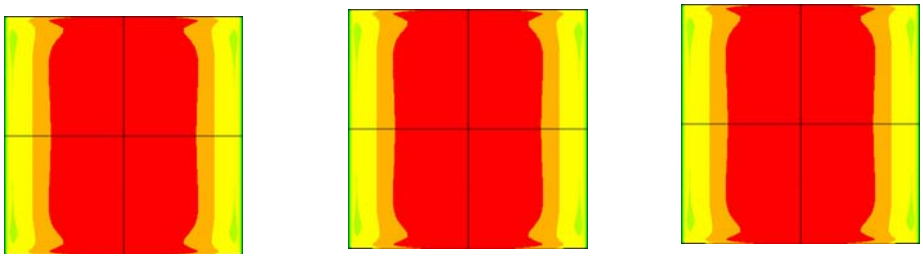

15 mins
Max σ_{11} = -50.459 MPa

20 mins
Max σ_{11} = -50.459 MPa

25 mins
Max σ_{11} = -50.459 MPa

Figure 7.2 FEA Predictions for the Horizontal Normal Stress Distribution in the Silicon Die (Considering Elastic-Plastic Properties for Underfill, UF1)

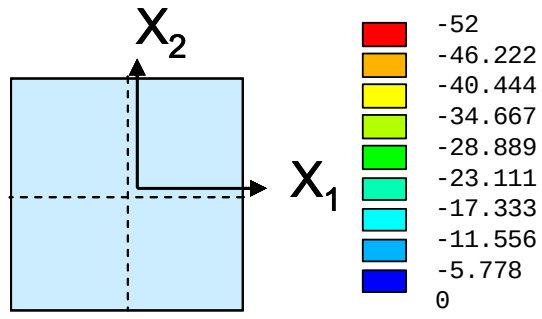

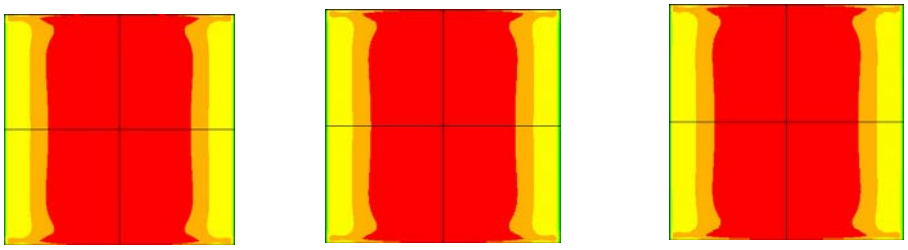

5 mins
Max σ_{11} = -51.167 MPa

10 mins
Max σ_{11} = -51.140 MPa

15 mins
Max σ_{11} = -51.110 MPa

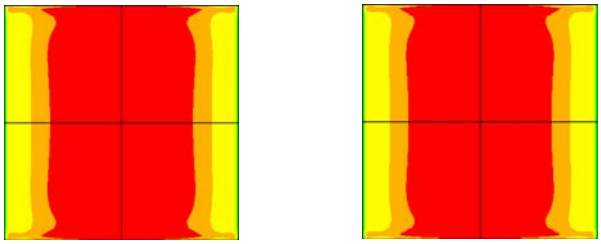

20 mins
Max σ_{11} = -51.083 MPa

25 mins
Max σ_{11} = -51.062MPa

Figure 7.3 FEA Predictions for the Horizontal Normal Stress Distribution in the Silicon Die (Considering Viscoelastic Properties for Underfill, UF1)

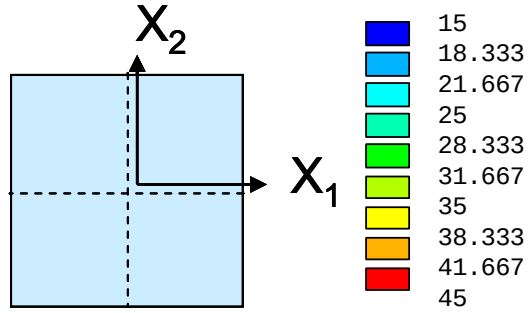

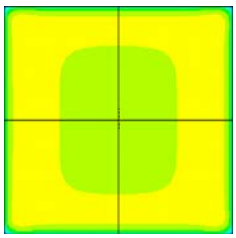

5 mins
Max σ_{11} = 36.752 MPa

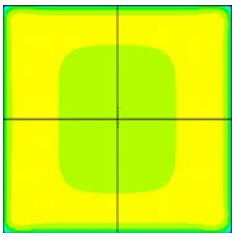

10 mins
Max σ_{11} = 36.752 MPa

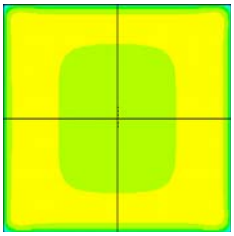

15 mins
Max σ_{11} = 36.752 MPa

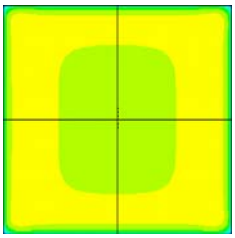

20 mins
Max σ_{11} = 36.752 MPa

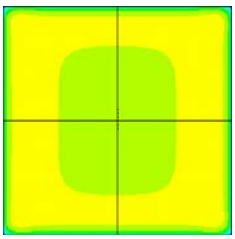

25 mins
Max σ_{11} = 36.752 MPa

Figure 7.4 FEA Predictions for the Horizontal Normal Stress Distribution in Underfill, UF1 (Considering Elastic-Plastic Properties for UF1)

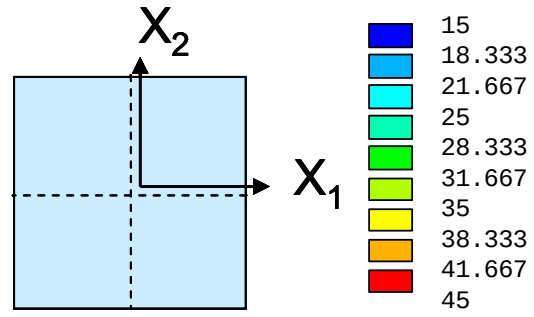

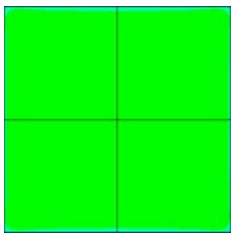

5 mins
Max σ_{11} = 31.139 MPa

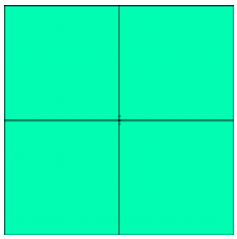

10 mins
Max σ_{11} = 29.123 MPa

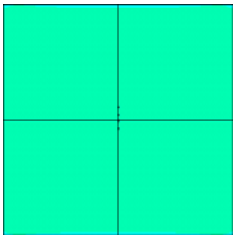

15 mins
Max σ_{11} = 28.108 MPa

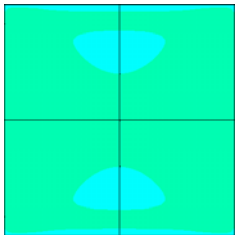

20 mins
Max σ_{11} = 27.43 MPa

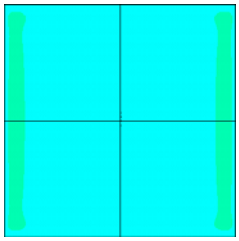

25 mins
Max σ_{11} = 26.863 MPa

Figure 7.5 FEA Predictions for the Horizontal Normal Stress Distribution in Underfill, UF1 (Considering viscoelastic Properties for UF1)

7.3 Simulation Results of UF2

Another quarter model of flip chip on laminate assembly with pitch of 1.25 mm was developed to explore the effect of moisture adsorption in underfill (UF2) layer as shown in Figure 7.6 (a) and 7.6 (b). The assembly was cooled down from 125 C to 25 C. The meshing of the assembly and applied boundary conditions are demonstrated in the same figure. The critical C4 joint was found to be the corner bump (shown in Figure 7.7) based upon the plastic work per volume. The finite element mesh for C4 joints along with copper pad is shown in Figure 7.8. The Anand parameters for SAC305 C4 joints and mechanical properties of the different components of the assembly are tabulated in Table 7.1 and 7.2 respectively.

The observed variations of stress before and after moisture exposure during cooling of the assembly are shown in Figures 7.9 through 7.12 for underfill and the silicon die. Figure 7.9 and 7.10 shows the results of the stress developed in the underfill (UF2) layer. It is seen that the maximum horizontal normal stress decreases after moisture exposure of 60 days which is similar to the tensile tests results where UF2 material properties degraded after moisture adsorption as a result of material softening. Whereas, in silicon die, almost identical magnitudes for the stress distributions are observed before and after moisture adsorption as are shown in Figures 7.11 and 7.12.

Moreover, when a crack is assumed to grow, there is an amount of energy released by the crack growth. So the finite element results of plastic work per volume have been observed to examine the plastic energy dissipated during the cooling. Figure 7.13 and 7.14 illustrates the effect of moisture on the plastic work per volume of solder

joints. As expected, the corner joint shows the maximum value which increased slightly after moisture exposure from a value of 0.193 MJ/m^{3}to 0.226 MJ/m^3.

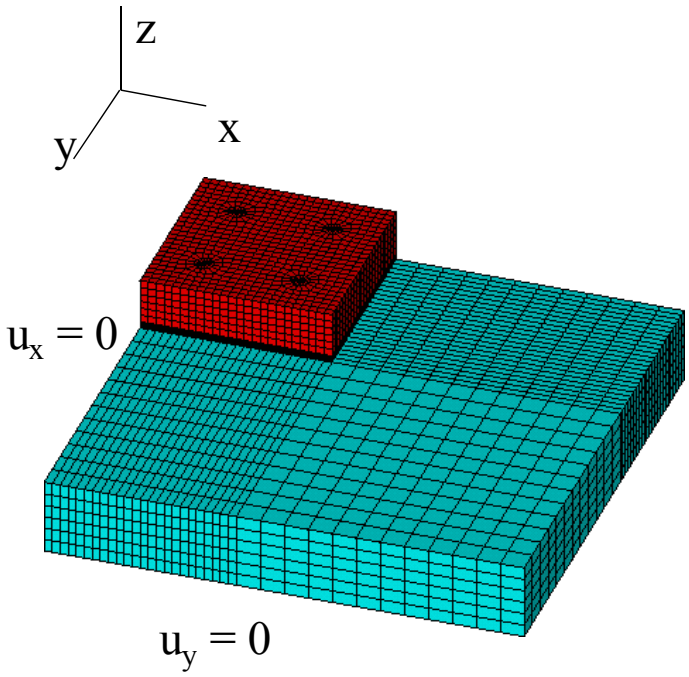

(a)

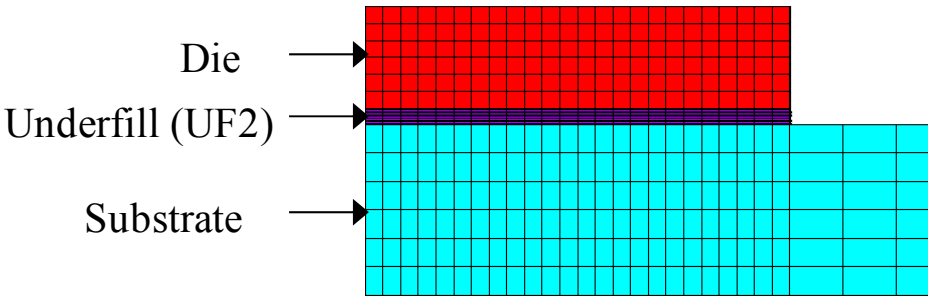

(b)

Figure 7.6 (a) Three Dimensional View and (b) Two Dimensional View of the Finite Element Mesh for the Quarter Model of Flip Chip on Laminate Assembly with UF2 Properties

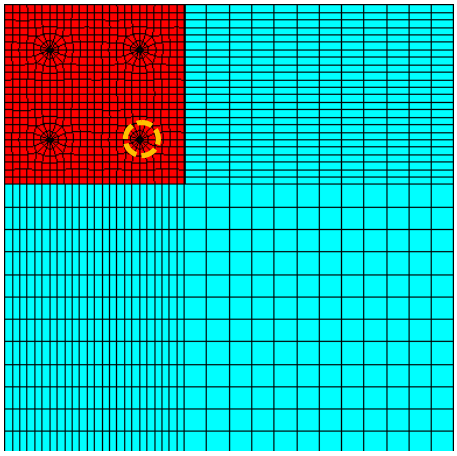

Figure 7.7 Location of Critical C4 Joint

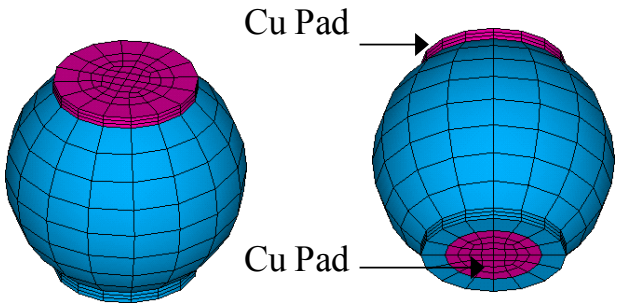

Figure 7.8 Finite Element Mesh for SAC 305 C4 Bumps

Table 7.1Anand Model Coefficients for SAC305

Constant Number	Model Constant	Units	Value for Underfill
1	s_0	MPa	21.0
2	Q/R	K	9320
3	A	sec^{-1}	3501
4	ξ	Dimensionless	4
5	m	Dimensionless	0.25
6	h_0	MPa	18×10^4
7	$\hat{s}$	MPa	30.2
8	n	Dimensionless	0.01
9	a	Dimensionless	1.78

Table 7.2 Material Properties at Room Temperature Used in the Finite Element Analysis

Material	**Elastic Modulus (GPa)**	**Poisson's Ratio**	**CTE (ppm/C)**
Ceramic Substrate [109]	302.3	0.3	6.2
Underfill, UF2	11.957	0.35	35
Die	130.54	0.28	2.6
C4 Joint (SAC305)	45.2	0.36	21.6
Copper	128	0.34	17

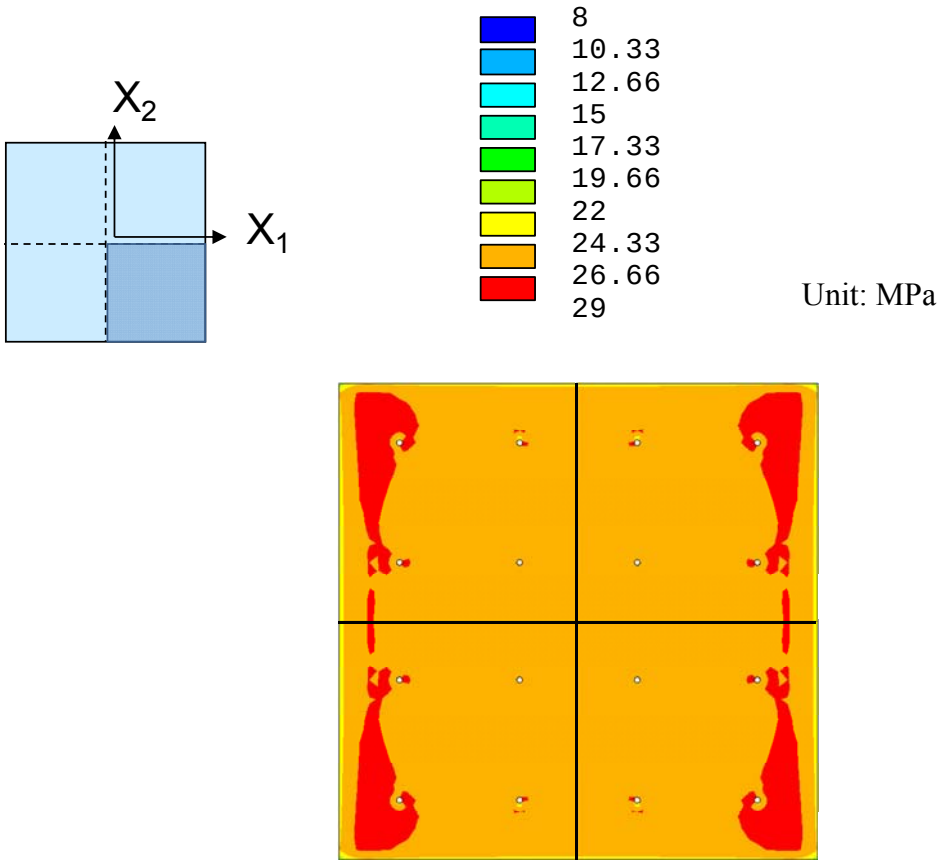

Figure 7.9 FEA Predictions for the Horizontal Normal Stress Distribution in Underfill, UF2 Before Moisture Exposure

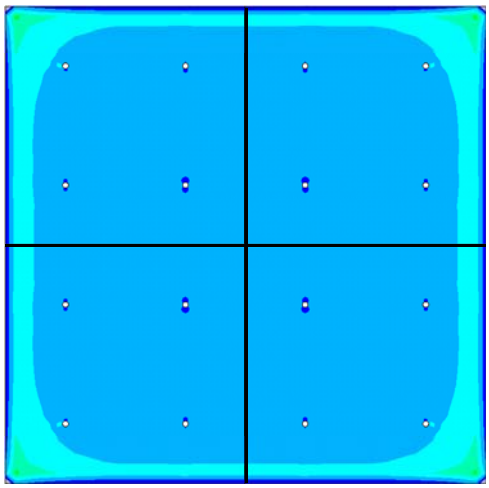

Figure 7.10 FEA Predictions for the Horizontal Normal Stress Distribution in Underfill, UF2 After Moisture Exposure of 60 Days

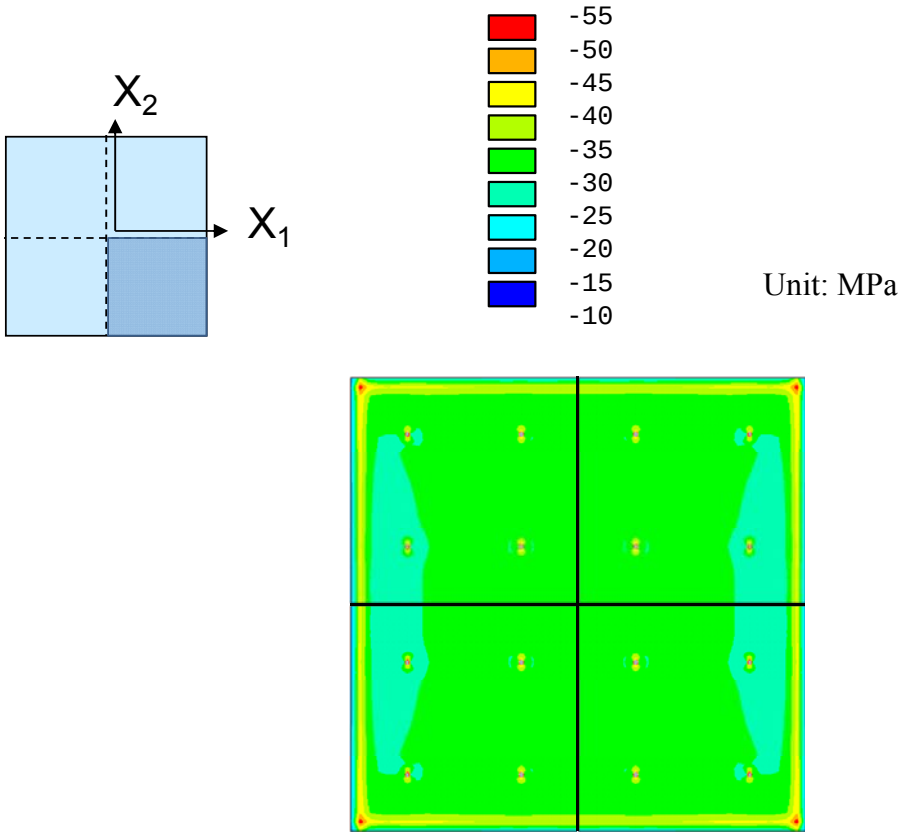

Figure 7.11 FEA Predictions for the Horizontal Normal Stress Distribution in the Silicon Die Before Moisture Exposure

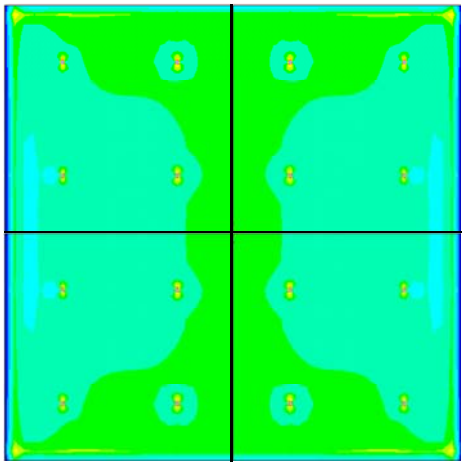

Figure 7.12 FEA Predictions for the Horizontal Normal Stress Distribution in the Silicon Die After Moisture Exposure of 60 Days

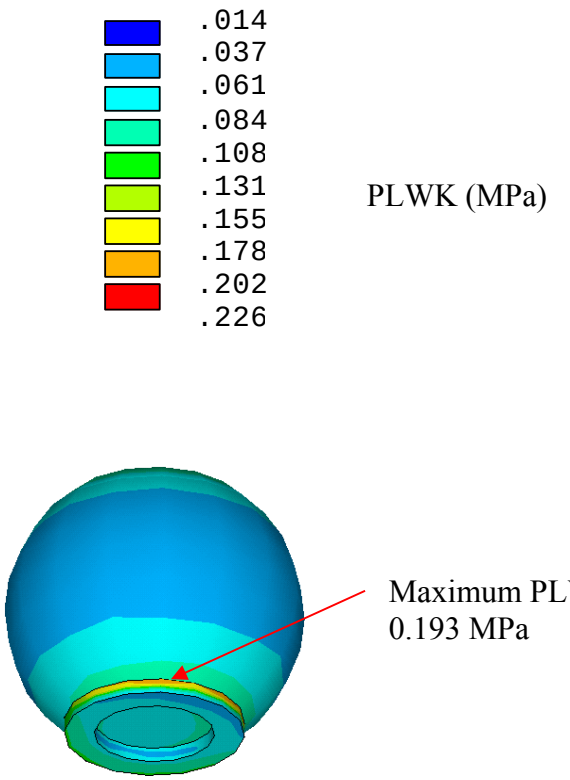

Figure 7.13 FEA Predictions for the Plastic Work per Volume in the Corner C4 Bump Before Moisture Exposure

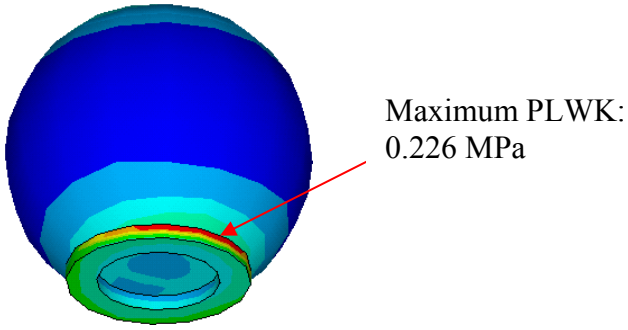

Figure 7.14 FEA Predictions for the Plastic Work per Volume in the Corner C4 Bump After Moisture Exposure of 60 Days

7.4 Summary and Discussion

Finite element analysis has been used to model the stresses in the silicon chip and underfill encapsulant in an underfilled flip chip assembly. In the first model, the underfill (UF1) has been modeled as both an elastic plastic material and as a viscoelastic material (linear viscoelastic). Similar die stresses were found for both analyses. Time dependent variation of the stress in the underfill is seen with the viscoelastic material model, whereas the underfill stress does not change for elastic-plastic material model. For both cases die stress is not seen to be effected by the stress developed in underfill (UF1). The second model was developed to study the effect of moisture adsorption in underfill (UF2) layer. The maximum horizontal normal stress in underfill (UF2) layer is seen to be decreased after moisture exposure whereas die stress is not seen to be effected significantly. The plastic work per volume of C4 joints is seen to increase slightly after moisture exposure.

CHAPTER 8

CONCLUSIONS

8.1 Literature Review

An extensive review has been performed on major topics on microelectronic packaging polymers including effect of fabrication, characterization, moisture effects, and constitutive modeling. The properties of underfill resins and other polymers are characterized to provide inputs for the FE models. In this work, a discussion on the constitutive model to depict the viscoelastic response of such materials under different loadings and thermal conditions has been included. Theoretical background of the model has also been studied considering moisture exposure. Although many constitutive models are available to describe the polymer material tensile properties and creep behaviors, there are no reports of constitutive models that take into account the mechanical behavior of such polymers before and after moisture absorption. In order to improve the reliability of packaging applications, constitutive models that include these parameters are necessary for use in FEA simulations.

8.2 Specimen Preparation and Experimental Setup

A unique specimen preparation procedure has been developed in this study to fabricate micro-scale uniaxial tensile specimens. A set of molds, made from stainless steel and coated with Teflon have been utilized to prepare the specimens. Typical uniaxial samples with nominal dimensions have been utilized.

Uniaxial tensile and creep tests have been performed by using a multifunctional microtester. In this study, the experimental data have been modeled by empirical constitutive laws so that the corresponding mechanical properties of materials can be extracted.

Moreover, DMA and DSC analysis have also been performed to study mechanical behavior of polymer materials. FTIR spectroscopy and microscopic views on fractured surfaces have also been examined to observe the effect of moisture on the mechanical properties of microelectronic packaging polymers.

8.3 Characterization of Underfill Encapsulants

The effects of temperature and strain rate on mechanical behavior have been examined by performing stress-strain and creep tests on two underfill materials, indicated as UF1 and UF2. For both cases, a three parameter hyperbolic tangent empirical model has been used to fit the raw stress-strain data and the log hyperbolic tangent empirical model has been shown to accurately fit raw creep data (strain vs. time).

For UF1, stress-strain behavior curves have been evaluated for T = 0 C to T = 130 C for strain rate of .001 sec^{-1}. Tensile tests have also been performed at different strain rates at T = 25, 50, 75, 100 and 125 C. The glass transition region was observed between 80-100 C. Creep experiments have been performed at T = 25, 50, 75, 100, and 125 C with different stress levels at each temperature. The Generalized Garofalo model has been shown to accurately fit the secondary creep rate data as a function of temperature and stress.

For UF2, stress-strain behavior curves have been evaluated for T = 25, 50, 75, 100, 125 and 150 C for strain rate of .001 sec^{-1}. The glass transition region was observed

after 100 C. Creep experiments have been performed at T = 25, 80, 100, and 125 C with different stress levels at each temperature.

The tensile results show that elastic modulus and ultimate strength have a linear dependence at different temperatures as well as at different strain rates. For creep, higher creep strains are attained with increasing stress level or increased test temperature as expected. As times passes, strain rate decreases gradually.

8.4 Constitutive Modeling for Polymers

In this study, Anand viscoplastic model and Prony Series viscoelastic model have been applied to fit the mechanical response data of underfill. Optimum model constants have been calculated and the correlations of the models to the data have been evaluated. The Anand model predictions were found to match the UF1 experimental stress-strain curves fairly well at low strain levels. However, the model and data deviate significantly at higher stress and strain levels.

The three-dimensional linear viscoelastic model based on prony series response functions has been applied to fit the stress-strain and creep data of both UF1 and UF2. Optimum model coefficients have been calculated, the correlations of the models to the data have been evaluated and excellent correlation has been obtained. The Prony series viscoelastic model has been found to represent both the rate dependent stress-strain curve data well at all temperatures and the creep curve data well at all temperatures and applied stress levels.

The correlations of the Prony Series viscoelastic model predictions using finite element and analytical approach with experimental data also exhibit good agreement. The qualitative agreement of the results implies the validity of the analytical approach.

8.5 Effect of Moisture Exposure on Mechanical Properties of Microelectronic Packaging Polymers

The effects of moisture exposure on the mechanical behavior of microelectronic packaging polymers have been studied. In each case, the uniaxial test specimens were exposed in an adjustable thermal and humidity chamber to combined hygrothermal exposures for various durations. After moisture preconditioning, a microscale tension-torsion testing machine was used to evaluate the complete stress-strain behavior of the materials at several temperatures. It was found that moisture exposure caused plasticization and strongly reduced the mechanical properties of the materials. Reversibility tests were also conducted to evaluate whether the degradations in the mechanical properties were recoverable.

In this study, three different microelectronic packaging polymers have been considered to study the effect of moisture on the mechanical properties:

a. Polymer Encpsulant

b. Polycarbonate

c. Flip Chip Underfill (denoted as UF2)

The uniaxial test specimens of polymer encapsulant were exposed at 85 C and 85% RH for various durations up to 10 days. It was found that moisture exposure reduced the mechanical properties of the encapsulant including the initial elastic modulus and ultimate tensile stress. After reversibility tests, a 25% permanent reduction in the elastic modulus was observed due to hydrolysis, where water molecules had chemically modified the organic structure of the material. This was verified by observations of permanent changes in the FTIR spectra of the material.

The polycarbonate uniaxial test specimens were exposed to combined hygrothermal exposures of 60 C and 90% RH, 60 C and 50% RH, and 40 C and 50% RH for various durations (0, 3, and 10 days). Then complete stress-strain behavior of the material was evaluated at several temperatures (T = 20, 40, 60 C). It was found that moisture exposure strongly reduced the strain to failure of the polycarbonate, with larger reductions occurring with the more severe moisture exposures. However, no changes occurred in the initial elastic modulus and ultimate stress due to moisture exposure. Reversibility tests were also conducted. Upon redrying, the polymer was found to recover most of its original mechanical properties. Moreover, the polycarbonate sample fracture surfaces were observed by optical microscopy. The microscopic features of the moisture exposed samples contained fragments and cavities, whereas no fragments were observed on the surface of the non-exposed samples.

The underfill (UF2) specimens were exposed at 85 C and 85% RH for various durations up to 60 days. It was evident that moisture exposure caused plasticization and strongly reduced the mechanical properties of the underfill including the initial elastic modulus and ultimate tensile stress. The Prony series viscoelastic model was then utilized to predict the stress-strain behavior of the tested underfill and again excellent correlation was achieved in case of moisture exposed samples. A set of constants has been found for the tested underfill that can be used to accurately represent mechanical behavior of the material before and after moisture absorption by including the effects of moisture exposure on the glass-transition temperature in the WLF equation. Since underfills are epoxy based, the modified model for including the moisture effect has the

potential to be applied for modeling moisture absorption behavior of other microelectronic packaging polymers such as molding compounds and adhesives.

8.6 Finite Element Modeling

The effects of viscoelastic properties of underfiil (UF1) on the mechanical responses of die in a simplified flip chip assembly have been studied and the results have been compared with those obtained for elastic-plastic underfill. For both cases die stress has not been seen to be effected by the stress developed in underfill. Time dependent variation of the stress in the underfill is seen with the viscoelastic material model, whereas the underfill stress does not change for elastic-plastic material model. The second model was developed to study the effect of moisture adsorption in underfill (UF2) layer. The maximum horizontal normal stress in underfill (UF2) layer is seen to be decreased after moisture exposure whereas die stress is not seen to be effected significantly. The plastic work per volume of C4 joints is seen to increase slightly after moisture exposure.

REFERENCE

[1] http://www.gslb.cleanrooms.com/ElectroIQ/en-us/index/display/Semiconductor_Article_Tools_Template._printArticle.articles.advanced-packaging.volume-15.issue-5.features.the-back-end-process.underfill-technology.html

[2] Gwinn, J. P., and Webb, R. L., "Performance and Testing of Thermal Interface Materials", Microelectronics Journal, Issue 34, pp. 201-210, 2003.

[3] Early, M., Lee, S., and Pellilo, M., "Thermal Performance of Interface Material in Microelectronics Packaging Applications," Proceedings of the IEPS Conference, pp. 534-544, 1995.

[4] Shu, H., "Enhanced Polymer Passivation Layer for Wafer Level Chip Scale Package," Ph.D. Dissertation, Department of Electrical & Computer Engineering, Auburn University, 2012.

[5] Fritz, N. T., "Materials, Design and Processing of Air Encapsulated MEMS Packaging," Ph.D. Dissertation, Department of Chemical & Biomolecular Engineering, Georgia Institute of Technology, 2012.

[6] Benson, R. C., Farrar, D., and Miragliotta J. A., "Polymer Adhesives and Encapsulants for Microelectronic Applications", Johns Hopkins APL Technical Digest, Vol. 28(1), pp. 58-71, 2008.

[7] Scheirs, J., Compositional and Failure Analysis of Polymers: A Practical Approach, Wiley, 2000.

[8] Characterization and Failure Analysis of Plastics, ASM, 2003.

[9] http://www.sjsu.edu/faculty/selvaduray/page/mate234/Packaging%20Materials%20Issues.pdf

[10] Vincent, J., Structural Biomaterials, Third Edition, Princeton University Press, pp. 1-28, 2012.

[11] Sadeghinia, M., "Failure and Delamination in Microelectronic Packages", M.Sc. Thesis, Department of Mechanical Engineering, Khaje Nasir Toosi University of Technology, Iran, 2013.

[12] Feustal, F., Wiese, S., and Meusal, E., "Time Dependent Material Modeling for Finite Element Analyses of Flip Chips", Proceedings of the 50th Electronic

Components and Technology Conference (ECTC), pp. 1548-1553, Las Vegas, NV, May 21-24, 2000.

[13] Qian, Z., Wang, J., Yang, J., and Liu, S., "Visco-Elastic-Plastic Properties and Constitutive Modeling of Underfills," IEEE Transactions on Components and Packaging Technologies, Vol. 22(2), pp. 152-157, 1999.

[14] Rao, Y., Shi, S. H., and Wong, C. P., "Improved Methodology for Determining Temperature Dependent Moduli of Underfill Encapsulants," IEEE Transactions on Components and Packaging Technologies, Vol. 23(3), pp. 434-439, 2000.

[15] Shi, X. Q., Wang, Z. P., Pang, H. L. J., and Zhang, X. R., "Investigation of Effect of Temperature and Strain Rate on Mechanical Properties of Underfill Material by Use of Microtensile Specimens," Polymer Testing, Vol. 21, pp. 725-733, 2002.

[16] Islam, M. S., Suhling, J. C., Lall, P., Xu, B., and Johnson, R. W., "Measurement and Modeling of the Temperature Dependent Material Behavior of Underfill Encapsulants," Proceedings of the 53rd Electronic Components and Technology Conference (ECTC), pp. 1636-1643, New Orleans, LA, May 27-30, 2003.

[17] Islam, M. S., Suhling. J. C., and Lall, P., "Measurement of the Temperature Dependent Constitutive Behavior of Underfill Encapsulants," IEEE Transactions on Components and Packaging Technologies, Vol. 28(3), pp. 467-476, 2005.

[18] Lall, P., Islam, S., Tian, G., and Suhling, J. C., "Nano-Underfills for High-Reliability Applications in Extreme Environments," IEEE Transactions on Components and Packaging Technologies, Vol. 31(1), pp. 114-125, 2008.

[19] Kuo, C. T., Yip, M. C., and Chiang, K. N., "Time and Temperature-Dependent Mechanical Behavior of Underfill Materials in Electronic Packaging Application," Microelectronic Reliability, Vol. 44, pp. 627-638, 2004.

[20] Wun, B., and Lau, J., "Characterization and Evaluation of the Underfill Encapsulants for Flip Chip Assembly", IEEE/CPMT Int'l Electronics Manufacturing Technology Symposium, pp. 139-146, 1994.

[21] Sham, M., Kim, J., "Experiment and Numerical Analysis of the Residual Stresses in Underfill Resins for Flip Chip Package Applications", Journal of Electronic Packaging, Vol. 127, pp. 47-51, 2005.

[22] Gilleo, K., Witt, M., Blumel, D., and Ongley, P., "Towards a better understanding of underfill encapsulation for flip chip technology: proposed developments for the future", Microelectronics International, Vol. 16(2), pp. 39 – 43, 1999.

[23] Calcagno, B., Lakes, R., Osswald, T., and Crone, W., "Comparison of Viscoplastic Properties for Polycarbonate, Polypropylene and High Density Polyethylene" Journal of Plastics Technology, Vol. 6(5), pp. 228-254, 2010.

[24] Boyce, M. C., Parks, D. M., and Argon, A. S., "Large Inelastic Deformation of Glassy Polymers: Part I: Rate Dependant Constitutive Model", Mechanics of Materials, Vol. 7(1), pp. 15-33, 1988.

[25] Boyce, M. C., "Large Inelastic Deformation of Glassy Polymers", Ph.D. Dissertation, Department of Mechanical Engineering, Massachusetts Institute of Technology, 1986.

[26] Stachurski, Z. H., "Deformation Mechanisms and Yield Strength in Amorphous Polymers", Progress in Polymer Science, Vol. 22(3), pp. 407-474, 1997.

[27] G'Sell, C., "Strength of Metals and Alloys, ed. McQueen, H. J., Bailon, J. P., Dickson J. I., and Jonas, J. J., ICSMA, pp. 1943, 1985.

[28] Lobo, H., and Croop, B., "A Robust Methodology to Calibrate Crash Material Models for Polymers", NAFEMS World Congress Crete, Greece, pp. 1-14, 2009.

[29] Feng, J., Hao, J., Du, J., and Yang, R., "Effects of Organoclay Modifiers on the Flammability, Thermal and Mechanical Properties of Polycarbonate Nanocomposites Filled With a Phosphate and Organoclays", Polymer Degradation and Stability, Vol. 97, pp. 108-117, 2012.

[30] Pérez, J. M., Vilas, J. L., Laza, J. M., Arnáiz, S., Mijangos, F., Bilbao, E., Rodríguez, M., and León, L. M., "Effect of Reprocessing and Accelerated Ageing on Thermal and Mechanical Polycarbonate Properties", Journal of Materials Processing Technology, Vol. 210, pp.727–733, 2010.

[31] Ronkay, F., "Effect of Recycling on the Rheological, Mechanical and Optical Properties of Polycarbonate", Acta Polytechnica Hungarica, Vol. 10 (1), pp. 209-220, 2013.

[32] Lin, J.,Teng, A., and Yuen, M. M. F., "A Fast, Low Cost Method to Check for Moisture in Epoxy Molding Compound," Proceedings of the Electronics Packaging Technology Conference, pp. 359–361, 1998.

[33] Ferguson, T., and Qu, J., "Effect of Moisture on the Interfacial Adhesion of the Underfill/Solder Mask Interface," Journal of Electronic Packaging, Vol. 124, pp. 106-110, June 2002.

[34] Fan, X., Bang, G. Q., Van Driel, W., and Ernst, L. J., " Analytical Solution for Moisture-Induced Interface Delamination in Electronic Packaging," Proceedings of the IEEE Electronic Components and Technology Conference, pp.733-738, 2000.

[35] Fan, X. J., and Lim, T. B., "Mechanism Analysis for Moisture-Induced Failure in IC Packages", Proceedings of the ASME International Mechanical Engineering Congress & Exposition, 11th Symposium on Mechanics of Surface Mount Assemblies, IMECE/EPE-14, pp. 1-12, 1999.

[36] Ferguson, T. P., and Qu, J., "Moisture and Temperature Effects on the Reliability of Interfacial Adhesion of a Polymer/Metal Interface," Proceedings of the 54th Electronic Components and Technology Conference, pp. 1752 - 1758, Las Vegas, NV, June 1-4, 2004.

[37] Ferguson, T. P., and Qu, J., "Elastic Modulus Variation Due to Moisture Adsorption and Permanent Changes Upon Redrying in an Epoxy Based Underfill," IEEE Transactions on Components and Packaging Technologies, Vol. 29(1), pp. 105-111, 2006.

[38] Ferguson, T. P., "Moisture and Interfacial Adhesion in Microelectronic Assemblies," Ph.D. Dissertation, Department of Mechanical Engineering, Georgia Institute of Technology, 2004.

[39] Luo, S., and Wong, C. P., "Influence of Temperature and Humidity on Adhesion of Underfills for Flip Chip Packaging," IEEE Transactions on Components and Packaging Technologies, Vol. 28(1), pp. 88-94, 2005.

[40] Zhang, Y. L., Shi, X. Q., and Zhou, W., "Effect of Hygrothermal Aging on Interfacial Reliability of Flip Chip on Board (FCOB) Assembly," Proceedings of the 6th Electronics Packaging Technology Conference, pp. 404 - 409, 2004.

[41] Lu, M. G., Shim, M. J., and Kim, S. W., "Effects of Moisture on Properties of Epoxy Molding Compounds," Journal of Applied Polymer Science, Vol. 81, pp. 2253-2259, 2001.

[42] Park, C. E., Han, B. J., and Bair, H. E., "Humidity Effects on Adhesion Strength between Solder Ball and Epoxy Underfills," Polymer, Vol. 38(15), pp. 3811-3818, 1997.

[43] Tian, G., Lin, C., Suhling, J. C., Johnson, R. W., Lall, P., and Ghosh, K., "The Effects of Cure Profile Upon the Properties and Thermo-Mechanical Reliability of Flip Chip Underfills," Proceedings of the 2006 SMTA International, pp. 515-523, Chicago, IL, September 24-28, 2006.

[44] Lin, C., Suhling, J. C., and Lall, P., "Physical Aging and Evolving Mechanical Behavior of Underfill Encapsulants," Proceedings of 10th IEEE Intersociety Conference on Thermal and Thermomechanical Phenomena in Electronic Systems (ITherm 2008), pp. 695-704, Orlando, FL, May 28-31, 2008.

[45] Lin, C., Suhling, J. C., and Lall, P., "Isothermal Aging Induced Evolution of the Material Behavior of Underfill Encapsulants," Proceedings of the 59th IEEE Electronic Components and Technology Conference (ECTC), pp. 134-149, San Diego, CA, May 27-29, 2009.

[46] Lin C., Chhanda N. J., Suhling J. C., and Lall P., "The Influence of Aging on the Creep Behavior of Underfill Encapsulants," Proceedings of the ITherm 2010, pp. 1-11, Las Vegas, NV, June 2-5, 2010.

[47] Chhanda, N. J., Suhling, J. C., and Lall, P., "Effects of moisture exposure on the mechanical behavior of Polymer encapsulants in microelectronic packaging" Proceedings of the ASME 2013 International Technical Conference and Exhibition on Packaging and Integration of Electronic and Photonic Microsystems, InterPACK, Burlingame, CA, USA, July 16-18, 2013.

[48] Long, T. S. and Sokol, R. J., "Molding Polycarbonate: Moisture Degradation Effect on Physical and Chemical Properties", Polymer Engineering and Science, Vol. 14 (12), pp. 817-822, 1974.

[49] Weibin, G, Shimin, H., Minjiao, Y., Long, J., and Yi, D., "The effects of hydrothermal aging on properties and structure of bisphenol A polycarbonate", Polymer Degradation and Stability, Vol. 94, pp. 13-17, 2009.

[50] Cao, B., and Campbell, G. A., "Viscoplastic-Elastic Modeling of Tubular Blown Film Processing.",AIChE journal, Vol. 36(3), pp. 420-430, 1990.

[51] Zhang, C. Y., Zhang, Y. W., Zeng, K. Y., and Shen, L., "Nanoindentation of Polymers with a Sharp Indenter", Journal of Materials Research, Vol. 20(06), pp. 1597-1605, 2005.

[52] Dupaix, R. B., and Boyce, M. C., "Constitutive Modeling of the Finite Strain Behavior of Amorphous Polymers in and Above the Glass Transition", Mechanics of Materials, Vol. 39, pp. 39–52, 2007.

[53] Amagai, M., "Characterization of Chip Scale Packaging Materials", Microelectronics Reliability, Vol. 39, pp. 1365-1377, 1999.

[54] Drozdov, A. D., "Finite Viscoelasticity and Viscoplasticity of Semicrystalline Polymers", Continuum Mechanics and Thermodynamics, Vol. 19(1-2), pp. 111-132, 2007.

[55] Qian Z., Lu M. and Liu S., "Constitutive Modeling of Polymer Films from Viscoelasticity to Viscoplasticity," ASME Transactions, Journal of Electronic Packaging, Vol. 120, pp.145-149, 1998.

[56] Kermouche, G., Aleksy, N., and Bergheau, J. M., "Viscoelastic-Viscoplastic Modelling of the Scratch Response of PMMA", Advances in Materials Science and Engineering, pp. 1-10, 2013.

[57] Woishnis, W.A., and Wright D.C., "Select Plastics to Avoid Product Failure", Adv Mater Processes, Vol. 146(6), pp. 39–40, 1994.

[58] Majda, P., and Skrodzewicz, J., "A modified creep model of epoxy adhesive at ambient temperature", International Journal of Adhesion & Adhesives, Vol. 29, pp. 396–404, 2009.

[59] Qian, Z., Wang, J., Yang, J., and Liu, S., "Visco-Elastic-Plastic Properties and Constitutive Modeling of Underfills", IEEE Transactions on Components and Packaging Technology, Vol. 22 (2), pp. 152-157, June 1999.

[60] Qu, J., and Wong C. P., "Effective Elastic Modulus of Underfill Material for Flip-Chip Applications", IEEE Transactions on Components and Packaging Technologies, Vol. 25(1), pp. 53-55, 2002.

[61] Wang, H., Qian, Z., Lu, M., Liu, S., Wu, J., and Wong, C. P., "Study on Rate-dependent Behaviors of Underfills Based on Two-phase Composites", Eleclronic Components and Technology Conlerence, pp. 348-352, 2000.

[62] Yang, D. G., Zhang, G. Q., Ernst, L. J., Caers, J. F. J., Bressers, H. J. L., and Janssen, J., " Combined Experimental and Numerical Investigation on Flip Chip Solder Fatigue with Cure-Dependent Underfill Properties", Proceedings of Electronic Components and Technology Conference, IEEE, pp. 919-924, 2001.

[63] Kiasat, M. S., Nijhof, A.H.J., Blokland, H. and Marissen, R., "Shrinkage and Stress Build up in Unsaturated Polyester Resin during Curing," Polymers and Ceramics, vol. 2, pp. 95-102, 1997.

[64] Kiasat, M.S., "Curing shrinkage and residual stress in viscoelastic thermosetting resins and composites," Ph.D. dissertation, Delft University of Technology, Delft, 2000.

[65] Ernst, L.J., Hof, C. van 't , Yang, D.G., Kiasat, M.S., Zhang, G.Q., Bressers, H.J.L., Caers, J.F.J., Boer, A.W.J. den, Janssen, J., "Mechanical characterisation and simulation of curing packaging polymers," MicroMat 2000, Berlin, April 2000.

[66] Hof, C. van 't, Yang, D.G., Kiasat, M.S., Ernst, L.J., Zhang, G.Q., Bressers, H..JL., Caers, J.FJ., Boer, A.W.J. den, Janssen, J., "Thermo-Mechanical Characterization of Packaging Polymers during the Curing Process," Poly'99, Paris, December 1999.

[67] Ernst, L.J., Hof, C. van 't, Yang, D.G., Kiasat, M.S., Zhang, G.Q., Bressers, H.J.L., Caers, J.F.J., Boer, A.W.J. den, Janssen, J., "Determination of visco-elastic properties during the curing process of encapsulate materials," 50th ECTC, Las Vegas, May 2000.

[68] Yang, D.G., Ernst, L.J., Hof, C van 't, Kiasat, M.S., Bisschop, J., Janssen, J., Kuper, F., Liang, Z.N., Schravendeel, R., Zhang G.Q., "Vertical die crack stresses of Flip Chip induced in major package assembly processes," Microelectronics Reliability, vol.40, pp. 1533- 1538, 2000.

[69] Thompson, J., Groothuis, S., Tang, H., Suny, B., and Koeneman, P., "Transient Behavior of a Polymer Fill Material with Time Dependent Viscoelastic Properties".
(http://www.ansys.com/Resource+Library/Conference+Papers/Transient+Behavior+of+a+Polymer+Fill+Material+with+Time+Dependent+Viscoelastic+Properties)

[70] Ma, X., Jansen, K. M. B., and Ernst, L. J., "Moisture Effects on the Creep of Thermosetting IC Packaging Polymers," Proceedings of the 7th Int. Conf. on Thermal, Mechanical and Multiphysics Simulation and Experiments in Microelectronics and Micro-Systems, EuroSimE, pp. 1-5, Como, Italy, April 24 - 26, 2006.

[71] Ma, X., Jansen, K. M. B., Zhang, G. Q., and Ernst, L. J., "Filler Contents Effects on the Moisture Absorption and Viscoelasticity of Thermosetting IC Packaging Polymers," Proceedings of the 7th International Conference on Electronics Packaging Technology, pp. 1-5, Shanghai, China, August 26-29, 2006.

[72] Popelar, C. F., and Liechti, K. M., "Multiaxial Nonlinear Viscoelastic Characterization and Modeling of a Structural Adhesive," Journal of Engineering Materials and Technology, Vol. 119, pp. 205-210, July 1997.

[73] Nitta, K., and Yamaguchi, M., "A constitutive equation for nonlinear stress-strain curves of crystalline polymers," Journal of Materials Science, Vol. 33, pp. 1015-1021, 1998.

[74] Chen, L., Zhang, Q., Wang, G., Xie, X., and Cheng, Z., "The Effects of Underfill and Its Material Models on Thermomechanical Behaviors of a Flip Chip Package," IEEE Transactions on Advanced Packaging, Vol. 24(1), pp. 17-24, February 2001.

[75] Sham, M., Kim, J., and Park, J., "Numerical Analysis of Plastic Encapsulated Electronic Package Reliability: Viscoelastic Properties of Underfill Resin," Computational Materials Science, Vol. 40, pp. 81-89, 2007.

[76] Chae, S., Zhao, J., Edwards, D. R., and Ho, P., "Characterization of the Viscoelasticity of Molding Compounds in the Time Domain," Journal of Electronic Materials, Vol. 39(4), pp. 419-425, 2010.

[77] Chhanda, N. J., Suhling, J. C., and Lall, P., "Implementation of A Viscoelastic Model for the Temperature Dependent Material Behavior of Underfill Encapsulants," Proceedings of ITherm 2012, pp. 269-281, May 30 - June 1, 2012.

[78] Chhanda, N. J., Suhling, J. C., and Lall, P., "Effects of Moisture Exposure on the Mechanical Behavior of Flip Chip Underfills in Microelectronic Packaging," Proceedings of ITHERM 2014, pp. 333-345, May 27 – May 30, 2014.

[79] Garofalo, F., "An Empirical Relation Defining the Stress Dependence of Minimum Creep Rate in Metals", Transactions of the Metallurgical Society of AIME, Vol. 227, pp. 351-356, April 1963.

[80] http://www.pslc.ws/mactest/dsc.htm

[81] Chew, S., and Lim, E., "Monitoring glass transition of epoxy encapsulant using thermal analysis techniques", Proceedings of ICSE'96. 1996 IEEE International Conference on Semiconductor Electronics, pp. 266-271, 1996.

[82] Paroli , R. M., and Penn, J. J., "Measuring the Glass-Transition Temperature of EPDM Roofing Materials: Comparison of DMA, TMA and DSC Techniques", Assignment of the Glass Transition, ASTM STP 1249, Seyler, R. J., Ed., American Society for Testing and Materials, Philadelphia, pp. 269-276, 1994.

[83] Sichina, W. J., "Measurement of T_g by DSC", Thermal Analysis: Application Note, 2000.

[84] Sichina, W. J., "Characterization of Epoxy Resins Using DSC", Thermal Analysis: Application Note, 2000.

[85] Sichina, W. J., "Characterization of Electronic Materials Using Thermal Analysis", Thermal Analysis: Application Note, 2000.

[86] Sichina, W. J., "Characterization of Polymers by TMA", Thermal Analysis: Application Note, 2000.

[87] http://www.tainstruments.co.jp/application/pdf/Thermal_Library/Thermal_Solutions/TS054.PDF

[88] http://www.tainstruments.co.jp/application/pdf/Thermal_Library/Thermal_Solutions/TS066.PDF

[89] http://www.uzaktanegitimplatformu.com/UEP/uep_ylisans/ey2/ey2_download/DSC%20Thermal2.pdf

[90] Sherman Hsu, C.-P., "Infrared Spectroscopy", Handbook of Instrumental Techniques for Analytical Chemistry, Settle, F. A., Ed., Prentice-Hall, Inc., New Jersey, pp. 247-283, 1997.

[91] González-González, M., Cabanelas, J. C., and Baselga, J., "Applications of FTIR on Epoxy Resins-Identification, Monitoring the Curing Process, Phase Separation and Water Uptake", Infrared Spectroscopy - Materials Science, Engineering and Technology, Theophanides, T., Ed., InTech, pp. 261-284, 2012.

[92] Lau, J. H., Flip Chip Technologies, New York, McGraw-Hill, 1996.

[93] Skrzypek, J. J., and Hetnarski, R. B., Plasticty and Creep - Theory, Examples and Problems, CRC Press, 1993.

[94] Anand, L., "Constitutive Equations for the Rate Dependent Deformation of Metals at Elevated Temperatures," Journal of Engineering Materials and Technology, Transactions of the ASME, Vol. 104 (1), pp. 12-17, 1982.

[95] Anand, L., "Constitutive Equations for Hot-Working of Metals," International Journal of Plasticity, Vol. 1, pp. 213-231, 1985.

[96] Brown, S. B., Kim, K. H., and Anand, L., "An Internal Variable Constitutive Model for Hot-Working of Metals," International Journal of Plasticity, Vol. 5, pp. 95-130, 1989.

[97] Chang, R. W., and McCluskey, F. P., "Constitutive Relations of Indium in Extreme-Temperature Electronic Packaging Based on Anand Model", Journal of Electronic Materials, Vol. 38 (9), pp. 1855-1859, 2009.

[98] Wang, G. Z., Cheng, Z. N., Becker, K., and Wilde, J., "Applying Anand Model to Represent the Viscoplastic Deformation Behavior of Solder Alloys", Journal of Electronic Packaging, Vol. 123, pp. 247-253, 2001.

[99] Qiang, W., Lihua, L., Xuefan, C., Xiaohong, W., Liu, Y., Irving, S., and Luk, T.,"Experimental Determination and Modification of Anand Model Constants for Pb-Free Material 95.5Sn4.0Ag0.5Cu", Proceedings of International Conference on the Thermal, Mechanical and Multi-Physics Simulation Experiments in Microelectronics and Micro-Systems, 2007 (EuroSime 2007), pp.1-9, 2007.

[100] Brinson, H. F., and Brinson, L. C., Polymer Engineering Science and Viscoelasticity, Springer, 2008.

[101] Christensen, R. M., Theory of Viscoelasticity, 2nd Edition, Academic Press, 1982.

[102] Chen, T., "Determining a Prony Series for a Viscoelastic Material from Time Varying Strain Data", NASA/TM-2000-210123, ARL-TR-2206, pp. 1-21, 2000.

[103] ANSYS Theory Reference Release 12.1, Chapter 4. Structures with Material Nonlinearities, 4.10 Viscoelasticity.

[104] Scherer, G. W., Relaxation in glass and composites, John-Wiley & Sons. New York. 1986.

[105] Mottahedi, M., Dadalau, A., Hafla, A., and Verl, A., "Numerical Analysis of Relaxation Test Based on Prony Series Material Model," Integrated Systems, Design and Technology 2010, pp. 79-91, Springer, 2011.

[106] Nunez, L., Villanueva, M., Fraga, F., and Nunez, M. R., "Influence of Water Adsorption on the Mechanical Properties of a DGEBA (*n* = 0)/1, 2 DCH Epoxy System," Journal of Applied Polymer Science, Vol. 74, 353-358, 1999.

[107] Dynamic Mechanical Analysis (DMA), A Beginner's Guide http://www.mse.iastate.edu/files/2013/11/DMA-technique-pamphlet-PerkinElmer.pdf.

[108] "Glass Transition and Modulus of Materials Used in High Density Interconnection (HDI) and Microvias -DMA Method" Test Method Manual, IPC-TM-650.

[109] Elshabini, A., Wang, G., and Amey, D., "Overview of Ceramic Interconnect Technology" Ceramic Interconnect Technology Handbook, Barlow, F. D., and Elshabini, A., Eds., CRC Press, Boca Raton, Florida, USA, pp. 8-9, 2007.

APPENDIX A

EFFECTS OF MOISTURE ON POLYCARBONATE

A.1 Baseline Data with No Environmental Exposure (T = 20 C)

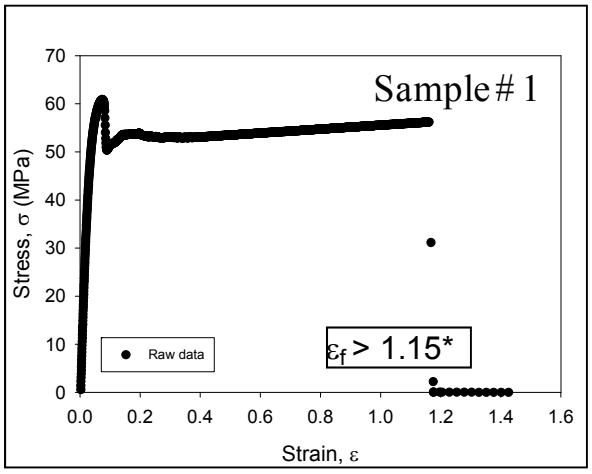

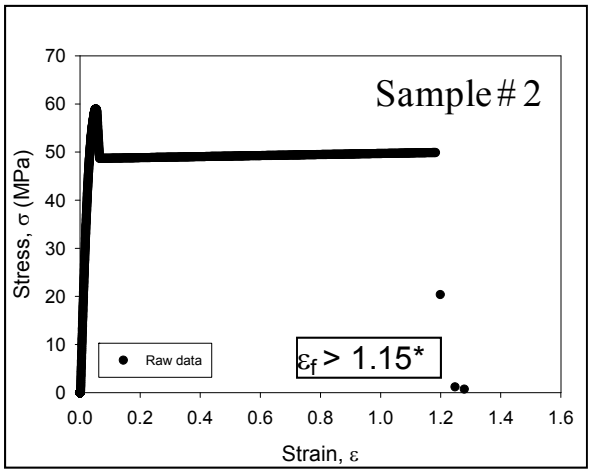

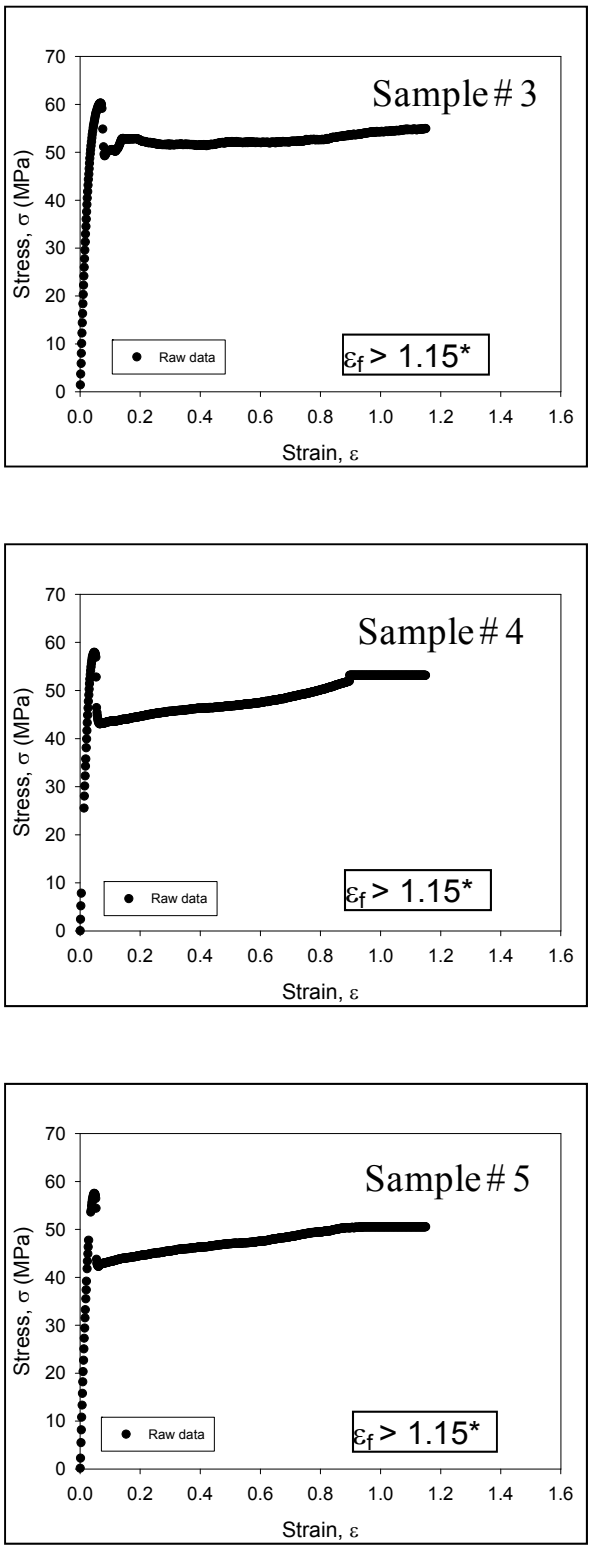

Figure A.1 Raw Data of Stress-Strain Curves for Polycarbonate at T = 20 C

A.2 Baseline Data with No Environmental Exposure (T = 40 C)

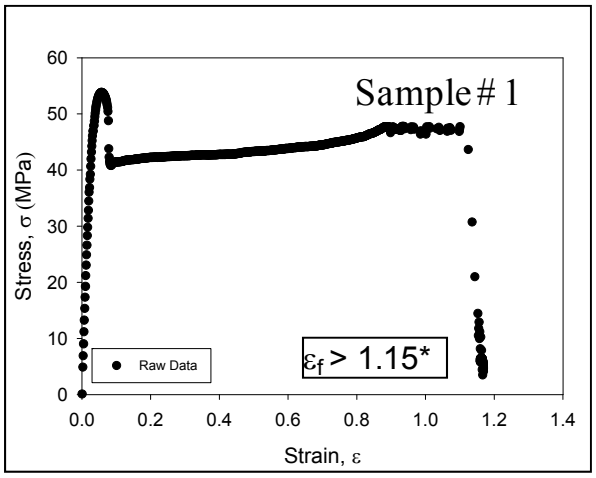

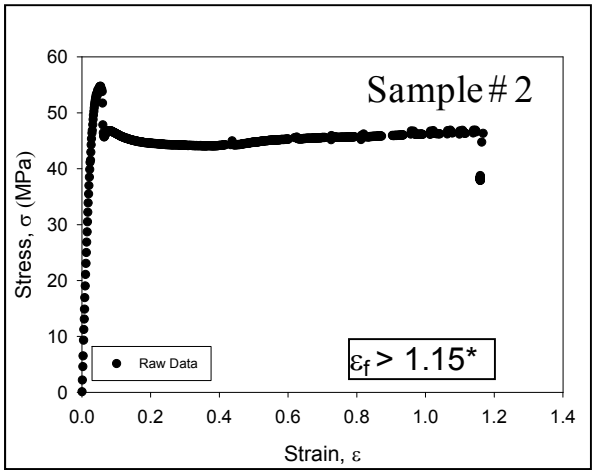

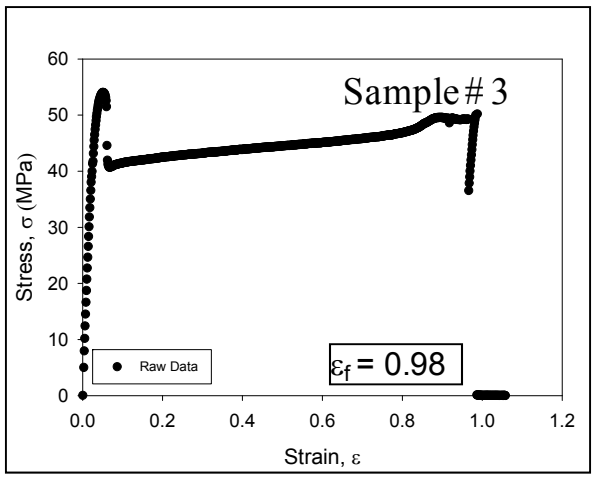

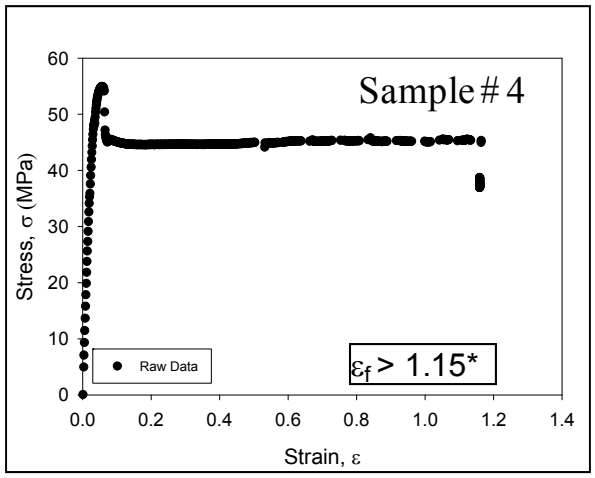

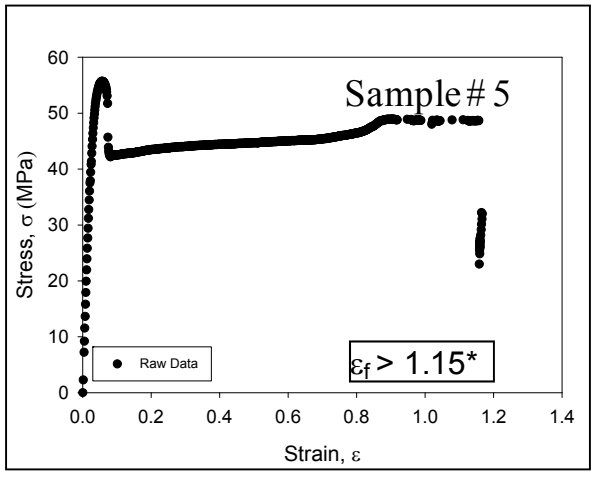

Figure A.2 Raw Data of Stress-Strain Curves for Polycarbonate at T = 40 C

A.3 Baseline Data with No Environmental Exposure (T = 60 C)

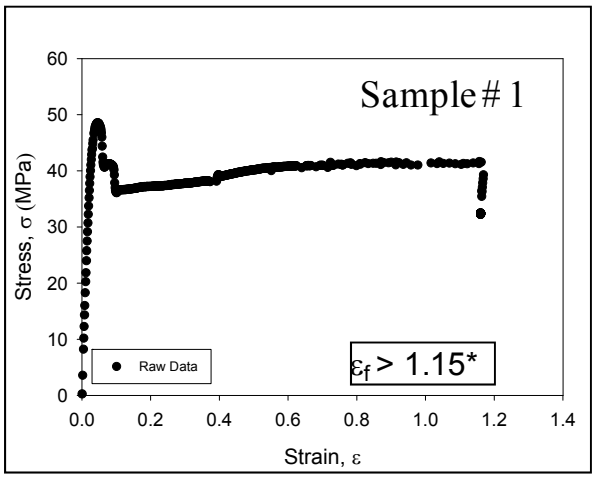

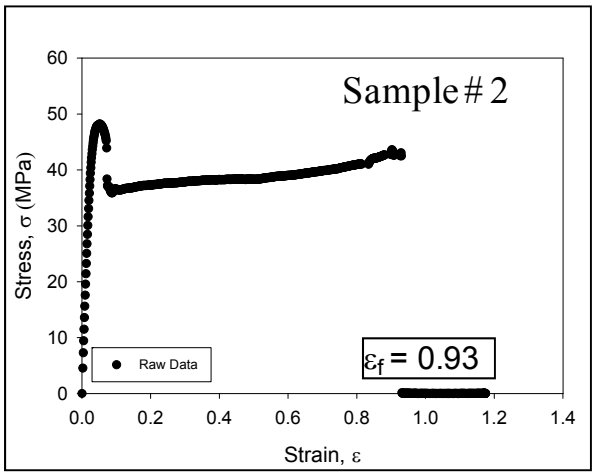

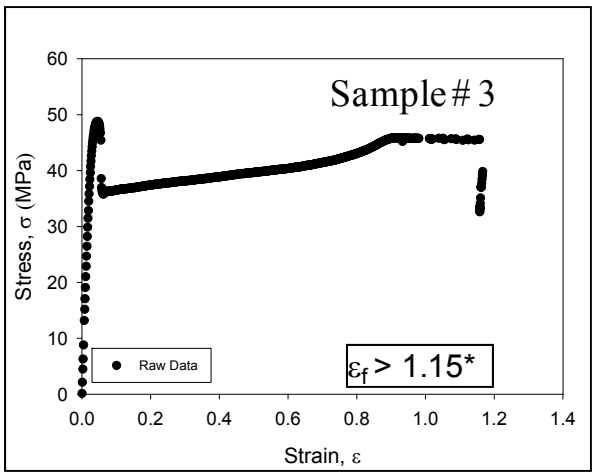

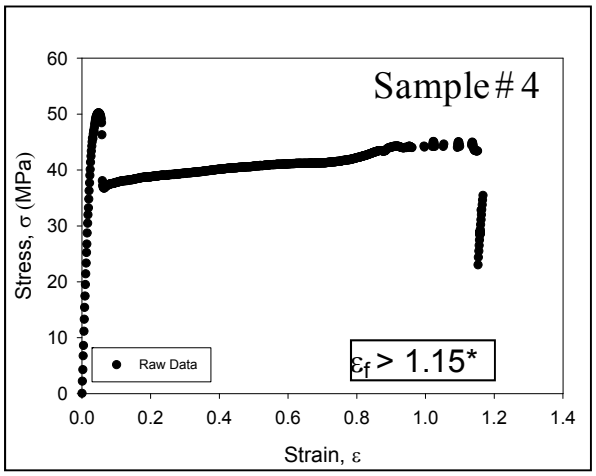

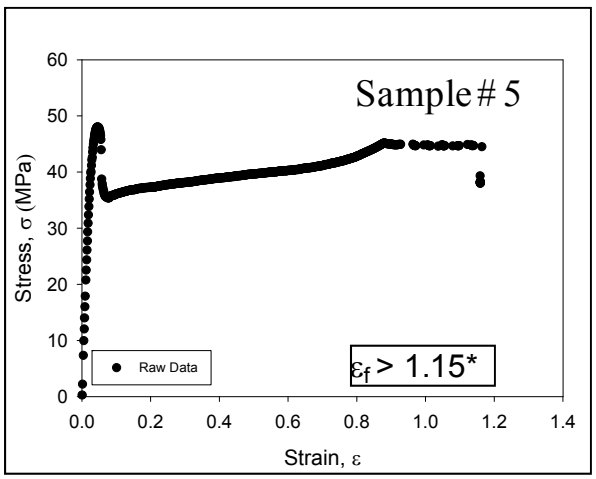

Figure A.3 Raw Data of Stress-Strain Curves for Polycarbonate at T = 60 C

APPENDIX B

STRESS-STRAIN CURVES OF UNDERFILL (UF2) FROM FEA PREDICTION

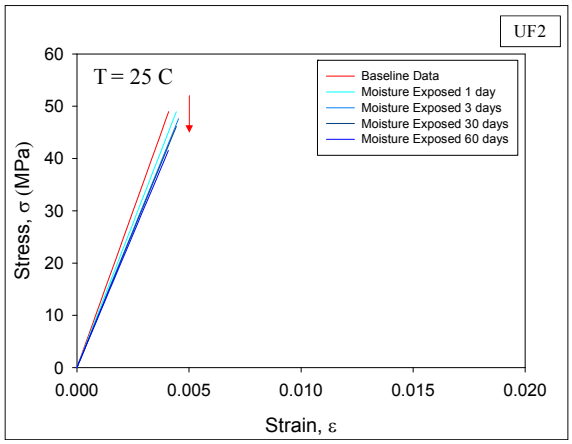

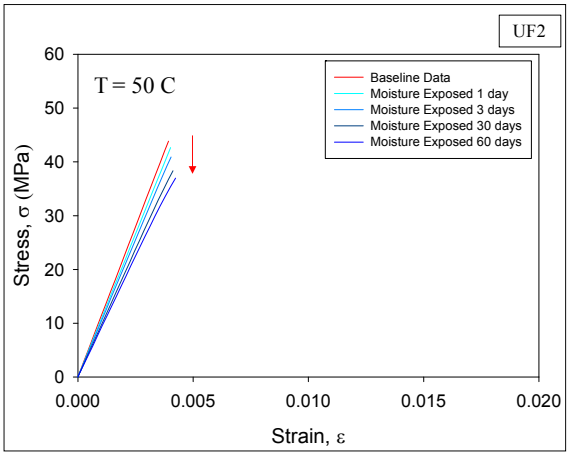

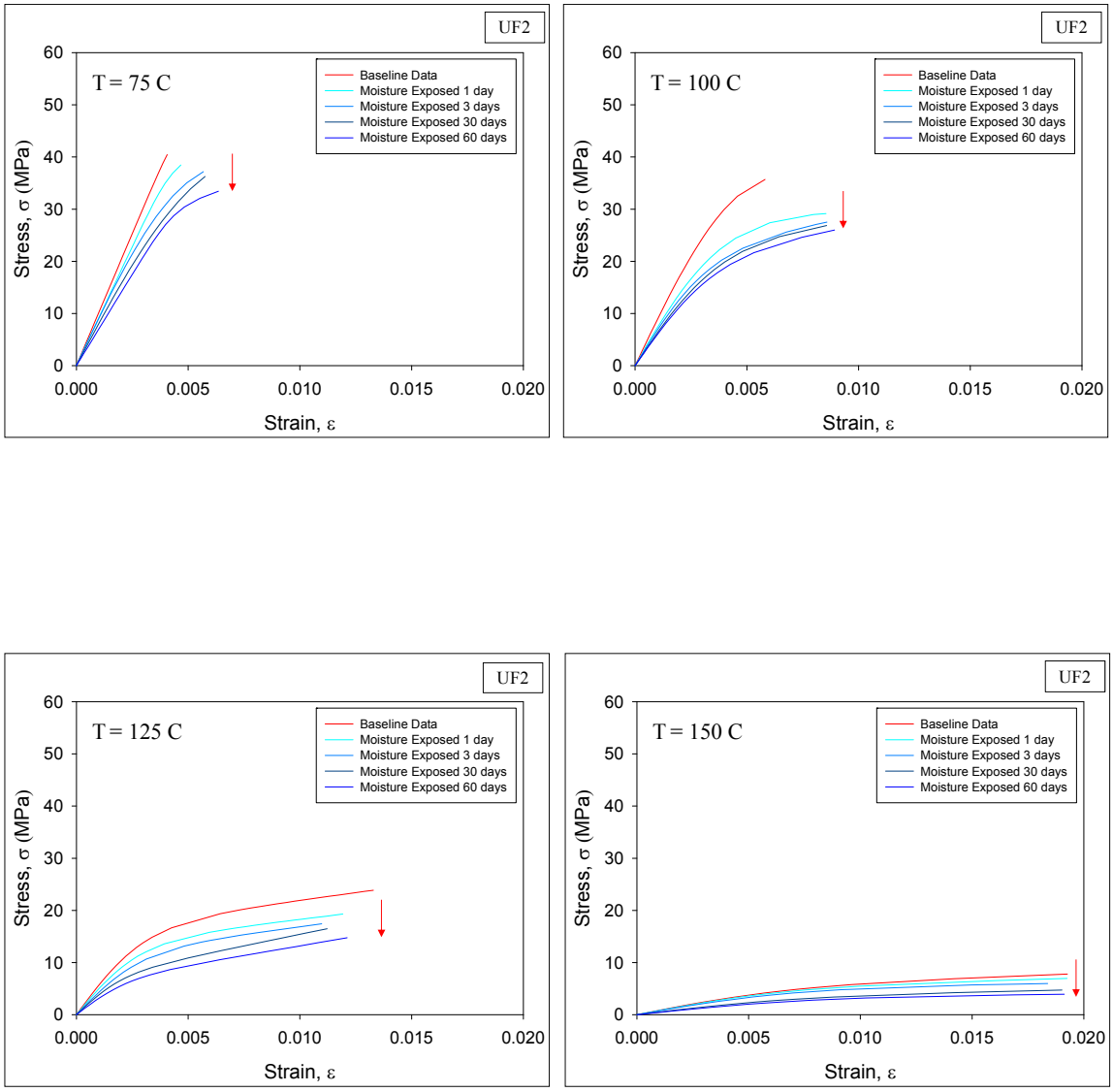

Figure B.1 Comparison of Stress-Strain Curves (from FEA Prediction) of Underfill (UF2) for Moisture Exposed and Dry Sample

APPENDIX C

COMPARISON OF SECONDARY CREEP RATE OF UNDERFILL (UF1)

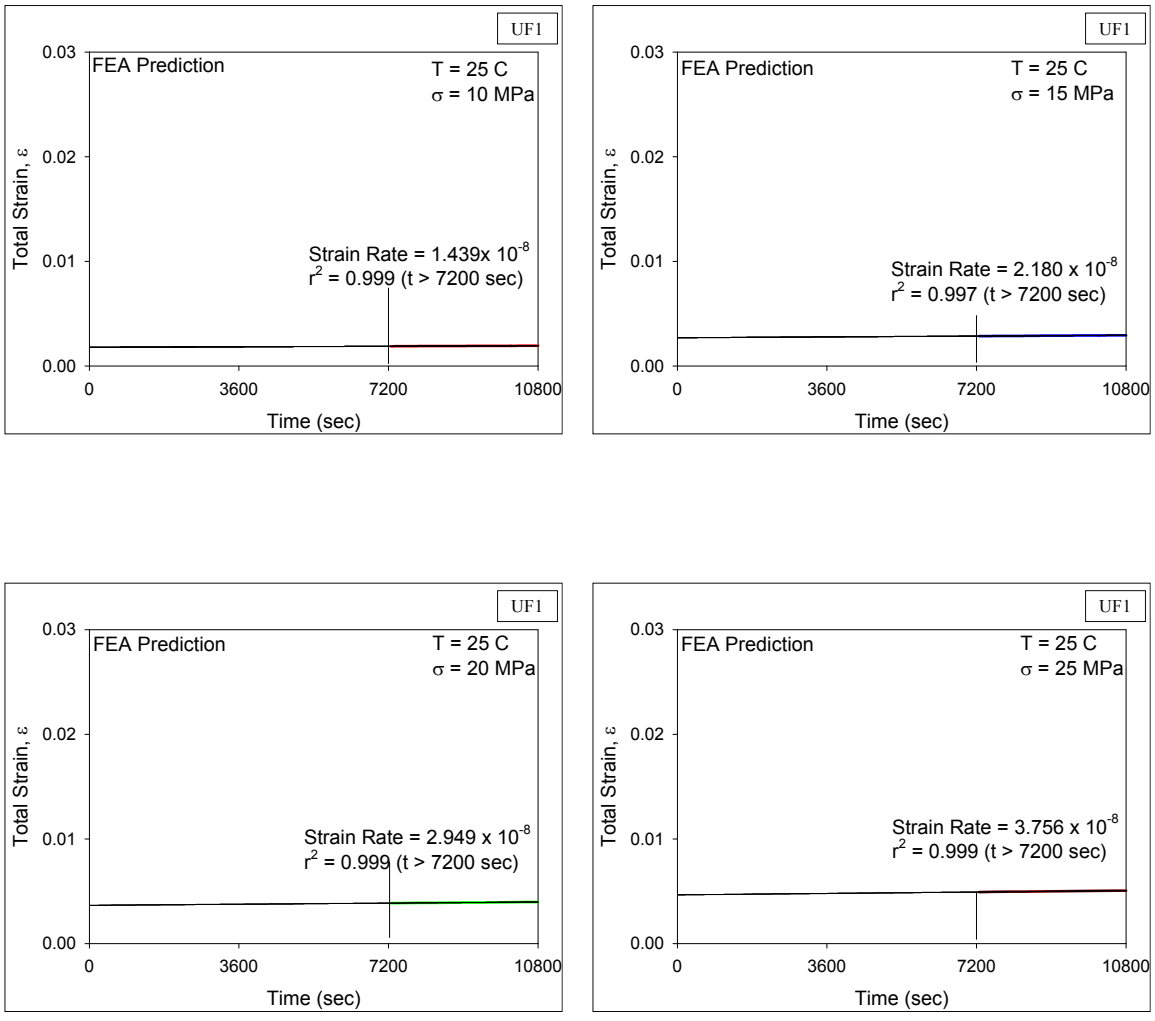

Figure C.1 Determination of Strain Rate from FEA Prediction of Creep Data of UF1 at T = 25 C

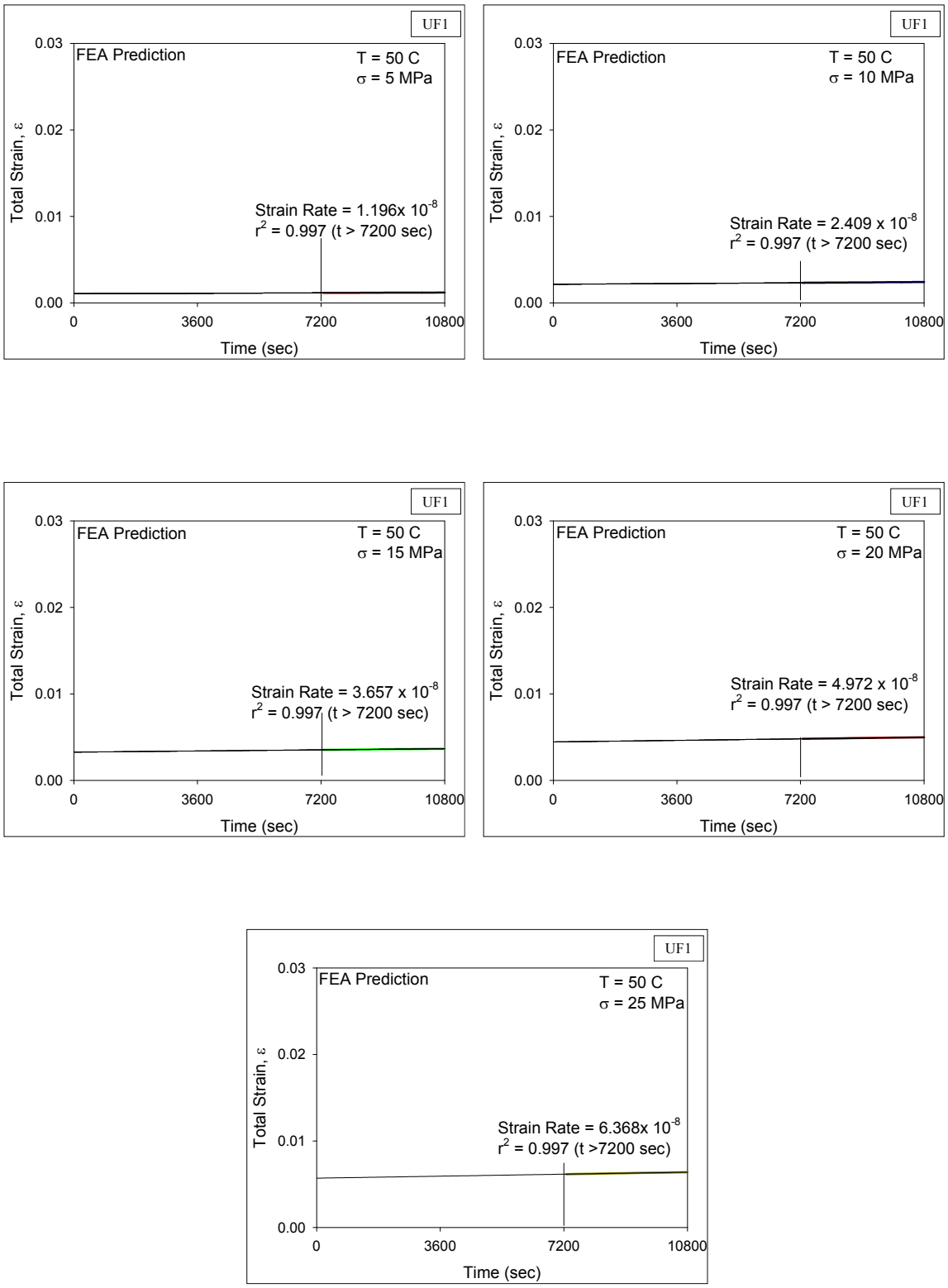

Figure C.2 Determination of Strain Rate from FEA Prediction of Creep Data of UF1 at T = 50 C

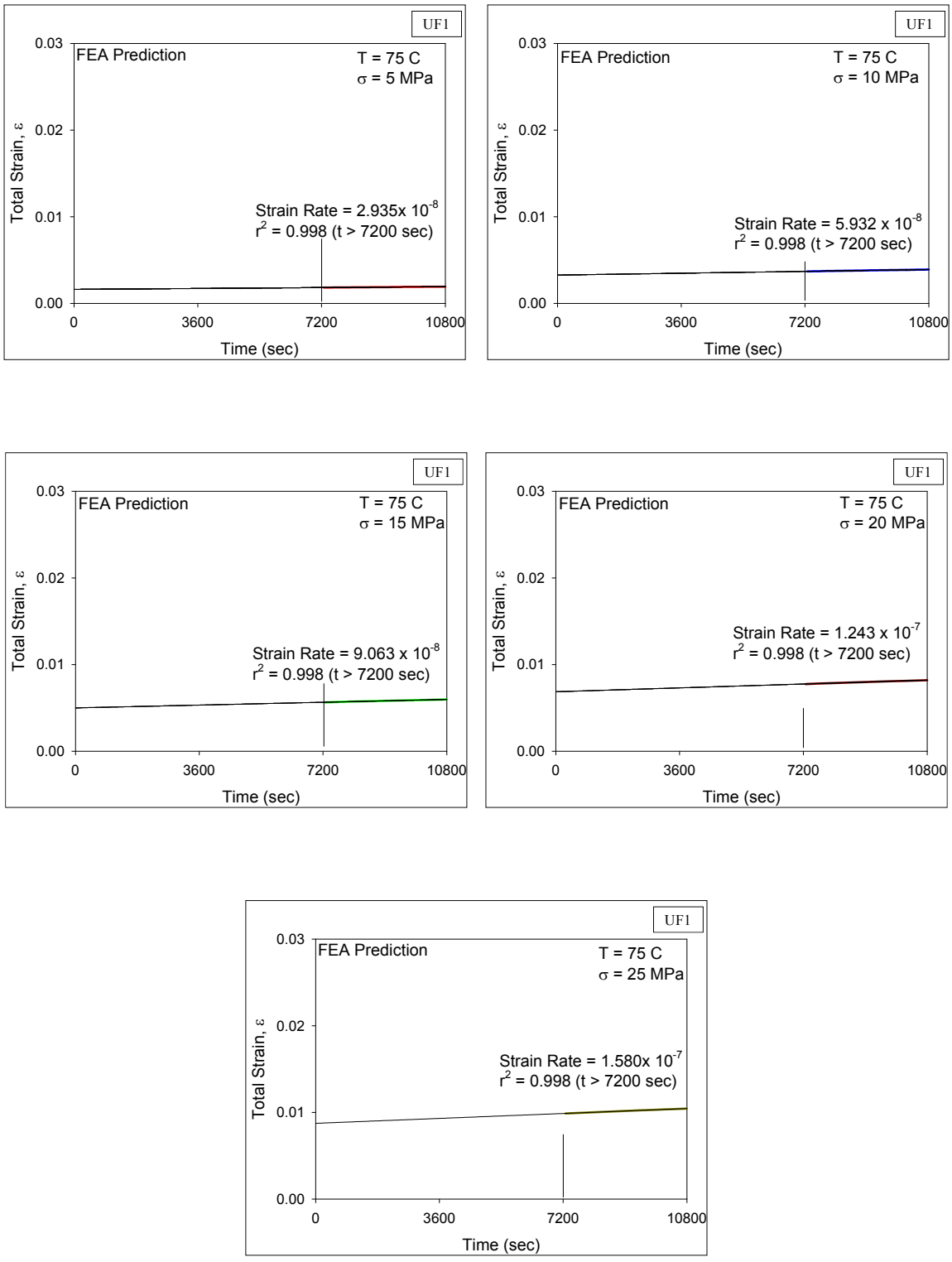

Figure C.3 Determination of Strain Rate from FEA Prediction of Creep Data of UF1 at T = 75 C

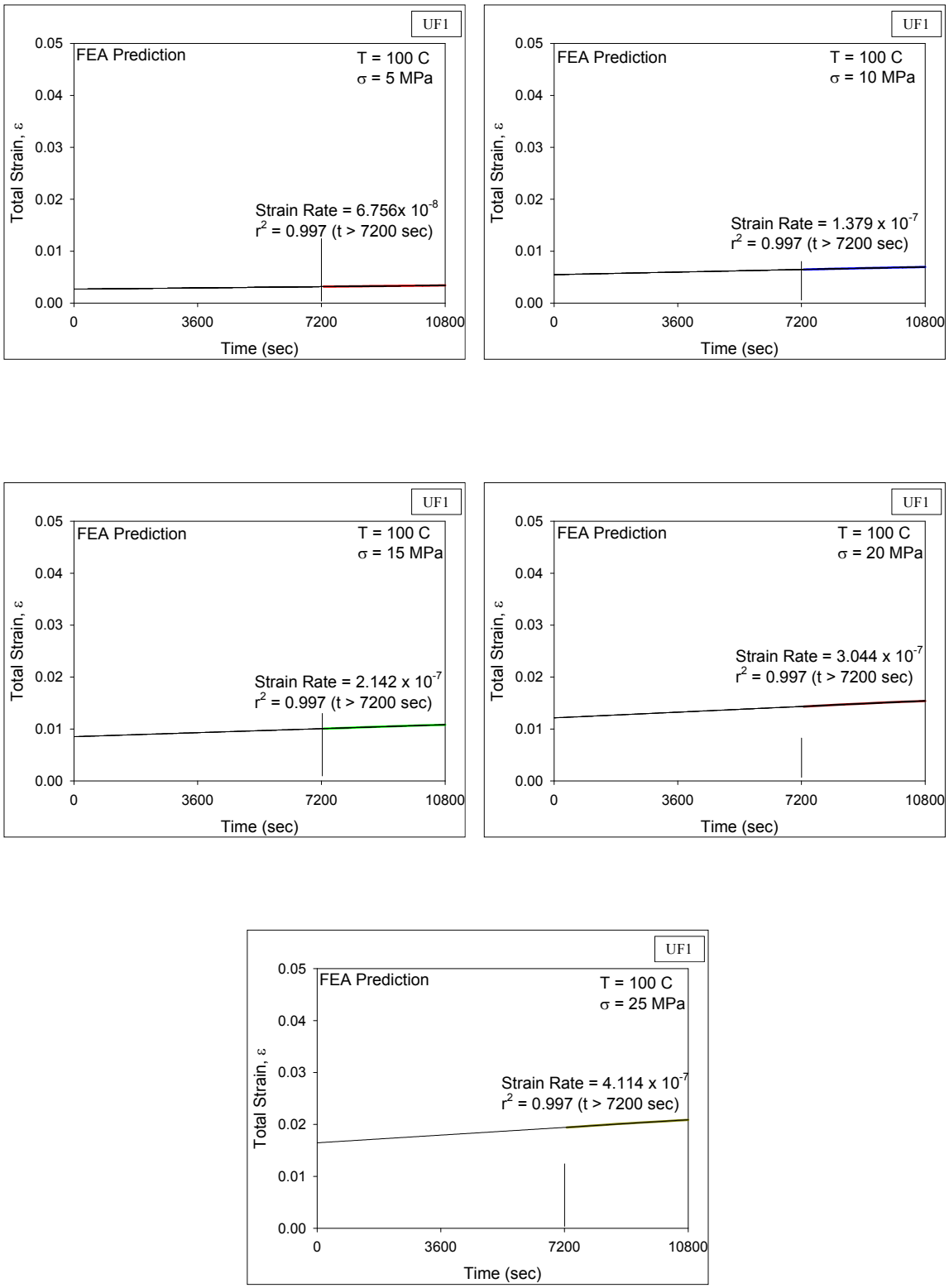

Figure C.4 Determination of Strain Rate from FEA Prediction of Creep Data of UF1 at T = 100 C

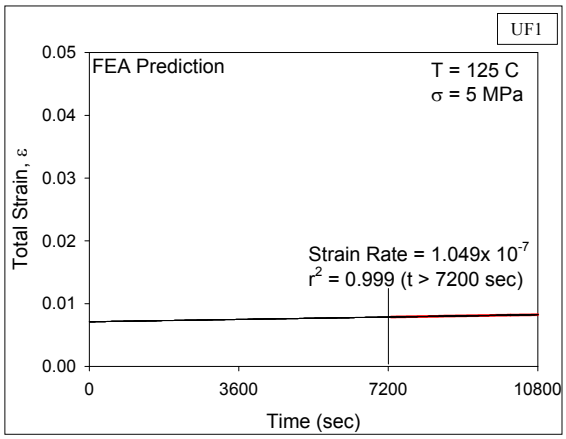

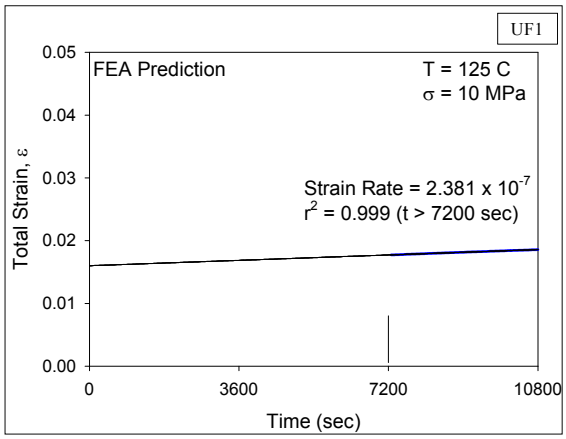

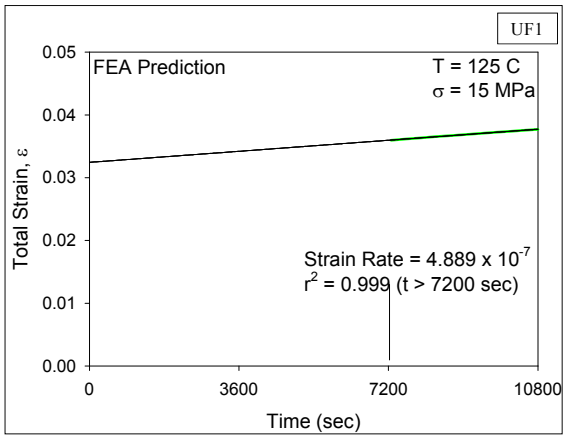

Figure C.5 Determination of Strain Rate from FEA Prediction of Creep Data of UF1 at T = 125 C

APPENDIX D

COMPARISON OF SECONDARY CREEP RATE OF UNDERFILL (UF2) BEFORE MOISTURE ADSORPTION

D.1 Determination of Strain Rate from Experimental Data of UF2

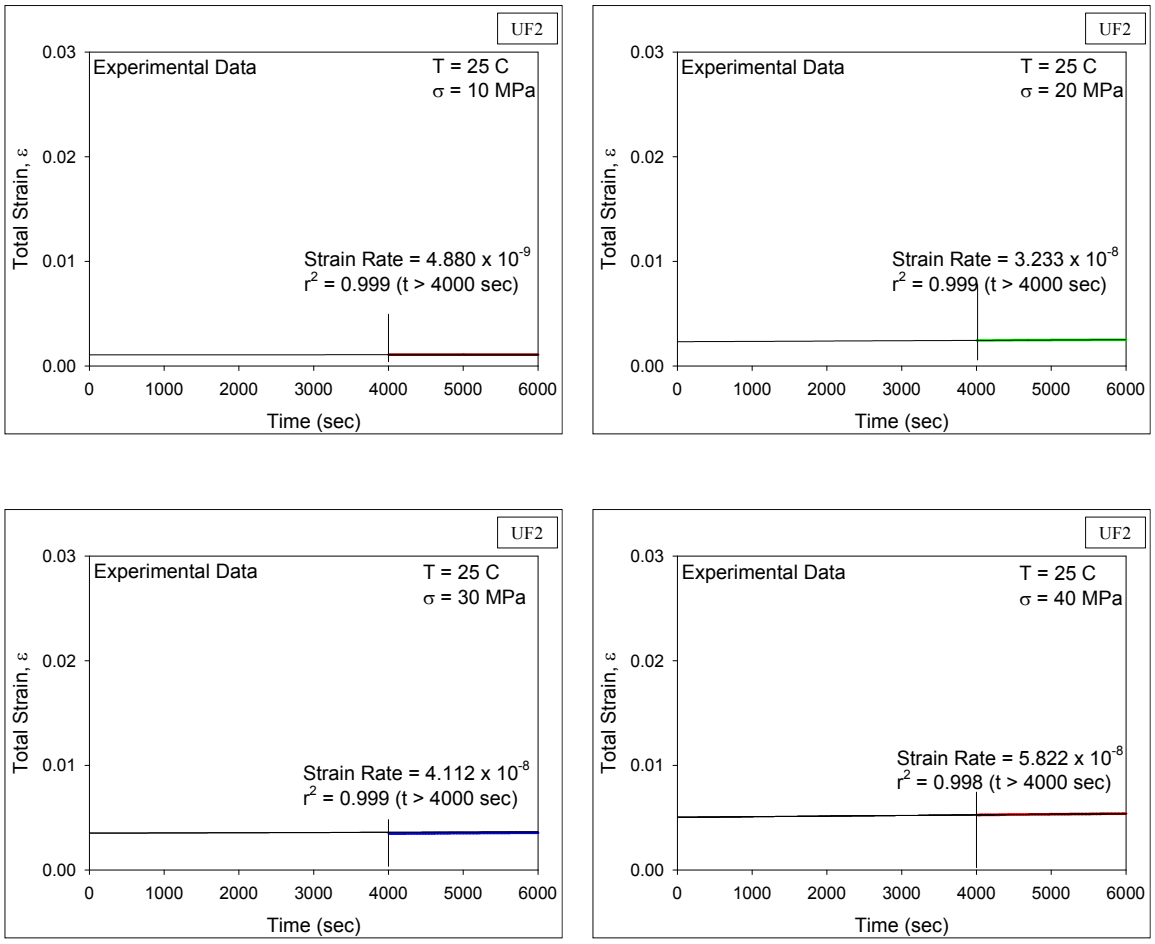

Figure D.1 Determination of Strain Rate from Experimental Creep Data of UF2 at T = 25 C

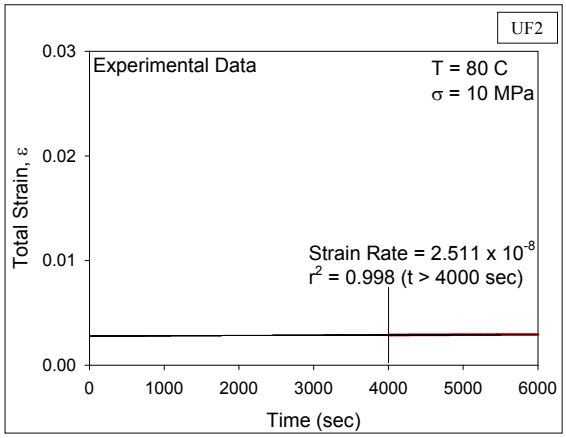

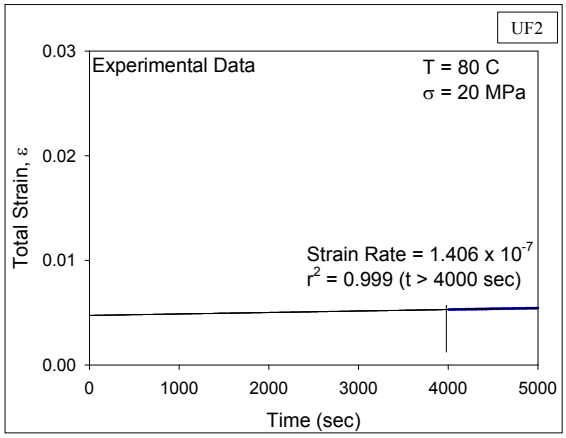

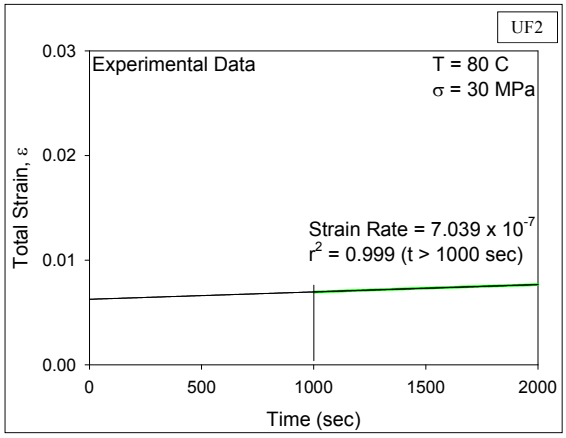

Figure D.2 Determination of Strain Rate from Experimental Creep Data of UF2 at T = 80 C

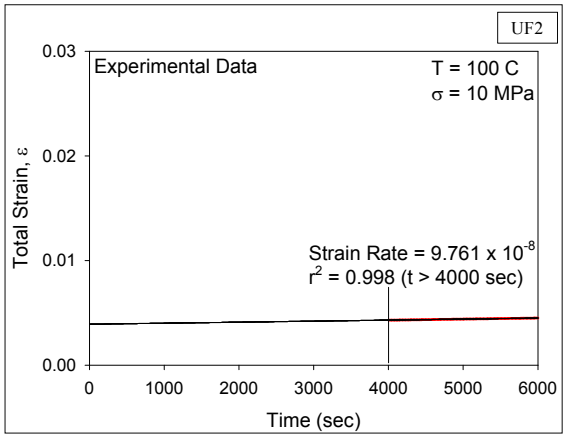

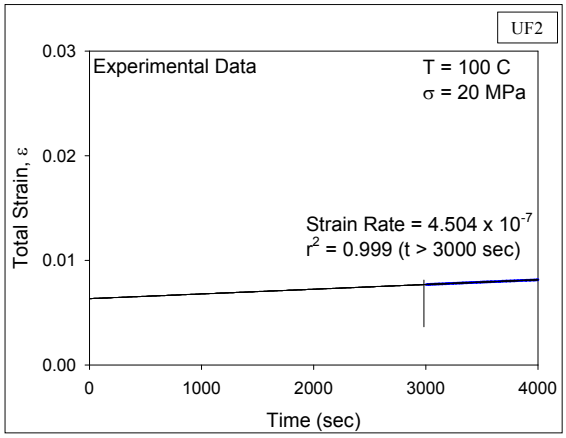

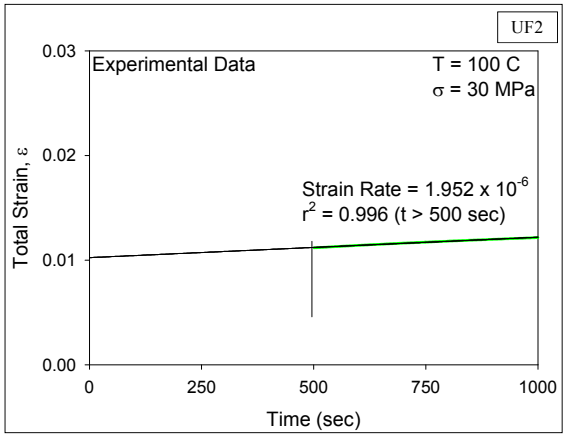

Figure D.3 Determination of Strain Rate from Experimental Creep Data of UF2 at T = 100 C

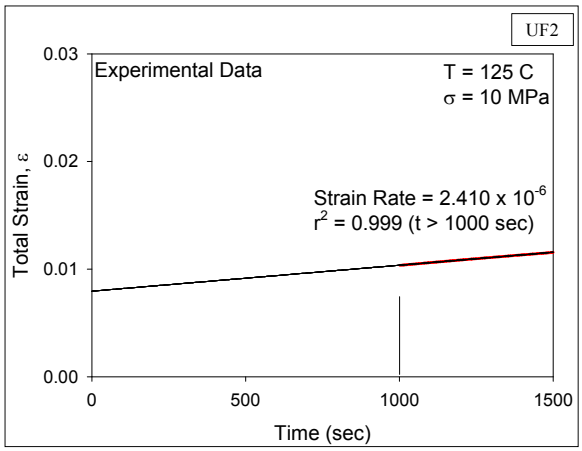

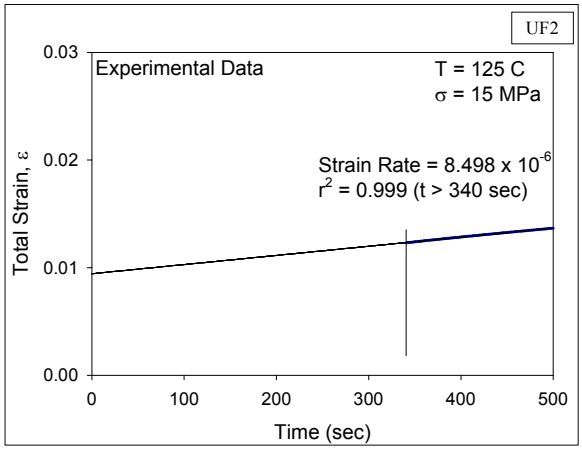

Figure D.4 Determination of Strain Rate from Experimental Creep Data of UF2 at T = 125 C

D.2 Determination of Strain Rate from FEA Prediction of UF2

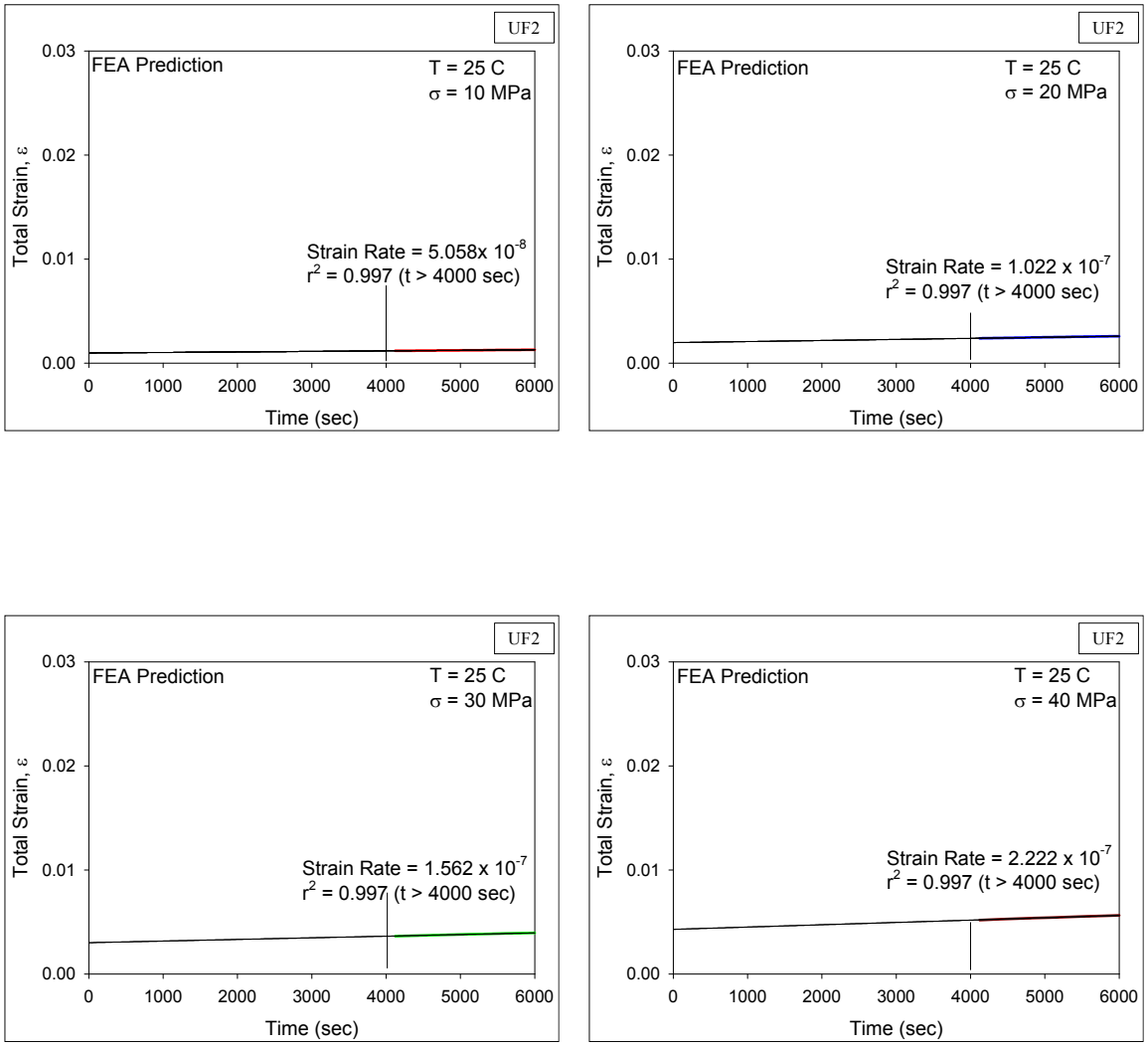

Figure D.5 Determination of Strain Rate from FEA Prediction of UF2 at T = 25 C

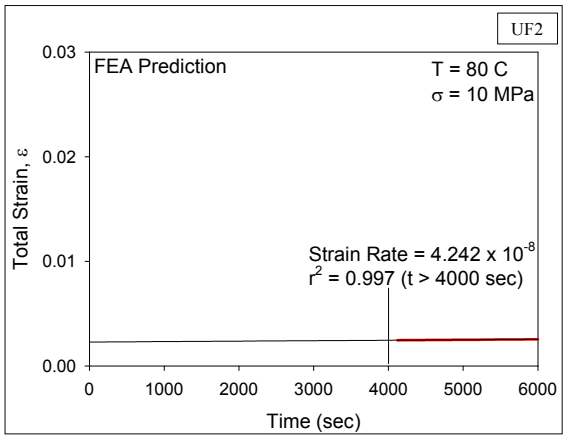

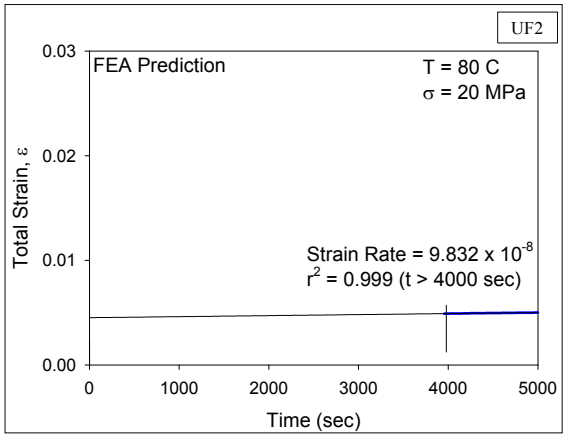

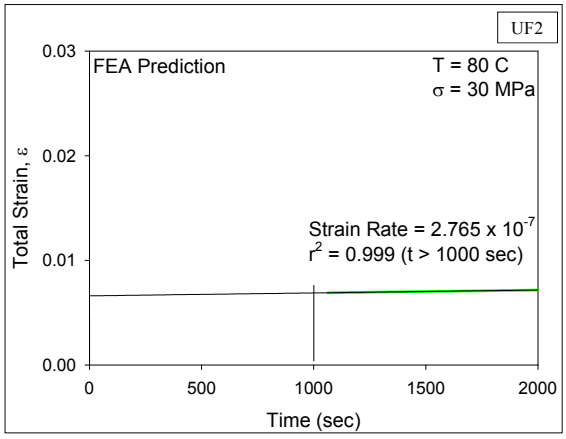

Figure D.6 Determination of Strain Rate from FEA Prediction of UF2 at T = 80 C

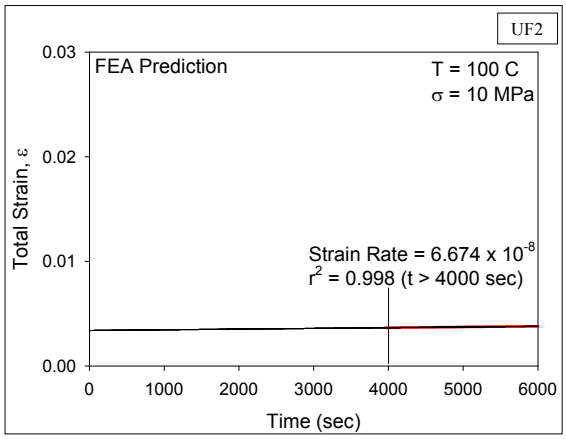

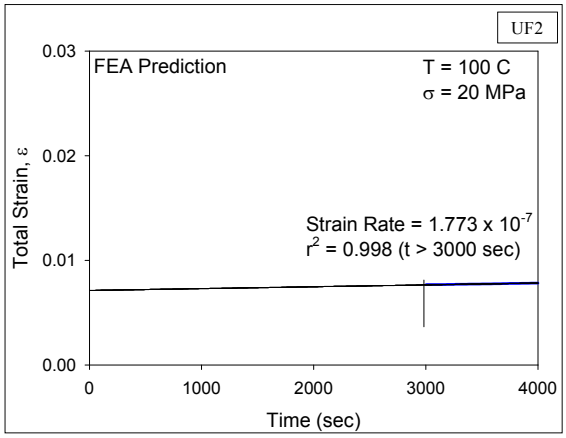

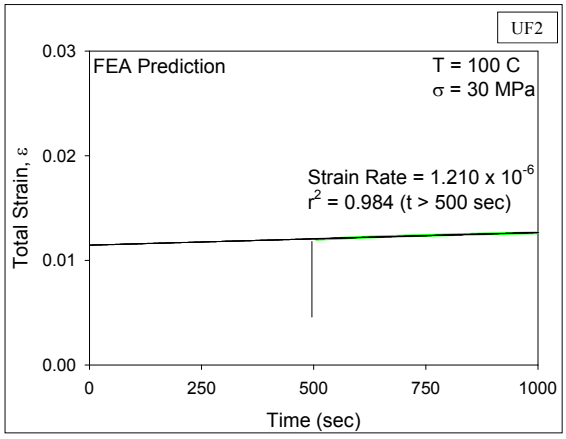

Figure D.7 Determination of Strain Rate from FEA Prediction of UF2 at T = 100 C

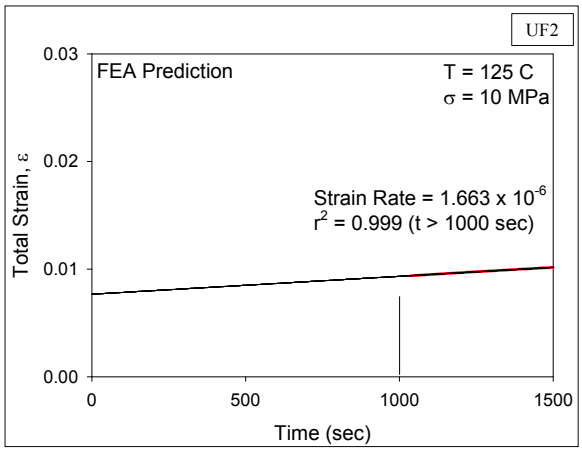

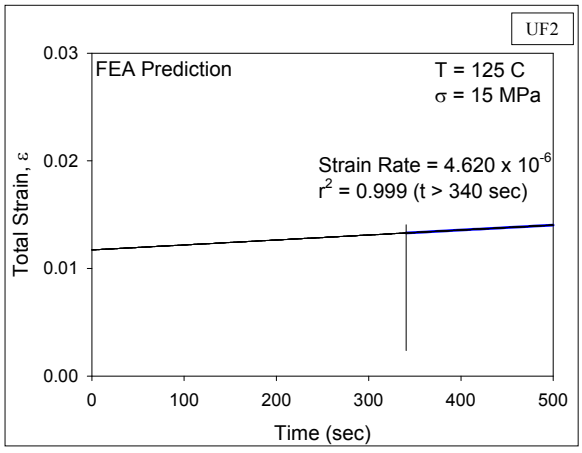

Figure D.8 Determination of Strain Rate from FEA Prediction of UF2 at T = 125 C

D.3 Determination of Strain Rate from Analytical Results of UF2

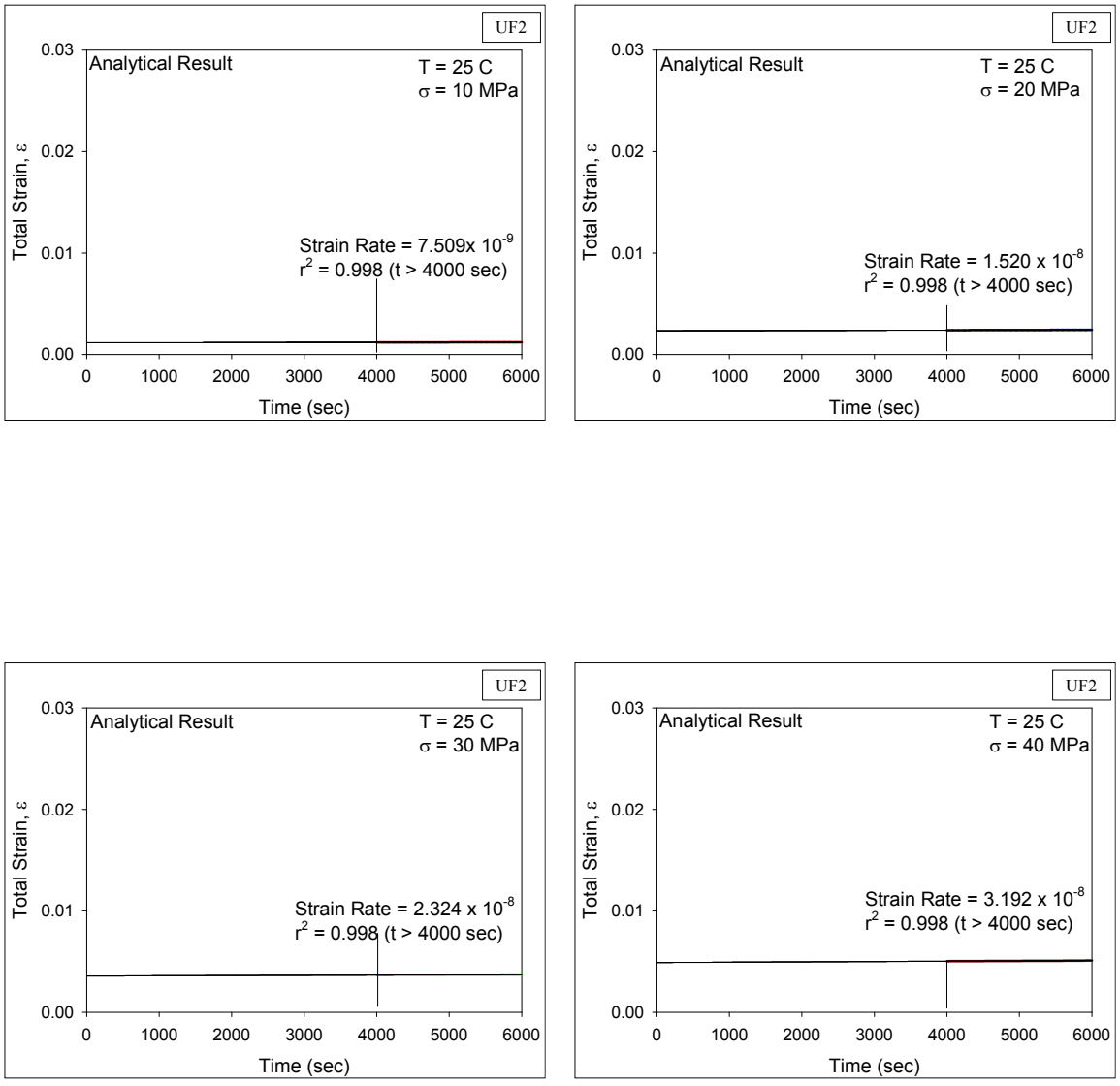

Figure D.9 Determination of Strain Rate from Analytical Result of UF2 at T = 25 C

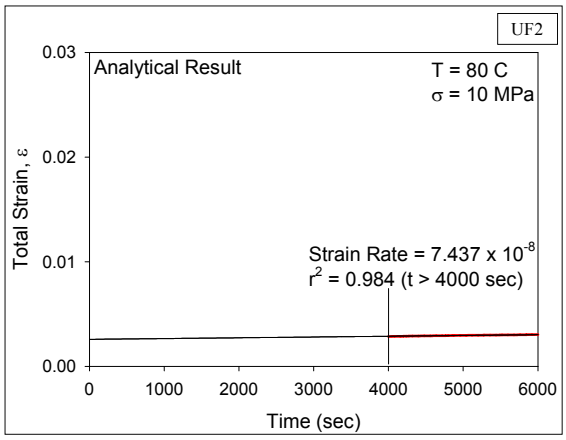

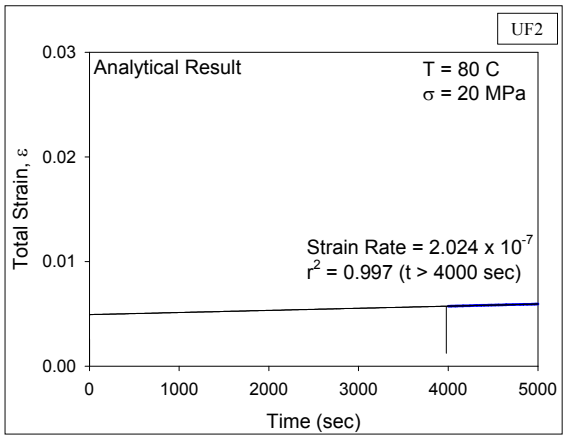

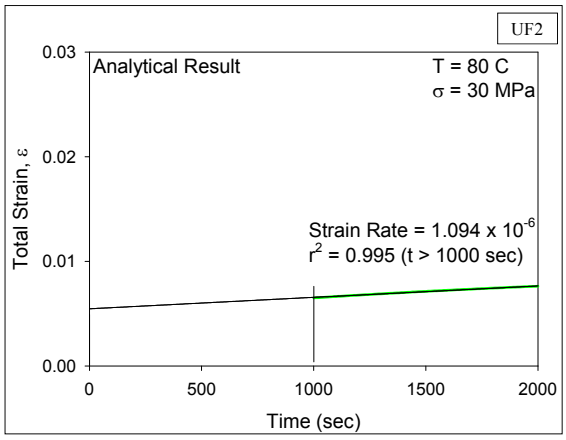

Figure D.10 Determination of Strain Rate from Analytical Result of UF2 at T = 80 C

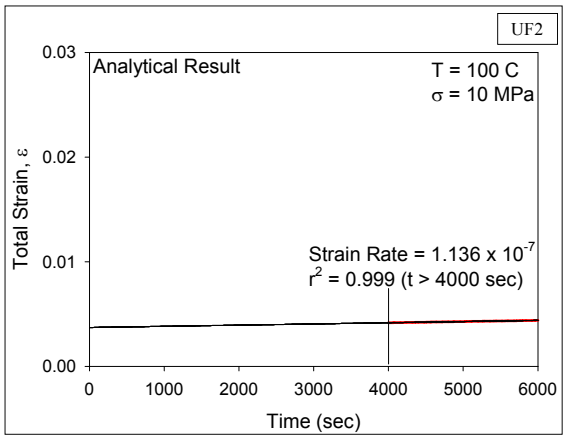

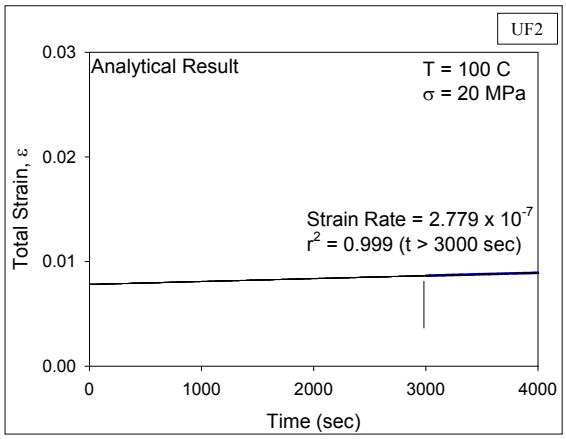

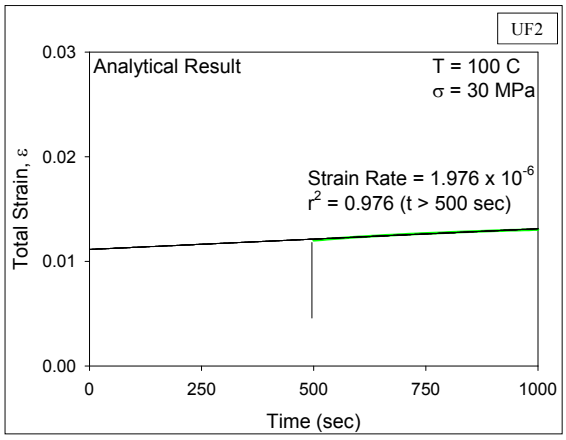

Figure D.11 Determination of Strain Rate from Analytical Result of UF2 at T = 100 C

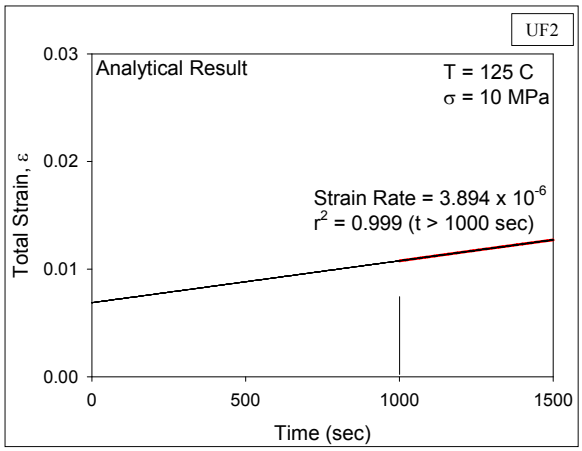

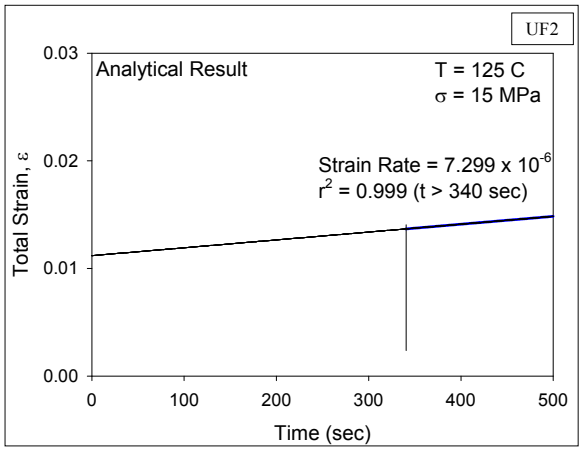

Figure D.12 Determination of Strain Rate from Analytical Result of UF2 at T = 125 C

APPENDIX E

COMPARISON OF SECONDARY CREEP RATE OF UNDERFILL (UF2) AFTER MOISTURE ADSORPTION AT ROOM TEMPERATURE

E.1 Determination of Strain Rate from Experimental Data of UF2

Moisture Exposure for 1 Day at 85 C, 85% RH

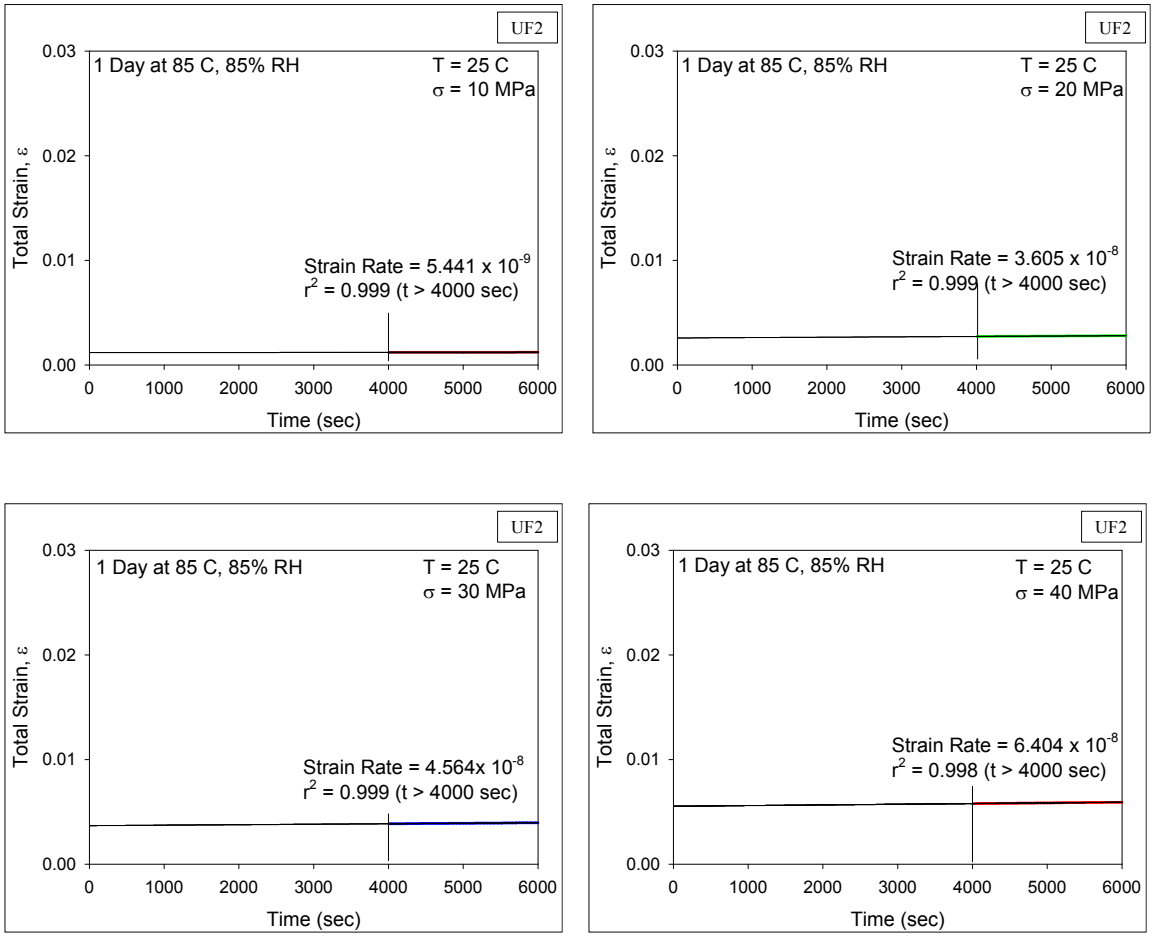

Figure E.1 Determination of Strain Rate from Experimental Data of UF2 at T = 25 C (after 1 Day at 85 C, 85% RH)

Moisture Exposure for 3 Days at 85 C, 85% RH

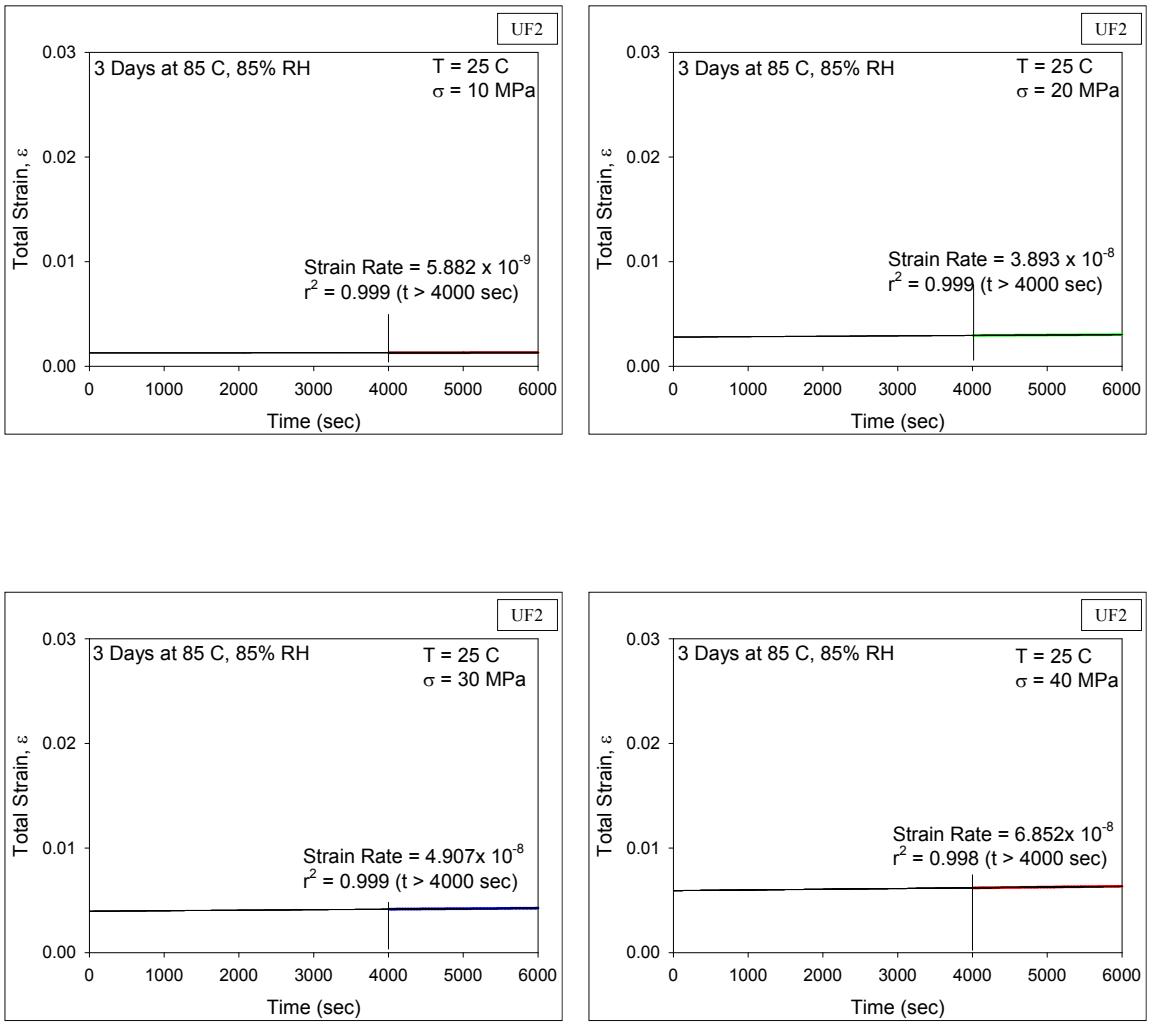

Figure E.2 Determination of Strain Rate from Experimental Data of UF2 at T = 25 C (after 3 Days at 85 C, 85% RH)

Moisture Exposure for 30 Days at 85 C, 85% RH

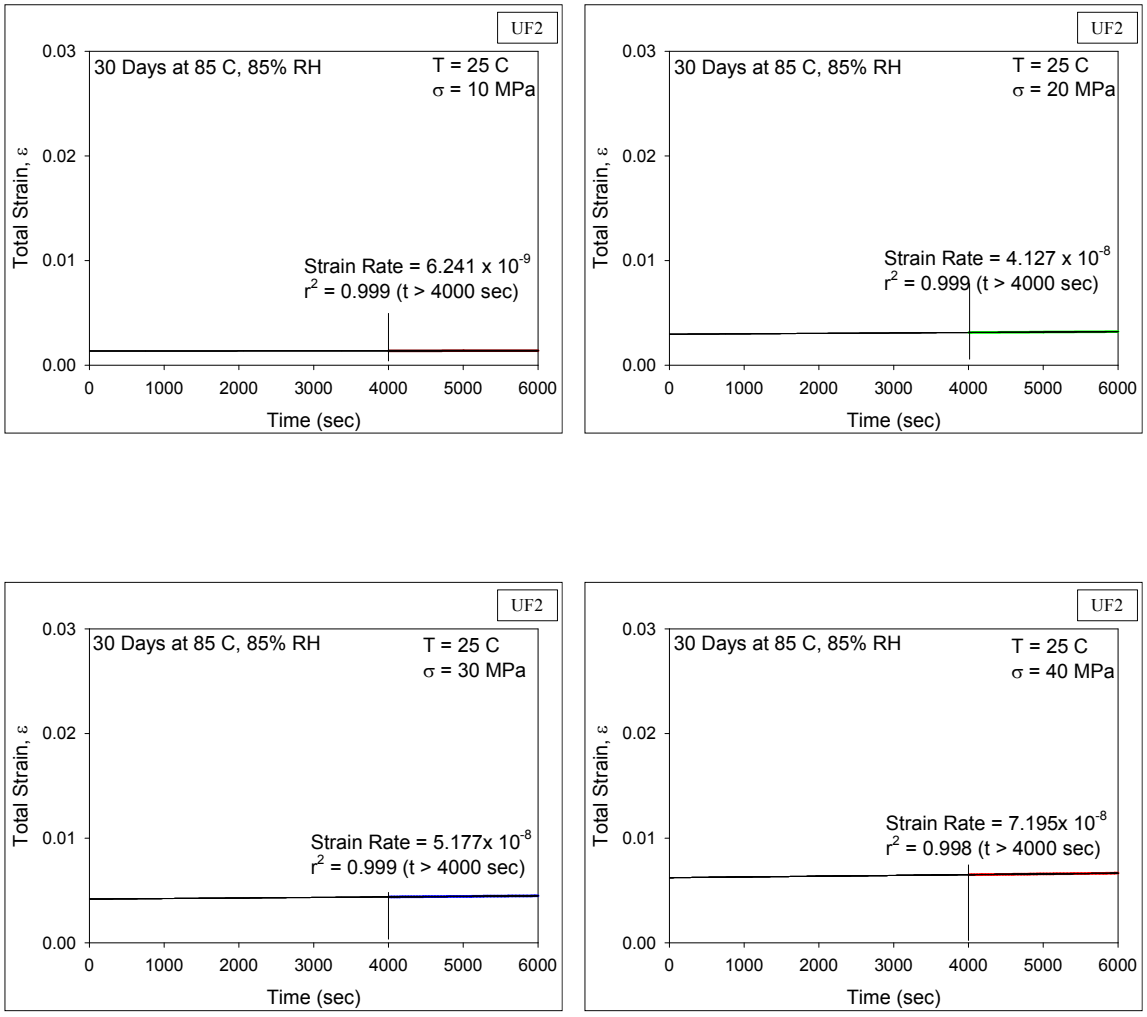

Figure E.3 Determination of Strain Rate from Experimental Data of UF2 at T = 25 C (after 30 Days at 85 C, 85% RH)

Moisture Exposure for 60 Days at 85 C, 85% RH

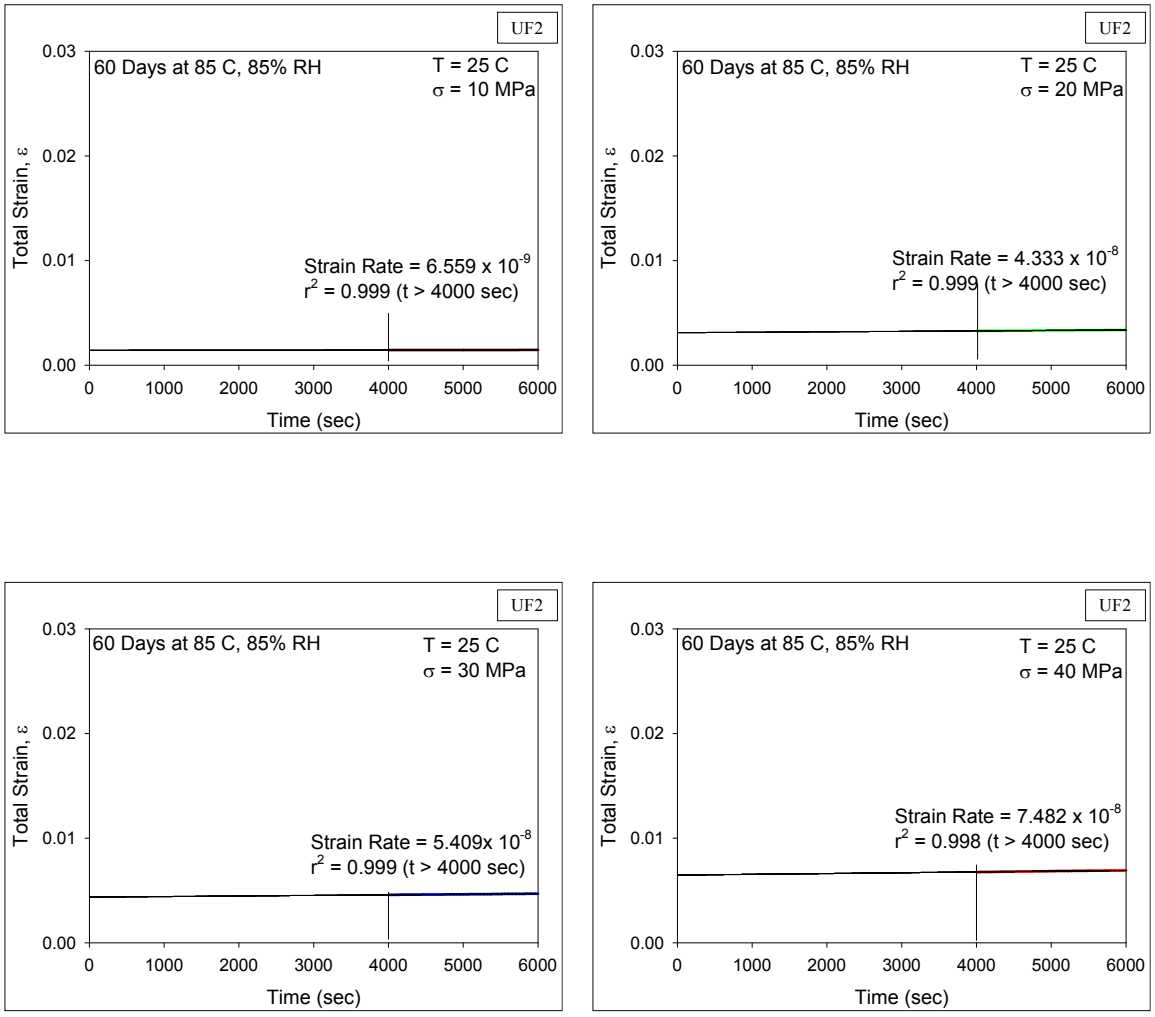

Figure E.4 Determination of Strain Rate from Experimental Data of UF2 at T = 25 C (after 60 Days at 85 C, 85% RH)

APPENDIX F

MATLAB CODE FOR CREEP PROBLEM

```
%=====================Creep Analysis ==========================
clc;
clear;
syms t x
E=7562.6;              %Secant Modulus
nw=0.35;               %Poisson's Ratio
T=100;                 %Temperature (C)
stress=20;             %Stress Level
ainfg=0.01179;
ainfk=0.04815;
%*****************Prony Constants*****************************
ag=[0.30055 0.19892 0.32473 0.16401];
ak=[0.90618 0.00499 0.01633 0.01703 0.00732];
tg=[44.13 1378.1 35530 9.8788e5];
tk=[0.00195 9.2235 136.43 10921 3.1206e5];
%====================Sfift Function============================
Tr=106.63;
c1=-50.064;
c2=-651.89;
a=-(c1*((T+273)-(Tr+273))/(c2+((T+273)-(Tr+273))));
cc=10.^a;
tgT=cc*[44.13 1378.1 35530 9.8788e5];
tkT=cc*[0.00195 9.2235 136.43 10921 3.1206e5];
%=================================================================
Go=E/(2*(1+nw));
Ko=E/(3*(1-2*nw));
sum1=0;
sum2=0;
n=1;
m=1;
q=1;
z=2;
c=laplace(x);
%*****************Deviatoric part*****************************
for i=1:1:4
    igg=Go*ag(i)*exp(-(x/tgT(i)));
    sum1=sum1+igg;
end;
ig=2*(Go*ainfg+sum1);
Dev=laplace(ig);

%*****************Volumetric part*****************************
for j=1:1:5
    jkk=Ko*ak(j)*exp(-(x/tkT(j)));
    sum2=sum2+jkk;
end;
```

```
jk=3*(Ko*ainfk+sum2);
Vol=laplace(jk);
%*****************Creep calculation*****************************
J1L=c/Dev;
ss=(2/3)*stress*laplace(dirac(x-z));
a=J1L*ss;
dd=ilaplace(a);
for t=0:10:6100
    ddd(m)=double(subs(dd));
    m=m+1;
end;
dddd=ddd';

J2L=c/Vol;
ss=stress*laplace(dirac(x-z));
b=J2L*ss;
vv=ilaplace(b);
for t=0:10:6100
    vvv(q)=double(subs(vv));
    time(n)=t;
    n=n+1;
    q=q+1;
end;
vvvv=vvv';
%***************Total Strain*********************************
strain=dddd+(1/3)*vvvv;

     sum1=0;
     sum2=0;
     timel=time';
%================================end============================
```

APPENDIX G

MATLAB CODE FOR STRESS-STRAIN PROBLEM

```
%======================Stress-Strain Analysis ========================

clc;
clear;
syms x s
T=25;                %==========Temperature
E=11957;             %==========Elastic Modulus
UT=0.35 ;
nw=0.35;
ainfg=0.01179;
ainfk=0.04815;
L=60 ;
%******************Prony Constants*****************************
ag=[0.30055 0.19892 0.32473 0.16401];
ak=[0.90618 0.00499 0.01633 0.01703 0.00732];
tg=[44.13 1378.1 35530 9.8788e5];
tk=[0.00195 9.2235 136.43 10921 3.1206e5];
%====================Sfift Function============================
Tr=106.63;
c1=-50.064;
c2=-651.89;
a=-(c1*((T+273)-(Tr+273))/(c2+((T+273)-(Tr+273))));
cc=10.^a;
tgT=cc*[44.13 1378.1 35530 9.8788e5];
tkT=cc*[0.00195 9.2235 136.43 10921 3.1206e5];
%=============================================================
Go=E/(2*(1+nw));
Ko=E/(3*(1-2*nw));
sum1=0;
sum2=0;
l=1;
n=1;
m=1;
q=1;
b=1;
d=1;
u=0;
r=1;
f=1/s;
c=ilaplace(f);
p=laplace(c);
%******************Deviatoric part*****************************
for i=1:1:4
    igg=Go*ag(i)*exp(-(x/tgT(i)));
    sum1=sum1+igg;
end;
```

```
ig=2*(Go*ainfg+sum1);
G1=laplace(ig);
%******************Volumetric part*****************************
for j=1:1:5
    jkk=Ko*ak(j)*exp(-(x/tkT(j)));
    sum2=sum2+jkk;
end;
jk=3*(Ko*ainfk+sum2);
G2=laplace(jk);
%***************** calculation*****************************
sum2=0;
sum1=0;
ulimit=UT;           %==========maximum displacement
delu=ulimit/5;      %==========
Ea=((3*G1*G2)/(G1+2*G2));

for t=1:1:5 %==========
strain=sqrt(((1+(u/L))^2)+(0.054*(-nw*u/L))^2+(8.3e-3*(-nw*u/L))^2)-1;
Ess=ilaplace(Ea);
Esss(b)=double(subs(Ess));
b=b+1;
u=u+delu;
strain2(l)=strain;
l=l+1;
time(n)=t;
n=n+1;
end;
m=1;
l=1;
Et(1)=E;
stressK(1)=0;
for i=1:1:5          %==========
 Et(i+1)=Esss(i);
end
for m=2:1:5   %==========
dst=strain2(m)-strain2(m-1);
dss=Et(m-1)*dst;
stressK(m)=stressK(m-1)+dss;
end
strainF=strain2';
stressF=stressK';
%======================end=========================================
```